

***Understanding shell cracking during de-wax
process in investment casting***

By

Kevin Lee

A thesis submitted to the School of Engineering

Of the University of Birmingham

For the degree of

Doctor of Philosophy

Department of Chemical Engineering

School of Engineering

University of Birmingham

September 2015

word count: 48623

UNIVERSITY OF
BIRMINGHAM

University of Birmingham Research Archive

e-theses repository

This unpublished thesis/dissertation is copyright of the author and/or third parties. The intellectual property rights of the author or third parties in respect of this work are as defined by The Copyright Designs and Patents Act 1988 or as modified by any successor legislation.

Any use made of information contained in this thesis/dissertation must be in accordance with that legislation and must be properly acknowledged. Further distribution or reproduction in any format is prohibited without the permission of the copyright holder.

ABSTRACT

In investment casting, the removal of wax from the shell is a critical step which may cause shell failure. It would be advantageous to predict the stress development during de-waxing process with computer simulation. The process was simulated with the consideration of two aspects: (i) The thermo-physical data required to model the shell and wax behaviour in the autoclave environment and (ii) A simulation capable of capturing the interaction between shell, wax and the autoclave environment. Data on mechanical properties, thermal properties, permeability, rheology, thermal expansion and density was gathered for wax and shell as appropriate. FLOW-3D® was used to simulate the de-wax process such that the shell and wax can be simultaneously modelled. It is shown that the Von misses stress exceeded the expected critical failure stress at certain nodes after steam was introduced to the system. Waxes with higher viscosity were predicted to reach the critical stress sooner. The simulation showed that for the selected drainage orifice sizes there was no or little difference in the time taken to reach the critical stress. Wax compressibility which was considered to represent shell permeability was predicted to have a large effect on shell cracking prediction. In general, the statistics of failure in validation test limited the conclusions that could be drawn. Waxes predicted to show differences in cracking and drainage with increasing orifice size did so in the experiment. The simulated drainage times were greater than determined experimentally by around 380 s and this requires further investigation.

ACKNOWLEDGEMENT

First and foremost I want to thank my supervisor Stuart Blackburn. I appreciate all his contributions including the technical advices and time for proof reading this thesis. I am also thankful for his motivation during the Ph.D pursuit and the positive comments that he gave which had always reassured the confidence in my work. He has taught me to be a better researcher both consciously and unconsciously.

I also thank my industrial supervisor Stewart T. Welch for proposing this Ph.D. He has been patiently keeping track of the work progress every month and offer helpful comments. I would also like to acknowledge the in depth introduction of modelling work and MATLAB® by my secondary supervisor Phillip Robbin which lead to a better understanding on how finite difference works.

I have appreciated the advice from Hector Basoalto on the methods to analyse the stress on shell calculated by FLOW-3D. I also thank Dan Milano from Flow Science, Inc. for the modelling support all the way from creating CAD files to exporting results file. I also thank Alex Cendrowicz for the insightful discussion on experiment procedures and Paul Withey for the derivation of Young's modulus for the wedge geometry. Thanks also Samantha Jones and Chen Yuan for sharing their expert knowledge in investment casting process with me. I must also thank the technicians - Grant Holt, John Wedderburn, Katy Lewis, Frank Biddlestone and Carl Meggs for their technical support and setting up testing equipment for surface tension, thermal expansion and de-waxing flow rate test.

I gratefully acknowledge the funding from Birmingham University and Rolls Royce Plc that made my Ph.D work possible. I am also grateful to use the IRC facilities to carry out

most of the investment casting work. I would like to thank the Casting group for allowing me to use their FLOW-3D® licenses and PRISM2 for their supercomputer. I also appreciate the experimental advices from James Bowen who also carried out the tests on the Micromeritics Auto Pore IV Mercury Porosimeter and MicroXAM2 Interferometer. These instruments were obtained through Birmingham Science City: Innovative Uses for Advanced Materials in the Modern World (West Midlands Centre for Advanced Materials Project 2), with support from Advantage West Midlands (AWM) and part funded by the European Regional Development Fund (ERDF). I would also like to thank the Materials and Metallurgy Department allowing me to use the facilities such as Scanning Electron Microscopy and X-ray Diffraction.

Lastly, I would like to thank my parents for their constant encouragement to finish this thesis. Thanks.

Table of Contents

1. INTRODUCTION	1
1.1 The investment casting process	1
1.2 De-waxing process and issues	4
1.3 Motivation of the Project	11
1.4 Objective	12
2. LITERATURE REVIEW	14
2.1 Microstructure of wax	14
2.2 Permeability and Porosity	14
2.3 Mechanical Properties of Shell	18
2.4 Thermal expansion and density	24
2.5 Specific heat capacity	27
2.6 Wax melting point	28
2.7 Thermal conductivity	30
2.8 Rheological behaviour	32
2.8.1 Rotational rheometer	32
2.8.2 Capillary rheometer	34
2.9 Surface tension	35
2.10 Interface heat transfer coefficient	36
2.11 Numerical Simulation of the Process	39
PART 1 – MATERIALS CHARACTERISATION	42
3. MATERIALS AND METHOD	43
3.1 Microstructure	50
3.1.1 Scanning Electron Microscope (SEM)	50
3.1.2 Reflective optical microscope	51
3.1.3 Interferometer	51
3.1.4 Transmission Light Optical Microscope	52
3.2 Chemical compound analysis	54
3.3 Permeability	54

3.4	Flexure strength	58
3.4.1	Flat bar test	58
3.4.2	Wedge test	60
3.5	Young's modulus	61
3.5.1	Flat bars	61
3.5.2	Wedge geometry	64
3.6	Density and Thermal Expansion	65
3.6.1	Density	65
3.6.2	Thermal expansion	67
3.7	Specific heat capacity	72
3.8	Thermal conductivity	73
3.9	Parallel plate rheometry	77
3.10	Capillary rheometry	80
3.11	Surface tension/Adhesion tension of wax	83
4.	RESULTS AND DISCUSSION	92
4.1	Microstructure	92
4.2	Chemical compound analysis	101
4.3	Permeability	103
4.4	Flexure strength	104
4.4.1	Three point bend test	104
4.4.2	Wedge test	114
4.5	Young's modulus	116
4.5.1	Flat bars	116
4.5.2	Wedge geometry	118
4.6	Density and thermal expansion	119
4.6.1	Shell density	119
4.6.2	Shell Thermal expansion	121
4.6.3	Wax Density	122
4.6.4	Wax Thermal Expansion	123
4.7	Specific heat capacity	127
4.8	Solid to liquid phase transformation	129
4.9	Thermal conductivity	132
4.10	Parallel plate rheometry	139
4.11	Capillary rheometry	147

4.12	Surface tension/Adhesion tension of wax	152
PART 2 – MODELLING		158
5. COMPUTER SIMULATION		159
5.1	Theoretical basis of the model	160
5.1.1	Heat transfer	163
5.1.2	Solidification drag model	167
5.1.3	Viscosity	167
5.1.4	Gravity/Force	171
5.1.5	Surface tension	171
5.1.6	Density evaluation	173
5.1.7	Bubbles and phase change	176
5.1.8	Elastic stress model	178
5.1.9	Fluid structure interaction (FSI) model	179
5.2	Modelling procedure	181
5.2.1	Mesh Type	182
5.2.2	Model conditions	184
5.2.3	Model assumptions	184
5.2.4	Stress analysis method	185
5.3	Results and discussion	188
5.3.1	Shell stress analysis	188
5.3.2	Sensitivity analysis	198
6. MODEL VALIDATION		205
6.1	Procedures	205
6.1.1	Visual shell cracking inspection	206
6.1.2	Mould discharge flow rate	207
6.2	Results and discussion	211
7. CONCLUSION AND FUTURE WORK		220
7.1	Conclusions	222
7.2	Future work	226
8. REFERENCES		231
9. PUBLICATIONS		237
10. APPENDICES		238

List of Figures

Figure 1-1: Stages in the investment casting process.....	4
Figure 1-2: Schematic diagram of an autoclave. There are two separate chambers with the main chamber to de-wax the shells and the rear chamber to produce high pressure steam.....	6
Figure 1-3: Saturated steam enthalpy as a function of pressure (Rogers & Mayhew, 1994). Steam enthalpy (gas) increase rapidly with steam pressure up to 0.8-0.9 MPa and then more slowly beyond that.....	7
Figure 1-4: Wax and core structure of a pattern tree which commonly cracks at the overhang position. The pink section would be made of unfilled wax while the green parts would be made of filled wax and the yellow is the ceramic pouring cup	8
Figure 1-5: Adhesive aluminium foil and pop vent to reduce a shell cracking problem. 10	
Figure 2-1: Actual permeability at different furnace temperature. D has 2 prime coat and the 2 nd coat is stuccoed with 30-80 Alumino-Silicate (one less back up coat). E and F has same number of coats except there is different in composition of fillers in back up coat which not described (Hahn & Rosmait, 2002).	17
Figure 2-2: Permeability of wax through shell apparatus (Cendrowicz, 2004)	18
Figure 2-3: Illustration of 3-point bend test setup (left) and 4-point bend test setup (right) (ASTM C1161-13, 2013). Blue arrows indicate the direction of force exerted on the samples. Red arrows indicate the stress state of samples during testing which can be relate to the stress during pressurisation of wax expansion in shell.	20
Figure 2-4: Schematic diagram showing the setup of the wedge test with trailing edge blade test piece (Hyde, et al., 1995).....	22
Figure 2-5: Burst test setup to measure the hoop stress of a cylindrical geometry shell mould (Synder, et al., 2003).....	23
Figure 2-6: Comparison of expansion behaviour (Beeley & Smart, 1995).....	26
Figure 2-7: Illustration of the heat convection on the melted surface of wax pattern (Jones, <i>et al.</i> , 2002)	37
Figure 2-8: Determination of the temperature drop ΔT at the interface alloy/mold (Konrad, Brunner, Kyrgyzbaev, Volk, & Glatzel, 2011).....	38
Figure 3-1: Wax D injected into an aluminium die to make 5 rectangular bars, 4 bars are removed. 1 pence for scale.....	44
Figure 3-2: Schematic diagram of wax injection machine setup.....	45
Figure 3-3: Quicklock Boilerclave™ by Leed and Bradford Boiler Company Ltd, UK. Autoclave for de-waxing in IRC laboratory. The dark and pressurised condition which is used has limit the understanding of de-waxing process.	47
Figure 3-4: The pressurisation and depressurisation profile for the autoclave used in the IRC laboratory	47
Figure 3-5: The shelled flat bar wax was cut after drying to the required test bar dimensions and then separated by cooling in a refrigerator.....	48
Figure 3-6: a. cross light and b. parallel light. A – Analyser, P – Polariser (Olympus)	53
Figure 3-7: Anisotropy between cross light (Olympus)	53
Figure 3-8: Schematic diagram of wax permeating the shell during de-waxing process. This process occurs prior to the bulk wax melting process.....	55
Figure 3-9: Water permeability setup	57

Figure 3-10: (i) Initial setup after solidifying a thin layer of wax (left), (ii) standard shelling (middle), (iii) setup after wax pellets are melted inside the steel pipe (right) ..	58
Figure 3-11: Edge test pattern bar with 11° degree angle (left), example of wedge test sample (right).....	60
Figure 3-12: Linear line (red line) represents the stress strain gradient to obtain Young's modulus.	61
Figure 3-13: Schematic diagram for the impulse excitation of vibration setup. Samples are struck mid span.....	62
Figure 3-14: Experimental setup discussed in ASTM C1259-14 to obtain Young's modulus of material. Point M1 was used as the non-contact sensor point.....	63
Figure 3-15: Thin section of the wedge test sample was focussed to obtain the strain during testing. Green arrows indicating the direction of stress on a wedge sample	65
Figure 3-16: TMA setup to measure thermal expansion of shell	68
Figure 3-17: Container for measurement of liquids in the dilatometer (left) and setup in the dilatometer (right).....	69
Figure 3-18: Expansion b_1 - b_2 of the silicon seal on the Netzsch capsule. a and b are defined here for Equation 3-7.....	70
Figure 3-19: Density bottle setup.....	70
Figure 3-20: The sample holder and calorimeters in a DSC 7 (PerkinElmer, 2014)	72
Figure 3-21: Schematic diagram showing the positions of the thermocouples used to predict the changes of thermal conductivity with temperature and time. Shell is covered by copper foil to prevent steam penetration (right). The cross section shows the relative location of the thermocouples and shell configuration	74
Figure 3-22: Top view of the autoclave in IRC laboratory showing the thermocouple and pressure sensor ports	75
Figure 3-23: Schematic diagram of thermocouple setup for the wax thermal diffusivity measurement.....	77
Figure 3-24: Schematic diagram of parallel plates geometry setup	78
Figure 3-25: Schematic description of the capillary rheometer used in the project.....	80
Figure 3-26: Bagley plot used to obtain entrance pressure loss (P_o) (Barnes, et al., 2005)	81
Figure 3-27: Schematic representation of the initial de-waxing process where wax is forced into the porous ceramic shell. In the models where Poiseuille's law was assumed, the pores are represented as horizontal tubes.	84
Figure 3-28: XRD data showing that the primary slurry to remained as zircon and did not be dissociate during the sintering process.	87
Figure 3-29: The Wilhelmy plate method setup in an oven using a load frame to submerge the ceramic into the molten wax and then emerge it from the same wax. The maximum submersion depth is 1 mm.	88
Figure 3-30: A typical submersion and retraction curve for Wax C. It shows the advancing and receding force of Wax C in this case did not have any obvious hysteresis behaviour. The horizontal orange line shows the averaged adhesion tension value.	89
Figure 3-31: Results of the system calibrated using borosilicate microscope glass with water.....	90
Figure 3-32: Schematic diagram with platinum ring for Du-Nuoy ring test setup to replace the flat plate in Wilhelmy method.....	91
Figure 4-1: Shell after de-waxing and before polishing.....	92

Figure 4-2: Shell structure after de-waxing focussing on secondary layer with SEM.....	92
Figure 4-3: De-waxed shell inner shell surface and wax D residuals. Some porous surface can be seen to be filled with fillers (right)	93
Figure 4-4: Surface roughness measurement on the prime coat surface. Scale on the right indicates the vertical height deviations.	94
Figure 4-5: SEM results showing the microstructure of 4 waxes –Wax A, B, C, E. Larger depth of field of SEM allows a three dimensional view of the structure of the commercial wax pellet to be observed.....	96
Figure 4-6: Polished wax pellet samples observed under the optical microscope at x10 magnification without cross polarised light.....	97
Figure 4-7: Wax B (left) and Wax D (right) shows that terephthalic acid exist as crystals and the broken cross linkage polystyrene appears to be have same colour as cross linkage polystyrene at 60°C with plain polarising filter.	98
Figure 4-8: Hot stage microscope comparing the filler structures in three different waxes measured at 60°C with cross polarising filter.	99
Figure 4-9: Hot stage microscope images in cross polarised showing before and after melting Wax C (The XLPS filler on left are dark because they are amorphous. The crystal of the base wax has melted in the right hand image showing angular filler only – probably TPA)	100
Figure 4-10: Surface roughness measurement on a 1mm x1mm wax surface before (left) and after (right) Trisol 60 plus cleaning for Wax D.....	101
Figure 4-11: FTIR results for Waxes A, B, C and E. An extra peak compared to others was found at 1650 to 1750 cm^{-1} for Wax E.....	102
Figure 4-12: Graphical representation of the data presented in Table 4-1. It shows the flexural strength of shell prepared with different methods.....	105
Figure 4-13: Graphical representation showing results of Table 4-2. There are not much difference in the flexural strength relating to specimen orientation either primary up or down.	106
Figure 4-14: Graphical representation of the flexural strength data presented in Table 4-3.	107
Figure 4-15: The width and thickness of each sample is noted with a line to assure the same location is being measured pre and post autoclave treatment.	111
Figure 4-16: A dried particle of silica sol (left) and autoclaved silica sol (right) using a transmitted light microscope. Particle size is approximately 1mm.....	113
Figure 4-17: XRD result show pattern before (top) and after autoclaving the silica sol. Both tests showing amorphous silica.	113
Figure 4-18: Load frame deflection calibration with 70 mm thick steel block. Steel block is assumed to have zero deflection and the load frame deflected 0.1 mm with 500 MPa stress.....	117
Figure 4-19: Results obtained using mercury porosimetry showing a large distribution of pores diameter.....	120
Figure 4-20: TMA data used to measure the thermal expansion of the shell. The expansion of the sample appears linear with the increasing temperature.....	122
Figure 4-21: Thermal expansion measured by NPL for Wax A-E	124
Figure 4-22: Thermal expansion tests using NETZSCH capsule for Wax A-E	124

Figure 4-23: Modified density bottle with wax, silicone oil mix during cooling down. Wax crystals start forming causing the silicone oil appear to be cloudy. Air bubbles from wax pellets are observed.....	125
Figure 4-24: Thermal expansion using the density bottle for waxes A-E.....	126
Figure 4-25: Comparing thermal expansion obtained using three different methods on Wax C	127
Figure 4-26: Specific heat capacity of shell measured using DSC	128
Figure 4-27: DSC heating scan with 10 °C·min ⁻¹ heating rate to observe the specific heat capacity of different waxes	129
Figure 4-28: Solid and liquid phase transition line is extrapolated from density bottle method data to obtain the start of semi-solid phase (onset) and end of semi-solid phase (end).....	130
Figure 4-29: Solid and liquid phase line is extrapolated from DSC data to obtain the start of semi-solid phase (onset) and end of semi-solid phase (end)	130
Figure 4-30: Comparison of the two thermal profile across shell obtained using same procedure.....	134
Figure 4-31: Comparison of thermal profile across the shell with and without steam penetration. Red linear line indicates the gradient of the thermal profile when steam is released into the autoclave chamber.	135
Figure 4-32: Thermal conductivity back calculated from the thermal profile using MATLAB. Graph D shows the average value taken as a constant for simulation.....	136
Figure 4-33: Thermal profile of wax measured in autoclave. MATLAB calculation for wax thermal conductivity for filled wax.....	138
Figure 4-34: Test to determine the importance of pre-shear prior to rheological testing. Shear stress versus shear rate for Wax C is plotted.	139
Figure 4-35: Shear stress vs. shear rates for Wax B. Results exhibit a higher yield stress as the temperature increases. The thixotropy hysteresis occurs when the temperature increases.....	140
Figure 4-36: Shear stress vs. shear rates for Wax C. Results exhibit a higher yield stress as the temperature increases. The thixotropy loop occurs when the temperature increases.....	141
Figure 4-37: Shear stress vs. shear rates for Wax A. Results exhibited no yield stress and the repeatability of the rheological behaviour at any temperature is very high. It has a dilatant behaviour.	142
Figure 4-38: Wax D has no obvious yield stress at low shear rate. The shear thinning and shear thickening effect is less obvious in Wax D.	142
Figure 4-39: The shear stress against shear rate relationship obtained from Wax E pattern wax is very reproducible. Wax E exhibits a Newtonian fluid behaviour.	143
Figure 4-40: Shear stress vs. shear rate relationship for Wax C at 170°C. The first up curve exhibiting yield stress behaviour and all subsequent steps on same sample do not exhibit a strong yield.....	144
Figure 4-41: Shear stress vs. shear rate relationship for Wax E at 170°C and no yield stress behaviour is observed.....	144
Figure 4-42: Example of relationship between yield stress and normal stress. Results shows that the two parameter have a close relationship measured at 170°C on wax C.	146

Figure 4-43: Viscosity and shear rate relationship at 55°C, 57.5°C and 60°C for Wax A	148
Figure 4-44: Viscosity and shear rate relationship at 55°C, 57.5°C and 60°C for Wax B	148
Figure 4-45: Viscosity and shear rate relationship at 55°C, 57.5°C and 60°C for Wax C	149
Figure 4-46: Viscosity and shear rate relationship at 55°C, 57.5°C and 60°C for Wax D	149
Figure 4-47: Viscosity and shear rate relationship at 47.5°C, 50°C and 52.5°C for Wax E	150
Figure 4-48: Viscosity change with temperature increases has good relation with solid loadings at 15 s ⁻¹ shear rate	151
Figure 4-49: Combination of rheology data of Wax B from rotational rheometry and capillary rheometry after converting strain rate to shear rate (left). Viscosity plotted against temperature at constant 200 s ⁻¹ shear rate.	152
Figure 4-50: The adhesion tension force of molten wax is averaged and plotted	154
Figure 4-51: Morphology of wax on inner surface of shell after de-waxing process with fillers particles remains on the surface	155
Figure 4-52: The surface tension force of molten wax is averaged and plotted for wax A	157
Figure 5-1: Thermal profile in Flow3D was found by trial and error to match the experimental thermal profile to represent the temperature at prime coat surface	165
Figure 5-2: Heat transfer coefficient for wax-shell interface increases linearly as wax is heated and expand. HTC is starting to drop after 800 s due to wax starting to melt and temperature difference at interface is low.	167
Figure 5-3: Wax A-E viscosity behaviour after fitting into the “Carreau” model	170
Figure 5-4: Compressibility of 40 % in-house blend filled wax at different temperatures with an average of 4.5x10 ⁻¹⁰ Pa ⁻¹ is observed (Torres, 2003)	174
Figure 5-5: Compressibility of 20 % in-house filled wax at different temperatures with an average of 5x10 ⁻¹⁰ Pa ⁻¹ is observed (Torres, 2003)	175
Figure 5-6: Compressibility of 0 % in-house filled wax at different temperature with an average of 5.5x10 ⁻¹⁰ Pa ⁻¹ is observed (Torres, 2003)	175
Figure 5-7: Compressibility of three different waxes at 50 MPa pressure	176
Figure 5-8: Wax slide down the shell wall during de-waxing creating a vacuum region	177
Figure 5-9: Merging the nodes with the nearest interface nodes (Flow-3D, 2014)	179
Figure 5-10: In focus of cylindrical mould corner (left) and out of focus (right). Mould radius is approximately 10mm	182
Figure 5-11: 2-dimension mesh boundary setup in flow-3D. Red is the mould and blue is support component (left) and cross section of the cylinder (right)	183
Figure 5-12: Location of stress at top edge (left) and hoop stress (right) of a cylindrical shell.	183
Figure 5-13: Indication of basic tensor stress direction	186
Figure 5-14: Temperature contour of Wax A with 2.5 mm orifice diameter when steam is introduced for 4 s (left) and 10 s (right)	189
Figure 5-15: Wax A with 2.5 mm orifice diameter. Temperature profile in Kelvin (left) and pressure with vector in Pa (right) at 10 s.	190

Figure 5-16: Wax A with 2.5 mm orifice diameter. Sharp top corner indicating Von misses stress is at 4.3 MPa. The shell of this setup is expected to crack at 10 s.....	191
Figure 5-17: Wax A with 2.5 mm orifice diameter. Von Misses stress (Pa) taken for analyse is the time (seconds) that just exceeded the shell stress limit.	192
Figure 5-18: Internal pressure (Pa) comparison between 2.5 mm (left) and 5 mm (right) orifice diameter at 10 s.....	193
Figure 5-19: Illustration of shell displacement in metres.....	194
Figure 5-20: Von Misses stress in the shell at the identified critical node in relation to time after heat is introduced. The red region indicates the failure pressure for the shell from experimental data (3-point bend test) and the yellow region is the failure pressure for wedge test data. The values indicate the mean strengths of the experimental data. Solid lines represent results for 2.5 mm orifice diameter and dashed lines for 5.0 mm orifice diameter.....	196
Figure 5-21: Maximum principal stress at critical node in relation to time after heat is introduced. The red region indicates the failure pressure for the shell from experimental data (3-point bend test) and the yellow region is the failure pressure for wedge test data. The values indicate the mean strengths of the experimental data.....	196
Figure 5-22: Data obtained from mercury porosimetry test. Two different gradient of the profile indicates the permeability of two different structure of shell and prime coat gradient was used to represent the volume loss as a function of pressure.	199
Figure 5-23: Stress observed as the compressibility is increased to take into account of the wax permeation into shell.	201
Figure 5-24: Effect of shell Poisson ratio on shell stress.....	202
Figure 5-25: Temperature of shell at the wax top edge and effect of shell corner radii on shell stress.....	203
Figure 5-26: 10 mm external external radii (left) and 0 mm radii at 10 s. Temperature contour showing the wax-shell interface temperature for 10 mm radii geometry is higher than 0 mm radii.	203
Figure 5-27: Effect of the orifice diameter.....	204
Figure 5-28: 2.5, 5 and 10 mm (left to right respectively) orifice diameter. Internal pressure in Pa.....	204
Figure 6-1: Cylindrical pattern wax-150 mm and 50 mm diameter. Wax A, B, C, D, E in sequence from left to right.	206
Figure 6-2: Schematic diagram of the setup carried out in the autoclave to measure the flowrate of wax. Each increment of 20 mm is one stage.	208
Figure 6-3: Thermal profile of thermocouples in container measuring flowrate of wax. 'kinks' of thermal profile (red arrow) assumed molten wax had reached the level.....	209
Figure 6-4: Cylindrical shell mould wax broken after the de-waxing cycle. Residuals of wax below was observed after de-waxing.	210
Figure 6-5: Serious shell cracking on a cylindrical geometry on the closed end and at the corner (close end).....	211
Figure 6-6: Methyl blue stain to detect cracks on the top (left) and at the edge (right) after de-waxing.....	212
Figure 6-7: Shell cracking on cylinder mid-section due to hoop stress (left) and at the sharp edge of the orifice end (right). One penny coin for scale.	212

Figure 6-8: Repeatability test on Wax D to observe the flowrate and the graph legend indicates the orifice diameter and sample number. It was found that some flow rates does overlaps.....	217
Figure 6-9: Comparing the time required for two different orifice diameter to be fully empty. Wax starts to flow from 0 s but the “actual” flow start around 600 and 700 s for respective orifice diameter.	218

List of Tables

Table 1-1: Mechanism that occur simultaneously during the de-waxing process	13
Table 3-1: Prime coat slurry composition.....	45
Table 3-2: Backup coat slurry composition.....	46
Table 3-3: Standard specification for shell to cast steel	46
Table 3-4: Summary of experimental methods for sample preparation and mechanical testing.....	49
Table 3-5: Specification for surface polishing	50
Table 4-1: Shells samples prepared in different ways to observe the average strength	105
Table 4-2: Strength measurements with primary in tension and compression	106
Table 4-3: Steam test to observe the effect of moisture on the shell strength	106
Table 4-4: Comparing the thickness and width of shell before and after the autoclaving treatment.	111
Table 4-5: BET data of dried silica sol before and after autoclave treatment.....	112
Table 4-6: Wedge test compared to 3-point bend test results	116
Table 4-7: Comparison of strain at failure experienced by the flat bar and wedge sample	119
Table 4-8: Density measured using Helium pycnometer at 20°C	123
Table 4-9: The temperature range of wax in solid and liquid form	131
Table 4-10: Melting point and congealing provided by wax supplier	132
Table 4-11: Thermal conductivity of wax blend varies with filler percentage measured with laser flash analysis (Torres, 2003)	139
Table 5-1: Carreau model shear rate and temperature dependent fitted coefficients for Waxes	169
Table 5-2: values of viscosity obtained from curve fittings.....	170
Table 6-1: Percentage crack and de-waxing flow rate test results. Green flowrate indicates non-crack shell and red is cracked during the flow rate test	215
Table 6-2: Summary of the flow rate results from preliminary flow rate test and the repeatability flow rate test on Wax D.	217
Table 6-3: Summary of flow rate comparison on Wax C from the time steam enters the chamber	218

1. INTRODUCTION

The investment casting (IC) process is widely used to manufacture of metal components for different applications including those used in automotive, aircraft, and power gas turbines as well as in the areas of more traditional activity such as sculpture for decorative purposes (Paton, 2001). It allows components to be produced with accurate dimensions if the process is closely controlled compared to other casting methods (Yuan, et al., 2004, Campbell, 2011). The IC process is able to provide accurate dimensions with tolerances normally quoted to 0.5 % or smaller range (Piwonka, et al., 2000).

1.1 The investment casting process

Investment casting, a process traditionally known as lost wax casting, has been used for more than six millennia. Archaeologists proved that the technology was being used as early as 4500 BC in Thailand by the local tribes (Beeley& Smart, 1995). Around 1900, the process was used to manufacture gold fillings and dental inlays for false teeth. In 1932, the lost wax ceramic block mould process was developed to work with cobalt-chromium alloys known as “Vitallium”, for dental applications and orthopaedic purposes (Beeley & Smart, 1995).

The modern IC industry started during the Second World War when the capacity of the machine tool industry could not achieve the demand for military components. Attention turned to IC to produce precision components for armament and aircraft parts (Beeley& Smart, 1995). The applications in commercial markets have continued to grow and in 2012, the world sales value for castings reached to £ 7.53 Billion (Blayson, 2013).

The IC process is used to produce precise metal casts by moulding liquid metal within a ceramic container made of repetitive layers of ceramic derived from slurry and ceramic particles. The typical stages of IC processes are illustrated in Figure 1-1. Polymeric materials for example paraffin wax in the molten phase are injected into a negative mould usually made of aluminium and solidified to form a solid wax pattern. Multiple patterns are assembled onto a wax runner system and a pouring cup (ceramic) to form a pattern tree. Waxes to make typical pattern trees can be categorized into two basic types, unfilled and filled. Unfilled waxes are designed to be used in runner (or sprue) sections of a pattern tree because of their lower melting point and lower viscosity. This increases the de-waxing rate and reduces the possibilities of mould cracking. Filled waxes are commonly used as the main component as they have better mechanical properties and offer higher dimension accuracy with less shrinkage.

The pattern tree is washed with a chemical solution and rinsed with water to provide suitable surface condition for ceramic adhesion and dried. The dried wax patterns are dipped in the ceramic slurry and sprinkled with refractory particles 'stucco' on the surface before drying. The dipping-coating and drying process is generally repeated sequentially to build a layered structure comprising typically 6-8 layers. The first layer (known as prime coat) which come in contact with the molten metal (after de-waxing) during casting are preferably materials with good refractoriness such as Zirconium Silicate (Zircon), Zirconia, Alumina, Magnesia, Calcia or Yttria. The refractory material for the subsequent layers (backup coat) is usually selected on the basis of cost where materials such as Alumino-Silicate are preferred. The final coating (sealing layer) is normally the ceramic slurry without stucco which is applied before final drying. The wax is removed in the de-waxing process. Most commonly, the wax is removed in an

autoclave de-waxing machine or by introducing gas burners to the shell to melt the wax. This process is a crucial stage in the production of good quality shell moulds and the de-waxing process is the main focus of this thesis. The shell is then fired to burn out any remaining wax and organic components of the binders. The firing process also increases the mechanical strength of the shell by fusing the stucco together. The molten metal is then poured into the shell cavity and allowed to cool. Once the metal has solidified, the ceramic shell is removed by vibration and/or blasting with sand (sometimes with a water gun). The metal components are then cut off from the runner system and may be further machined and heat treated depending on the cast metal specifications. More detailed procedure on the process for this thesis is discussed in Chapter 3.

Should a hollow metal structure be required, the ceramic mould is then made with an integrated ceramic core. The ceramic core is usually manufactured by injection moulding and undergoes a de-binding process and firing before wax is injected around it. After the wax is injected around the core to form the pattern, they are assembled together with the runner system. The same procedure of slurry-stucco coating and drying is carried out. The wax is then melted out leaving the shell with an integrated ceramic core. Metal is then cast around the ceramic core. While the rest of the process is much the same, the metal components will require a leaching step to remove the core usually with a strong alkali.

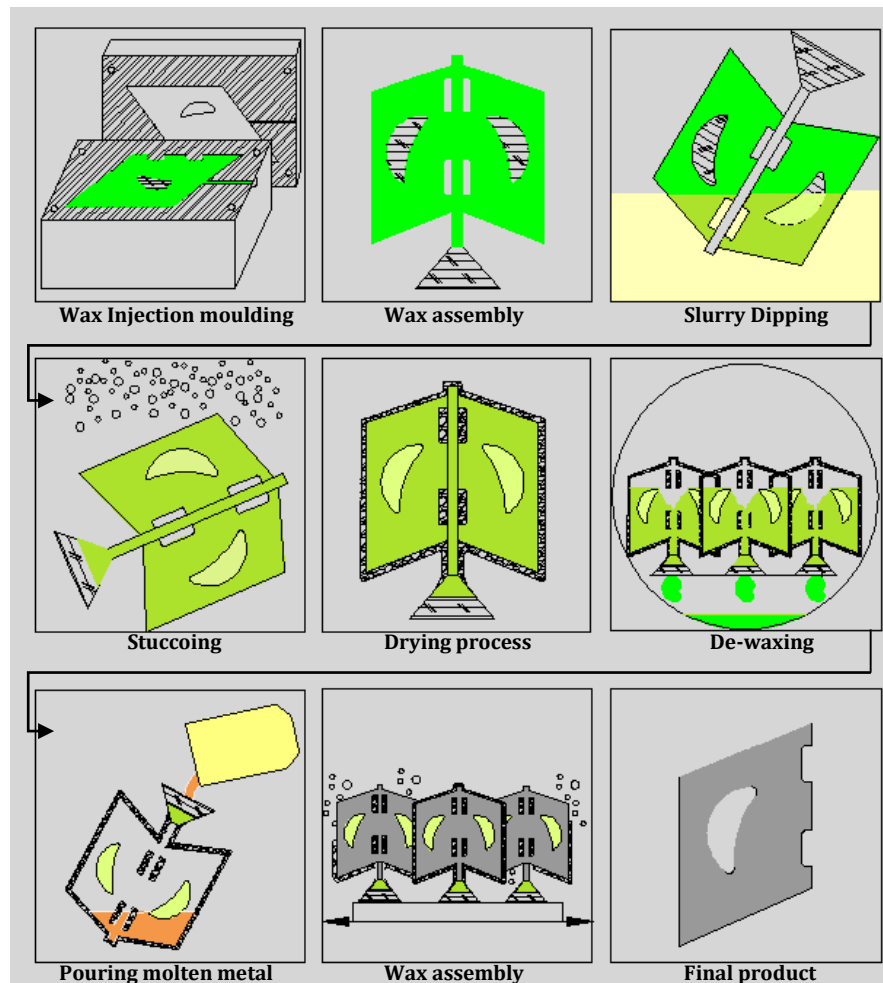


Figure 1-1: Stages in the investment casting process

1.2 De-waxing process and issues

There are few methods available to remove the wax from mould, they are solvent extraction, flash firing, microwave, autoclave heat treatment and other patented methods. Solvent extraction method allows the wax to be removed without heat thus wax expansion exerting stress on shell can be prevented. This method however is usually used for special purposes where wax pattern is soluble in the solvent (Beeley& Smart, 1995). In the flash firing process, the moulds are rapidly heated up to a temperature in excess of 800 °C in a convection furnace. The flash firing method has a downside where 'shadow' effects can shield certain parts of the mould, because the heat

transfer is by radiation (Beeley & Smart, 1995). Fabio *et al.* (2009) and Rani & Karunakar (2013) investigated the use of microwaves to de-wax. They found that microwave de-waxing allows wax to be more easily re-cycled due to the milder conditions compared to autoclaving, the wax structure and chemistry remain similar to the original even after repetitive cycling. This method sounds promising, however this de-waxing method is not commercially available.

There are other less common de-waxing methods available. There is a patented method which removes the wax by saturating the ceramic shell mould with water and then immersed slowly in a hot oil bath so that heat is introduced in localized areas for low stress wax removal (Yang, 2009). Branscomb (2010) patented a similar idea where the shell was immersed in a fluid having a relatively low boiling point to prevent shell cracking. The fluid selected should be hot enough to transfer heat through shell but low enough to limit steam generation from moisture in the shell. These methods can eliminate cracking of the mould but more work would need to be done to understand if the fluid affects the quality of the mould, through the introduction of shell inclusions or effects on the mould production rate.

At present, autoclave de-waxing is the most common method being used in foundries. De-waxing with an autoclave simply requires the wax pattern coated with ceramics to be placed in the chamber of the autoclave and allowing heat from steam to melt the wax either by heat transferred to the ceramic shell surface or directly on to the wax from the pouring cup. An autoclave consists of two chambers where the main chamber is used for the de-waxing process and the other chamber, located at the back of the machine is used to generate steam (Figure 1-2). Steam is compressed up to typically 0.8 - 0.9 MPa and

released into main chamber when the steam valve is open. Generally, the steam pressure in the de-waxing chamber rises up to required pressure within a few seconds and after a period of hold, the chamber is de-pressurised slowly to atmospheric pressure (typically $333.3 \text{ Pa}\cdot\text{s}^{-1}$). The low depressurisation rate is to prevent water in the shell pores re-boiling, expanding and cracking the shell. It also limits the sudden expansion of any remaining molten wax which could then lead to shell cracking.

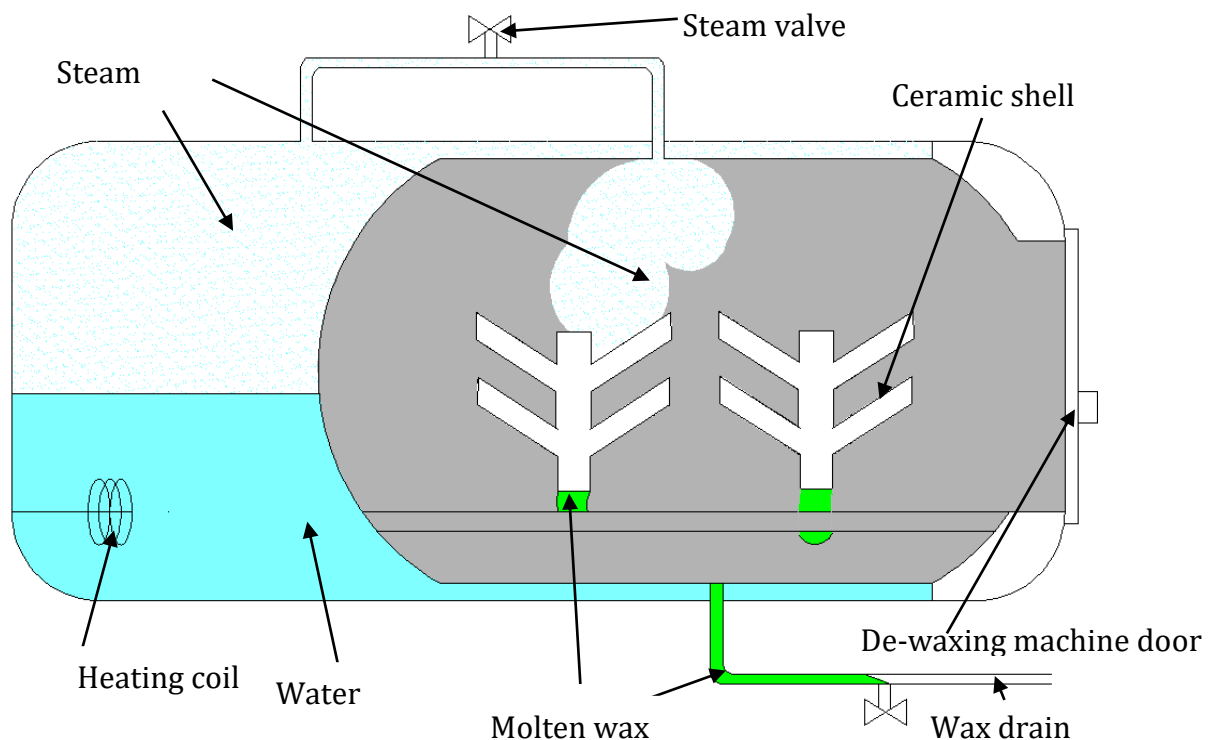


Figure 1-2: Schematic diagram of an autoclave. There are two separate chambers with the main chamber to de-wax the shells and the rear chamber to produce high pressure steam.

The advantage of de-waxing with steam (gas) is that it is able to provide higher energy per unit time compared to using heated water (liquid). De-waxing steam pressure is usually set at 0.8 MPa because the steam heat enthalpy does not increase greatly above that value according to the steam tables (Figure 1-3) and applying pressure above this setting is therefore inefficient. Jones *et al.* (2002) for example had set the maximum

pressure and temperature for the autoclave at approximately 0.7-0.8 MPa and 180- 200 °C respectively.

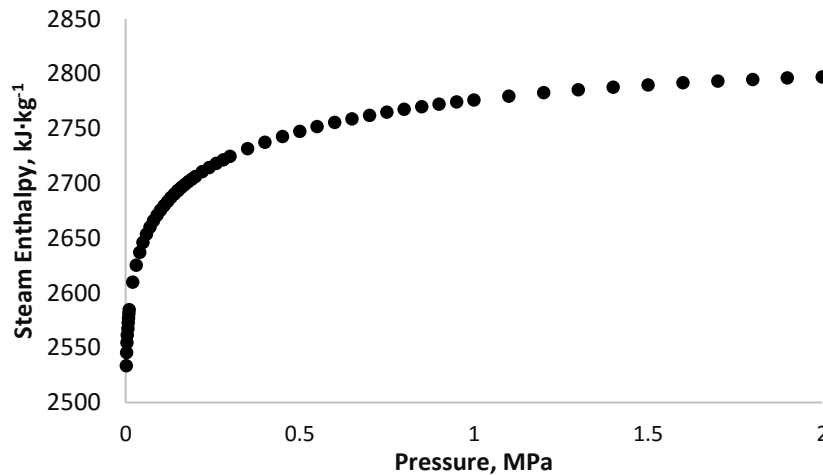


Figure 1-3: Saturated steam enthalpy as a function of pressure (Rogers & Mayhew, 1994). Steam enthalpy (gas) increase rapidly with steam pressure up to 0.8-0.9 MPa and then more slowly beyond that.

One of the major drawbacks using autoclave to de-wax is induced shell cracking. Shell cracking incidents are believed to be mainly caused by the expansion of wax during the rising pressure stage. This is because when steam in the autoclave heats the system, IC wax expands at a higher rate than the ceramic shells causing a pressure build up in the shell mould cavity. Mueller (2007) suggests that most edge features where cracks occur are pulled apart rather than pushed together, indicating that cracking is caused by internal pressure from the wax. A few other mechanisms have been suggested that contribute to shell cracking such as the autoclave not working properly, shelling process inconsistency (poor green strength), wax blend inconsistency, high depressurisation rate, inadequate gates for liquid wax flow, viscosity of the liquid wax being too high, permeability of the green shell mould is too low or the mould has too complicated a geometry. There are a few geometry designs such as overhangs, wax flow restrictions or

sharp edges which can cause shell cracking. Overhang (Figure 1-4) is where a wax pattern tree contains a cavity where waxes accumulate during the de-waxing process. The other design limitation is flow restriction where the structure of pattern which is usually in the form of ceramic cores in long thin sections restricting the flow of wax during de-waxing. Sharp edges are another design that leads to shell cracking due to stress concentration in that region.

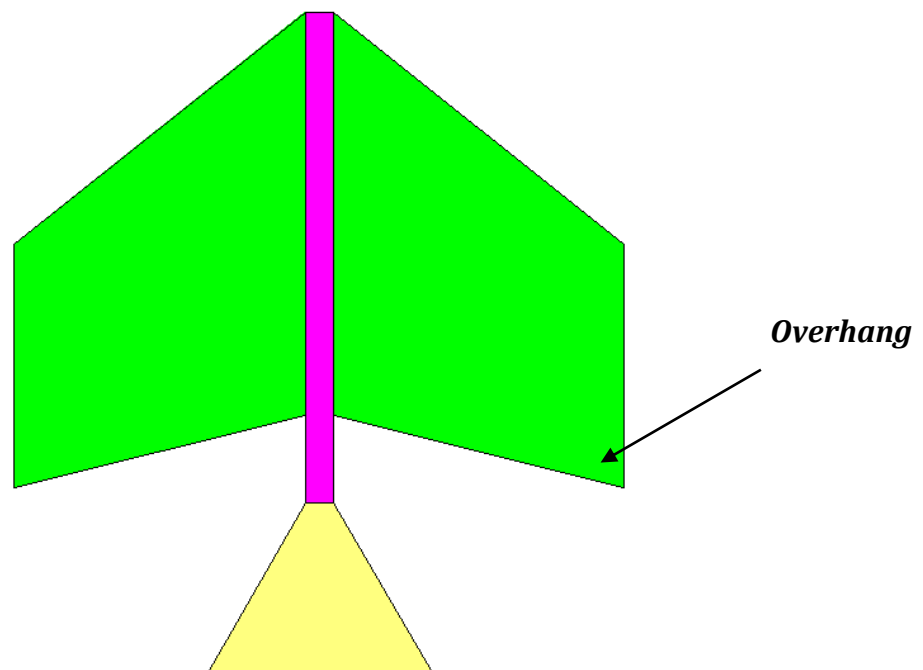


Figure 1-4: Wax and core structure of a pattern tree which commonly cracks at the overhang position. The pink section would be made of unfilled wax while the green parts would be made of filled wax and the yellow is the ceramic pouring cup

Any mechanism of mould cracking is not desirable and can be avoided by rapidly applying sufficient heat to the exterior of the ceramic shell to melt a thin layer of wax adjacent to the interior surface and allow the wax to seep into the pores of the shell before the bulk of the wax starts to expand. The effective loss of volume of the wax pattern allows the wax to expand freely and reduces the stress on the inner shell surface. Mueller (2007) found that cracking can be avoided if steam is directed to melt the

interior earlier (from bottom through the pouring cup) and allow the wax to collapse inward rather than heating the shell surface first.

Shell cracking has been reported to affect approximately 20 % of the total moulds being manufactured and it is believed that 80 % of shell cracks originate during de-wax (autoclave or flash-fire de-waxing) while the rest are probably caused by handling (Synder, et al., 2003). Snow (1998) appears to suggest even more shell cracking issues have actually occurred during de-waxing. He suggested that 90 % of shell cracks occur in the autoclave and at least 90 % of those originate from the interface of shell and wax (de-wax cracks).

Previously, many iterative experiments have been carried out to reduce shell cracking. Some foundries have tried to insulate the inside of complicated geometries such as hollow cylinders with paper packing or refractory wool, such that the wax melts progressively inwards from the exterior (Beeley& Smart, 1995). Occasionally, on sharp edges, the penetration of wax into the surface of shell to relieve pressure is not sufficient. Therefore, some have used adhesive aluminium foil tape to stop steam penetration locally (Figure 1-5). By doing this, it slows down the heating rate of the shell in the cracking prone region so that the wax does not expand and crack the shell. This method can prevent a crack under the foil, however, occasionally it tends to shift the stress and crack a previously “good” area. Some foundries are easing the pressure during de-waxing of particularly difficult moulds by venting configurations (known as weep or pop-vents). This method offers more orifices for the molten wax to flow out of the mould and relieves the pressure build up. However this method increases the risk of shell inclusion in the cast and this method should be used minimally. Another method

commonly used is to put a metal insert in the wax pattern and remove it prior to de-waxing. This allows the runner wax to have a cavity in which to melt and collapse inwards rather than bursting the shell. However, this only works if the cracks occur along the middle section of the pattern tree. Some foundries had achieved shell cracking prevention by cooling the pattern mould in a refrigerator to cool the wax surface and thus create a greater temperature differential between wax and heat source (Beeley & Smart, 1995). Snow (1998) had suggested that reducing the total mass of material in the autoclave by reducing the number of pattern moulds and waxy residue could help to reduce shell cracking. These trial and error studies are found to be useful and have been adopted as a common practice in some foundries.

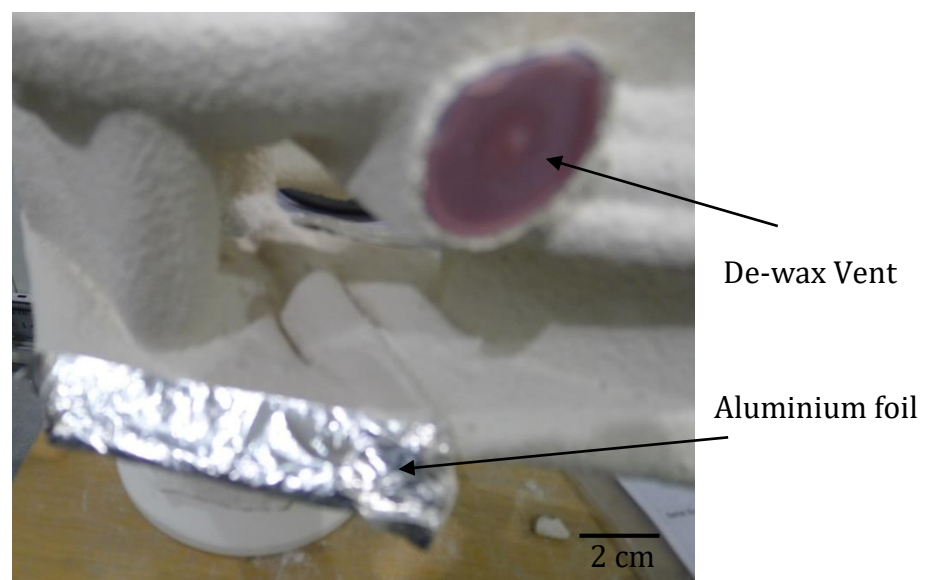


Figure 1-5: Adhesive aluminium foil and pop vent to reduce a shell cracking problem.

Addressing cracking issues is important because mould cracks increases labour intensive shell reworking, inclusion in cast, extra machining work (cast defects) and sometimes distortion in cast metal resulting in scrap metal. Shell mould cracking was identified as being critical to quality due to its impact on metal run-out and inclusion

scrap (Ferg, 2001). Fine shell cracks are usually repaired with ceramic paint (e.g. Magnacote®) or with ceramic paste (e.g. fire cement). However, occasionally, the shell is beyond repair and thus disposal is the only option. Scrapping shells is costly in terms of both raw material loss and in reduced output from the production line. With all these issues, it is important to address mould cracking problems in the early stage of the process before they increase the cost of the cast components in later stages.

1.3 Motivation of the Project

The motivation of this work arises from the uncertainty of the IC wax supply chain and because of this, there is a need to establish a quicker process of understanding and analysing the wax characteristics affecting mould cracking.

There are many aspects affecting the wax supply chain in the IC industry. An example of wax supply interruption is by natural disaster. All major resin manufacturers who had facilities in the Gulf Coast of the United States were devastated by the Hurricane Katrina in 2005 which was an unpredictable natural disaster. This caused a disruption in the supply chain of raw materials for IC wax manufacture. When the supply chain was interrupted, sourcing the raw materials from other suppliers varied the quality of wax, resulting in unpredictable wax behaviour. The characteristics of the raw materials also vary according to other factors such as the weather and environment. Another possible or even probable interruption to the supply chain occurs when specifications are forced to change to satisfy the standard of environmental control in the country. Some materials could possibly become unavailable for use in the wax mixture due to the regulations in the country of operation. Moreover, the merging of suppliers with small market shares has in the past also caused the discontinuation of their products suitable

for use in this industry. Verta (2013) found that the wax producers worldwide have shrunk from 21 to 7 between 1990 and 2013. This allows the companies to narrow their production line and increase profit margin (Verta, 2013). Beeley & Smart (1995) mentioned that some foundries tend to change wax suppliers from time-to time due to their business strategy to increase production rate, more to perceive superior quality and greater quality control, lower price, attain better service from supplier, or new injection machines with different injection criteria.

This volatile supply situation has put foundries in a position where predictive capacity of mould failure would be most helpful through computer simulation. Simulation however needs thermo-physical data to function well and methods for data gathering need to be readily available.

1.4 Objective

The main objective of this work was to develop a computer model to predict shell cracking in the IC process and to aid in eliminating the issues discussed in this chapter. This thesis builds on the pioneering work of Cendrowicz (2004) where he developed a simplified one dimensional model of the de-wax process. A range of waxes known to show differences in shell cracking propensity are studied including filled and unfilled types. Thermo-physical data on both shell and wax materials is required for input into the model and experimentation is required to be undertaken to verify the modelling output. The de-wax process can be simplified to the following sequence.

Table 1-1: Mechanism that occur simultaneously during the de-waxing process

Heat transfer stages	Shell properties	Wax properties
Steam energy transfer across the shell	Thermal conductivity Heat transfer coefficient Thermal expansion Specific heat capacity	
↓		
Heating of the wax		Thermal expansion Thermal conductivity Density Specific heat capacity
↓		
Melting of the wax and flow out of mould	Permeability	Melting point Viscosity Surface tension
↓		
Shell and wax interactions and properties relating to failure	Shell mechanical properties	

The thesis is divided into three main parts. First part (Chapter 2) is a literature review relating to the de-wax process. The second (Chapter 3 and 4) develops the characterisation methods of shell and wax under conditions close to those that develop in the autoclave and thus most applicable to modelling the de-wax process. The last section (Chapter 5) of the thesis describes the computational modelling work developed to predict shell cracking. In Chapter 6, additional experimental data on the de-waxing of a simple geometry designed to cause shell failure is reported to allow comparison to simulation data. The potential of the model is discussed and conclusions are drawn. Recommendations are made for future work.

2. LITERATURE REVIEW

This chapter presents the published work related to de-waxing process or the fundamental theories required to understand the process. It covers the work published in journal and conference papers (IC specific) related to the characterisation work on shell and wax systems. This chapter also includes discussion on IC studies with computer simulation.

2.1 Microstructure of wax

Investment casting waxes occur in two forms, filled and unfilled. IC waxes are complex mixture of materials including natural or synthetic waxes, natural or synthetic resins, solid organic fillers, and even water (wolff, 1999). Fillers are added to conventional pattern waxes to improve dimensional stability and are usually made from cross-linked polystyrene (XLPS), terephthalic acid, isophthalic acid, poly-alpha-methyl-styrene and water (Torres, 2003).

Torres (2003) studied a commercial wax (Hyfill B417) containing XLPS filler using laser diffraction and found the mean size of the filler to be 60 μm with a wide size distribution. Torres also measured the content of filler using x-ray diffraction and nuclear magnetic resonance and showed it to be 40 volume %. These values appear typical of commercial waxes.

2.2 Permeability and Porosity

The shell build process, where slurry and stuccos are laid layer upon layer produces shells with high porosity typically in the region of 20 %. Porosity of the shell can be

determined by several methods including mercury intrusion, Archimedes, gas absorption and simple mass volume measurements but it is permeability of the shell which is of most important in determining the flow of gas (steam) and wax into the structure. The permeability, K and porosity of the shell are important as they allow the steam to penetrate the shell for efficient heat transfer and also allow wax to permeate the shell to relieve pressure. The heat from the steam both melts and expands the wax applying a pressure sufficient to allow the wax to penetrate into the shell (Gebelin, et al., 2001). Snow (1998) carried out a burst strength test on a cylindrical geometry showing that the shell cracked when applied pressure reaches 2.2 MPa and assumed 1.7 MPa as a pressure for wax to penetrate the shell. Snow *et al.* (2002) estimated that the wax could penetrate the shell to a depth of 2.54 mm in 30 seconds at a pressure of 896 kPa without cracking the shell. Even though it is understood that wax does permeate into the shell, there is still a restriction to the flow of wax which can lead to failure. Cendrowicz (2004) suggested that the colloidal silica network holding the filler and stucco particles together limits the wax infiltration into the shell during autoclaving. Jones *et al.* (2003) postulated that only the base wax (liquid) can enter the primary coat and the fillers (solid) are prevented from penetrating the fine silica colloidal network by filtration.

Synder *et al.* (2003) found that permeability was not directly related to the total shell porosity in a shell layer but to size distribution of pore throats. This means that measurement of shell porosity is not a true representation of the permeability, K of the shell. Cendrowicz (2004) had use the relationship of $0.5 \times K^{0.5}$ to estimate the average pores diameter. This relationship was derived originally by Brinker & Scherer (1990) who carried out work on sol gel processing.

Synder *et al.* (2003) showed that the overall permeability of shell is usually determined by the primary coat which is in contact with the wax. Whitehouse & Dahlin (2008) suggest that the prime coat controls as much as 50 % of the permeability of the entire shell in a system of a single prime coat and six layer shell. They also found that the number of layers of prime coat has less effect on shell cracking than porosity of prime coat (varied by different slurry composition).

The permeation of the shell by wax is also dependent on other variable such as the viscosity and surface tension of the wax (Whitehouse & Dahlin, 2008). In their study, it was shown that wax viscosity had a significant effect on shell cracking, the higher the viscosity the more shell cracking was observed. Snow *et al.* (2002) showed that wax permeation increased as the wax viscosity decreased (with increasing wax temperature) resulting in greater penetration into ceramic shell. Hahn & Rosmait (2002) found that the permeability of the shell tends to increase with a decrease in temperature (Figure 2-1). This shows that it is important to measure the permeability of shell at the temperature of interest. The permeability of IC shell materials can be measured using the procedures outlined in British Standards 1902-10.2:1994. This method uses a table tennis ball as negative mould to allow the ceramic shell to be applied to it. The sample is fired at 700 °C to completely burn off the table tennis ball and air is passed through the shell to determine the permeability.

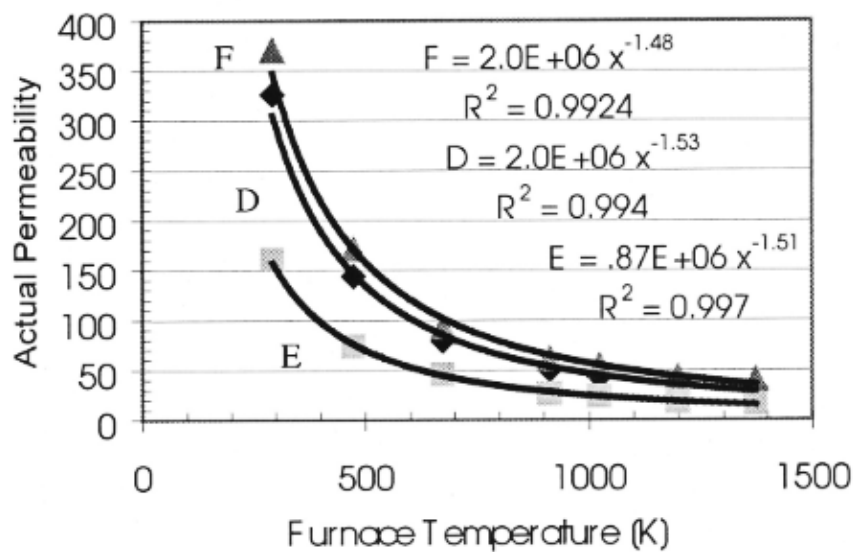


Figure 2-1: Actual permeability at different furnace temperature. D has 2 prime coat and the 2nd coat is stuccoed with 30-80 Alumino-Silicate (one less back up coat). E and F has same number of coats except there is different in composition of fillers in back up coat which not described (Hahn & Rosmait, 2002).

Cendrowicz (2004) used another method to measure shell permeability. The wax assembly was heated to melt the wax and pressure applied to force the wax through the shell (Figure 2-2). The flow rate of the permeating wax was determined by mass. The procedure was carried out by first injecting wax into a copper pipe and shelling one end of the assembly. The other end of copper pipe was connected to the gas compressor and the copper pipe was heated in an oven to melt the wax. The copper pipe was then pressurised and permeate collected. This method allows the measurement of the green shell permeability since it does not require the firing process.

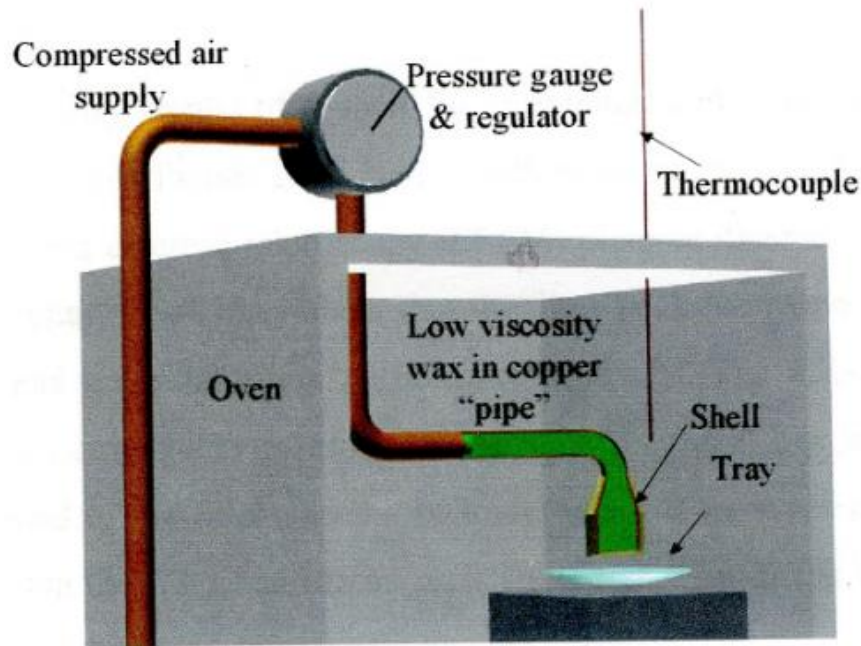


Figure 2-2: Permeability of wax through shell apparatus (Cendrowicz, 2004)

2.3 Mechanical Properties of Shell

Shell thickness is often increased in foundries to prevent shell cracking. The load bearing capacity of shell increases with the square of thickness, but only linearly with the flexural strength (Bergna & Roberts, 2005). Cendrowicz (2004) however, argued that the shell thickness has a small effect on the shell stress based on a one-dimensional model simulation. This was because the simulation is operated solely on conduction and therefore the time to melt the wax surface is increased by a factor of four. Therefore, when the melting time was large, the shell stress became less sensitive to the changes in shell thickness.

A number of papers have shown that the shell's green strength was reduced when moisture from steam was introduced to the interstitial of colloidal binder system. Jones *et al.* (2003) undertook mechanical testing to examine the effect of moisture on the shell by immersing the samples in hot water prior to testing. Cendrowicz (2004) did the same

test and found that shells that were soaked in boiling water halved the ultimate failure stress compared to the normal dry shell (from 5.13 to 2.66 MPa). He also found the weakening effect was observed regardless of the soaking time.

It is common to add fibre or polymers into the ceramic slurry to enhance the mechanical properties of shell. Shell moulds produced with glass fibre and insoluble organic fibre additions have been found to be less susceptible to autoclave cracking due to increased green strength (Beeley & Smart, 1995). Yuan *et al.* (2004) investigated the influence of steam on polymer and organic fibre modified ceramic shells. The polymer modified system of a flat bar was found to have a 38 % reduction in strength from 7.8 MPa when shell was placed above steam bath for 15 minutes. Under the same condition, fibre modified system showed much less strength reduction. Jones *et al.* (2004) found that in dry condition, however, polymer modified systems were shown to have higher strength compared to fibre modified shells. Latex can be added to the binder systems to increase the mechanical strength of moulds (Jones, et al., 2002; C. Yuan, 2004). This was probably because the latex increased the elasticity of shell in green state and absorbed the expansion of wax during de-waxing.

In addition to moisture being introduced to the shell during autoclave de-waxing, there are other factors that affect the shell mechanical properties. Branscomb (2002) showed that shell samples that were hand coated were lighter in finished weight than the robot coated duplicate parts with green flexural strength of 2.75 MPa and 5.86 MPa, respectively. The difference being more than double is sufficient to prevent mould cracking. Jones *et al.* (2002) found that wax penetrated into the shell during the de-waxing process and that this penetrated wax increased the mechanical strength of shell

when tested at ambient temperature. This could be because of the wax residuals in the pores or on the surface of the shell. At the same time, penetration of wax into shell pores relieves the pressure developed in mould and allows the shell to survive. In a further paper, Jones *et al.* (2003) suggest that wax penetration into the shell provides extra volume for wax expansion increasing the probability for shell to survive the de-wax process (Jones, et al., 2003).

The mechanical strength of shell is usually determined in terms of flexural strength which can be measured using either 3-point bend test or 4-point bend test (Figure 2-3).

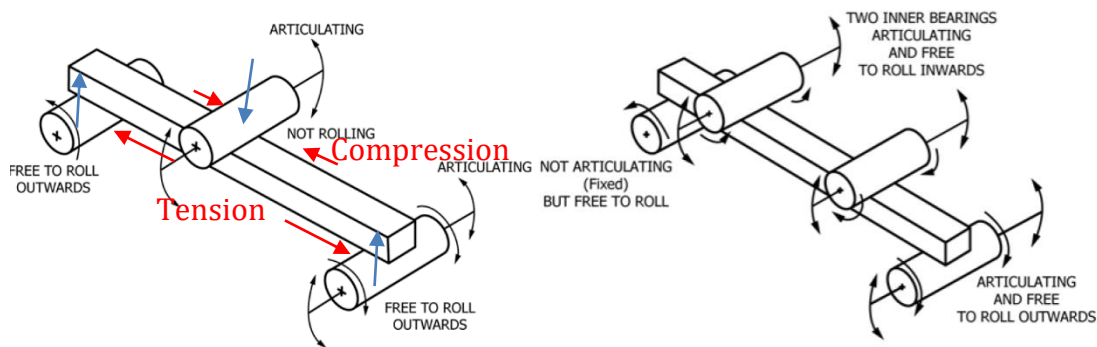


Figure 2-3: Illustration of 3-point bend test setup (left) and 4-point bend test setup (right) (ASTM C1161-13, 2013). Blue arrows indicate the direction of force exerted on the samples. Red arrows indicate the stress state of samples during testing which can be relate to the stress during pressurisation of wax expansion in shell.

Flexural strength is largely a measure of the flaw size distributed in the shells. The flaws are the location of stress concentrator which initiates the cracks. The critical flaws for strength in shells are frequently pores and chipped edges developed in sample preparation. The 3-point bend test gives a load pattern leading to maximum stress at the centre of the span, which means the test is most influenced by the small area under load (Jones, et al., 2002). The 4-point bend test however puts a greater proportion of the sample under uniform stress and facilitates finding the critical flaw that is randomly placed (Richards, et al., 2003). According to Richards *et al.* (2003) taking into account

the possible errors of the test, 77 samples are required to give reliable results, and he had used a total of 128 samples in his test. He showed that 3-point bend test gives 1 MPa higher mean strength than 4-point bend test and 3-point bend test has greater scatter in the results than 4-point bend test on investment casting shells. This large scatter is reasonable since if there is a flaw detected in a 3-point bend test-concentrated area, the shell exhibits low strength; whenever the flaws are away from the three point focus gives a relatively higher strength value. However, the probability for the flaws to be in a relatively small area reduces and thus giving an impression of higher flexural strength. It is important to note that this difference between the two tests is only distinct if there are sufficient samples tested. Richards *et al.* (2003) also compared the 4-point bend test with two different sample preparation method, moulded and sawn (then sanded), and results were shown to be similar. This is attributed by samples breaking prior to testing during the sanding process to leave the stronger samples to be tested.

Mechanical test designed specifically for shell evaluation is the wedge test (Figure 2-4). This test allows the wedge geometry strength to be used as a monitor of the overall shell strength since the sharp edge is prone to shell cracking (Yuan *et al.*, 2004). Wedge strength is generally lower than flat samples. This was suspected due to the processes of drying and expansion of wax in the autoclave resulting in higher concentration of stresses on trailing edge specimens (Hyde, et al., 1995). However, the mathematics of the strength tests should all give the same mechanical value if the materials presented to the test were all uniform in every respect.

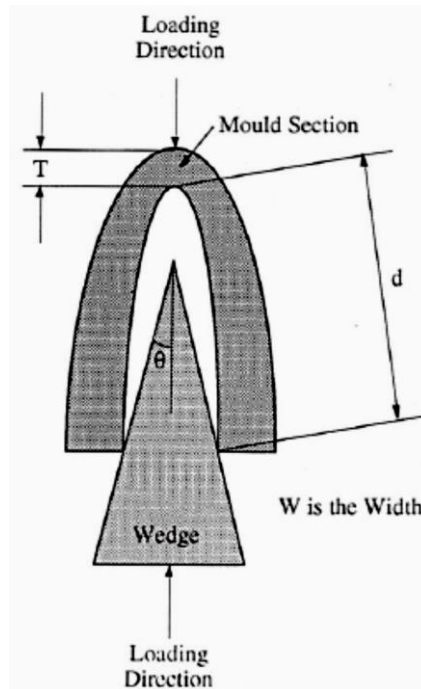


Figure 2-4: Schematic diagram showing the setup of the wedge test with trailing edge blade test piece (Hyde, et al., 1995)

Another form of mechanical strength test is known as the burst test method. It can be used to test the strength of shell by inducing a hoop stress to the surface of shell (Synder, et al., 2003). A polyvinylchloride pipe (or any high thermal contraction material, e.g. LDPE) is used to replace the wax to produce a cylindrical shape shell (Figure 2-5). The pipe is conventionally invested but the pipe is removed from the shell by freezing. This allows the pipe to shrink and the shell to be removed easily. Water is then used to pressurize the cylindrical shell until the shell cracks. The recorded pressure allows the calculation of shell strength. This test allows the green strength of shell to be measured without being affected by the wax residuals left from the de-waxing process but of course is more complex to perform and tests tensile strength in a different way to conventional bar bending.

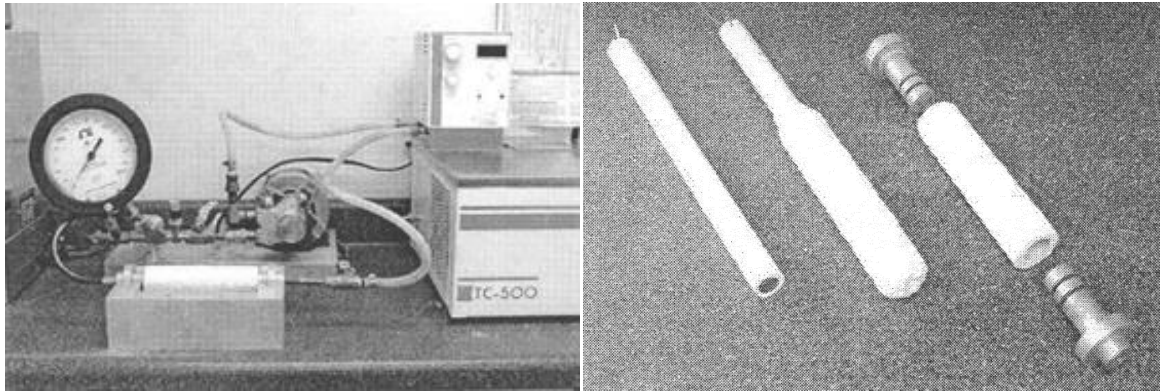


Figure 2-5: Burst test setup to measure the hoop stress of a cylindrical geometry shell mould (Synder, et al., 2003).

While it is normal procedure to measure strength for shell development and in production control for modelling of shell behaviour it is also important to know the Young's modulus, E (modulus of elasticity (MOE)) which is used to quantify the stiffness of a material. Snow (1998) and Cendrowicz (2004) determined the MOE with the results obtained from the 3-point bend test. The gradient of the linear region of a stress-strain curve from a 3-point bend test is used to represent the Young's modulus (Figure 3-12). However due to the very small deflections before failure in 3-point bend analysis of shell materials, the reliability of the test must be questioned. Young's modulus can also be determined by vibration in some systems this is achieved by ultra sound. Asmania *et al.* (2001) used the ultrasonic method to observe the effect of porosity on Young's modulus and Poisson's ratio of alumina ceramics. The advantage of using the ultrasonic method (especially for composite) is that the flexibility of directing the ultrasonic beam through the material at different axes and thus able to obtain the complete set of elastic constants (Brown, 1988). This means that Young's modulus (E), bulk modulus (B) and shear modulus (G) that vibrate on different axes or points can be obtained.

Poisson ratio can be determined if Young's modulus and shear modulus or bulk modulus and shear modulus are known (Liu, 1996). Li *et al.* (2014) used a Poisson ratio of 0.24 for the investment casting shell in their modelling work. The mathematical formula to obtain Poisson ratio, ν are described as below:

$$\nu = \frac{E}{2G} - 1 = \frac{3B - E}{6B} = \frac{3B - 2G}{2(3B + G)} \quad \text{Equation 2-1}$$

2.4 Thermal expansion and density

It is a common understanding that shell cracking will occur if the total expansion or expansion rate of wax is higher than the shell. Jones *et al.* (2002) showed that the cracking of shell is a direct result of wax expansion by observing the thermal profiles across the shell and wax during de-waxing. This section discusses the density of shell followed by wax. It is important to first understand that density is the inverse of specific volume and changes of these parameters with temperature is known as thermal expansion.

The temperature of interest for thermal expansion of shell is approximately 180 °C. Gebelin *et al.* (2001) suggests that the thermal expansion of each layer of shell should be measured before the subsequent layer is added. This would allow the prediction of the shell thermal expansion with a different configuration of layers (Gebelin, et al., 2001). This suggestion allows versatile shell thermal expansion results calculated in models, however the sample preparation is complex and consistent data is difficult to obtain. This procedure was recommended where different shell build varieties are frequently being used and an estimate of shell strength needs to be derived. Gebelin *et al.* (2001) measured the thermal expansion of prime coat on a conventional dilatometer and found

that the percentage of expansion was at the maximum when the temperature reaches approximately 70 °C and then reduced linearly with temperature. This observation could be accounted for by the expansion of moisture in the prime coat and as soon as the moisture evaporates, it starts to shrink. No experimental results were presented on this aspect with respect to the subsequent layers in this paper.

The measurement of wax thermal expansion can be more complex than shell as wax changes phase from solid to liquid as temperature increases over the range of interest. There are a few factors that have been found to affect the thermal expansion of wax. Fielder (1999) demonstrated that fillers added to the wax reduce the volumetric expansion. At a 40 % loading of cross linkage polystyrene filler, there was a 31.7 % average reduction in volumetric expansion at 67 °C and a 29.5 % reduction at 100 °C (Fielder, 1999). The thermal expansion can also be affected by the amount of crystallinity in the wax (Sunderland & Richards, 2001). Sunderland & Richards suggest that crystallinity in wax varies as a result of shear during wax injection and greater crystallinity in wax increases the volumetric expansion. Beeley & Smart (1995) showed that the addition of certain resins can reduce the crystalline structure and reduce the expansion and contraction as a result. It was observed that the thermal expansion of resin was linear with respect to temperature where a pure crystalline substance increases its expansion significantly as it melts (Figure 2-6). The mixture of resin and homogenous crystalline substance showed an intermediate thermal expansion curve labelled in Figure 2-6 as wax.

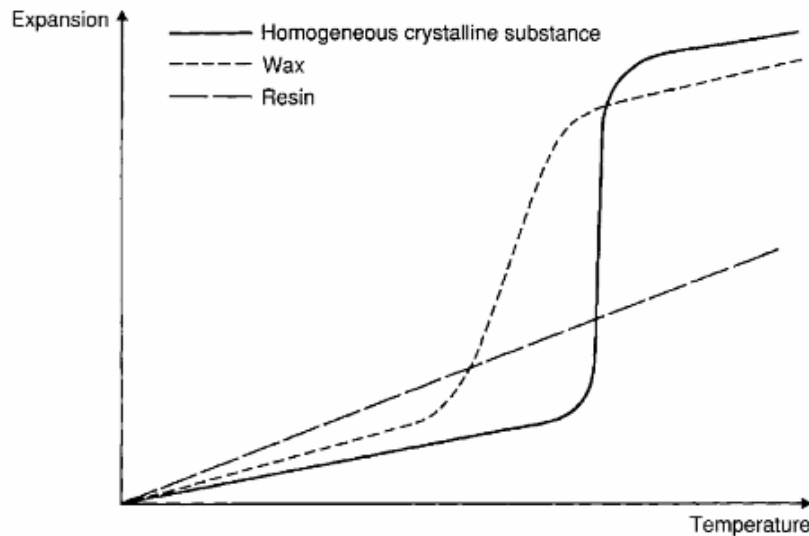


Figure 2-6: Comparison of expansion behaviour (Beeley & Smart, 1995)

It was found that the amount of crystalline material that converts to liquid was very similar between two different heating rates, but the temperature at which the maximum volume expansion occurred was different (Sunderland & Richards, 2001). They also found that thicker sections expand at a lower rate than the thinner sections. This could be because wax at thinner section experience more shear than thicker sections introducing more crystalline. This observation helps to explain the higher probability of shell cracking at sharp edges. Increasing the cooling rate of wax from $1\text{ }^{\circ}\text{C}\cdot\text{min}^{-1}$ to $10\text{ }^{\circ}\text{C}\cdot\text{min}^{-1}$ will increase the specific volume of pattern waxes by as much as 2 % and this is because the high cooling rate does not allow sufficient time for the wax crystals to arrange in a structured manner (Chakravorty, 1999). These factors affecting the thermal expansion could help to determine which waxes are prone to causing shell cracking.

Sabau & Viswanathan (2003) measured the thermal expansion of solid wax over the temperature range of $20\text{--}80\text{ }^{\circ}\text{C}$ by thermo-mechanical analysis (TMA) and when wax is fully melted, a hydrometer was used to obtain the density. The reliability of hydrometer was not discussed and is doubtful since it is not designed to be used at elevated

temperature and fillers in wax might restrict the floatation of a hydrometer. The thermal expansion of the wax as a function of pressure and/or temperature was measured using Pressure-Volume-Temperature (PVT) method (Torres, 2003; Chakravorty, 1999). This method was carried out using a high-pressure indirect dilatometer (Torres, 2003). Torres (2003) showed that as the pressure in PVT test is increased, the specific volume of wax changes less with increasing temperature. Torres (2003) also showed that the volume of wax change linearly due to temperature variations and it is greater in liquid phase than in solid phase. Cendrowicz (2004) found that the coefficient of thermal expansion for Hyfill B417 and Blayson A7-11 to be $0.00034 \text{ m}\cdot\text{m}^{-1}\cdot\text{K}^{-1}$ and $0.00043 \text{ m}\cdot\text{m}^{-1}\cdot\text{K}^{-1}$ respectively over the temperature range of 25 to 100 °C.

The thermal expansion of material measured by one dimensional methods (for example TMA) is convertible to a three dimensional value using Equation 2-2 providing that there are no viscous effects in the volumetric deformation (Cendrowicz, 2004).

$$\alpha = \frac{1}{L} \frac{dL}{dT} = \frac{1}{3V} \frac{dV}{dT} \quad \text{Equation 2-2}$$

where L is length of sample, V is volume of sample, α is the coefficient of thermal expansion and T is the temperature.

2.5 Specific heat capacity

Specific heat capacity is the amount of heat required to raise a specific amount of material by a degree temperature.

The conventional method to measure heat capacity is differential scanning calorimetric (DSC) which compares the rate of heat inputs for the same rate of temperature rise

(Brown, 1988). Snow *et al.* (2002) used DSC and found fused silica (usually used in backup coat) to have a heat capacity half that of zircon (usually used in prime coat). The backup coat however is usually comprised number of six to eight layers where as the prime coat is a single layer and not representative of the shell system. If only one number is required to represent the heat capacity of shell system, the weighted average heat capacity of the two materials taking into account the layer ratio is reasonable.

The specific heat capacity of IC wax has been measured by DSC (Cendrowicz, 2004; Torres, 2003; Shobanjo 2011). Unfilled wax was found to have higher specific heat capacity than filled wax; it was suggested to be due to the fillers acting as heat conductors (Torres, 2003). The measurement using DSC also depends on the heating rate. It was shown that higher heating rates results in lower softening point temperature in the specific heat capacity versus temperature plots (Torres, 2003; Shobanjo, 2010). Shobanjo (2010) also clarified that the thermal history of wax does not affect the specific heat capacity of wax.

2.6 Wax melting point

The melting temperature range for IC wax to transform from solid to liquid is largely due to the blend of different materials (fillers and resins) in the wax. Torres (2003) and Shobanjo (2010) shows that when filler is added into waxes (polydispersed) it increases the range of melting temperature compared to homogeneous wax. Filler addition to the blend also increases the melting point of wax (Shobanjo, 2010). As mentioned in section 2.4, resins are not crystalline and they do not have sharp melting points. This feature will therefore increase the melting temperature range.

Latent heat, L that is released during the transformation from liquid to solid can simply be found by measuring the heat capacity of solid wax and melted wax and calculating the value from the heat balance equation (Brown, 1988):

$$m_{melt}C_{melt}(T_f - T_{i,melt}) = -m_{solid}L_{f,solid} - m_{solid}C_{solid}(T_f - T_{i,solid}) \quad \text{Equation 2-3}$$

where m is mass, C is specific heat capacity, T is temperature and the subscript for melt is molten wax, solid is solid wax.

Alternatively, if the pressure-temperature diagram is obtained, the latent heat of wax can be determined using the Clausius–Clapeyron relationship. For example, a filled wax (Cerita 29-51) was found to have a latent heat of 70-90 kJ·kg⁻¹ determined using this relationship (Sabau & Viswanathan, 2003):

$$\frac{dP}{dT} = \frac{L}{T\Delta V} \quad \text{Equation 2-4}$$

where dP is change of pressure, dT is the temperature change, L is latent heat, T is the temperature and ΔV is the change of volume of material.

It is common to have wax data specification from supplier measured in terms of ring on ball softening point and Ubelhode Drop Melt Point. Drop melt method uses a specially shaped cup with a small orifice at the end and the wax is heated until first drop of wax fall from the hole. The ring and ball method utilizes a ball bearing resting on a shaped piece of the wax under test and wax is usually heated using water bath until the ball falls through. Niles *et al.* (2002) found that the ring on ball method generally produces lower values compared to the drop melt method. This is probably because of the extra weight from the ball bearing causing the wax to giveaway at lower temperature.

2.7 Thermal conductivity

Thermal conductivity describes the ability of a material to transfer heat. Most conventional thermal conductivity instruments first measures the thermal diffusivity which allows the calculation of thermal conductivity provided that density and heat capacity are known. Sabau & Viswanathan (2001) and Cendrowicz (2004) suggested transient line source method can be used to measure thermal conductivity of shell materials. Transient line source method is carried out by supplying a known amount of energy to the sample and measuring the temperature rise allowing the determination of thermal conductivity. Commonly, this method is also known as laser flash analysis. Sabau & Viswanathan (2001) also mentioned that a hot disk technique (or transient plane source method) can be used to determine thermal conductivity of shell but it is not as accurate. The reason was not discussed but it is postulated to be due to the possibility of poor surface contact.

Some researchers have used the less conventional method to obtain the thermal conductivity. Cendrowicz (2004) measured the thermal diffusivity of shell by using a dynamic one-dimensional heat flow method. He measured the temperature change of flat plate coated with investment casting shell then dipped into low melting alloy (250 °C) and the thermal diffusivity was calculated using Equation 2-5. This method is valid in the range where the mid-plane temperature has changed by a significant amount and not yet reached equilibrium with its surrounding (Cendrowicz, 2004). Jones *et al.* (2003) undertook a similar test using hot water as the heat source. They found that the thermal conductivity of a shell used to cast steel is increased by a factor of two using hot water as heat source compared to molten metal, and suggest hot water would simulate the

environment of autoclave. This could be because the wetting of hot water in the pores of shell increased the total heat transferred across the shell:

$$\alpha = \frac{-4l^2 \text{Ln}\left(\frac{\pi(T_f - T_m)}{4(T_f - T_i)}\right)}{\pi^2 t} \quad \text{Equation 2-5}$$

where α is the thermal diffusivity, l is the shell thickness, T_f is the final temperature, T_m is the mid-plane temperature, T_i is the initial temperature of ceramic shell and t is the time.

Measuring the thermal conductivity of wax is more complicated as wax changes phase and expands significantly over the temperature of interest. Hot disk technique was found to be un-suitable for measuring thermal conductivity of wax as the thermal expansion of wax is relatively large and it pulls away from the sensor plate (Sabau & Viswanathan, 2002). Torres (2003) and Cendrowicz (2004) measured the thermal conductivity of wax (by CMold Laboratory Services) using transient line source method. Torres (2003) found the thermal conductivity of filled wax and unfilled wax above 60 °C yield very similar value and as temperature fell below 60 °C, the unfilled wax had a lower thermal conductivity than the filled waxes and this was thought due to the loss contact between wax and thermocouple as the wax shrinks (Torres, 2003). This could also due to unfilled wax shrinking more than the filled wax. This shows that differentiating the thermal conductivity between filled and unfilled wax is non-trivial.

2.8 Rheological behaviour

The IC waxes are mainly a form of paraffin wax – a hydrocarbon compound. Torres (2003) showed that waxes with higher molecular weight have higher viscosity. High viscosity waxes reduces the rate of de-waxing and increase the possibility of mould cracking. The addition of filler material into wax also led to increases in the wax viscosity (Fielder, 1999; Torres, 2003; Cendrowicz, 2004). Fielder (1999) measured the viscosity of waxes with four different types of filler (cross-linked polystyrene, cross-linked acrylic, terephthalic acid (TPA) and water. His results showed that TPA filler had the least effect with 310 % viscosity rise at 40 wt % solids loading while cross-linked polystyrene (XLPS) gave the largest rise of 600 % - 680 % at 40 wt % solids loading. Adding cross linked acrylic (XLA) at 40 wt % solids loading increased the viscosity by 400 % - 440 %, depending on the temperature. Wax with XLPS filler has higher viscosity compared to XLA and this is because XLPS had finer particle size, which would increase the rate of collisions causing greater internal resistance flow (Fielder, 1999). Torres (2003) also mentioned that the flow in filled waxes appears to follow all the rules of particles in a suspension, for example they can be modelled using Krieger-Dougherty equation.

2.8.1 Rotational rheometer

The rheological behaviour of molten wax is usually measured using rotational rheometer with a flat parallel plate setup to shear the wax. Torres (2003) used parallel plates instead of cone and plate to measure wax rheology because the blends could not be held in within the cone geometry. Cendrowicz (2004) agreed that cone geometries

should not be used as waxes with filler particles or even solid wax crystals tend to migrate to the apex of the cone, thus causing erroneous data. Concentric cylinder setup is not recommended as the viscosity varies with respect to time as the filler sediments at low shear (Torres, 2003). Another advantage of using parallel plates compared to geometries is that the gap between two plates can easily be varied (Cendrowicz, 2004). The sample preparation prior to test was found to be important. Cendrowicz (2004) showed that preparing the wax with a thermal and a shear history changes the freshly melted wax viscosity to the viscosity of samples obtained from wax injection machines.

Cendrowicz (2004) showed that during the de-waxing, the shear rate that occurs during the permeation of the liquid wax through the shell would typically be 1000 s^{-1} . Cendrowicz drew an exponential trend-line on the viscosity against temperature data measured at 1000 s^{-1} for computer simulation purposes and the trend line had the form of Equation 2-6:

$$\mu = \mu_{ref} \exp - \xi(T - T_{ref}) \quad \text{Equation 2-6}$$

where μ_{ref} is the reference viscosity at the reference temperature T_{ref} (taken as 0°C), and ξ is the exponent of viscosity in relation with temperature.

Torres (2003) uses the same equation to model the viscosity of wax with the assumption that the wax was Newtonian, had constant heat capacity, thermal conductivity and density. Cendrowicz (2004) also modelled the wax viscosity using Arrhenius type equation (Equation 2-7). This equation could represent both the viscosity before and after the melting point. The two equations (Equation 2-6 & Equation 2-7) however, do

not vary with shear rate and constant shear rate (for example 1000 s^{-1}) has to be assumed.

$$\mu = A \exp \left(\frac{E}{RT} \right) \quad \text{Equation 2-7}$$

where T is absolute temperature in Kelvin, R is universal constant, E_a is the activation energy for viscosity and A is the Arrhenius constant.

Gebelin *et al.* (2004) used the Carreau model to fit the wax viscosity as a function of temperature and shear rate, $\dot{\gamma}$. The parameters - η_0 , η_∞ , λ and n are in function of temperature which is obtained from experimental rheological data fitting (Gebelin, et al., 2004). These parameters have no physical meaning. The Carreau model is described by:

$$\eta = \eta_\infty + (\eta_0 - \eta_\infty)(1 + \lambda^2 \dot{\gamma}^2)^{\frac{n-1}{2}} \quad \text{Equation 2-8}$$

2.8.2 Capillary rheometer

A capillary rheometer is an instrument that enables measurements of the pressure difference through a capillary with a known flow rate of a material. Torres (2003) suggested the use of an extrusion rheometer to study the behaviour of waxes in semi-solid state because the material in the die is kept under pressure, thus wall slip is less likely to occur.

Torres (2003) carried out experiments on filled model waxes at temperatures between 47.5 and 55 °C. He found that significant viscous heating induced apparent shear thinning behaviour. He estimated the increase in temperature from viscous heating was 9 °C with test geometry of 24 mm capillary length and 1.5 mm diameter at 47.5 °C. The experiments were thus conducted between 0 and 500 s^{-1} to minimise errors from

viscous heating. To obtain data to represent the de-waxing process, low temperature rheological behaviour should be carried out with low shear rate. This is more representative since no significant shear will be introduced on wax during the de-waxing process which mainly dependant on gravitational force. However, it is important to note the rheological behaviour varies from wax to wax and the range of shear rate value do vary with waxes.

2.9 Surface tension

Surface tension (γ) of wax influences the penetration of wax into the porous shell and the flow of molten wax out of the mould. Surface tension or wettability of a liquid on a solid surface measures the cohesive energy present between molecules at the interface. There are a few factors that affect the wetting of a surface such as substrate surface roughness, heterogeneity of the surface, temperature, rate of wetting and liquid properties (viscosity, surface tension and density) (Kumar & Prabhu, 2007).

The wettability of a fluid on a solid surface can be determined in terms of contact angles. Jones *et al.* (2002) observed the contact angle between a molten wax droplet resting on a shell prime coat material. This method is also known as sessile drop test. They found that the greater the temperature, the smaller the contact angle. However, they suspected that the contact angle reduces with temperature increment because of wax ingress into the shell. This method to observe the surface wetting has its limitations since the shells are porous.

A common surface tension test is the Du-Nuoy ring test which uses a circular wire often made of Platinum. Torres (2003) had used this test to obtain the surface tension of wax with different fillers particle compositions. Torres showed that the surface tension of

wax decreases with increasing temperature and increases with filler addition. High surface tension may increase the shell cracking probability.

Sauer & Dipaolo (1991) measured the surface tension of high molecular weight polymers at elevated temperature using the Wilhelmy plate method. This method is usually done by dipping and pulling a flat solid plate from the liquid and observes the angle of meniscus interacting with the surface of solid. The same method was used by Krup & Luyt (2001) to observe the properties of blends of linear low density polyethylene (solid plate) and an oxidized paraffin wax (liquid). The Wilhelmy method is appropriate for heterogeneous and porous material such as wood (Petric, et al., 2009; Bryne, 2008). Porous materials like IC shells however have not been tested with this method. The Wilhelmy method gives reliable results with low variance therefore it is preferred over sessile drop method (Lander, *et al.*, 1993). The wettability studies using dynamic measurements (for example Wilhelmy method) are advantageous over static methods (for example sessile drop method) as they better represent the conditions in which the materials are used (Kvitek, *et al.*, 2002).

2.10 Interface heat transfer coefficient

A thin layer of undisturbed fluid in contact with a solid surface will exist when the solid body is being heated or cooled by gas or liquid flowing over the surface. The heat transfer restriction created by the undisturbed fluid is represented in terms of the heat transfer coefficient.

At the shell-autoclave interface, the steam losses its latent heat and condenses on the surface of the shell during de-waxing. This layer of condensate film affects the heat

transfer coefficient at the shell-steam interface. Heat transfer across an interface depends on surface wetting, the film thickness and the temperature gradients in the film (Brown, 1988). Heat transfer across the interface also depends on adsorbed gases, pressure, surface finish, hardness and fluid trapped between two surfaces (Brown, 1988). At the shell-wax interface, when heat is transferred from the shell to the wax during the de-waxing process, some heat is lost in the gap between the shell and wax.

The complexity of the system increases as soon as the heat melts the solid wax at the interface and the heat transfer coefficient in the gap changes. Jones *et al.* (2002) suggest that the wax is fluid enough to enable heat transfer to take place by convection when at 120 °C (Figure 2-7). They also proposed that the heat transferred through the shell is immediately removed from the wax shell interface and transferred to the wax solid-liquid interface where the thermal energy is used to further melt the wax. If this idea holds true, the heat transfer coefficient will reduce as the layer of liquid increases.

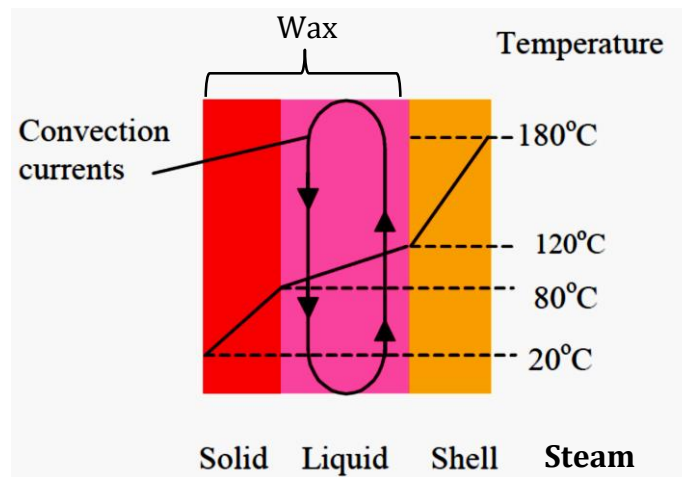


Figure 2-7: Illustration of the heat convection on the melted surface of wax pattern (Jones, *et al.*, 2002)

Snow (1998) uses $220.6 \text{ W}\cdot\text{m}^{-2}\cdot\text{K}^{-1}$ for the shell-wax interfacial heat transfer coefficient in his work but the source of this value was not discussed. As a comparison, the interface

heat transfer coefficient of $250 \text{ W}\cdot\text{m}^{-2}\cdot\text{K}^{-1}$ between the wax and aluminium injection die was used based on preliminary estimations from experimental data by Sabau & Viswanathan (2002). This shows that the heat transfer coefficient in both situations is comparable. As a guidance for heat transfer coefficient measurement techniques in wax, work carried out on metal casting can be used. The heat transfer coefficients for shell-metal interface were determined by measuring the temperature on both the solidifying metal and the mould then calculate with an inverse heat conduction method (Konrad *et al.*, 2011). This technique estimates the heat transfer coefficient with the temperature difference, ΔT at the alloy and mould interface (Figure 2-8). This method has not been applied to waxes.

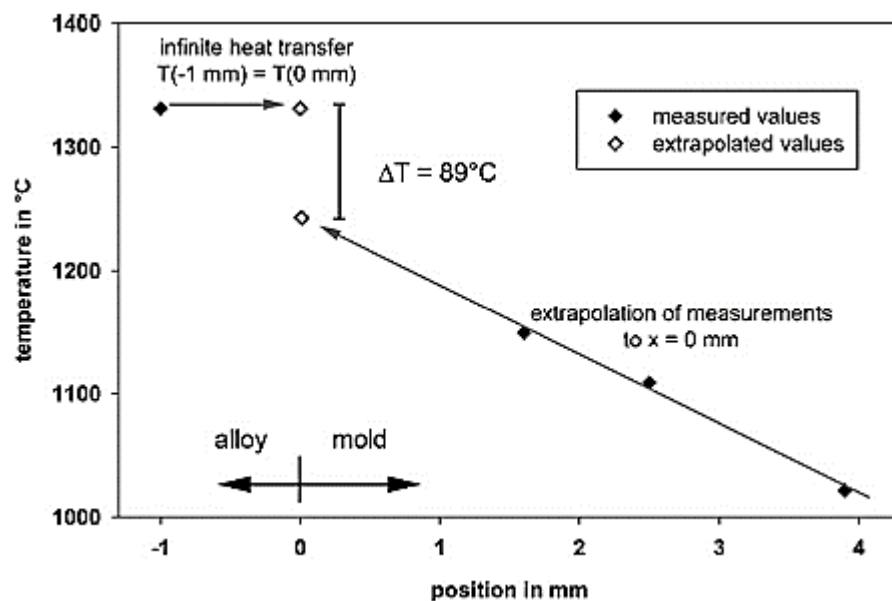


Figure 2-8: Determination of the temperature drop ΔT at the interface alloy/mold (Konrad, Brunner, Kyrgyzbaev, Volkl, & Glatzel, 2011)

2.11 Numerical Simulation of the Process

To model the de-waxing process, a few mechanisms which occur simultaneously have to be considered and the solution from one mechanism might be used to calculate the simulation of next mechanism. Zienkiewicz *et al.* (2005) described it as two or more physical systems interacting with each other, with the independent solution of any one system requiring simultaneous solution of the others to continue. Computational modelling requires appropriate parameter relationships to simulate the de-waxing condition accurately.

Gebelin *et al.* (2001) had made an attempt to model the thermal profile at the shell-wax interface during de-waxing process using Physica+ code. They suggested that the melting of wax can be modelled with two basic balance equations, the energy balance and the momentum balance. The energy equation should take into account the heat capacity of wax in solid and liquid phase. The momentum equation takes into account changes of phase which affect the viscosity of wax. The simulation was found to be accurate for the first ten seconds but then to diverge as the predicted heating rate slowed down compared to the experimental work. They postulated that this may have been due to the coarse mesh size which was set at a 3 by 3 mm element size or possibly because the thermocouple used experimentally was restricting the flow of molten wax.

Cendrowicz (2004) simulated the shell cracking with a one-dimensional model. A weak ceramic shell system is believed to be induced during the de-wax stage due to excessive wax expansion (Cendrowicz, 2004). He found the first few seconds of de-waxing are critical in terms of shell cracking. He suggests that the wax melts about four seconds earlier in the case where steam penetrates the shell according to the model. This

indicates that it is important to model the de-waxing process taking into account of the energy contributed by steam being either restricted to the surface or in the mould pores. Cendrowicz (2004) commented that it is unclear if air remained trapped as a cushion between wax and the condensate, or if it was trapped somewhere else within the pore network. Another issue he raised was what would happen when the air in pores was heated as it would expand (Cendrowicz, 2004). The limitation of the Cendrowicz approach is that the latent heat, heat capacity, thermal conductivity, and density were assumed to be independent of temperature. The heat transfer coefficient of gas-shell and wax-shell interfaces was neglected since the boundary layer was relatively small compared to the thickness of shell. The heat transfer across the shell and the wax was assumed to take place purely by conduction. This assumption is valid as long as wax remains solid or the contact between the two surfaces remains. Cendrowicz (2004) also assumed the wax to be incompressible and neglected the hydrostatic pressure of the steam. This is a fair assumption since compressibility of IC wax is small, however it can double when wax changes from solid to liquid. Compressibility of wax increases from 3×10^{-10} to $6 \times 10^{-10} \text{ Pa}^{-1}$ in the phase transformation (Torres, 2003).

Currently, there is little simulation data on pattern wax shell cracking in the literature. There are more works published on investigating the shell cracking with rapid prototyping pattern especially the laser stereolithography (SLA) patterns. In modelling SLA pattern, the pattern is usually assumed to disintegrate into gas phase at its softening point. This assumption eliminates the need of modelling the wax flow mechanism. Li *et al.* (2014) developed a fully coupled transient thermo-mechanical nonlinear finite element model to predict shell cracking during the foam pattern removal process. They had formulated a crack detection surface as the indicator of shell cracking when stress

reaches the maximum in the stress-strain curve. They found that it was less susceptible to crack development on shell with corner radii. Their model was verified by experimental work where the shell cracks are inspected visually. Yao & Leu (1999) looked at shell cracking during the burn out of patterns built with epoxy. The thermal expansion coefficient of the epoxy resin was found to be one order of magnitude larger than that of investment casting shell. They found that from finite element analysis (FEA), the predicted cracking temperature is about 35 °C at which point the induced stress exceeds the flexural strength of the ceramics material (Yao & Leu, 1999). They verify their work by measuring the induced stresses on the shell with strain gauges. Ferreira & Mateus (2003) performed FEA looking at the shell cracking cause by SLA using Pro-Mechanica® 20 software. The FEA model predicts the stress fields showing a fracture zone in the internal square-frame structure of SLA pattern (Ferreira & Mateus, 2003). Chen *et al.* (2011) have look at the circumferential stress of a turbine blade cross section by applying transient thermo-mechanical FEA. The displacement of ceramic shell was used to calculate the contact boundary between SLA patterns and ceramic shell allowing the prediction of high stress area. From the FEA results, they found that the circumferential stress turbine blade geometry of the shell enlarges by the SLA patterns.

PART 1 – Materials Characterisation

This part consists of two chapters - Chapter 3 and 4 to understand the behaviour of materials relevant to the de-waxing process. Chapter 3 explains the experimental procedures to characterise the shell and wax and Chapter 4 discussed the experimental results. The properties of shell and wax obtained experimentally will be considered with a view to their inclusion as data in the computer simulation of the de-waxing process.

3. MATERIALS AND METHOD

This chapter describes the experimental procedures applied and in most sections the adopted procedures are for shell followed by those for wax. All ceramic shell moulds were prepared in IRC laboratory (Birmingham University) and the waxes were provided by commercial wax suppliers such as Remet, Blayson and Paramelt. In this project, five types of wax (denominated as Wax A, B, C, D and E) were used for comparison. The wax materials used in this project were waxes which are commonly used in the commercial investment casting process at Rolls-Royce Plc. However, for certain tests, only four waxes were studied as one of the wax (Wax D) arrive later in the project and was not subjected to the full sets of tests (only those then established as critical). The production of Wax A has been terminated by the manufacturer and it is now used as a benchmarking for a non-shell cracking wax since no shell cracking issues were raised when in operation. Wax B, C and D were filled waxes intended to replace Wax A, however, these waxes were causing shell cracking in foundries and thus interruption to production. Wax E was an unfilled wax generally used as runner wax (sprue section) which relieves the pressure in the shell mould more effectively due to having a lower melting point and viscosity but to the detriment of the mechanical strength and dimensional accuracy offered by filled waxes. With information from the wax supplier, the waxes can be categorised into three types; where Wax A and D contained one type of filler, Wax B and C contained two types of filler, and Wax E was unfilled wax. Due to confidentiality, the information on the fillers specifications was not available from the supplier.

The shell samples in this study were prepared by coating wax patterns with alternate layers of slurry and ceramic particles (stuccos). Wax bars measuring 200 x 30 x 5 mm were prepared by injecting molten wax at around 2 MPa and 63 °C (Wax D –filled wax) into aluminium die (ambient temperature) to obtain a rectangular wax pattern (Figure 3-1).

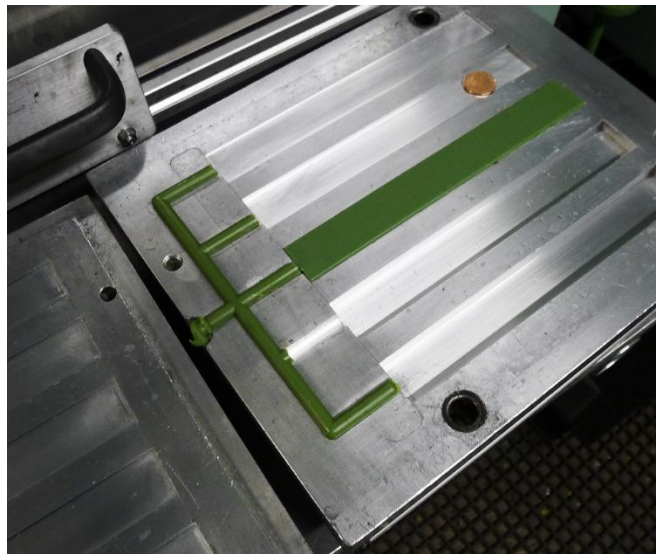


Figure 3-1: Wax D injected into an aluminium die to make 5 rectangular bars, 4 bars are removed. 1 pence for scale.

The wax was injected with a standard Mueller Phipps International (MPI) Model 55 wax injection machine and the basic principal of wax injection is shown in Figure 3-2.

Once removed from the die, the solidified wax was then cleaned with degreaser solution (Trisol 60 plus from Blayson) and left to dry. The wax pattern was then dipped in the primary slurry which had the formulation given in Table 3-1. After a drainage period of 30 seconds, the wet surface was sprinkled with 0.149 mm zircon sand stucco (100 mesh), supplied by TW Logistics Limited and left overnight in the drying room. This layer is referred to as prime coat in this work.

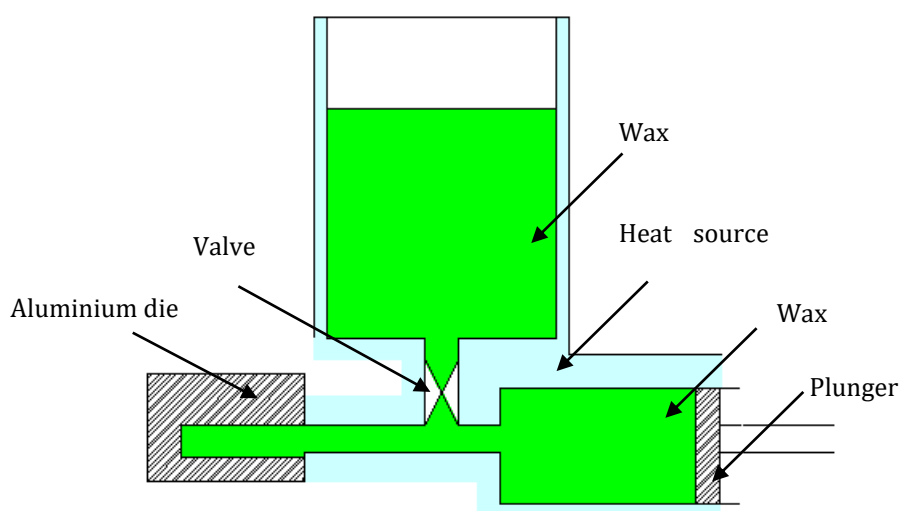


Figure 3-2: Schematic diagram of wax injection machine setup

The drying room condition was set at 50 % relative humidity and 21 °C. This was followed by dipping in secondary slurry, the formulation being given in Table 3-2. After drainage, the wet surface was sprinkled with 0.177 – 0.595 mm size (30-80 mesh) Molochite™ (Imerys) stucco and dried. This step was repeated for another layer with the 30-80 mesh stucco. Then, four subsequent layers were added following a similar procedure using a coarser grain 0.595 – 1.190 mm size Molochite stucco (16-30 mesh). A final coating known as the sealing layer was made by dipping in the secondary slurry without stucco sprinkling and the final assembly left overnight to dry. All the subsequent layers after the prime coats are referred as the backup coat. The procedure to produce standard shell to cast steel is summarised in Table 3-3.

Table 3-1: Prime coat slurry composition

Initial formulation	Mass (%wt)
Filler (Zirconia silicate - 74 µm)	79.83
Binder (Remasol silica)	17.00
Polymer (REMET Adbond ADII)	1.20
Wetting Agent (REMET Victawet 12)	0.06
Antifoam (REMET Burst RSD10)	0.10
Deionised water	1.81

Table 3-2: Backup coat slurry composition

Initial formulation	Mass (%wt)
Filler (fused silica - 74 μm)	43.05
(Mullite - 74 μm)	14.37
Binder (Remasol silica)	32.83
Polymer (REMET Adbond BV)	3.34
Wetting Agent	-
Antifoam (REMET Burst RSD10)	0.22
Deionised water	6.19

Table 3-3: Standard specification for shell to cast steel ¹

Slurry	Stucco	Layers	Dip time, s	Drain time, s	Air speed, ms^{-1}	Dry time, h
Primary	Zircosil granular	1	30	60	0.4	24
Secondary	30-80 Molochite™	2	30	60	3.0	1.5
Secondary	16-30 Molochite™	4	30	60	3.0	1.5
Seal	-	1	30	60	3.0	24

The standard shell samples were then treated using different methods before being evaluated for various properties the methodologies of which are described in section 3.4. The bars were either de-waxed using a conventional autoclave (Figure 3-3) with a specific steam pressure profile given in Figure 3-4, followed by a controlled depressurisation cycle at $1.67 \text{ kPa}\cdot\text{s}^{-1}$ or by first cutting the dried shell and wax to the desired shape, followed by chilling overnight (12 hours) at around 5°C to release the wax from the shell (Figure 3-5). The autoclave was preheated before any actual de-waxing process was carried out. This step was intended to reduce heat loss to the chamber wall and through the door. In both wax removal methods, shell specimens of $50 \times 20 \times 6 \text{ mm}$ were typically prepared by tile cutter. The bars were stored under atmospheric conditions until further evaluation.

¹ Note that all shells were hand dipped in slurry and stuccoed from a sieve by the author and any value here is not comparable to a shell system slurry dipped using robot arms and stuccoed with a rainfall sander or fluidised bed.



Figure 3-3: Quicklock Boilerclave™ by Leed and Bradford Boiler Company Ltd, UK. Autoclave for de-waxing in IRC laboratory. The dark and pressurised condition which is used has limit the understanding of de-waxing process.

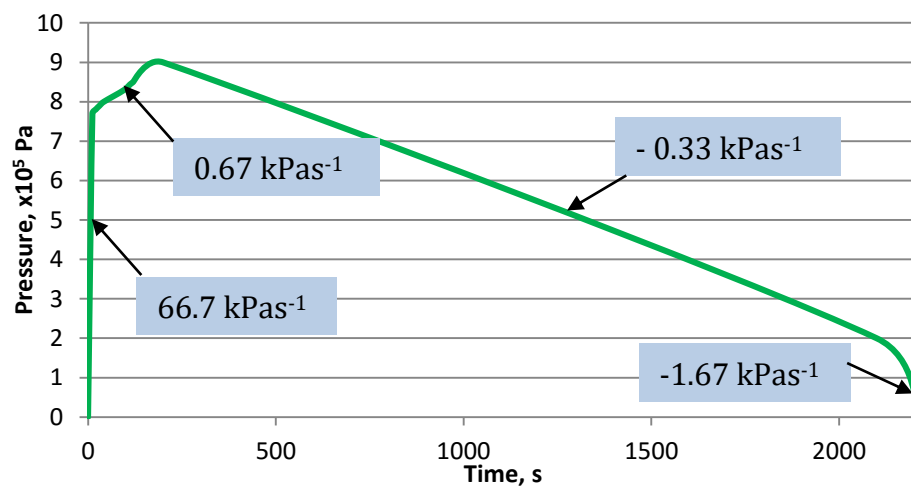


Figure 3-4: The pressurisation and depressurisation profile for the autoclave used in the IRC laboratory



Figure 3-5: The shelled flat bar wax was cut after drying to the required test bar dimensions and then separated by cooling in a refrigerator.

The sample prepared by either autoclave or fridge de-waxing were either sent for testing in that condition or were further treated before being examined. Those that were further treated were subjected to one of the following:

- Boiled in water and then mechanically tested while wet
- Boiled in water and then mechanically tested after drying
- Autoclave treated under standard conditions and then mechanically tested wet
- Autoclave treated under standard conditions and then mechanically tested after drying
- Steam treated by suspension bars above boiling water, followed by mechanical testing when wet
- Steam treated by suspension bars above boiling water, followed by mechanical testing after drying

This gave a total of 16 permutations and eleven different treatments being evaluated.

The methods are summarised in Table 3-4.

Table 3-4: Summary of experimental methods for sample preparation and mechanical testing.

Initial dewax method	Autoclave for second time	Post dewax treatment	Tested dry or wet	Tested primary up or down	Method notation
Autoclave	No	Dry		Up	1(a)
				Down	1(b)
		Wet		Up	
				Down	
		Steam	Dry	Up	
				Down	
			Wet	Up	
				Down	
		Boil	Dry	Up	
				Down	
			Wet	Up	3(a)
				Down	3(b)
	Yes	Dry		Up	9
				Down	
		Wet		Up	5
				Down	
		Steam	Dry	Up	11
				Down	
			Wet	Up	10(a)
				Down	10(b)
		Boil	Dry	Up	
				Down	
			Wet	Up	
				Down	
Fridge	No	Dry		Up	2(a)
				Down	2(b)
		Wet		Up	
				Down	
		Steam	Dry	Up	
				Down	
			Wet	Up	
				Down	
		Boil	Dry	Up	7
				Down	
			Wet	Up	4(a)
				Down	4(b)
	Yes	Dry		Up	8
				Down	
		Wet		Up	6
				Down	
		Steam	Dry	Up	
				Down	
			Wet	Up	
				Down	
		Boil	Dry	Up	
				Down	
			Wet	Up	
				Down	

3.1 Microstructure

3.1.1 Scanning Electron Microscope (SEM)

SEM was used to observe the structure of the ceramic shell layers and the stucco in green state (after autoclaving). Thin mould samples from the test bars were cut and embedded in slow curing epoxy resin (Struers, Epofix) with the desired layered section facing down. The embedded specimens were placed into a vacuum unit (Struers, Epovac) for 10 minutes to purge out air bubbles and for the intrusion of resin into the pores of the specimens to take place. The specimens and resin were left for 24 hours to set. The surface of the specimens were polished with increasing grade of polishing disc from coarse to fine and grades of diamond solutions (DS) with the specifications shown in Table 3-5. The polished specimens were then coated with carbon. SEM was conducted using the XL30 FED ESEM Electron Microscope with 15.0 kV beam and at 0.012 Pa vacuum.

Table 3-5: Specification for surface polishing

Polishing stages	Polishing Grade	Disc	Speed (rpm)	Solution	Time (mins)
1	220 piano		250	Water	10
2	Allegro		125	9 KDS	20
3	Largo		125	9 KDS	20
4	Map		125	1 KDS	5

A Scanning Electron Microscope (SEM) was also used to observe the microstructure of fillers in wax pellets. The wax samples for this test were prepared by freezing the wax pellets in liquid nitrogen and breaking the pellets in half. These samples were embedded in epoxy resin and coated with gold as the wax has low electrical conductivity. SEM was

conducted using an XL30 FEG ESEM Electron Microscope focused with a 5 kV electrons beam.

3.1.2 Reflected light optical microscopy

After de-waxing, wax residues are expected to remain on the prime coat surface. This hypothesis was verified by observing the de-waxed shell under a reflective optical microscope (LEICA LEITZ DMRX) along with 3CCD Colour Vision Camera Module. 20 x 5 x 6 mm samples (after autoclave de-waxing) were prepared by cutting the mould using a tile cutter. The samples were then embedded in epoxy resin followed by polishing. Plasticine was attached on the opposite surface to the wax pellet and pressed on a specimen levelling press to obtain a flat surface and perpendicular specimen.

An optical microscope was also used to observe the microstructure of wax pellets. Samples are prepared by moulding the wax pellets in epoxy resin, followed by surface polishing to remove epoxy resin covering the wax surface. Polishing disc was changed more frequent to avoid wax residues on the disc smearing on the surface sample.

3.1.3 Interferometer

The average surface roughness of the prime coat surface was characterised based on the mean vertical deviations of the roughness profile. The surface irregularities were measured by the interferometry method performed using a MicroXAM2 interferometer (Omniscan, UK), which operated with a white light source. The image of the shell prime coat surface was acquired using a 20 x magnification objective lens and Scanning Probe Image Processor software (Image Metrology, Denmark). Ten images were taken continuously across the sample horizontally and ten vertically to obtain a total of 100

images. These images were then 'stitch' together to obtain a larger image for a representative surface roughness of the prime coat surface (approximately 1 x 1 mm) post de-wax.

The MicroXAM2 interferometer was also used to measure the surface roughness of wax pattern. The surface roughness of the wax pattern was inspected before and after treating with degreaser solution. Samples were prepared by cutting the wax pattern into two 20 x 20 x 10 mm rectangular bars. One of the samples was soak in degreaser solution for 30 seconds and rinsed with deionised water and the other sample was used as a control. That wax pattern was left overnight to dry. Again, ten images were captured continuously across the wax surface horizontally and ten vertically to obtain a total of 100 images. These images are then 'stitch' together to obtain a larger image for a more representative measure of the surface roughness.

3.1.4 *Transmission Light Optical Microscope*

The waxes were observed under an optical transmitted light microscope with polarising filters. The device used either crossed or plain polarised light, when cross polarised light is used, no light is transmitted through to the observer unless the specimen interferes with the passage of light (Figure 3-6 a). However, in the presence of transparent crystalline materials or anisotropy (except cubic) there will be interference with the light path allowing the light to pass (Figure 3-7) generating interference colours. In these cases, the material will only be visible if the light is not in extinction. The colours observed will vary depending on materials refractive index and thickness. In contrast, plain polarised light allows light to transmit through the system all the time proving the specimen is transparent (Figure 3-6 b).

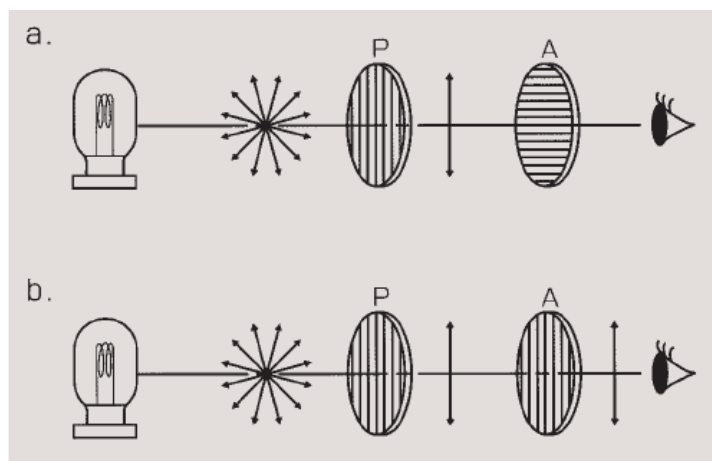


Figure 3-6: a. cross light and b. parallel light. A - Analyser, P - Polariser (Olympus)

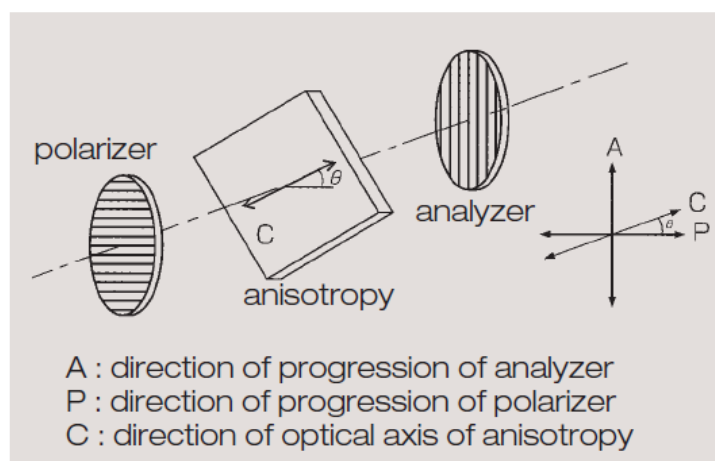


Figure 3-7: Anisotropy between cross light (Olympus)

The microscope used long focal length lenses which allowed it to be used in conjunction with a hot stage. A thin slice of wax pellet was cut using a razor blade and melted on a microscope glass slide with a gas light torch. The glass slide was then fitted to an Olympus BX51-P microscope and heated to required temperature using the hot stage (LINKAM THMSG 600). In general, the two filters (polariser and analyser) would be set for light to be extinct at all angles when no wax is present. When the wax is present, light will be seen but only if the crystals are not at their extinction angle. When the wax is

melted, the light will be in extinction again due to the amorphous nature of the fluid. Some filler material may remain visible as they do not melt under the test conditions.

3.2 Chemical compound analysis

The chemical compounds within the IC waxes were observed using the Fourier Transform Infrared Spectroscopy (FTIR). A pellet of solid wax was clamped in a diamond compression cell to flatten the sample to a thin uniform thickness between a pair of diamond windows allowing the monochromatic infrared beam to pass through the sample. The chemical compound analysis was undertaken on a Thermo Scientific Nicolet 8700. Chemical groups within the wax absorb some of the light at specific frequencies of energy and some light is transmitted through the thin sample. The light transmitted is recorded by the detector as interferogram signal for final measurement. The measured interferogram signal was then 'decoded' by Fourier transformation analysis and the compounds that absorbed the particular wavelength identified.

3.3 Permeability

It was historically understood (Cendrowicz, 2004; Branscomb, 2010; Jones *et al.*, 2001), that as wax melts, a small volume of wax will penetrate into the shell to relieve the pressure developed in the mould (Figure 3-8). A few different tests were carried out in this study to quantify the permeability of the mould.

The permeability of shell has conventionally been measured using the ping-pong ball test as described in Section 2.2. Determining the green shell permeability (before autoclaving), however, is not as well documented and the permeability is believed to be reduced in the shell after firing.

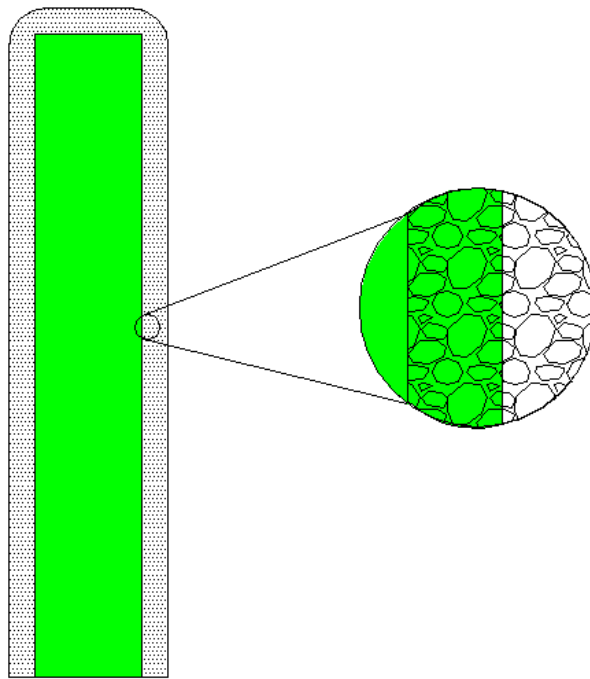


Figure 3-8: Schematic diagram of wax permeating the shell during de-waxing process. This process occurs prior to the bulk wax melting process.

Permeability is important to be able understand how the wax that might penetrate into the shell. Wax expansion is inevitable and the passage of wax into the porous shell gives an apparent reduced expansion of the bulk wax. Permeability was evaluated by pressurising either water or wax across the shell from the prime coat surface to the backup coats. Mass flowrate of water or wax was measured and permeability, K was determined using Darcy's law (Equation 3-1). The application of the Darcy's law is with the assumption that the shell is homogenous, however, in reality the prime coat is the main factor that determine the flow of wax instead of the backup coats.

$$K = \frac{m \mu L}{\rho A (P_{in} - P_{out})} \quad \text{Equation 3-1}$$

where m is mass flow rate, μ is dynamic viscosity, L is thickness of shell, ρ is density of fluid, A is permeability surface area, P_{in} is pressure from air compressor and P_{out} is atmospheric pressure.

Darcy's law is applicable in this situation since the flow of wax through the shell has satisfied the condition with Reynolds number (Re) less than 1 ($Re \approx 4.03 \times 10^{-6}$). The pore diameter can then be estimated from the permeability using $0.5 \times K^{0.5}$ (Brinker & Scherer, 1990).

In the test for water as permeate fluid, the prime coat and two subsequent secondary layers were first coated on a thin cylindrical wax pattern of 50 mm in diameter. The shell cylinder was ground at the edge and refrigerated allowing the shell to be removed easily from the wax. The three layered ceramic shell was then attached to one end of a 46 mm diameter steel pipe with sticky wax (Figure 3-9). The sticky wax has soft texture similar to plasticine that can work as a temporary glue. The sticky wax was cleaned with Trisol 60 plus using a cotton bud and then air dried. The assembly was then coated with further 4 layers of back up coat followed with the seal layer. The other end of the steel pipe was used to fill the chamber with de-ionized water then sealed with an orifice connected to a compressor. The steel cylinder was pressurized with air at 27579 Pa (4 psi) and water that passed through the ceramic shell collected at the other side with a petri dish. The mass flow rate of water was obtained allowing the permeability to be calculated. Note that this test was carried out at ambient temperature.

A different permeability test was carried out using wax as permeate fluid, a thin layer of wax was first solidified at the open end of the 50 mm diameter steel pipe (Figure 3-10). The thin layer of wax had to be strong enough to avoid distortion during slurry dipping due to lower density of wax relatively to slurry, and sufficiently weak so that wax expansion would not pre-crack the shell before the test.

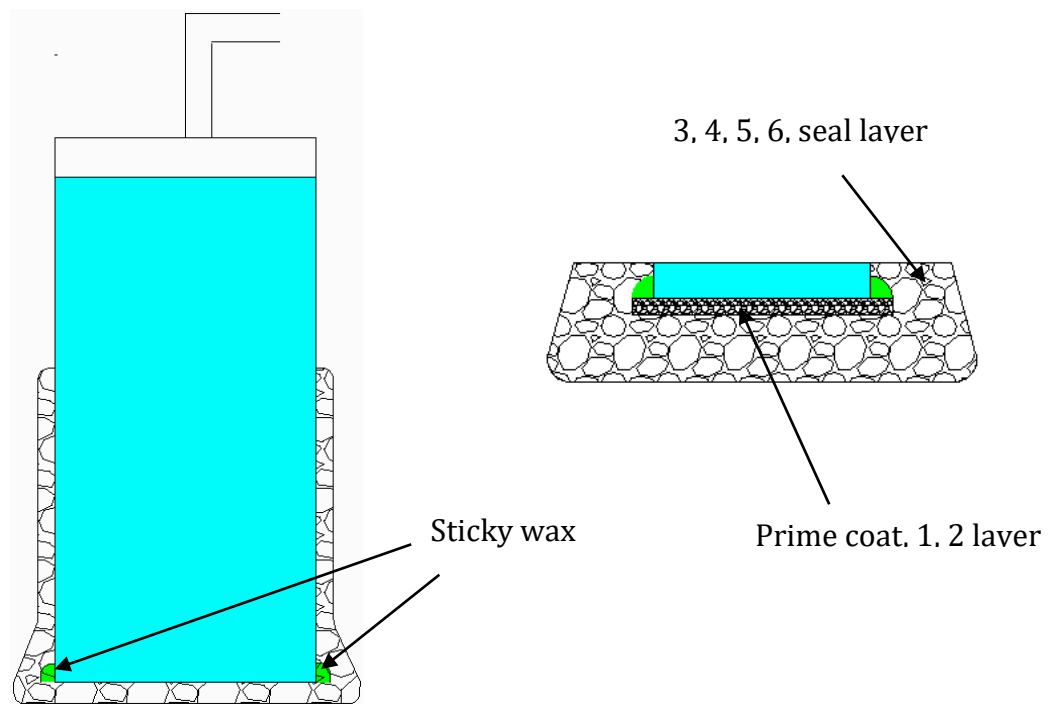


Figure 3-9: Water permeability setup

The wax surface was cleaned with degreaser solution and shell coating was carried out following the standard procedure. The assembly was heated at 110 °C to melt the thin layer of wax and more molten wax was added into the steel pipe (from the top inlet). The permeability test was carried out with 100000 Pa pressure differential. Time was recorded from the point when the pressure was turned on and stopped when pressure was removed. This allows the time to wet the shell or any restriction in flow by the pore necks to be taken into account in the permeability calculation. Other researchers for example Cendrowicz (2004) only start to time when the wax starts flowing. The amount

of wax flowing through the shell was collected on a petri dish and the mass of wax recorded. This allows the permeability of wax across the shell to be calculated. Filled and unfilled waxes were used as permeate fluid for comparison to observe if fillers in wax increase the infiltration resistance as the wax penetrates into shell.

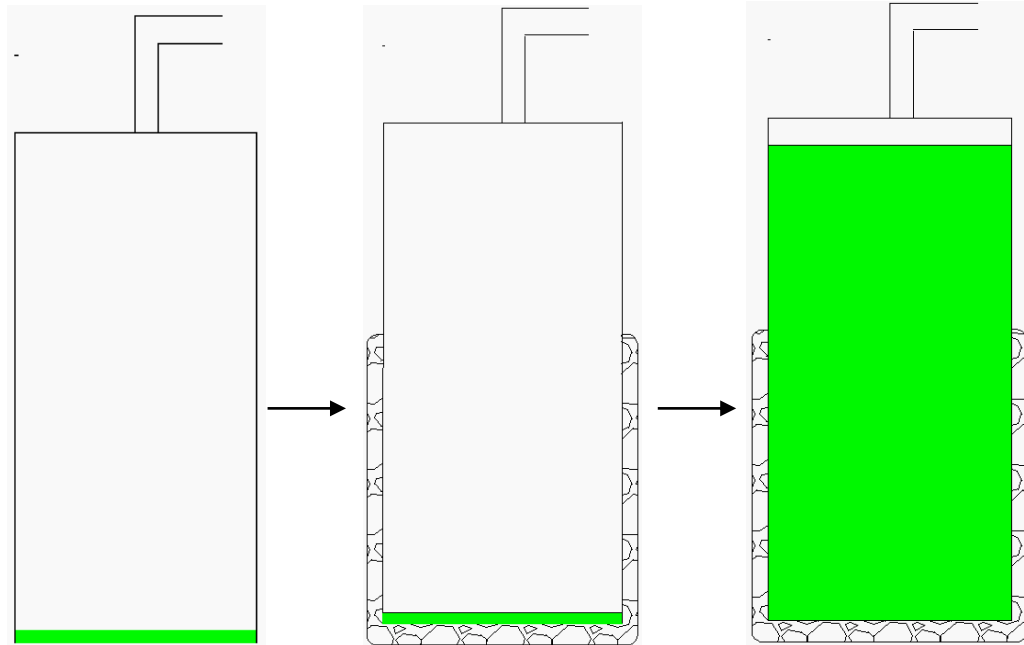


Figure 3-10: (i) Initial setup after solidifying a thin layer of wax (left), (ii) standard shelling (middle), (iii) setup after wax pellets are melted inside the steel pipe (right)

3.4 Flexure strength

3.4.1 Flat bar test

Two common methods are available to measure the strength of a shell – 3-point bend test and 4-point bend test. 4-point bend flexure tests produce peak stresses over an extended region of the sample potential exposing more defects and flaws. This includes defects along the edge of samples produced during sample preparation. Surface polishing to smooth out the edge is not possible in this case as the stucco particles are relatively large and the primary coat is fragile. Furthermore, shells that are weaker in a

batch may break during the polishing stage due to handling introducing bias into the test and reporting an artificially high mechanical strength. Even though the 4-point bend test is preferred for most strength characterisation purposes, the sensitivity of the test will generally give lower shell strength. Due to larger area the test covers, 4-point bend test requires relatively high numbers of samples with at least 77 samples being recommended by Richard *et al.* (2003). It is stated that materials of a composite nature should use 3-point bend test if the material break within the 5 % strain limit (ASTM D790-10, 2010) and shell system in this work typically exhibited 3-4 % strain before crack initiation. Most importantly, with the simplicity of sample preparation and also simpler test fixtures, 3-point bend test was used to determine shell strength in this work. The failure strength of ceramic shell using 3-point bend test, σ_{max} can be calculated using:

$$\sigma_{max} = \frac{3 P_{max} L}{2 W H^2} \quad \text{Equation 3-2}$$

where P_{Max} is the fracture load, W and H are the width and thickness of sample fracture area respectively (ASTM C1161-13, 2013).

Shells were prepared using the procedures outlined in Table 3-4 and samples were cut to a sample size of approximately 60 x 20 mm. A minimum of ten samples were tested. The flexural strength of the shell was measured using 3-point bend geometry on an Instron 4467 load frame with a 1 kN load cell and a loading speed of 1 mm·min⁻¹. The span length was set at 50 mm. The flexure stress on shell mould was calculated based on simple beam theory with assumption that the material was isotropic and homogenous.

It has to be noted that the mechanical strength of samples do vary from batch to batch. To compensate for this, the results listed in each results table are from the same batch of samples. Comparison between different result tables should be evaluated with caution.

3.4.2 Wedge test

The wedge test which measures the strength at sharp edges usually gives lower mechanical strength and this best represents the lower value of shell strength expected before crack initiation in the simulation. To prepare shells sample for the wedge test, the standard dipping procedures was performed on a wax pattern bar with diamond cross section (Figure 3-11). Shell samples were cut to have a width of approximately 10 mm.

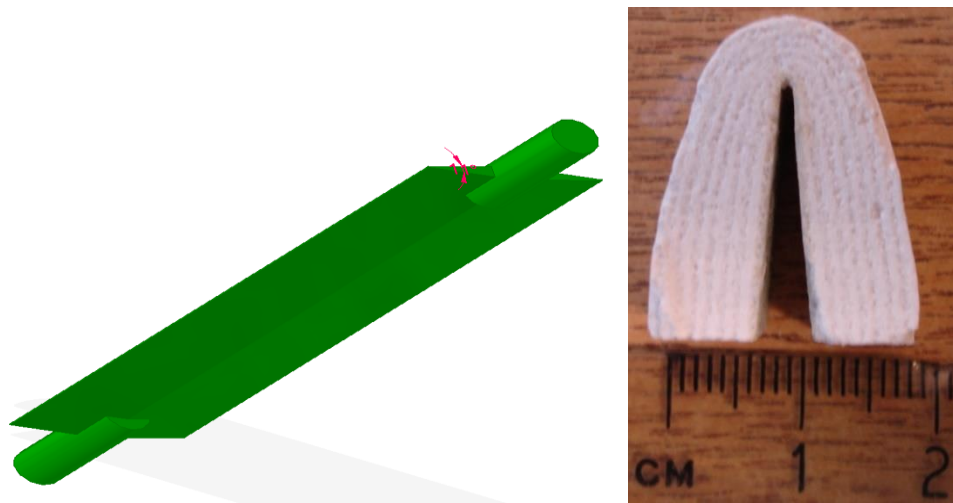


Figure 3-11: Edge test pattern bar with 11° degree angle (left), example of wedge test sample (right)
Equation 3-3 was derived to allow the calculation of stress at the sharp edge (Hyde, et al., 1995). The theory of the testing method had been discussed in the section 2.3. The $\sin\theta \cdot \cos\theta$ term modifies the applied load (vertically) into the force required to open the wedge sample.

$$\sigma_{wedge} = 12.2 \frac{\sin\theta \cos\theta Fd}{WT^2} \quad \text{Equation 3-3}$$

where F is load applied to the wedge, W is width and other dimensions can be found in Figure 2-4.

3.5 Young's modulus

3.5.1 Flat bars

Two different methods were used to obtain Young's modulus of shell using flat bar geometries. The first method estimated Young's modulus from the stress-strain data measured during 3-point bend testing. A 1 kN load cell was used to displace the shell sample and stress on the sample was calculated at the same time as strain was recorded. Figure 3-12 shows how Young's modulus can be obtained from the stress strain curve. Data after the linear line was not considered since the shell is already cracked and is beyond interest in this project.

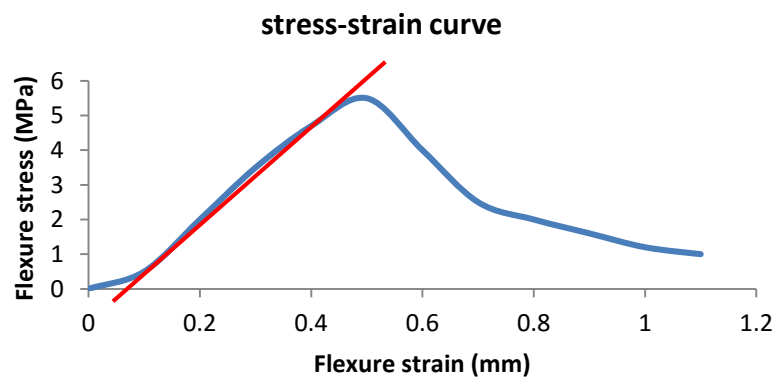


Figure 3-12: Linear line (red line) represents the stress strain gradient to obtain Young's modulus.

The deflection of the instrument (for example, the flexure of the horizontal beam on the load frame and fixtures) was understood to affect the results. A 70 mm thick steel bar was used to calibrate the system.

The second method used to measure Young's modulus was impulse excitation of vibration. The experiment was carried out according to the procedure in ASTM C1259-14 and a linear displacement laser sensor (M5 laser triangulation sensor, model D-85386) was used to replace the microphone sensor. This was due to the ambient noise in experimental laboratory affecting the reproducibility of the frequency measured. The M5 sensor is suitable for use on ceramic surfaces as it is not highly reflective. The experimental setup was calibrated with a brass bar.

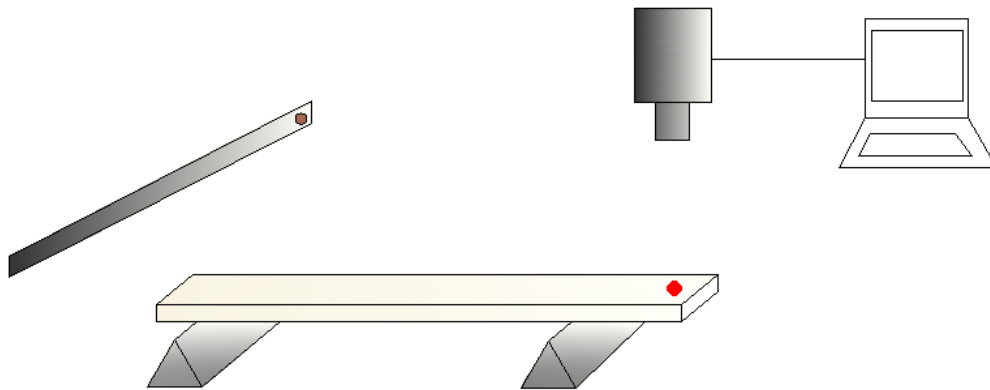


Figure 3-13: Schematic diagram for the impulse excitation of vibration setup. Samples are struck mid span.

The measured Young's modulus of brass bar was 103.4 GPa which correlates well with the literature (Oberg, 2012) and the system is believed to be able to give reliable results. The shell samples were prepared with the same procedure as discussed in section 3.1. The shell was then cut at the edge to prepare a 190 x 25 mm shell sample. The shell sample together with the wax was refrigerated overnight allowing the shell to be removed from the wax pattern without force (method 2). Some samples were further

autoclaved (method 6). Shell samples were dried at 110 °C in a drying oven until mass was constant before testing at room temperature.

The primary coat side of shell was hit with a zirconia ball attached to a flexible steel rod at point X1 and a laser beam (non-contact sensor) was shone at point M1 to record the frequency of shell vibration (Figure 3-14).

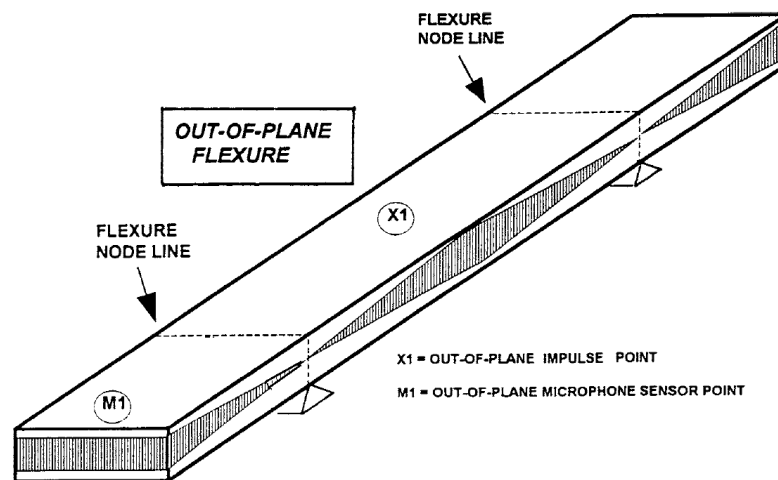


Figure 3-14: Experimental setup discussed in ASTM C1259-14 to obtain Young's modulus of material. Point M1 was used as the non-contact sensor point

The vibration of the shell was analysed in LabVIEW 2012 (32 bits) software to calculate the frequencies and then used to determine the Young's modulus. The distance between the two flexure node lines (support point) was determined depending on the ratio of thickness to length of the shell, and for the shell system in this study, it was set at 105 mm. The primary layer was set as the impulse point surface and the seal layer surface rested at the contact points.

The same shell was further autoclaved in the standard cycle and the frequencies were obtained post treatment. Frequency was recorded and Young's modulus, E was calculated using Equation 3-4:

$$E = 0.9465 \left(\frac{mf^2}{b} \right) \left(\frac{L^3}{t^3} \right) T_1 \quad \text{Equation 3-4}$$

where m is mass of the bar, b is the width of the bar, L is the length of the bar, t is the thickness of the bar, f is the fundamental resonant frequency of the bar in flexure and T₁ is the correction factor.

3.5.2 Wedge geometry

The Young's modulus of wedge sample was determined from the stress-strain curve. Division of stress by strain allows the determination of the Young's modulus of the material. Stress of the shell at the concentrated location (directly above the test knife edge) can be calculated using Equation 3-3. The strain measured by the load frame has to be converted to the strain experience by the particular section on a wedge sample (Figure 3-15). The Equation to calculate the strain (ϵ_x) of wedge geometry was calculated (Appendix A) and is shown as Equation 3-5. The equation was derived based on the bending beam theory by focusing on a small section of the wedge geometry at the cracking initiation location. The shell samples were made with the same procedure outlined in section 3.1 and prepared under two different conditions– method 2 and method 6 (refer to Table 3-4 for method descriptions).

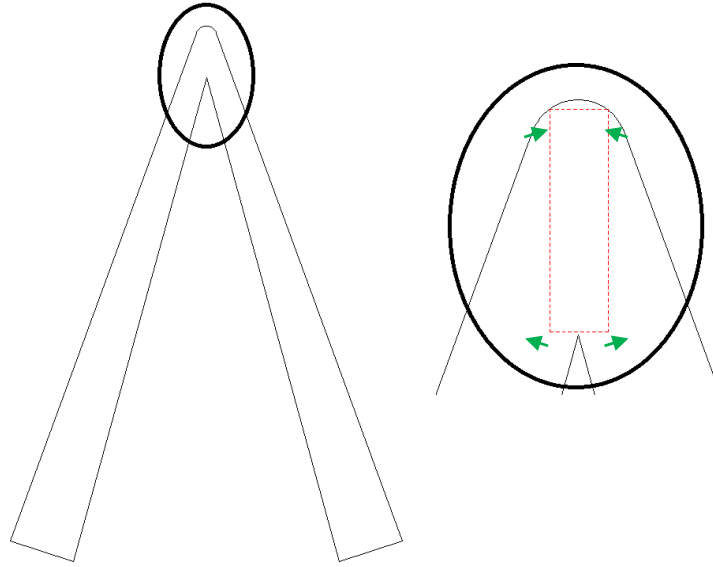


Figure 3-15: Thin section of the wedge test sample was focussed to obtain the strain during testing. Green arrows indicating the direction of stress on a wedge sample

$$\varepsilon_x = \frac{y}{\frac{c \cdot \tan \theta}{2} + \frac{d^2}{2 \cdot c \cdot \tan \theta}}$$

Equation 3-5

where c is the displacement of crosshead, y is half thickness of shell and other parameters are shown in Figure 2-4.

3.6 Density and Thermal Expansion

Experimental procedures to obtain density of shell and wax are described in section 3.6.1 and the thermal expansion for shell and wax is described in section 3.6.2.

3.6.1 Density

The density and porosity of a shell prepared by method 2 were measured by mercury porosimetry at ambient temperature. Shell prepared by method 2 was used in the measurement as it represents shell without contamination from wax. Autoclaved shell (method 1) may possibly contain entrained wax from the process which would reduce

the penetration of mercury into pores and affect the ‘real’ volume of pores being measured.

Shells samples were cut into 10 x 10 mm squares and air dried. Samples were then weighed and added to a glass penetrometer. The penetrometer was sealed, and the sample analysed using an Auto Pore IV mercury porosimeter (Micromeritics, UK) at pressures in the range of 3 kPa - 207 MPa. Mercury intrusion into the sample was analysed using the Washburn equation in order to determine the pore diameter distribution:

$$D = -\frac{4\gamma}{P} \cos \theta \quad \text{Equation 3-6}$$

where D is pore diameter, P is the applied pressure, γ is the surface tension of Hg at 20 °C, which was assumed to be 0.485 N·m⁻¹, and θ is the contact angle between the Hg and the porous solid, which was assumed to be 130°.

The skeletal density of the shell at room temperature was verified using a helium pycnometry (Micro Meritics Accupyc II 1340). Shells samples were cut into 10 x 10 mm size and air dried. The mass of the shell sample was weighed to two decimal places and volume of helium gas was released into the chamber and density of shell was calculated by the division of mass of shell by volume occupied by the shell.

The helium pycnometer was also used to obtain the density of wax at ambient temperature. The same procedure was used as that for shell analysis. The density of wax at ambient temperature was used as a starting point for the thermal expansion measurement which is discussed in section 3.6.2.

3.6.2 Thermal expansion

The thermal expansion of shell was carried out using thermo-mechanical analysis (TMA) and for wax was carried out at Birmingham University using two different methods: (i) NETZSCH capsule in a dilatometer, (ii) Modified density bottle.

The thermal expansion of the wax was also carried out with the Pressure, Volume and Temperature (PVT) method at the National Physical Laboratory (NPL). Even though PVT test was not carried out as part of this work, the method and results are included in the discussion for comparison, therefore this sub-section includes the methods applied by NPL.

3.6.2.1 TMA on Shell

The thermal expansion of shell was measured with Perkin Elmer TMA 7. Shell samples were cut into 10 x 10 mm size and pre-dried in a fan oven at 110 °C for 3 hours to remove any water in the shell system, as this was seen to affect the expansion of shell. This is because shells with water vapour tend to shrink initially when the water vapour was lost. In the wet condition of the autoclave, shrinkage should not occur and only expansion will be observed. The sample was placed on the sample holder and a vertical glass rod lowered down to the surface of the sample with a load of 10 N. The heating rate used in TMA was set at 10 °C·min⁻¹ to give sufficient heat equilibrium time. A pre-test cycle was carried out to eliminate the expansion on the sample holder and glass rod.

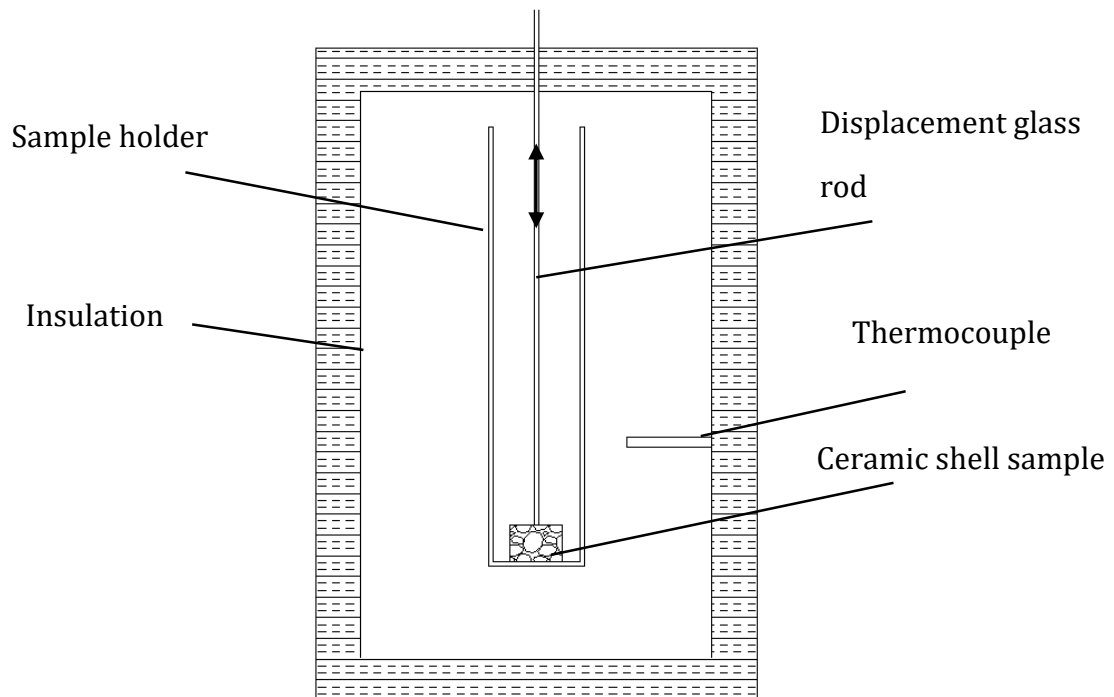


Figure 3-16: TMA setup to measure thermal expansion of shell

3.6.2.2 PVT method by NPL on wax

PVT test method was carried out by NPL to compare the thermal expansion of the waxes to the other methods adopted. Mass of the wax sample was weighed to 2 decimal places prior to loading into the PVT cell (cylinder). The bottom of the cylinder was blocked off with a fixed piston and a PTFE seal. The hydraulic upper piston applied pressure to the specimen in the cylinder with the piston position registered by a displacement transducer. The wax was heated to 120 °C at 20 MPa and held under this condition for 8 minutes. The specimen was then cooled at 10 °C·min⁻¹ to 20 °C and displacement recorded. The same cycle was repeated a second time on the same sample. At the end of the test, the wax sample was removed from the instrument and weighed to give the final weight of specimen. A correction was made to the specific volume values for the initial run for the percentage difference in mass between the initial and final weights of the specimen as an indication of specimen leakage past the seals. The specific volume values

for the repeat cycle (second run) were calculated based on the final weight of the specimen.

3.6.2.3 Netzsch Capsule method on wax

The Netzsch capsule method was used to measure the thermal expansion of wax with a sealed container (capsule) supplied by Netzsch. It allows the measurement of wax expansion when used together with the Netzsch electronic dilatometer (Model No. TASC 414/3) (Figure 3-17). The wax pellets were first placed in the capsule and melted in the oven. When the wax was completely molten the next wax pellet was put in the container until the container was completely filled with wax. After the cooling, the excess wax was cut with a razor blade to form a flush end. Silicone rubber was laid on top of the container and the container lid screwed in place.

The dilatometer was programmed to heat from 20 to 180 °C at 1 °C·min⁻¹ and allowed 10 minutes equilibrium time for every 10 °C increment in temperature. The dilatometer was calibrated with a 30 mm alumina rod without taking into account capsule expansion. This is because the leakage of calibration fluid from the seal at high temperature resulted in unreliable calibration data.

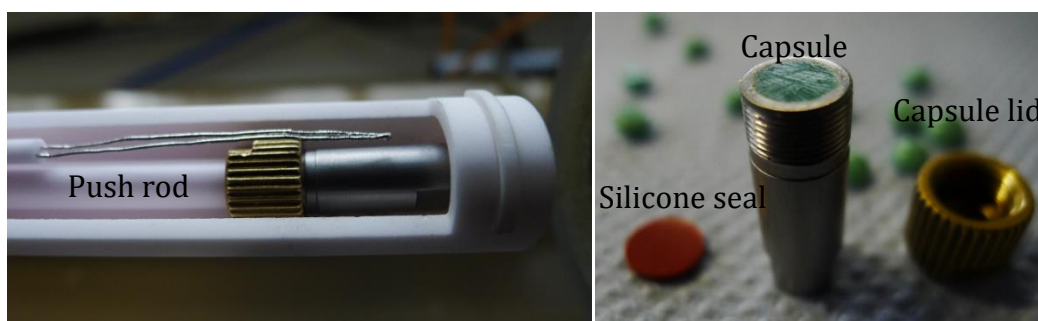


Figure 3-17: Container for measurement of liquids in the dilatometer (left) and setup in the dilatometer (right)

The thermal expansion measured in one dimension was then converted to a volumetric thermal expansion, V using Equation 3-7, by assuming that the expansion of wax under the silicone seal progress as a dome shape or prolate ellipsoid (Figure 3-18).

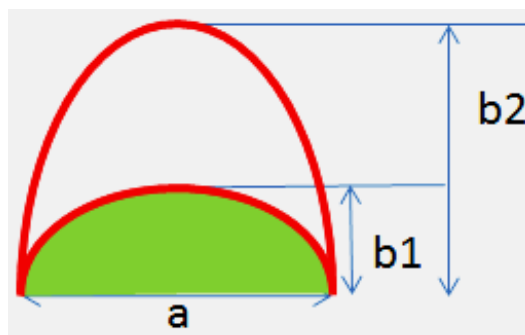


Figure 3-18: Expansion b_1 - b_2 of the silicon seal on the Netzsch capsule. a and b are defined here for Equation 3-7.

$$V = \frac{4}{3}\pi a \Delta b^2 \quad \text{Equation 3-7}$$

3.6.2.4 Modified density bottle method on wax

The thermal expansion of the wax was also measured using a standard density bottle fitted with a calibrated capillary rod (Figure 3-19).

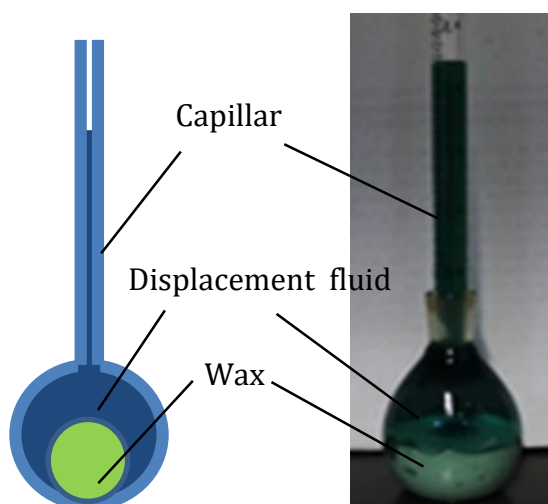


Figure 3-19: Density bottle setup

This modified density bottle method was developed as an alternative method to allow high temperature measurement (up to 180 °C) at constant atmospheric pressure. The volume in the capillary rod at ambient temperature was calibrated by Jaytec Glass Limited together with the density bottle and it was accurate to $\pm 0.025 \text{ cm}^3$ at 25 °C. The setup was further calibrated with the silicone fluid to obtain the thermal expansion of density bottle and capillary rod up to 180 °C. In order to determine the thermal expansion of wax, the system must first be calibrated with a fluid which is immiscible with the wax over the temperature range of interest and has a well-documented thermal expansion of coefficient. The calibration fluid used in this test was DOW CORNING silicone fluid 350 cSt (thermal expansion data was provided by supplier). The thermal expansion of wax was calculated based on the volume fraction in the container as shown in Equation 3-8:

$$\alpha_{\text{silicone}} \frac{V_{\text{silicone}}}{V_{\text{mixture}}} + \alpha_{\text{wax}} \frac{V_{\text{wax}}}{V_{\text{mixture}}} = \alpha_{\text{mixture}} \quad \text{Equation 3-8}$$

where α is volumetric thermal expansion and V is volume.

The wax pellets were first weighed before inserting into the density bottle. As much wax as possible was added to the bottle and silicone fluid 350 cSt was added to fully occupy the remaining cavity in the bottle. The bottle was placed in vacuum overnight to remove entrapped air. The capillary was then fitted and the excess of fluid wiped away. The first reading was recorded under this condition. A trial and error test was carried out and found an equilibration time of 1.5 hours should be allowed in between each reading taken at each temperature increment. This equilibrium time was selected as it is the shortest time required to fully heat this vessel size with the heating system available.

3.7 Specific heat capacity

The specific heat capacity of shell and wax were determined with Perkin Elmer DSC7 differential scanning calorimetry (DSC). The DSC was used along with the Perkin Elmer Thermal Analysis Controller TAC 7/DX to control the heating rate and record the data. The DSC has two calorimeters, a sample calorimeter and a reference calorimeter where the reference calorimeter is calibrated to give identical responses to the sample calorimeter (Figure 3-20). The heat flow to the sample was the difference of heat flow between the reference calorimeter and the sample calorimeter. The instrument was calibrated with high purity metal standards (indium) to ensure accuracy of the temperature scale.

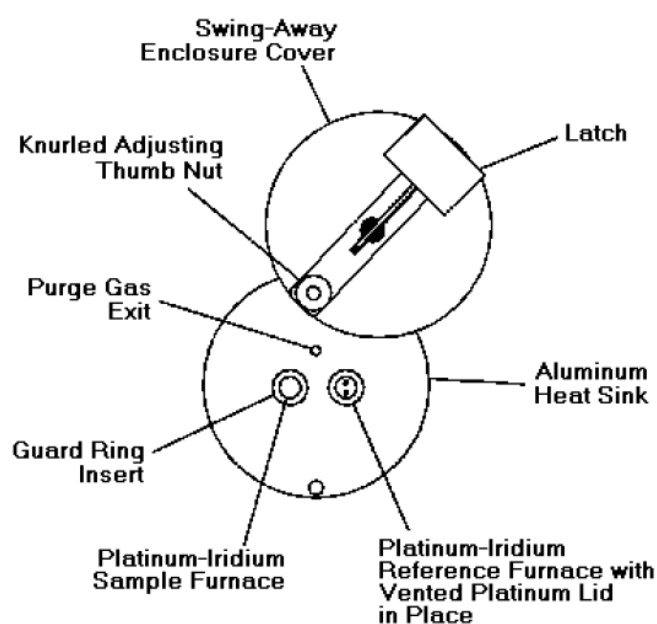


Figure 3-20: The sample holder and calorimeters in a DSC 7 (PerkinElmer, 2014)

The shell sample was prepared by grinding the shell to powder form using a mortar and pestle. A preliminary cycle was run with $10\text{ }^{\circ}\text{C}\cdot\text{min}^{-1}$ from $25\text{ }^{\circ}\text{C}$ to $180\text{ }^{\circ}\text{C}$ to erase the thermal history. The DSC of shell was then measured from room temperature ($25\text{ }^{\circ}\text{C}$) to $180\text{ }^{\circ}\text{C}$ at a controlled heating rate of $10\text{ }^{\circ}\text{C}\cdot\text{min}^{-1}$.

For wax, samples were prepared from the five different commercial waxes – Wax A, B, C, D, E. The wax pellets were polished with sand paper (1500 grit) to obtain a thickness that would fit into the aluminium sample pan. All wax samples were melted at 80 °C and then cooled down to room temperature before starting the experiment to give an intimate thermal contact with the pan. The preliminary cycle was run at 10 °C·min⁻¹ from 25 °C to 180 °C to erase the thermal history. For each wax, measurements were made from room temperature (25 °C) to 180 °C at controlled heating rate of 10 °C·min⁻¹.

3.8 Thermal conductivity

The thermal conductivity of a porous shell system is usually measured using laser flash method. However, the steam in autoclave is known to change the characteristics of shell in terms of thermal conductivity, density and heat capacity. When steam is introduced onto the shell mould in the autoclave, the steam condenses on the mould surface and in the pores, releasing latent heat. To the authors knowledge, it is still unknown if the steam does penetrate through the pores to reach the wax under the high pressure condition in the autoclave. It is also unknown if it does penetrates through the shell to the wax surface, does it actually do this in the form of liquid or gas. The effect of steam or condensed steam penetrating the pores will be significant and should not be neglected.

Tests were carried out to show the effect of steam penetration into the pores had on heating rate across the shell. 50 mm diameter and 150 mm long cylindrical wax patterns were coated with alternate layers of slurry and stucco (specification as Table 3-3). High sensitivity J Type thermocouples were fitted underneath the ceramic coating as shown schematically in Figure 3-21. A total of six thermocouples were placed through the shell

thickness. The other end of the thermocouples was pulled through the autoclave ports shown in Figure 3-22 and connected to National Instruments data acquisition system.

The sample was held using a retort stand in the autoclave and thus the orientation of the thermocouple was assured to be consistent each time. The temperature in the autoclave during de-waxing process was measured and recorded using national instruments LabVIEW 2012 (32 bit) software.

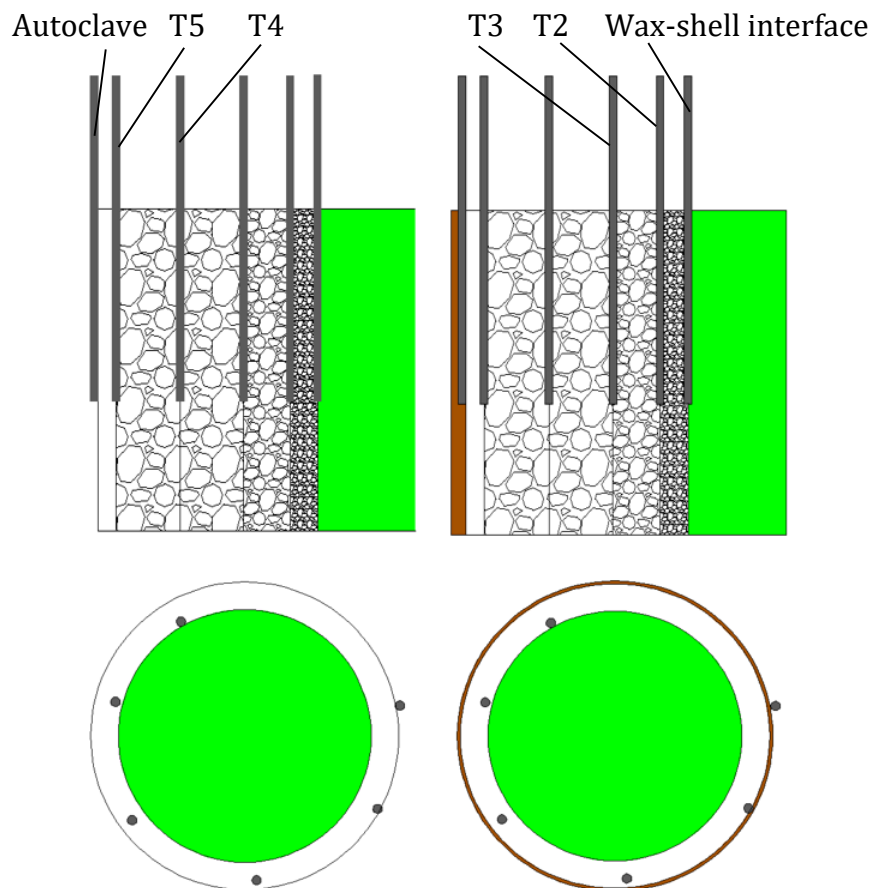


Figure 3-21: Schematic diagram showing the positions of the thermocouples used to predict the changes of thermal conductivity with temperature and time. Shell is covered by copper foil to prevent steam penetration (right). The cross section shows the relative location of the thermocouples and shell configuration

The wax pattern coated with ceramic shell was de-waxed in the autoclave and the temperature profile of shell was recorded. The same procedure was repeated on the

ceramic coating wrapped with copper foil to prevent steam penetrating the porous shell during de-waxing. Copper foil was selected for its high thermal conductivity allowing all heat including heat transferred from water that condense on the surface of the foil. The thermal profiles obtained from the two setups are shown in Figure 4-31. The space (distance) between thermocouples was measured after autoclaving and average thickness taken as following - 0.77 mm, 1.53 mm, 1.75 mm and 1.86 mm for prime coat layer, 2-3th layer, 4-5th layer and 6-8th layer respectively.



Figure 3-22: Top view of the autoclave in IRC laboratory showing the thermocouple and pressure sensor ports

The thermal conductivity was obtained by back calculating with the thermal profile measured across the shell, which has taken into account the effect of steam in pores. The partial differential equation of heat equation derived from Fourier's law was solved in MATLAB® to obtain the thermal conductivity. The heat equation was solved implicitly with the code provided in MATLAB®.

$$\rho(T)C_p(T)\frac{dT}{dt} = k(T)\frac{d^2T}{dx^2} + \frac{dT}{dx}\frac{dk}{dx} \quad \text{Equation 3-9}$$

where ρ is density, C_p is the heat capacity, k is thermal conductivity, T is temperature and x is distance.

The shell was discretized into five segments to simulate the thermocouples implanted across the shell. The heat equation (Equation 3-9) can be approximated by finite difference,

$$\rho(T_i)C_p(T_i)\frac{T_i^{n+1} - T_i^n}{2\Delta t} = k_i^n \left(\frac{T_{i+1}^n - 2T_i^n + T_{i-1}^n}{\Delta x^2} \right) + \left(\frac{T_{i+1}^n - T_i^n}{2\Delta x} \right) \left(\frac{k_{i+1}^n - k_i^n}{2\Delta x} \right) \quad \text{Equation 3-10}$$

where n is time and i is space.

The external boundary temperature of shell was assumed to be same as the autoclave and the internal boundary temperature assumed to be the same as the wax temperature. The 'solve' function built in MATLAB® allows the heat equation to be solved implicitly.

The thermal conductivity of wax was determined using the same technique. A 50 mm diameter and 150 mm long wax cylinder was formed by injecting Wax D (filled wax) into an aluminium die. High sensitivity J Type thermocouples were implanted in the wax cylinder 12.5 mm apart (Figure 3-23) by first melting 80 mm deep holes with a hot steel wire (0.5 mm). The wax cylinder was then shelled with alternate layers of slurry and stucco (Table 3-3 for formulation). At the top of the cylinder, the shell was slit open with a tile cutter to allow the wax to melt freely without cracking the shell containing the molten wax while measurements were taken. The thermal conductivity test was only undertaken on Wax D after realising that the thermal profile measured has low repeatability. This method of testing requires the thermocouples to be absolute stagnant in the wax which was found to be difficult to achieve as the expansion of wax and changing from solid to liquid moved or bent the thermocouples. One out of three thermal profiles was selected for wax thermal conductivity analysis base on 'smoother' profile and this is discussed in section 4.9.

$$\rho(T_i)C_p(T_i)\frac{T_i^{n+1} - T_i^n}{2\Delta t} = k_i^n \left(\frac{T_{i+1}^n - 2T_i^n + T_{i-1}^n}{\Delta x^2} \right) \quad \text{Equation 3-11}$$

The thermal conductivity of wax was obtained using the same method as shell with a modification to Equation 3-10. It was modified to produce Equation 3-11 since wax is a homogenous material and thermal conductivity does not vary with position.

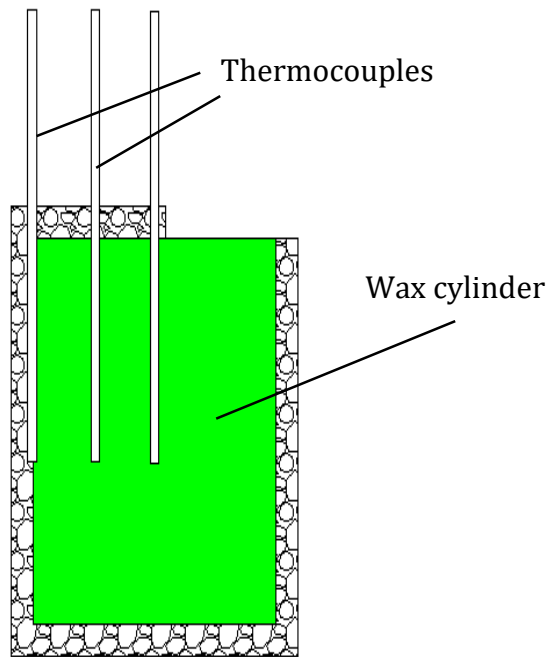


Figure 3-23: Schematic diagram of thermocouple setup for the wax thermal diffusivity measurement

3.9 Parallel plate rheometry

The rheological properties of the five waxes was determined using a TA instruments AR 500 rotational rheometer. The rheological behaviour of interest in this project is during the de-waxing process. The autoclave environment is extreme and at equilibrium, the wax would reach to the chamber temperature, typically 180 °C. Thus, for this study a wide range of temperatures were investigated. The viscosity of the wax was measured as functions of shear rate at different temperatures.

Flat plate geometry was chosen to determine the rheological behaviour rather than cone and plate. This was because the flat plates 'held' the fillers in place better compared to a cone and plate geometry. The parallel plate consisted of a rotating top plate and a fixed base plate. The base plate had a built in heating element and the top plate was adjustable to the gap size required (Figure 3-24). For consistency, the unfilled wax (Wax E) was tested using the flat plate geometry even though it could have been argued that cone and plate would yield a better result. A 40 mm diameter flat plate was chosen to measure the rheology of all waxes. The controlled variable on the rheometer was the shear stress and was set to increase linearly up to a maximum shear stress possible based on the wax type and testing temperature.

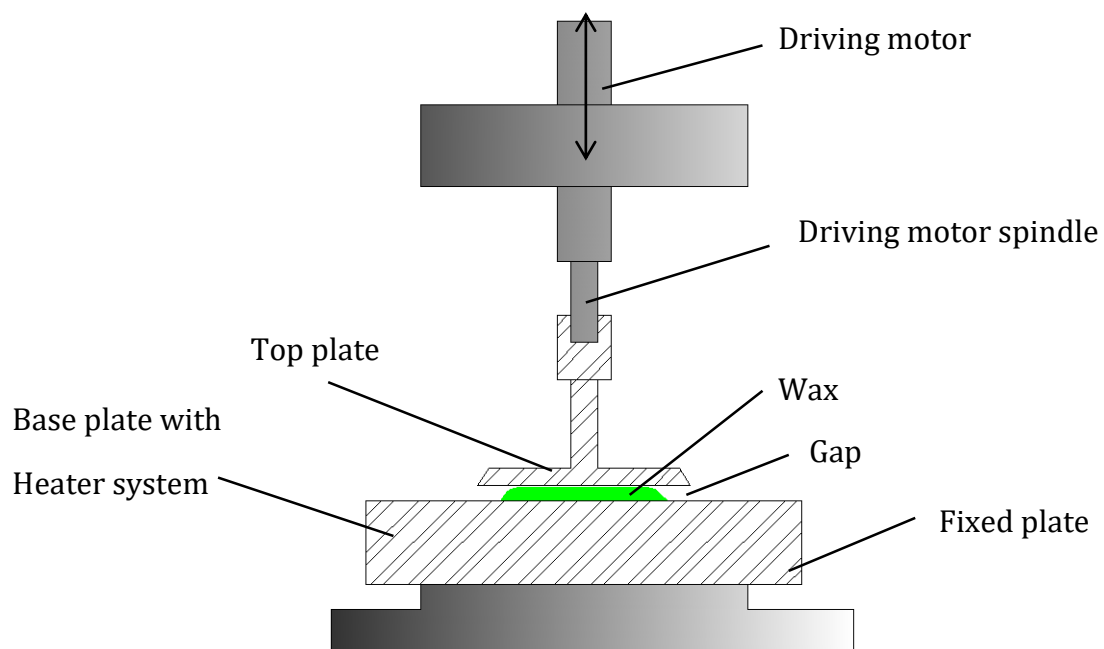


Figure 3-24: Schematic diagram of parallel plates geometry setup

The shear rate ($\dot{\gamma}$) and shear stress (τ) of the flat plate geometry are given by:

$$\dot{\gamma} = \frac{R}{d} \times \bar{\omega} \quad \text{Equation 3-12}$$

$$\tau = \frac{2}{\pi R^3} \times T \quad \text{Equation 3-13}$$

where r is the radius of the plate, d is the height of the gap, $\bar{\omega}$ is the angular velocity and T is the torque.

The wax sample was prepared by melting the wax on the bottom plate for two minutes at 80 °C for filled wax and 70 °C for unfilled wax. The gap was set at 200 μm for filled waxes as smaller gaps caused inconsistency due to filler interference but larger gaps caused losses of material. For unfilled wax the gap was reduced to 100 μm to prevent material loss during testing because filler interference was not present. The top plate was then moved to the gap size required with a maximum force pushing the plates together of 40 N. The wax was then cooled to 20 °C and allowed to achieve equilibrium for another two minutes. This is to introduce a consistent thermal history to the freshly melted wax. Wax was heated up again to the desired temperature and left for another two minutes before testing began. The temperature range was chosen to mimic the actual conditions during the de-waxing in autoclave, which is from 90 °C up to 170 °C.

The sensitivity of wax sample to any pre-shearing prior to the rheological test was carried out on filled wax (Wax C). The rheological examination was carried out on samples which had experienced a pre-shear rate at 100, 1000 s^{-1} and with no pre-shear. For each pre-shear rate, the wax was pre-sheared for two minutes then cooled to 20 °C and the rotational rheological test described in the preceding paragraph was carried out. From the analysis of these tests, no pre-shear was applied to any further examinations.

Tests were carried out to observe the repeatability of wax rheology measurement on AR 500 instrument. Only three waxes (three different types – wax A, C and E) were chosen for the repeatability test. It is unnecessary to repeat for all wax since the test is to observe the repeatability of the instrument rather than the wax itself. Those waxes were run at 90 °C with controlled shear rate (10, 100 and 1000 s⁻¹) with ten repeats using fresh wax each time. The same procedure was repeated at 170 °C.

3.10 Capillary rheometry

Capillary rheometer was used to investigate the rheological behaviour of wax at the solid-liquid transformation stage. The setup of the capillary rheometer is shown in Figure 3-25.

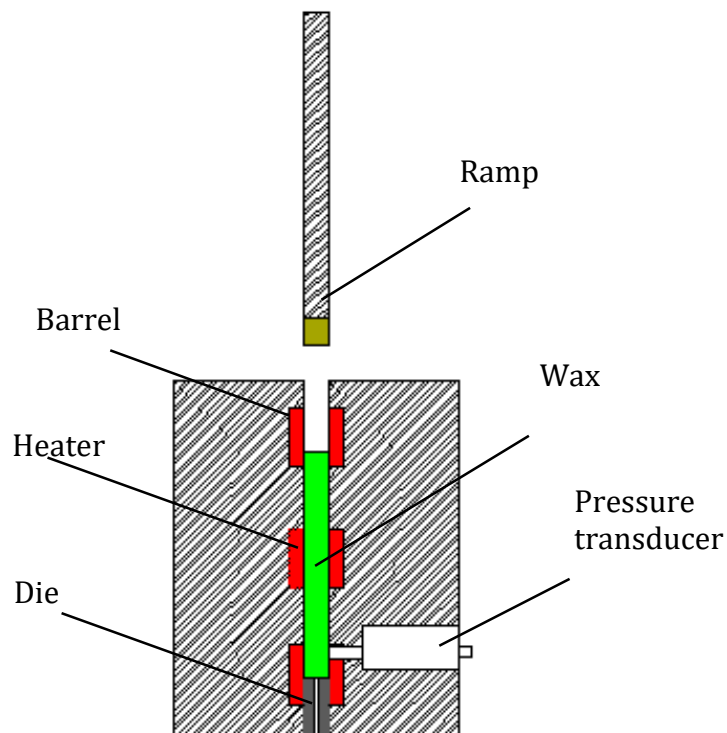


Figure 3-25: Schematic description of the capillary rheometer used in the project

The shear stress, τ_w at the wall of die was obtained using:

$$\tau_w = \frac{(\Delta P - \Delta P_0)D}{4L} \quad \text{Equation 3-14}$$

where ΔP is the total pressure drop, ΔP_0 is the additional pressure introduced by entry effects, D is the die diameter and L is the die length.

A modified Bagley plot, Figure 3-26 was used to correct the entry effects. The entrance pressure loss was obtained when the L/D was zero. It has to be noted that the extrusion velocity here was constant. From the Bagley plot, the Bagley correction, ΔP_0 can be determined.

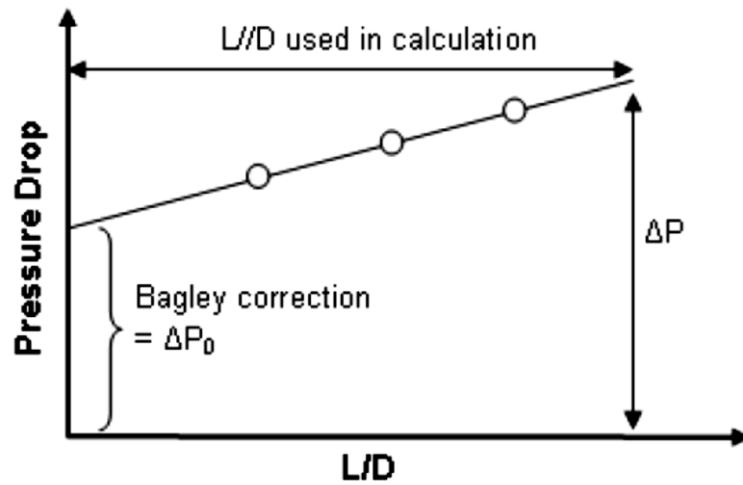


Figure 3-26: Bagley plot used to obtain entrance pressure loss (P_0) (Barnes, et al., 2005)

The apparent shear rate at the wall $\dot{\gamma}_{app}$ was determined using:

$$\dot{\gamma}_{app} = \frac{8\bar{V}}{D} \quad \text{Equation 3-15}$$

where the bulk average velocity in the die, $V = 4Q/\pi D^2$, Q is the volumetric flow-rate through the die and D is the diameter of capillary die.

The actual shear rate at the wall, $\dot{\gamma}_w$ was obtained by multiplying the apparent shear rate with the Rabinowitsch-Mooney correction (Equation 3-16) (Steffe, 1996). This correction was to account for changes in the shear rate between a Newtonian profile and a non-Newtonian profile. n' is the slope of $\ln(\tau)$ versus $\ln(Y_{app})$.

$$\dot{\gamma}_w = \left(\frac{3n' + 1}{4n'} \right) \frac{8\bar{V}}{D} \quad \text{Equation 3-16}$$

The viscosity, μ can then be calculated using the relationship:

$$\mu = \frac{\tau_w}{\dot{\gamma}_w} \quad \text{Equation 3-17}$$

Viscous heating occurs when shearing generates heat within wax sample which may be sufficient to affect the viscosity in the sample that is further from the barrel wall. The temperature increment due to viscous heating can be estimated using Equation 3-18:

$$\Delta\bar{T} = \frac{\Delta P}{\rho \cdot C_p} \quad \text{Equation 3-18}$$

where ΔT is the mean increase in temperature, ΔP is the pressure difference across the capillary, ρ is density and C_p is specific heat capacity.

A Rosand RH-7 capillary viscometer was used to investigate the flow behaviour of the five waxes over the semi-solid temperature range. The 0-3.5 MPa pressure transducer was selected for the purpose of this test. Three 1 mm diameter capillary dies with length to diameter (L/D) ratios of 0.25, 10 and 16 were used in the test.

To carry out the test, a capillary die with L/D of 0.25 and 1 mm diameter was fitted and the barrel of rheometer heated to the required testing temperature. Filled waxes were measured at 55, 57.5 and 60 °C in separate tests and unfilled wax at 47.5, 50, and 52.5 °C.

The barrel was then filled with wax pellets. The wax pellets were compressed with the ram and allowed a period of 1 hour to reach thermal equilibrium. The wax pellets were then further compressed until wax started to emerge from the capillary. Another 5 minutes was allowed for the wax pellets to reach equilibrium before the experiment started. Ram speeds between 0.7 – 105 mm·min⁻¹ were selected (by trial and error) to give the largest ram speed range with a fully loaded barrel. At faster ram speeds, a longer duration of piston travel was allowed until the pressure reading was stable. The test was repeated with 1 mm diameter capillary dies of 10 and 16 L/D.

3.11 Surface tension/Adhesion tension of wax

Obtaining the depth of wax penetration into the shell using Equation 3-20 or Equation 3-22 with a known shell surface area would allow prediction of the total volume of wax that would penetrate the shell. The adhesion tension, $\gamma \cos(\theta)$ where θ is the contact angle, was determined using the Wilhelmy method and compared to surface tension, γ measured with Du-Nuoy ring to understand the interaction between ceramics and wax.

The flow of liquid (wax) into porous materials is governed by the Washburn equation (Washburn, 1921),

$$\frac{dl}{dt} = \frac{r}{\mu} \frac{\gamma}{4l} \cos \theta \quad \text{Equation 3-19}$$

where r is radius of pores (m), μ is the viscosity of permeate (Pa·s) and l is the depth of penetration (m).

Equation 3-19 is derived from the Poiseuille's law where volumetric flow rate is replaced with length of fluid flow over time. Hagen-Poiseuille equation is used to describe the flow of liquids passing through horizontal pipes, neglecting the effect of gravity (Figure 3-27). The length of penetration, L_{lf} can be found by integrating the Washburn equation,

$$L_{lf} = \sqrt{\frac{\gamma D_e \cos(\theta)}{4\mu} t} \quad \text{Equation 3-20}$$

where D_e is diffusivity ($\text{m}^2 \cdot \text{s}^{-1}$), μ is viscosity ($\text{kg} \cdot \text{m}^{-1} \cdot \text{s}^{-1}$), t is time (s).

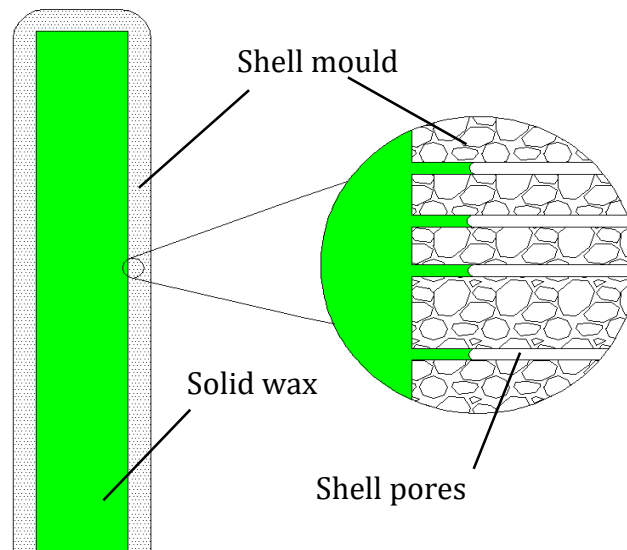


Figure 3-27: Schematic representation of the initial de-waxing process where wax is forced into the porous ceramic shell. In the models where Poiseuille's law was assumed, the pores are represented as horizontal tubes.

Masoodi & Pillai (2010) showed how Darcy's law can be integrated with the continuity equation (volume-averaged liquid velocity in all directions is equal to zero) to give

Equation 3-22 in which the surface tension effect is taken into account. Darcy (1856) showed flowrate of permeates can be described as:

$$Q = \frac{-KA}{\mu} \frac{(P_b - P_a)}{l} \quad \text{Equation 3-21}$$

where Q is the flowrate of permeate ($\text{m}^3 \cdot \text{s}^{-1}$), A is the surface area pores (m^2) and $(P_b - P_a)$ is the pressure difference across the porous media (Pa).

The integration gives Equation 3-22 which has the similar form as Equation 3-20. Both equations contains the parameter of surface tension, contact angle, viscosity and either permeability or mass diffusivity.

$$L_{lf} = \sqrt{\frac{2Kp_c}{\varepsilon_f \mu}} t^2 \quad \text{Equation 3-22}$$

where K is permeability (m^2), ε_f is porosity of the porous medium (defined as the ratio of pore volume to the total volume), $P_c = 2 \gamma \cos(\theta) / r$ and r is the radius of capillary.

Most Du-Nuoy rings are made of platinum where the contact angle of most liquids on the surface of platinum can be assumed to be zero as it has high surface energy. If this method is used, it would not adequately represent the interaction between wax and ceramic. Adhesion tension is suggested as a complimentary measure to surface tension because other solids may have surface energies significantly different to platinum. If the Du-Nuoy ring method is used then the contact angle would have to be measured separately and at an elevated temperature this becomes an issue due to light diffraction and reflection and therefore, errors can be significant. Comparing the adhesion tension,

$\gamma \cos(\theta)$ with surface tension, γ allows the contact angle to be determined. The general equation to obtain the surface tension, γ from the Wilhelmy method is given by:

$$\gamma = \frac{W_g}{l \cos \theta} \quad \text{Equation 3-23}$$

where W_g is the force observed, l is the perimeter of the rectangular plate and θ is the contact angle of liquid with plate.

Harkins & Harkins (1929) show that the surface tension force from the Du-Nuoy ring method can be calculated using:

$$\gamma = \frac{W_g}{4 \pi R} \times F \quad \text{Equation 3-24}$$

where γ is the surface tension and R is the radius of the ring. F is the correction factor.

Kawanishi *et al.* (1970) suggested a correction equation for adhesion tension force measured using Wilhelmy method (Equation 3-25). The correction factor takes into account the meniscus correction and a peripheral correction. Meniscus correction is to compensate for the slight lowering of the liquid surface as a certain amount of liquid is required to form the meniscus around the plate. The peripheral correction includes the correction term, l_0 to obtain the effective peripheral length of the plate and is expressed as $L+l_0$. L is the geometrical peripheral length of the plate.

$$\sigma_{corrected} = \sigma \frac{[1 - (s - S)]}{\left[1 + \left(\frac{l_0}{L}\right)\right]} \quad \text{Equation 3-25}$$

where σ is the adhesion tension force observed, S is the surface area of vessel containing liquid, s and L are cross sectional area and peripheral length respectively of the sample.

The value of l_0 for plate geometry used ranges from -0.08 to -0.1 mm. The l_0 being used is independent of material and purely dependant on geometry (Kawanishi, et al., 1970). In this case, a value of -0.09 mm was used.

The dynamic Wilhelmy plate technique was used to evaluate the adhesion tension force. The Wilhelmy method test samples were prepared from primary slurry (Table 3-1) which was slip cast into 20 x 80 mm rectangular bars. These bars were then fired with a ramp rate of $10\text{ }^{\circ}\text{C}\cdot\text{min}^{-1}$ up to $1650\text{ }^{\circ}\text{C}$ and left two hours to sinter. A fully dense sample was required to prevent wax penetration into the test samples. X-ray Diffraction (XRD) was carried out after the sintering process to confirm that no dissociation of zircon had occurred (Figure 3-28). The zircon prime coat composition has been preserved after the sintering process as zircon only dissociates to zirconia and silica at $1676\text{ }^{\circ}\text{C}$ (Pavlik Jr. & Holland, 2001).

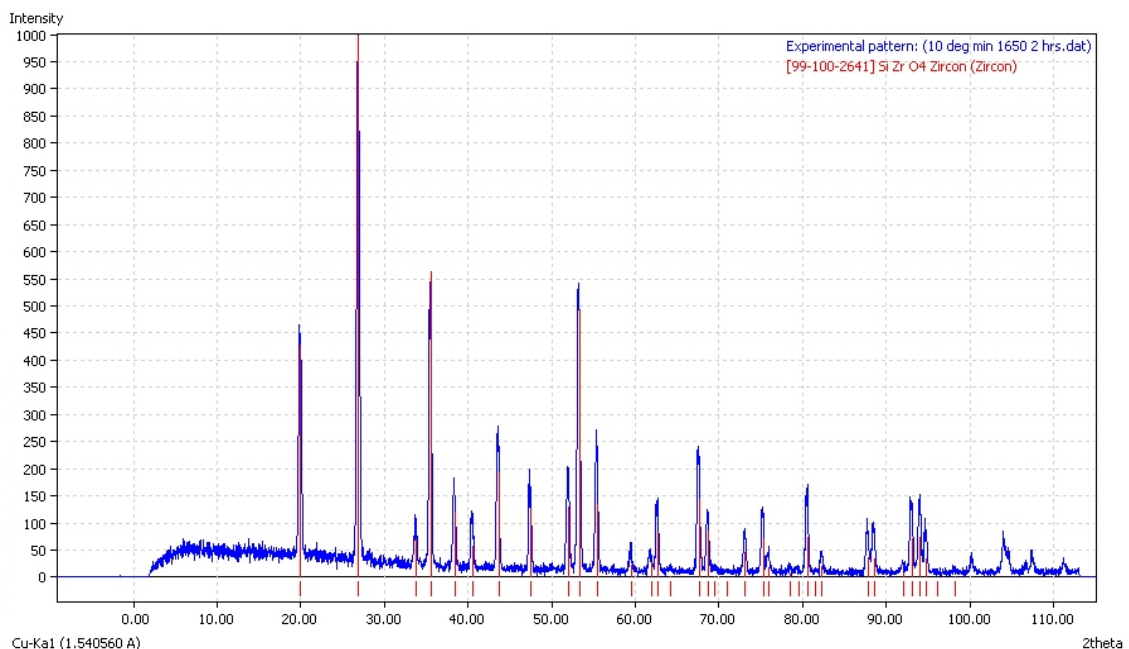


Figure 3-28: XRD data showing that the primary slurry to remained as zircon and did not be dissociate during the sintering process.

There could be an induced error compared to evaluating the unfired shell due to changes in the state of the silica sol and other minerals present and this aspect will be discussed in section 4.12 as well as how the methods accuracy would be lost if porous samples were used.

The bars were cut into smaller samples of approximately 20 x 10 x 6 mm rectangular bars. The bars were polished using P400, P1200 and P2500 polishing papers consecutively with water as lubrication. This was performed on the Buehler Metaserv 2000 grinder polisher at 200 r.p.m.

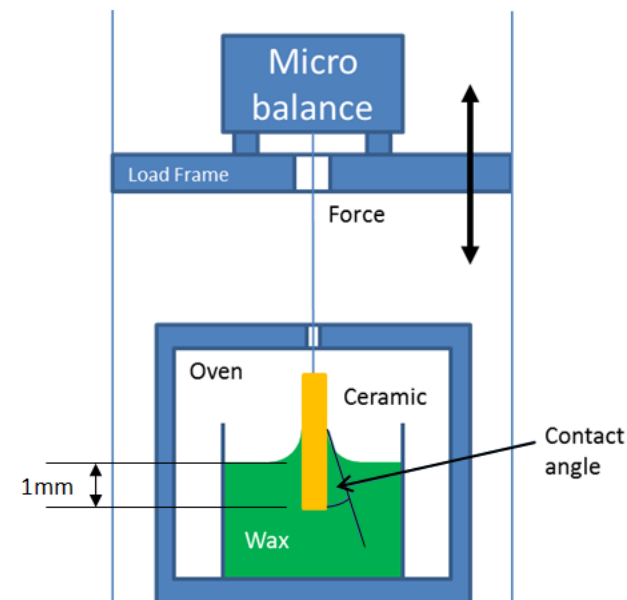


Figure 3-29: The Wilhelmy plate method setup in an oven using a load frame to submerge the ceramic into the molten wax and then emerge it from the same wax. The maximum submersion depth is 1 mm.

A 0.2 mm diameter steel wire was hung from the microbalance and a crocodile clip was placed at the free end (Figure 3-29). The samples were rinsed with ethanol to remove any organic material prior to testing. The crocodile clip was used to hold the samples. The sample and wax were slowly heated to the required temperature and left for a further

10 minutes to equilibrate. The test was carried out at 90, 110, 130, 150 and 170 °C. Approximately 10 grams of solid wax was melted on the petri dish for each test.

The bottom surface of the ceramic sample was immersed in the molten wax to a depth of 1 mm from the surface of wax at constant velocity of 1 mm·min⁻¹ and removed at the same rate without a hold period (Figure 3-29).

The removal continued until a fixed mass was recorded. A typical submersion-retraction curve is shown in Figure 3-30. There was an instantaneous increase of weight as the plate touched the liquid, then the weight started to reduce as the plate penetrated the liquid, displacing more liquid by submersion, (line a-b). After submerging to a depth of 1 mm, the sample was retracted. During this stage, the adhesion force continued to increase, (line c-d) as shown in Figure 3-30.

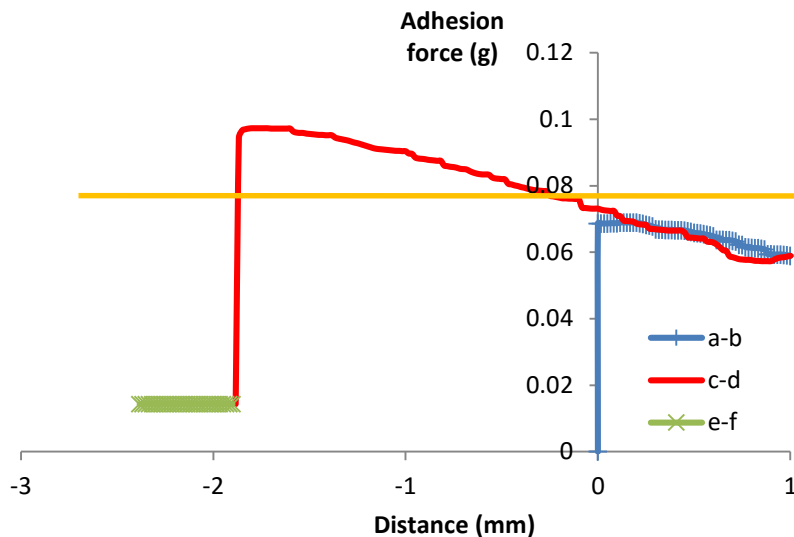


Figure 3-30: A typical submersion and retraction curve for Wax C. It shows the advancing and receding force of Wax C in this case did not have any obvious hysteresis behaviour. The horizontal orange line shows the averaged adhesion tension value.

When the plate was pulling away from the surface of the liquid, a constant weight, which was the weight of liquid wax that remained on the surface of the plate was recorded. The

advancing and receding forces were averaged to obtain the adhesion tension value (Figure 3-30). It is important to note that the maximum receding force effectively contains an offset equivalent to the residual wax weight left on the bar and this is subtracted before calculating the mean mass. The calculated mass was then converted to force.

The system of measurement was calibrated using a borosilicate microscope glass slide and water at varying temperatures from room temperature to 68 °C (Figure 3-31). The results was rather scattered because the test was not carried out in a close environment and water evaporation is possible as the temperature increased. The surface tension of water measured by this route was the same as found in the literature (Kawanishi, Seimiya, & Sasaki, 1970; Vargaftik, Volkov & Voljak, 1983).

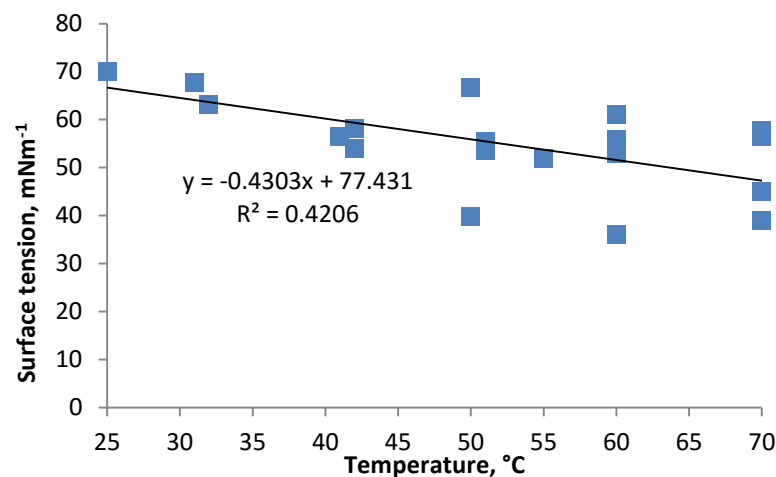


Figure 3-31: Results of the system calibrated using borosilicate microscope glass with water

In Du-Nuoy ring tests, a platinum ring was used to replace the ceramic plates (Figure 3-32). All of the rest of the system remained the same. In this case, the correction factor applied for surface tension Du-Nuoy rings ranges from 0.87 to 0.86 for

temperature range of 90 to 170 °C respectively. The correction factor varies as the surface tension force of ring reduces with temperature.

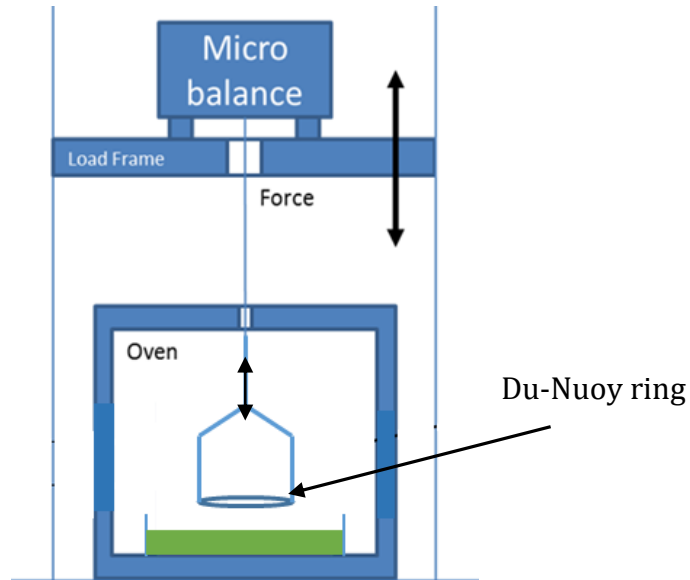


Figure 3-32: Schematic diagram with platinum ring for Du-Nuoy ring test setup to replace the flat plate in Wilhelmy method

4. RESULTS AND DISCUSSION

4.1 Microstructure

A typical shell mould structure is shown in Figure 4-1. The microstructure of shell was further observed under the scanning electron microscope (SEM) and a typical image is given in Figure 4-2. It shows the structure of shell system which was developed layer by layer with slurry fillers and stuccos. Pores are also observed however, it was uncertain if the pores are introduced during the shelling process or during the shell section preparation step through material loss.

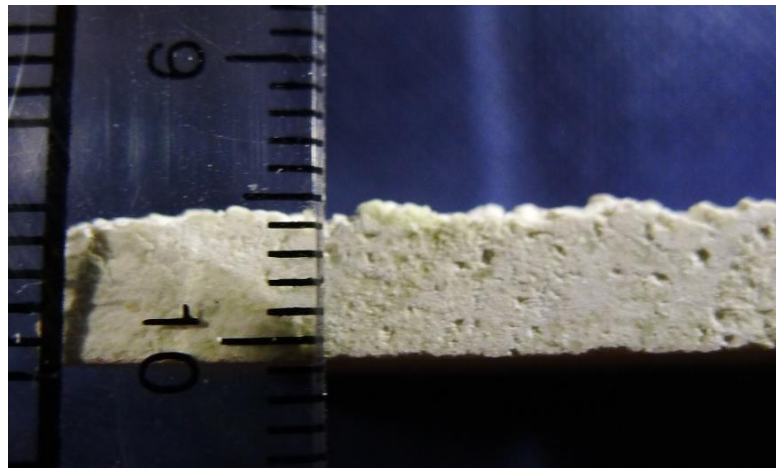


Figure 4-1: Shell after de-waxing and before polishing

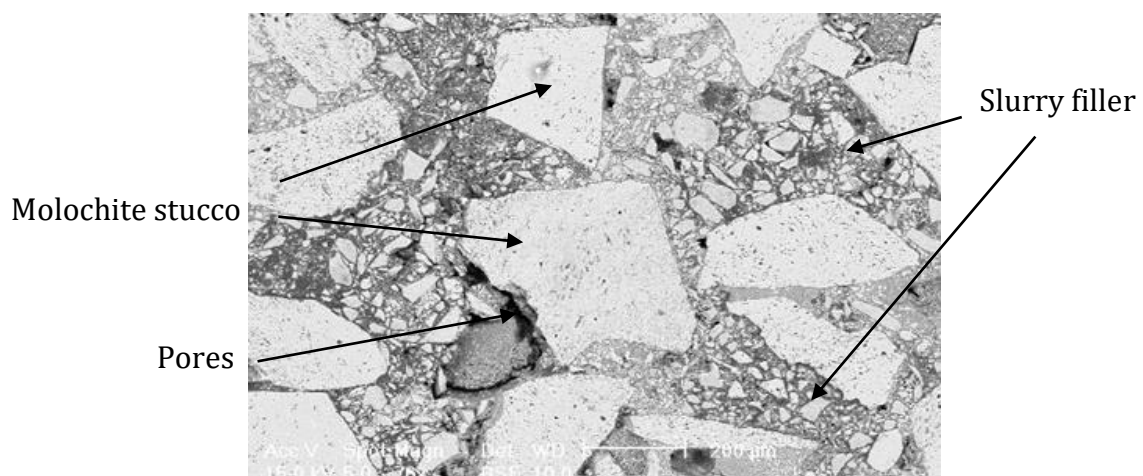


Figure 4-2: Shell structure after de-waxing focussing on secondary layer with SEM

During de-waxing, it is believed that wax penetrates into the porous shell through the prime coat surface due to the pressure developed. The base or carrier wax is believed to infiltrate the mould surface and to leave any fillers on the surface of the prime coat due to the fillers being larger than the mean pore diameter of mould. With this, the depth of penetration with the green wax is expected to be observed. When the shell was examined under reflective light after the de-waxing process, residual wax fillers were found on the surface of the shell and it was found that some fillers had penetrated into the surface porous structure (Figure 4-3). Filler particles of approximately 50 μm remained on the flat surface and smaller particles (20 μm) were found in the open pores. This process was postulated to affect the permeability of wax into the shell as the fillers accumulate on the surface and increase the infiltration resistance. This will be discussed further in the context of shell permeability in section 4.3. From this observation, it could be postulated that the residual wax and filler remain after de-waxing and the wax does not drain fully from the shell. The colour of the wax, however, was not obvious and so it was not possible to demonstrate the penetration of wax into the porous shell.

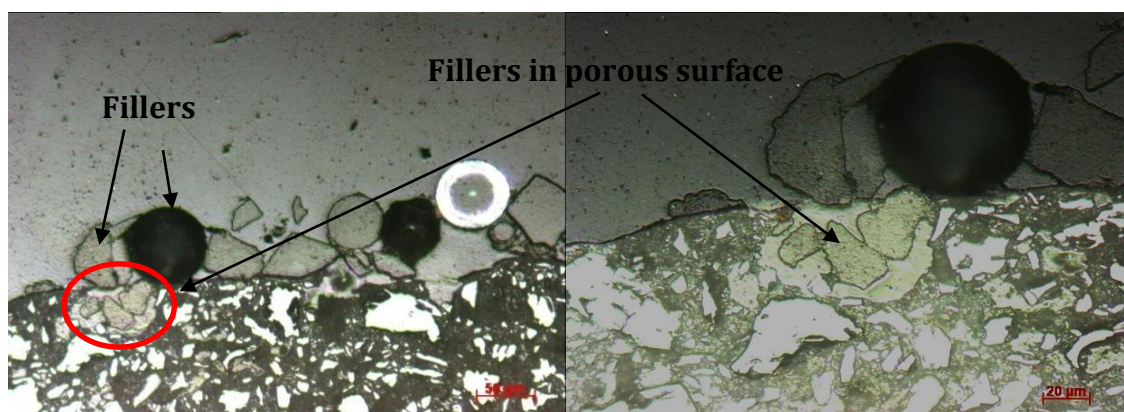


Figure 4-3: De-waxed shell inner shell surface and wax D residuals. Some porous surface can be seen to be filled with fillers (right)

Microstructure of shell prime coat surface was also observed with interferometry to obtain the surface roughness (Figure 4-4). The surface roughness is important as it does affect the surface quality of a casting. This parameter is also required to calculate the wall drag force to hold the wax pattern when the wax is in solid state (initial condition). When wax is in liquid phase, the surface tension coefficient between the two surfaces are assumed to be dominant. Surface roughness of prime coat is also required to estimate the heat transfer coefficient when wax starts to melt and flow under gravity parallel to the shell surface. The prime coat surface of the shell was found to have an average roughness, S_a of $6.38 \mu\text{m}$.

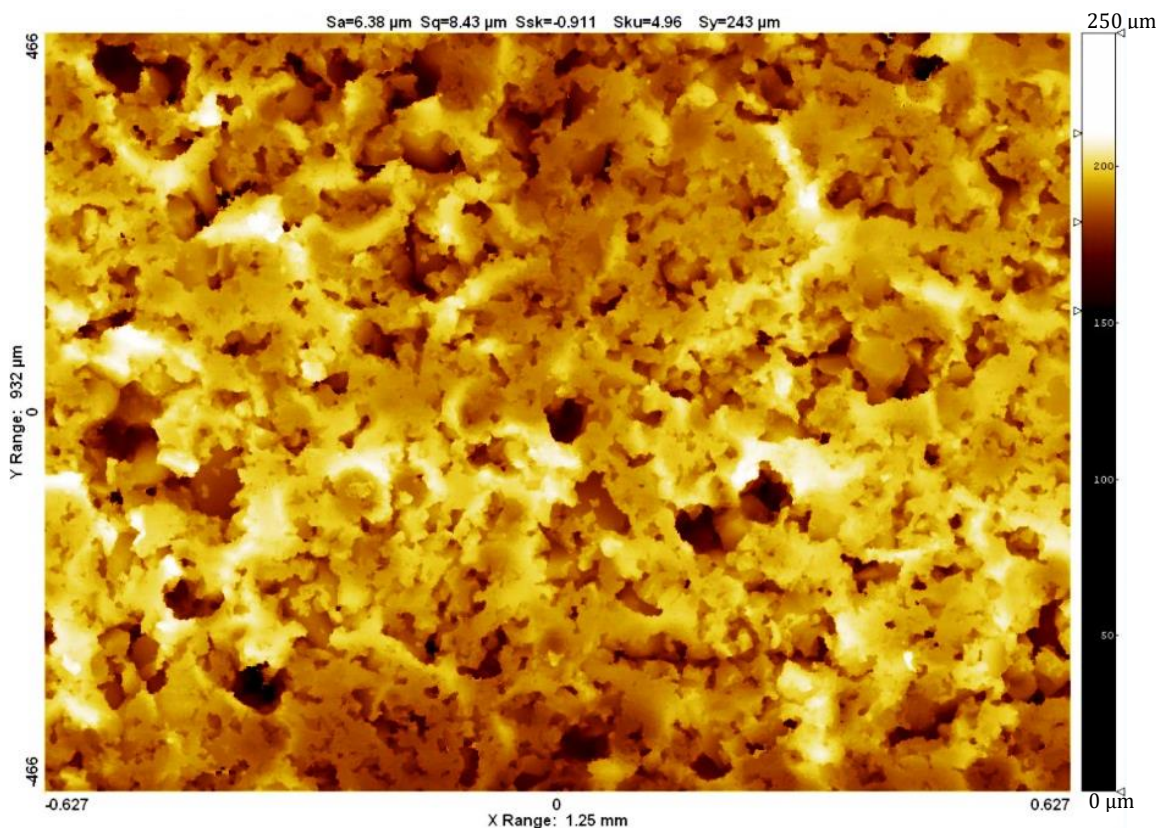


Figure 4-4: Surface roughness measurement on the prime coat surface. Scale on the right indicates the vertical height deviations.

SEM was used to observe the morphology of wax. It was found that all the tested filled waxes contained spherical fillers which according to the wax suppliers are cross linked

polystyrene (XLPS). SEM with its larger depth of field allows the observation of the fillers in the wax pellet. The XLPS particles are exposed on fracture surface of the wax allowing measurement of particle size distribution from Figure 4-5, the maximum particle size was estimated to be about 100 μm and the minimum 20 μm . However, using SEM to observe the microstructure had limitation when observations of the terephthalic acid fillers (TPA) were present (Wax B and C according to wax supplier). This was because if the fracture was entirely transgranular, it was not possible to observe the presence of filler. However, Wax B and Wax C appears to have rougher surface than Wax A. For waxes with TPA, this would appear to be the case. The XLPS on the other hand is exposed as the fracture is intergranular.

In optical microscopy with plain polarised light the waxes with filler can be seen to contain either one filler phase or two. There are near spherical particles XLPS and an angular-shaped filler (TPA filler). This phase was observed in Wax B and C (Figure 4-6) but not in the SEM images. Wax A and Wax D contain only one type of filler - XLPS (wax supplier information). However, it was found that Wax D contained fillers with both rounded and angular morphology yet apparently the same composition. The angular shape fillers in Wax B and C are in low relief where those in wax D protruded from the surface (out of the image). Thus it can be concluded that the angular-shaped fillers in Wax B and C are different from those found in Wax D but these fillers were better understood using polarised light.

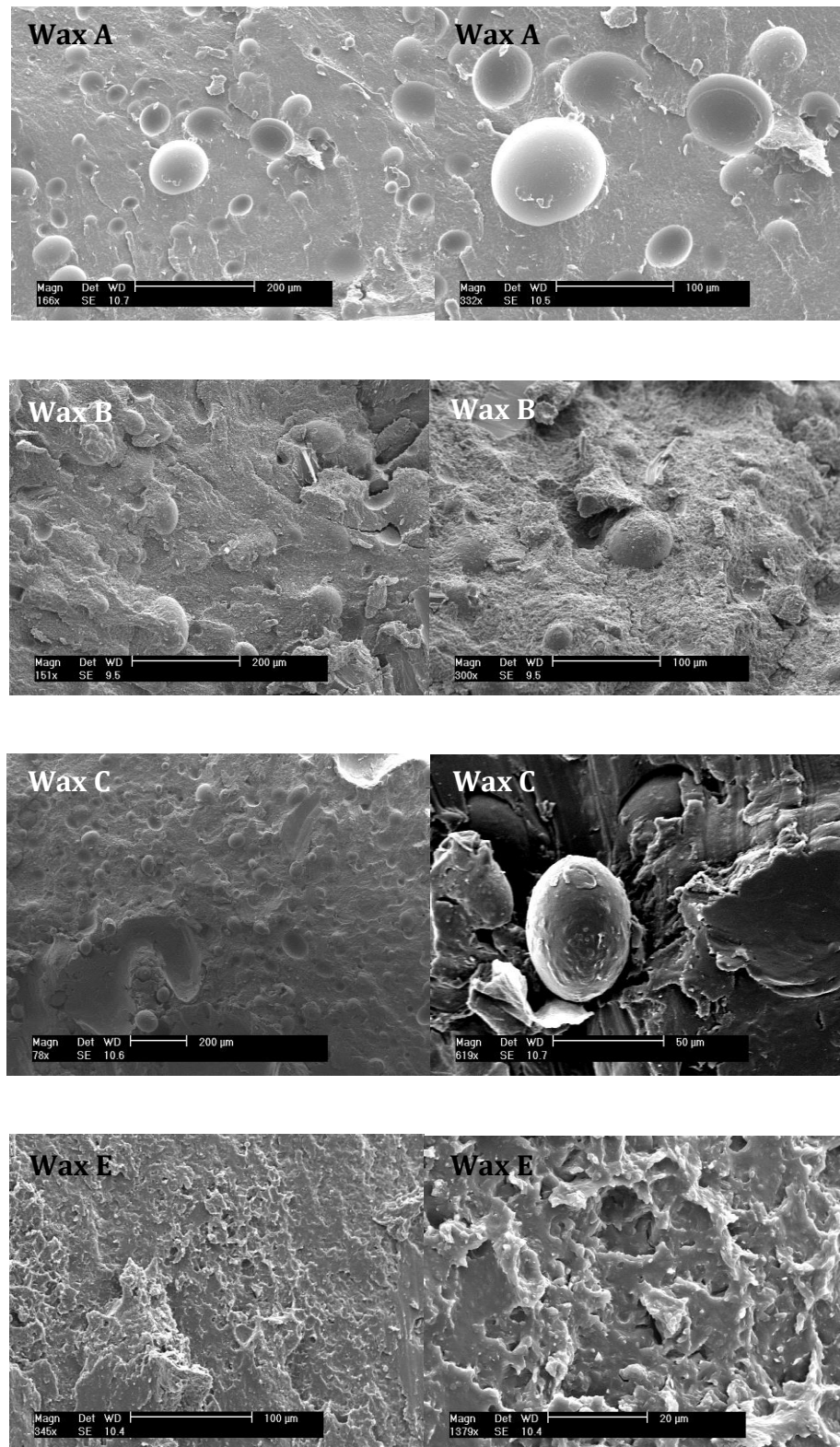


Figure 4-5: SEM results showing the microstructure of 4 waxes -Wax A, B, C, E. Larger depth of field of SEM allows a three dimensional view of the structure of the commercial wax pellet to be observed

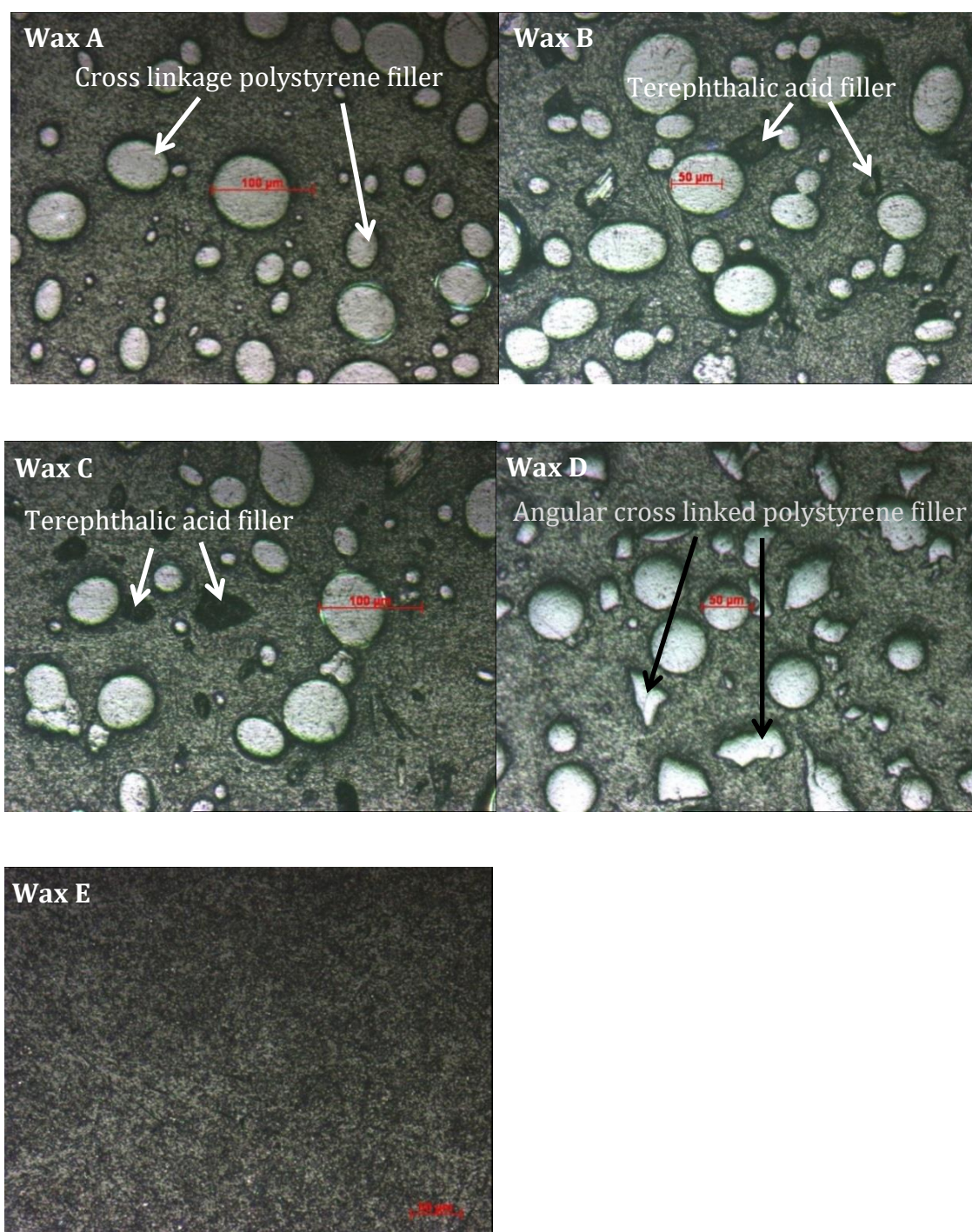


Figure 4-6: Polished wax pellet samples observed under the optical microscope at x10 magnification without cross polarised light.

The angular shape fillers in Wax B and D were compared under the microscope with the temperature set at 60 °C. Figure 4-7, shows that both waxes have angular fillers, however the colour of angular fillers in Wax B appear to be brownish-orange whilst the angular fillers in Wax D remain the same colour as the spherical cross-linked polystyrene present in the sample. This different colour was produced by the diffraction of light by the crystals in the fillers as the light enters the crystalline fillers. The brownish-orange colour reflects the body colour of the material though as some of the sample was rotated it changed shade due to pleochroism. According to the filler specification from wax supplier and the images, it was concluded that the angular shape fillers in Wax D were ground cross-linked polystyrene filler fragments. The angular fillers in Wax B and C are thought to be terephthalic acid filler.

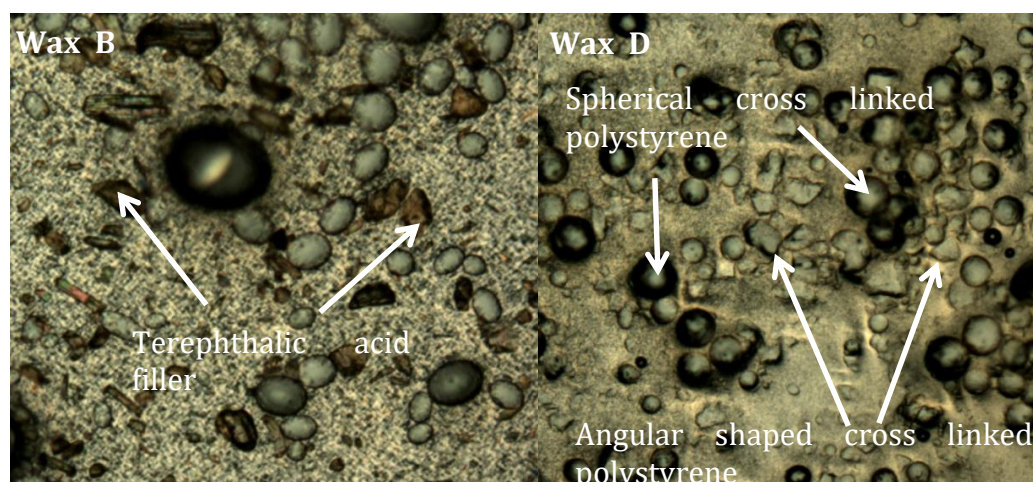


Figure 4-7: Wax B (left) and Wax D (right) shows that terephthalic acid exist as crystals and the broken cross linkage polystyrene appears to be have same colour as cross linkage polystyrene at 60°C with plain polarising filter.

With the information gathered to this stage, it can be postulated that Wax B, C and D have contributed to shell cracking partially due to the angular-shaped fillers which possibly restrict flow. There is also a possibility that the wide size distribution (especially the smaller particles) could clog the neck of the pores in the shell causing less

wax to permeate into the shell layer thus resulting in the shell cracking due to a reduced pressure release mechanism.

With the cross polarised light, the three different types of waxes, Wax A, C and E were compared. The spherical fillers found in Wax A and Wax C were cross-linked polystyrene and the orange angular shaped fillers found in Wax C are terephthalic acid filler as shown in Figure 4-8. The angular filler in Wax C is orange coloured. This is a reflection of the body colour (as seen in the plain polarised light) and the colour generated by birefringence. It was suggested that the fillers in Wax A are XLPS which are known to be amorphous. The spherical fillers in Wax A were observed to be black in the middle and the circumferences are brown in colour. The larger the diameter of fillers, the browner colouration is observed. However, the brown circumference should not be confused with the fillers being an anisotropic material. This brown circumference effect is known as a diffraction artifact around the particles. As expected, wax E contained no particles, only fine wax crystals when observed below the melting point.

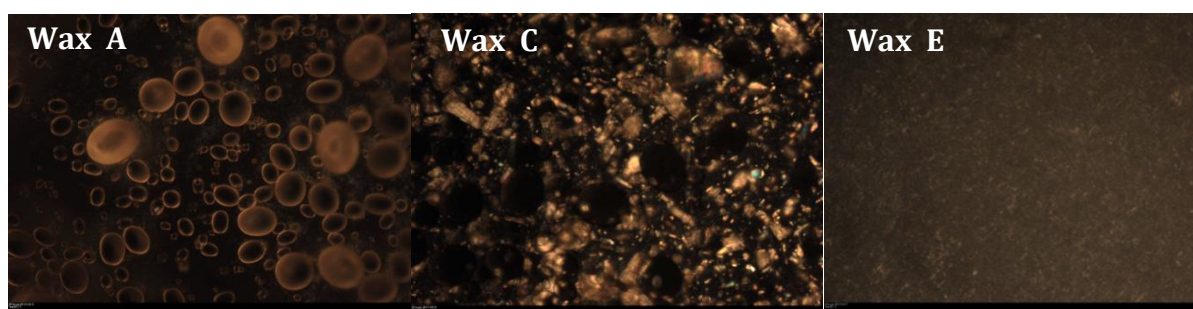


Figure 4-8: Hot stage microscope comparing the filler structures in three different waxes measured at 60°C with cross polarising filter.

To observe the microstructure of the wax with relationship to temperature, a hot stage was employed. Figure 4-9 shows that the images get darker as the temperature increases. This is because as more liquid is formed more light is extinguished

(amorphous material showing no birefringence). As the XLPS is amorphous, only TPA will be visible once the wax has melted with them in between its angles of extinction.

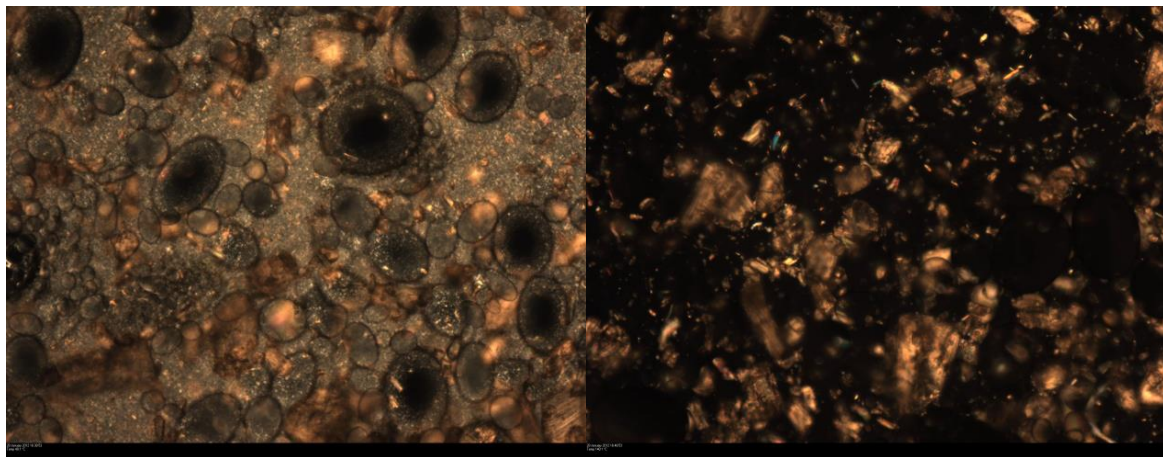


Figure 4-9: Hot stage microscope images in cross polarised showing before and after melting Wax C (The XLPS filler on left are dark because they are amorphous. The crystal of the base wax has melted in the right hand image showing angular filler only – probably TPA)

As part of the IC process, wax patterns were usually cleaned with degreaser to improve prime coat adhesion. With the interferometer, a comparison of the wax surface before and after cleaning the wax pattern with Trisol 60 plus was carried out (Figure 4-10). The surface roughness of wax will be reflected on the surface of the prime coat applied to that surface. This also means that the wax and prime coat surface are expected to be similar. Wax patterns that were not treated showed a higher contrast of colours due to the greater depth of deviation from the average roughness profile. The wax pattern that was treated with Trisol 60 plus had an average roughness (S_a) of $4.44\text{ }\mu\text{m}$ and untreated was $4.83\text{ }\mu\text{m}$. The difference of surface roughness before and after cleaning was found to be insignificant. This topographic data also showed that the wax and prime coat surface roughness (Figure 4-4) were slightly different (approximately $2\text{ }\mu\text{m}$). This was to be expected as the prime coat is formed mostly of particulate and wax. However, this difference could be because the point taken for measurement on the wax and shell were

not exactly the same. However, for the purpose of this work, sensitivity to this degree is believed to be unnecessary.

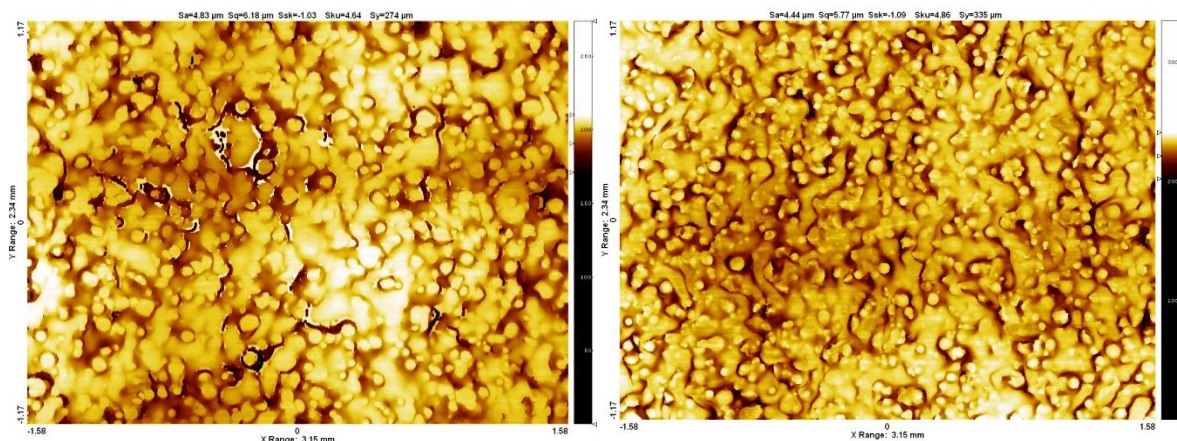


Figure 4-10: Surface roughness measurement on a 1mm x1mm wax surface before (left) and after (right) Trisol 60 plus cleaning for Wax D.

4.2 Chemical compound analysis

The compound analysis results obtained using FTIR are shown in Figure 4-11. Comparing the four waxes available at the time of the study, it was observed that the differences between the three filled wax (Wax A, B, and C) is not significant, indicating similar compositions have been used. This could be because all three filled waxes have large proportion of similar base wax which affects the detection of the specific chemical groups. The apparent higher absorbance of Wax E is due to a larger sample clamped between the diamond windows. This is possibly due to the softer nature of the unfilled wax – Wax E. However, it was observed that Wax E showed a higher absorbance at wavenumber 1710 cm^{-1} compared to other three waxes. This shows that Wax E has a higher proportion of carbonyl groups.

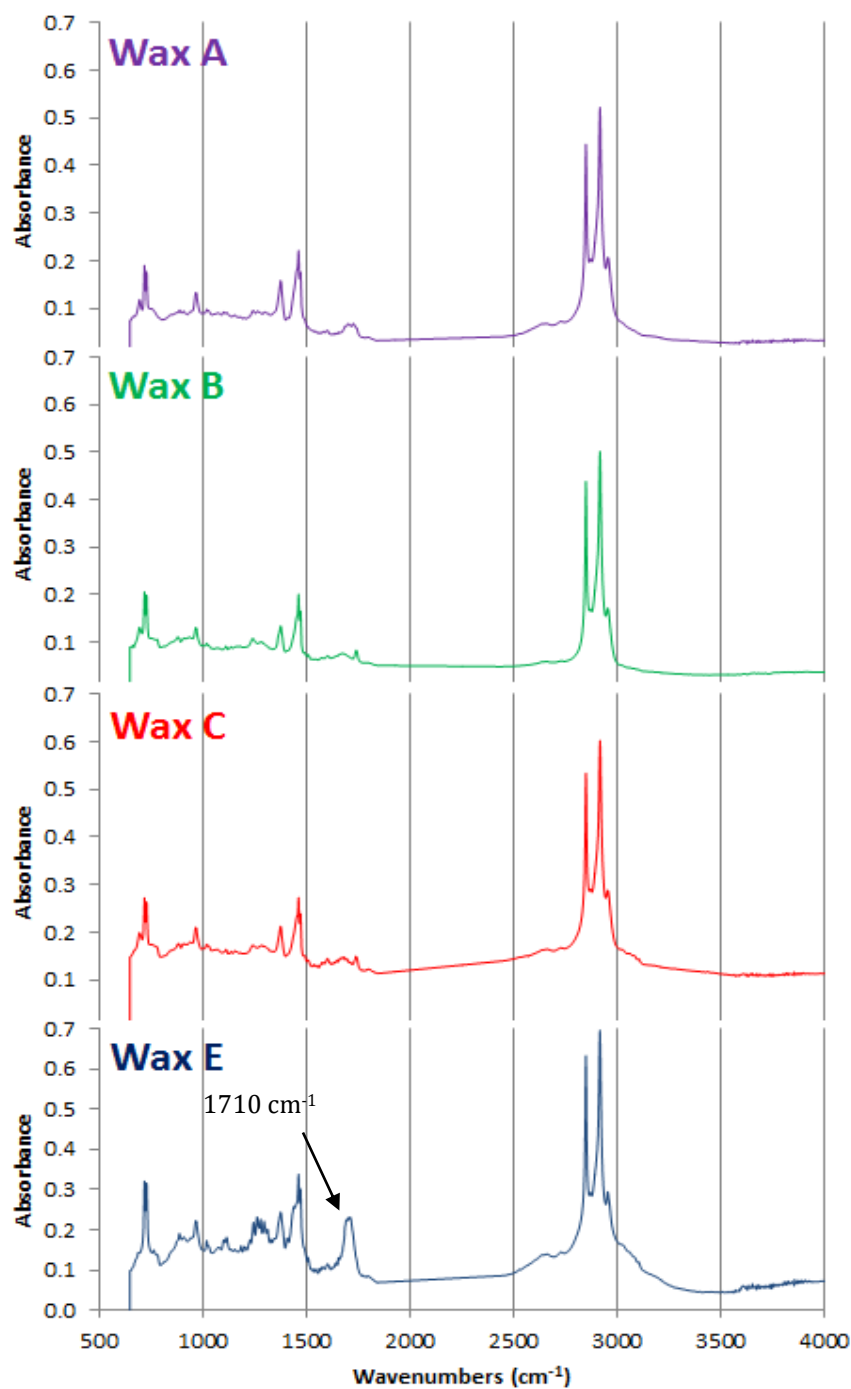


Figure 4-11: FTIR results for Waxes A, B, C and E. An extra peak compared to others was found at 1650 to 1750 cm^{-1} for Wax E.

4.3 Permeability

In the de-waxing process, the heating rate is rapid; so that bulk expansion of the wax does not occur before a proportion of the wax on the bulk surface penetrates the shell. However, how much wax is allowed to penetrate the shell will mainly depend on the permeability of shell.

The water permeability test showed that green shell had a permeability of $91 \pm 37 \text{ nm}^2$ and the corresponding effective pore diameter was approximately 4.77 nm which is 26 times smaller than the average pore diameter measured using mercury porosimetry. In comparison, the smallest pore diameter measured by mercury porosimetry was approximately 10 nm and this reflects the permeability measured by this method is relatively low. In another test with wax as permeate, it was found that the permeability was $22740 \pm 12054 \text{ nm}^2$ and corresponding effective pore diameter was 75.3 nm. The permeability measured with unfilled wax was $27822 \pm 10080 \text{ nm}^2$ and the corresponding effective pore diameter was 83.4 nm. It was found that permeability measured with wax especially filled wax is larger than with water. This could be because of an unidentified air leakage on the seal when pressurising the water. This means that less pressure was actually exerted resulting in a lower water flow rate. This postulation is reasonable when compared to the permeability of shell systems observe by other researchers.

Synder *et al.* (2003) found that the average fired shell permeability to be constant at around $135000 \pm 3600 \text{ nm}^2$ with nitrogen gas as permeate. The measurement is different from other cited literature but it is thought that permeability measurements can vary by two orders of magnitude (Synder, et al., 2003). The permeability measured by

Synder *et al.* (2003) is relatively larger. There are possibilities that Synder *et al.* (2003) were using different grade of stucco or slurry formulation to the work in this thesis which was not reported in the paper. It is important to note how significant changes to permeability can occur with minor changes in formulation. Wolfe *et al.* (2009) found their green shell permeability to be 10900 nm^2 and the fired shell permeability to be $2.96 \times 10^6 \text{ nm}^2$. Jones *et al.* (2003) found that the permeability of fired shell varied between $0.4 - 2.536 \times 10^5 \text{ nm}^2$ depending on the firing duration and stuccoing method (fluid bed or rainfall sanded). Cendrowicz (2004) found the permeability of his shell to cast steel to be approximately $1100 \pm 400 \text{ nm}^2$ and the equivalent pores size 17 nm. This value is also relatively large. The reason behind these differences could be attributed to the shell formulation or the shelling procedure, for example, if the slurry viscosity were different, or the coating method varied (hand coated, rainfall sander or fluidised bed), or even a different geometry used in sample preparation.

The permeability value from the wax permeability test will be used as it is more reasonable when compared to the literature and the mercury porosimetry results.

4.4 Flexure strength

4.4.1 Three point bend test

The measurement of mechanical strength for the shell was important to allow the prediction of the maximum stress the shell can sustain before the expansion of the wax cracks the shell during the de-waxing process. The shell flexural strength results are given in Table 4-1, Table 4-2 and Table 4-3 for different batches of shell build and allow different interrelationship to be examined systematically. Comparing the results

measured with the same methods presented in Table 4-1 and Table 4-3 it can be seen that there was variability in the returns batch to batch and hence there is a need to compare only results within a particular data set and table. For example, when samples were de-waxed by autoclave method 1 the mean flexural strengths ranged from 5.99 to 6.25 MPa. Figure 4-12-Figure 4-14 are figures representing the results of the analysis.

Table 4-1: Shells samples prepared in different ways to observe the average strength

Method	Ceramic Shells			Average strength (MPa)	Standard deviation
	Dewax method	Post-dewax treatment	Mechanical testing method		
1(a)	Autoclave	-	Prime up (PU)	6.26	0.79
1(b)			Prime down (PD)	6.25	0.67
2(a)	Fridge	-	Prime up	3.56	0.22
2(b)			Prime down	3.57	0.35
3	Autoclave	boil	Wet (PD)	4.66(decreased after boiled)	0.47
4	Fridge	boil	Wet (PD)	0.91	0.11
5	Autoclave	autoclave	Wet (PD)	4.37	0.61
6	Fridge	autoclave	Wet (PD)	4.55(increased after autoclaved)	0.48
7	Fridge	boil	Dry (PD)	2.86	0.17
8	Fridge	autoclave	Dry (PD)	5.88	0.59

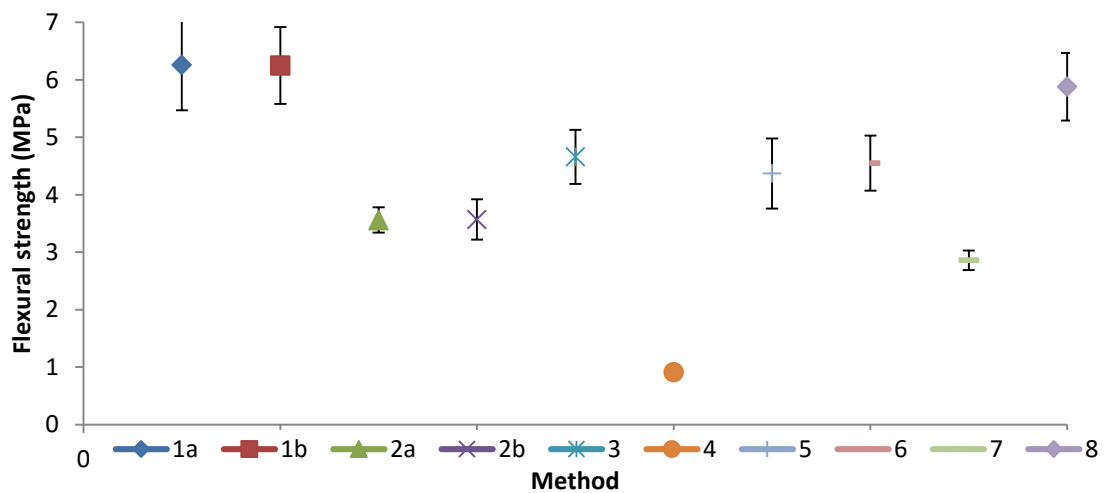


Figure 4-12: Graphical representation of the data presented in Table 4-1. It shows the flexural strength of shell prepared with different methods

Table 4-2: Strength measurements with primary in tension and compression

Method	Ceramic Shells			Average strength (MPa)	Standard deviation (MPa)
	Dewax method	Post-dewax treatment	Mechanical testing method		
3(a)	Autoclave	Boil	Wet (PU)	4.01	0.59
3(b)			Wet (PD)	4.56	0.88
4(a)	Fridge	Boil	Wet (PU)	0.92	0.09
4(b)			Wet (PD)	0.85	0.10

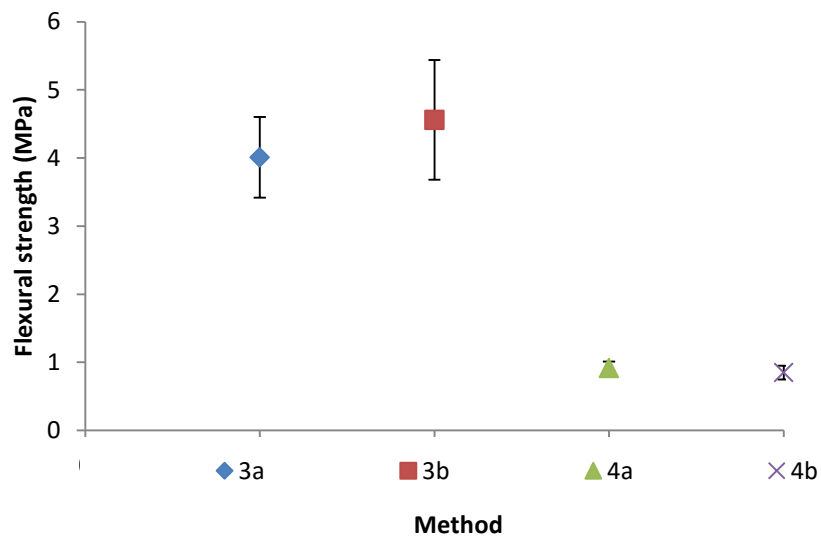


Figure 4-13: Graphical representation showing results of Table 4-2. There are not much difference in the flexural strength relating to specimen orientation either primary up or down.

Table 4-3: Steam test to observe the effect of moisture on the shell strength

Method	Ceramic shells			Average strength (MPa)	Standard deviation (MPa)
	Dewax method	Post-dewax treatment	Mechanical testing method		
1	Autoclave	-	Primary down (PD)	6.00	0.42
3	Autoclave	Boil	Wet (PD)	4.28	0.24
5	Fridge	Autoclave	Wet (PD)	4.60	0.24
6	Autoclave	Autoclave	Wet (PD)	4.47	0.45
9	Autoclave	Autoclave	Dry (PD)	5.61	0.38
10(a)	Autoclave	Steam	Wet (PU)	4.48	0.59
10(b)			Wet (PD)	4.45	0.25
11	Autoclave	Steam	Dry (PD)	5.05	0.38

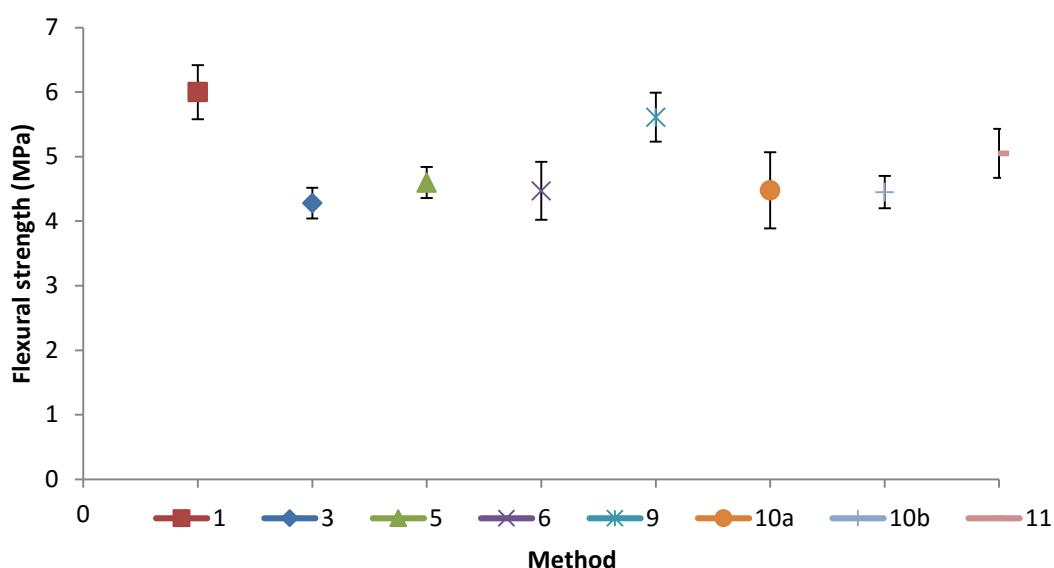


Figure 4-14: Graphical representation of the flexural strength data presented in Table 4-3.

4.4.1.1 Effect of different preparation method on shell mechanical strength

De-waxing by autoclave tested with the primary coat in compression (method 1 a) gave flexural strengths approximately 2.7 MPa greater than samples prepared by the fridge de-wax method (method 2a). The fall in strength was the same when testing prime coat in tension (methods 1b and 2b). This difference can be attributed to a combination of the penetration of wax into the shell and wax left on the inner surface of the shell in the samples prepared in the pressurised autoclave environment, and by any microstructural changes brought about by the thermal treatment.

To investigate the influence of autoclave steam on flexural strength, the fridge de-waxed shells were heat treated in the autoclave at 180 °C and 0.8 MPa for at least twenty minutes (method 6 and 8). The flexural strength increased by 0.98 MPa when tested wet and 2.31 MPa when the shell was dried after the autoclaving process. There are two possible mechanisms for this rise in mechanical strength, (i) The shells are compressed by the autoclave pressure to form a more compact structure (ii) Autoclaving increased

the coalescence of silica sol in the binder system offering a stronger structure. The cause of the increase in strength of the sol after autoclaving has been investigated further and those studies are discussed in section 4.4.1.2.

Comparing method 1a with 1b and 2a with 2b, Table 4-1 shows that testing the shells with primary coat in compression or tension did not lead to any significant difference in strength. The standard deviation was found to be significantly greater than the strength difference between the two orientations. However, there is a distinct difference when comparing the mechanical strength of shell tested wet or dry, either from autoclave steam or boiling water. Wet shells show a lower mechanical strength compared to dry shells. This is because the binder system from shells has been “softened” by the hot water or steam. Branscomb (2002) had observed similar behaviour where flexural strength decreased significantly when his samples were tested either wet (11 % drop) or hot and wet (23 % drop).

When comparing shell de-waxed by refrigerating (method 2b) with the shell boiled and then dried (method 7), the strength of shell was reduced by approximately 0.7 MPa in method 7. This shows that the binder system is affected by the boiling water and drying does not restore the mechanical strength to its initial state. The shell strength was reduced by approximately 2.7 MPa when the shell prepared by refrigeration was boiled and tested wet.

Method 3 showed that the flexural strength was reduced by 1.7 MPa (approximately 25 %) after the boiling process if the sample remained wet, when compared to method 1b. This is to be expected as the water softens the silica sol used in slurry and is consistent with data presented by Jones *et al.* (2003).

The samples de-waxed in the refrigerator were significantly weaker than the materials prepared by autoclave de-waxing. When the refrigerator samples were boiled and tested wet (method 4), the strength has further weakened by 2.65 MPa (approximately 75 %). This is attributed to the damage induced by the boiling process and the weakly integrated network of the silica gel. Jones *et al.* (2003) compared the refrigerator de-wax approach similar to method 6 with method 3 and found the shell strengths determined are comparable. This is because the initial autoclave de-waxed strength, although being relatively high, had significantly decreased after the soaking in the boiling process. The fridge de-waxed shells have lower mechanical strength prior to autoclave heat treatment, but this increased significantly after autoclaving the shells, due to either sol gel curing or compaction as mentioned earlier.

Table 4-2 shows that autoclave de-waxed and boiled shell tested wet (method 3) gave slightly different results when the samples were tested primary up or primary down. Jones *et al.* (2003) suggested it is important to choose which side of the shell is put into tension or compression. Primary down samples showed approximately 0.56 MPa higher strength compared to shells being tested with primary up. This may be due to differences in the surface roughness giving rise to stress concentrators on the rougher surface. However, there was no significant difference when comparing the primary up or down of the fridge de-waxed and boiled wet shell (method 4). This lead to a further suggestion that the variance in strength is due to the wax penetrating or sticking to the primary coat in method 3, which restricted the hot water penetrating the binder system through the primary coat side during the 5 minutes of the boiling water soak. The autoclave de-waxed boiled wet shells (method 3) have a higher standard deviation compared to fridge de-waxed boiled wet samples (method 4). It is postulated that the

penetration of wax into shell and any excess wax sticking to the inner shell surface may vary in volume, thus accounting for the greater variation in the shell strength found using method 3. It is also possible that the wax penetration into the shell is responsible for the slightly higher strength recorded for method 1 compared to method 2.

In the mechanical test, it was observed that both shell treatment methods (6 and 9) where the samples autoclaved twice and tested wet exhibited a 25 % decrease in strength compared to those tested dry (Table 4-3). By comparison, fridge de-waxed and autoclaved wet shell (method 5) exhibited a slightly higher strength than de-waxed autoclaved wet shells (method 6). This is probably due to the shell weakening during the autoclave de-waxing process in method 6 where the wax expands more than the shell mould. Another possibility is that the fridge de-waxed and then autoclave treated shells have incurred lower damage during cutting than the autoclave de-waxed shells, because the wax bar supports the shell. If the samples are dried after being re-treated in the autoclave or steamed (method 9 and 11 respectively) then there is partial recovery of the strength but not to that of the original autoclave samples when tested dry (method 1(b)).

4.4.1.2 Effect of Autoclaving treatment on the binder system

The two possibilities proposed to account for the increase in strength of shell after the autoclaving process are examined further in this section.

To evaluate the shells dimensional changes due to structure collapse, samples of fridge de-waxed shell were examined before and after autoclave retreatment using the dimensional test procedure outlined in Figure 4-15.



Figure 4-15: The width and thickness of each sample is noted with a line to assure the same location is being measured pre and post autoclave treatment.

The values reported in Table 4-4 showed a slight reduction in thickness and width with the autoclave treatment. However, the standard deviation is sixty times more than shrinkage observed. This also means that the external pressure exerted on the surface of the shell is not sufficient to show any geometrical changes that could contribute to the increase of shell strength. The skeletal density measured using Micrometrics AccuPyc ii 1340 gas pycnometer before and after autoclaving shows no obvious change in pores volume of the shell (Table 4-4). The density measurements also show no material loss during the autoclaving process.

Table 4-4: Comparing the thickness and width of shell before and after the autoclaving treatment.

Shell	Before autoclave	Standard deviation	After autoclaved	Standard deviation
Width (mm)	23.79	0.42	23.71	0.51
Thickness (mm)	6.12	0.64	6.11	0.63
Skeletal density (kg·m ⁻³)	2602.10	1.40	2601.00	0.70

It is believed that the mechanical strength of the shell is increased by immersion of the silica sol in the autoclave environment rather than by structural compression. The silica

sol used in slurry has a mean particle size of 14 nm, which will lead to very small inter-particulate pores if there is no coalescence. The surface area of the pores was determined using the nitrogen gas adsorption method (Micrometrics 2010) and the results are shown in Table 4-5. It was found that the average pore diameter of the silica sol increased by four times after the autoclaving treatment.

Table 4-5: BET data of dried silica sol before and after autoclave treatment.

	BET surface area (m²·g⁻¹)	Langmuir surface area (m²·g⁻¹)	Average pore diameter by BET (nm)
Room Dried Silica Sol	179.23 ± 0.52	247.68 ± 8.78	5.09
Autoclaved treated Silica Sol	31.48 ± 0.14	43.18 ± 1.10	21.28

Autoclave heat treatment gives greater coalescence of the gel indicated by a reduction in the total surface area with larger pores forming while pore volume is retained (Iler, 1978). However, autoclaving the gel network will not change the shape of gel framework, this is a common feature of gels as they become aged (Iler, 1978). Iler also mentioned that the resultant coalesced structures are not easily broken down when subjected to compaction. The pores in the silica gel grow larger to a point where the visible light reflects in the pores, reducing the light transmission so the gel appears opaque (Figure 4-16). Silica bodies which are opaque in nature exhibit higher strength (Bergna & Roberts, 2005). The higher the degree of coalescence of the particles in the powder aggregates, the harder the aggregates will be, and the less they are deformed by mechanical stresses (Bergna & Roberts, 2005). X-ray diffraction (XRD) results given in Figure 4-17 show no composition change following autoclaving the silica sol. This shows that autoclaving the silica sol purely changes the pore diameter and surface area of gel. From the BET test, it is strongly suggested that the extra mechanical strength of shell is

primarily due to the coalescence of silica sol during the autoclaving treatment. While this phenomena is clearly seen when comparing the fridge de-waxed samples before (method 2) and after autoclave treatment (method 6), it would also occur during the normal autoclave de-waxing process (method 1), but in this situation the strength is also influenced by the remnant and penetrating wax.

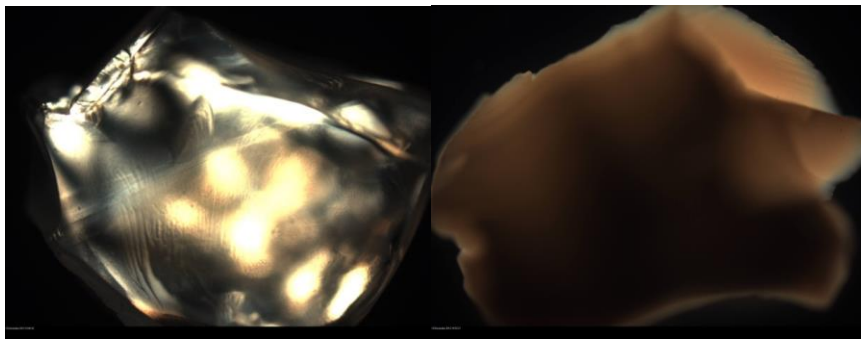


Figure 4-16: A dried particle of silica sol (left) and autoclaved silica sol (right) using a transmitted light microscope. Particle size is approximately 1mm

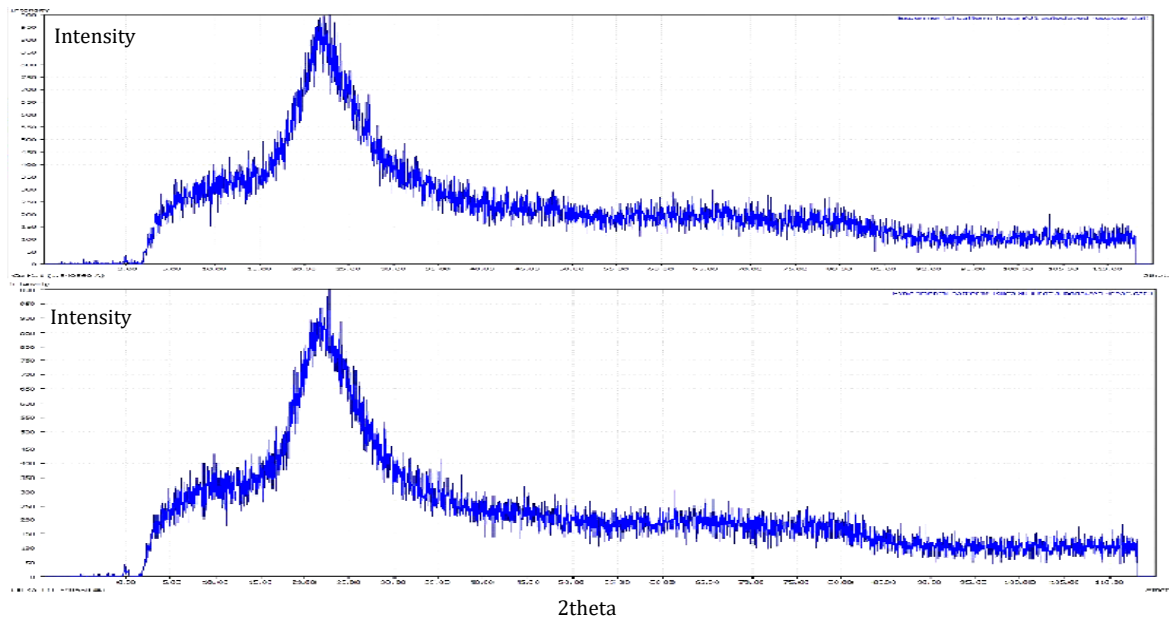


Figure 4-17: XRD result show pattern before (top) and after autoclaving the silica sol. Both tests showing amorphous silica.

From the results discussed in section 4.4.1.1 and 4.4.1.2, it becomes clear that it is important to determine which stage of de-waxing process is of interest whether that is

before or after the wax interacts with the shells. In the case of predicting de-wax shell failure, obtaining a lower limit of shell mechanical strength would perhaps be more representative of the process. Again, 4-point bend test would give a lower strength limit due to its sensitivity to detect flaws with either the size or location. However, it is also important to have sufficient number of samples and edge polishing is necessary to give consistent results. The autoclaving condition is found to increase the mechanical strength of the shell, as the silica sol in binder system coalesces and there is a contribution of wax permeating the shell. Tests using fridge de-waxing followed by autoclave and testing wet (method 6) produce the most useful result for green shell strength characterisation, as the shell is clean and less damaged from sample preparation. However, method 2 without post-autoclaving is suggested to be more representative of the fundamental shell strength in the green state at the point of de-waxing.

4.4.2 Wedge test

Sharp edges of any geometry, for example the wedge test sample, have the tendency to have thinner shell build because slurry in these areas drips off quicker relative to the rest of the geometry and the stucco does not coat as well on sharp edges due to trajectory and incident angles.

The wedge test reasonably represents the shell cracking of a sharp edge where the stresses are prone to focus within the shell during de-waxing due to thermal expansion of wax. It was observed that the wedge test has relatively lower strength and was nearly half the strength measured in a flat bar sample. The shelling formulation for both test (flat bars and wedge test) are the same, but it is important to note that IC shells are

formed in layers and are not homogenous. If the materials were the same then the flat bar and the edge test would or should give similar results but due to the changes in the deposition at the edge the materials can be considered to be different in structure. This argument can also be supported by examining the standard deviation of the mechanical testing prepared from same condition where higher standard deviation is found in wedge test compared to the flat bars. The result indicate that the probability for the slurry and stucco to coat consistently on the edge are lower than on a flat surface.

The wedge test was carried out on samples prepared by three different methods of which two of the methods gave the maximum and minimum values in the flat bar 3-point bend test. Samples prepared with these three methods were thought to best represent the autoclave condition. The autoclave de-waxed method (method 1) shows the flexural strength is approximately 2 MPa and is lower than samples prepared by refrigerator de-waxed then autoclave post treatment (method 6). It is suggested that this was because the autoclave de-waxed samples (method 1) are weakened by the thermal expansion of wax. Alternatively, samples prepared by method 6 could have higher mechanical strength due to the curing of silica sol in the slurry. The influence of curing silica sol was discussed in section 4.4.1.2 Method 1 shows a slightly higher strength than method 2 and this is postulated to be the effect of wax permeating into the porous shell, or residuals of wax left on the surface of shell layer offers the extra mechanical strength.

Generally, wedge test samples have lower flexure strength than 3-point bend test (Table 4-6). The most significant strength reduction was on samples prepared with method 1. The wedge test sample prepared with method 1 had reduced by one third. This was

suspected to be contributed to by the expansion and cracking of the sharp edges in autoclave prior to testing.

Table 4-6: Wedge test compared to 3-point bend test results

Method	Wedge test (MPa)	3-point bend test (MPa)
Autoclave de-waxed (method 1)	2.09 ± 0.59	6.25 ± 0.67
Refrigerator de-waxed (method 2)	1.80 ± 0.49	3.56 ± 0.34
Refrigerator de-waxed and Autoclave post treatment (method 6)	3.44 ± 0.60	4.54 ± 0.47

It is suggested that the refrigerator de-waxed method (method 2) should be use to represent the mechanical strength of a shell (either 3-point bend test or wedge test) for the de-wax simulation purely because shell cracking occurs at the start of a de-waxing cycle without the effect of wax penetration or the steam curing the silica sol.

4.5 Young's modulus

4.5.1 Flat bars

4.5.1.1 Stress-strain curve

Samples for Young's modulus measurement were prepared by two different methods, method 2b and method 6 (Table 3-4). Results shows that shells that were autoclaved (method 6) had nearly double the stiffness of the fridge de-waxed shell (method 2b). The stiffness loss on the equipment was checked using a 70 mm thick steel block. It was found that the instrument did deflect but with only 0.1 mm of deflection at 500 MPa. Figure 4-18 shows that at 5 MPa (average shell cracking limit), the deflection of the instrument is equivalent to approximately 0.001 mm. The standard deviation of the shell flexure is 0.2 mm which is relatively large in comparison to the deflection of the

instrument. This justifies that the loss of stiffness on the instrument is negligible and no correction was subsequently made to the data for the machine stiffness.

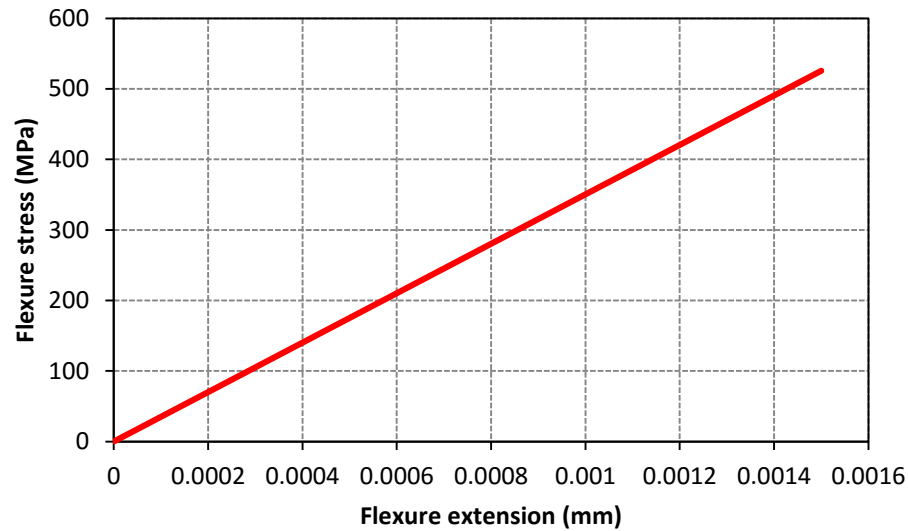


Figure 4-18: Load frame deflection calibration with 70 mm thick steel block. Steel block is assumed to have zero deflection and the load frame deflected 0.1 mm with 500 MPa stress.

The fridge de-waxed primary down sample (method 2b) presents a Young's modulus of 1.06 ± 0.20 GPa and fridge de-waxed autoclaved primary down wet (method 6) a Young's modulus of 2.21 ± 0.53 GPa. This shows that autoclaving doubled the stiffness of shell. The Young's modulus of samples prepared with method 2b is relatively low compared to the Young's modulus of IC shell found in the literature. Yuan *et al.* (2004) found the Young's modulus for fiber modified mould is 3.67 ± 0.49 GPa (sample preparation similar to method 1). Wet MOE (specimen first soaked in water) in the industry is typically 3.79 GPa (Snow, 1998). The relatively high Young's modulus found in literature could be contributed by the wax residue after de-waxing.

4.5.1.2 Impulse excitation of vibration

The vibrational wave from each strike detected by the laser beam was converted to frequency (using the function built into LabVIEW® 2012). Frequencies of 321.3 Hz and 335.2 Hz were recorded for the fridge de-waxed shell (method 2) and the fridge de-waxed autoclaved wet (method 6) respectively. These frequencies were then calculated in terms of Young's modulus producing values of 6.49 GPa for fridge de-waxed primary down shell and 7.05 GPa for fridge de-waxed autoclaved wet. The same situation was observed where stiffness of shell has increased due to the autoclaving process, however it is not as significant as modulus obtained from the stress-strain curve. It is suspected that the porous shell dampened the vibration and was not able to sense the potential difference of shell's Young modulus prepared with the two different methods (method 2 and 6). The exact reason behind this was uncertain and further work is required to verify the observation. Young's modulus measured using stress-strain curve was observed to be smaller than that determined impulse excitation.

The torsional vibration test to measure the shear modulus can be carried out by impulse excitation method, however, it is not reported here because of extremely low repeatability. This was due to the shell being lifted when the zirconia ball hit the sample edge.

4.5.2 Wedge geometry

With the wedge geometry, the stress was calculated based on Equation 3-3 and the flexure strain using Equation 3-5. The Young's modulus of fridge de-waxed sample (method 2) calculated by this method was 2.91 ± 1.81 GPa and fridge de-waxed autoclaved wet (method 6) 6.27 ± 2.16 GPa. Results show that shells that are autoclaved

have approximately double the stiffness of the fridge de-waxed shell, a similar result to that for flat bars. The high Young's modulus of wedge geometry could result from the relatively small flexure strain (Table 4-7), but could also be due to the microstructural damaged brought about by the build process. The flexure stress in a wedge sample before failure was half that of the flat bar but the flexure strain in a wedge sample bar was found to be one sixth the flat bar sample. The Young's modulus of wedge test sample was found to be double the flat bar prepared by method 2 and was triple the stiffness of a flat bar prepared by method 6. This could be one of the reasons why cracking usually occur at sharp edges where less stress relaxation is possible to relieve the pressure building up. However, the error in this test is relatively high compared to the data from stress-strain curve on flat bars.

Table 4-7: Comparison of strain at failure experienced by the flat bar and wedge sample

		Fridge (μm) (method 2)	Autoclave (μm) (method 6)	Difference (μm)
Strain	Flat bar	2.78 \pm 0.74	2.49 \pm 1.31	0.28
	Wedge	0.83 \pm 0.36	0.78 \pm 0.26	0.05

4.6 Density and thermal expansion

4.6.1 Shell density

For porous materials such as investment casting shells, density and porosity are inversely related. The average pore diameter measured by the mercury porosimetry was 131.2 nm and the porosity percentage was 21.63 %. The bulk density of the shell was 1925 kg·m⁻³ and the skeletal density was 2456 kg·m⁻³. The porosity and density was

found to be comparable with Cendrowicz (2004) finding. Cendrowicz found that for a shell designed to cast steel the porosity was 23.8 % with a bulk density of $1914 \text{ kg}\cdot\text{m}^{-3}$ and a skeletal density of $2512 \text{ kg}\cdot\text{m}^{-3}$.

The pressure in the mercury chamber allows measurement of pores with different diameter and the result shows it covers more than five orders of magnitude of pore size (Figure 4-19). It is important to point out that acquiring one number to describe the pore size as an average for such a large distribution does not fully represent the material. However, for simplicity, it is suggested that the average value be used to describe the porosity of shell in the modelling of de-wax.

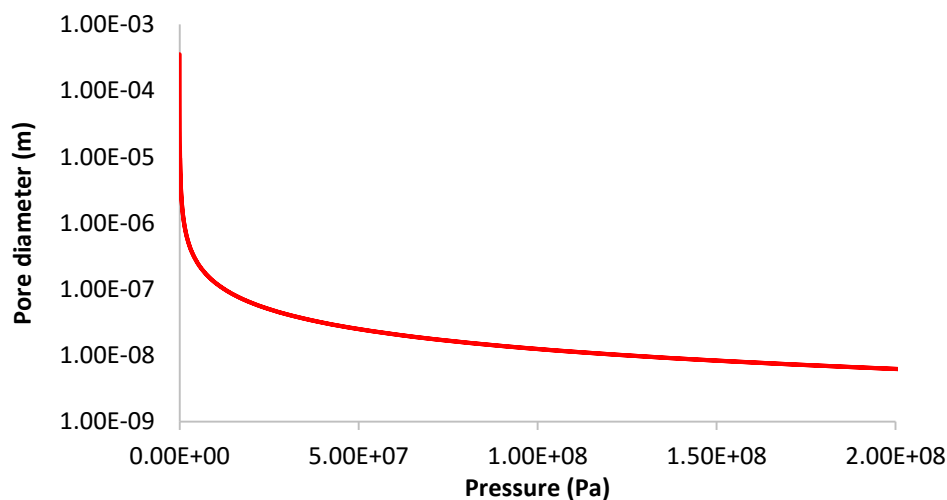


Figure 4-19: Results obtained using mercury porosimetry showing a large distribution of pores diameter.

A Micro-meritics Accupyc II 1340 helium pycnometer measured the skeletal density by filling the pores of the shell with helium gas. The density of shell measured using this method was $2602 \text{ kg}\cdot\text{m}^{-3}$. The skeletal density found with helium pycnometer was approximately $150 \text{ kg}\cdot\text{m}^{-3}$ higher than density measured with mercury porosimetry. It

was postulated that this was because the helium gas is capable of filling the pores more effectively than mercury.

The bulk density of shell used to cast steel ($1914 \text{ kg}\cdot\text{m}^{-3}$) will be used for the shell simulation work because this takes into account of the air trap in the pores of shell which in turn affects the heat transfer rate.

4.6.2 Shell Thermal expansion

A conventional dilatometer (high temperature range 0- 1600 °C) used to measure high temperature ceramics was found to be not suitable for measurement of shell expansions up to 180 °C due to the poor sensitivity of thermocouples in this temperature range. Another issue was that the push rod in the dilatometer had a larger surface area pushing on the shell's rough surface resulting in a non-uniform surface contact. Rough surface samples tend to slip or move resulting in low repeatability of results. As a result, the linear thermal expansion coefficient of standard steel shell was measured on a TMA and this gave a thermal expansion of $2.55 \times 10^{-6} \text{ }^{\circ}\text{C}^{-1}$ (Figure 4-20). Note that this test was carried out under non-steam condition. Thus, it did not take into account of shrinkage that occurred due to curing of silica sol by steam or any shell expansion that occurred due to steam condensation in shell pores (if that occurs). This is reasonable as in section 4.4.1.2, it was reported that curing of silica sol did not significantly vary the dimension of the shell, thus the influence of steam should be negligible when measuring the thermal expansion. The thermal expansion found with this method is similar to those found in the literature. Snow (1998) used an average of $5.28 \times 10^{-6} \text{ }^{\circ}\text{C}^{-1}$ in his computer simulation work. Cendrowicz (2004) obtained $2.2 \times 10^{-6} \text{ }^{\circ}\text{C}^{-1}$ for moulds to cast steel or aluminium when using a dilatometer.

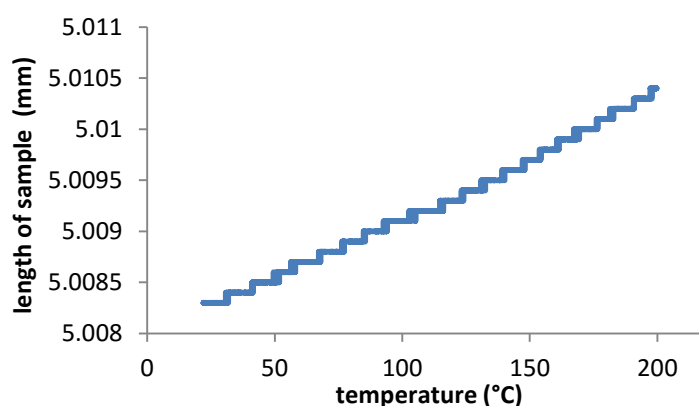


Figure 4-20: TMA data used to measure the thermal expansion of the shell. The expansion of the sample appears linear with the increasing temperature

4.6.3 Wax Density

The density of wax was measured by the helium pycnometer at laboratory temperature (20 °C) (Table 4-8). Results indicate that Wax E, which is an unfilled wax, had the lowest density among the five waxes tested. According to wax supplier (Blayson Olefines Ltd), the density of a typical acidic filler is 1070 kg·m⁻³ while a typical cross-linked polystyrene is 1030 kg·m⁻³. Among the four filled waxes, Wax A which was known to be a non-shell cracking wax has the lowest density. This indicates that the filler with high density has contributed to higher density of filled wax. From microstructural observation in section 4.1 and supplier's information, the higher density of Wax B and C can be attributed to the inclusion of acidic fillers. The high density of Wax D with only cross-linked polystyrene could be attributed to the higher filler packing density attained by the two forms of XLPS including the observed angular shaped grains. However, other test such as particle size distribution analysis would be required to clarify this hypothesis.

Table 4-8: Density measured using Helium pycnometer at 20°C

Wax	Density (kg·m⁻³)	Standard deviation (kg·m⁻³)
A	972.9	0.3
B	1017.1	0.3
C	1013.2	0.3
D	1025.2	0.3
E	949.6	0.2

4.6.4 Wax Thermal Expansion

This section reports the density variation of the wax with temperature up to the autoclaving temperature using three different methods – PVT, a dilatometry method using a capsule and modified density bottle. This section will first discuss on the results obtained from different methods followed by detailed method comparison.

The PVT results measured by NPL are shown in Figure 4-21. Wax E, which is an unfilled wax, was found to have a different trend line compared to the filled waxes. The total increase of specific volume for Wax E from 20 to 120 °C was greater than the other waxes. The standard deviation measured by NPL was $0.1 - 0.3 \times 10^{-5} \text{ m}^3 \cdot \text{kg}^{-1}$ depending on the wax. This error is far lower than those found in the other two methods applied to the waxes. NPL's PVT was limited to a maximum temperature of 120 °C and so did not reach the required temperature corresponding to the autoclave. Any temperature above that with 20 MPa pressure would probably cause excessive wax leakage.

Figure 4-22 shows the thermal expansion of five different wax measured using the NETZSCH capsule. The standard deviation of measurement ranges from $0.2 - 0.8 \times 10^{-5} \text{ m}^3 \cdot \text{kg}^{-1}$ increasing with increasing temperature. It was observed that the gradient of the Wax E curve reduce at temperatures above 160 °C. This is because Wax E with its lower melting point tended to leak passed the silicone rubber seal at high temperature (wax residues were observed in the dilatometer).

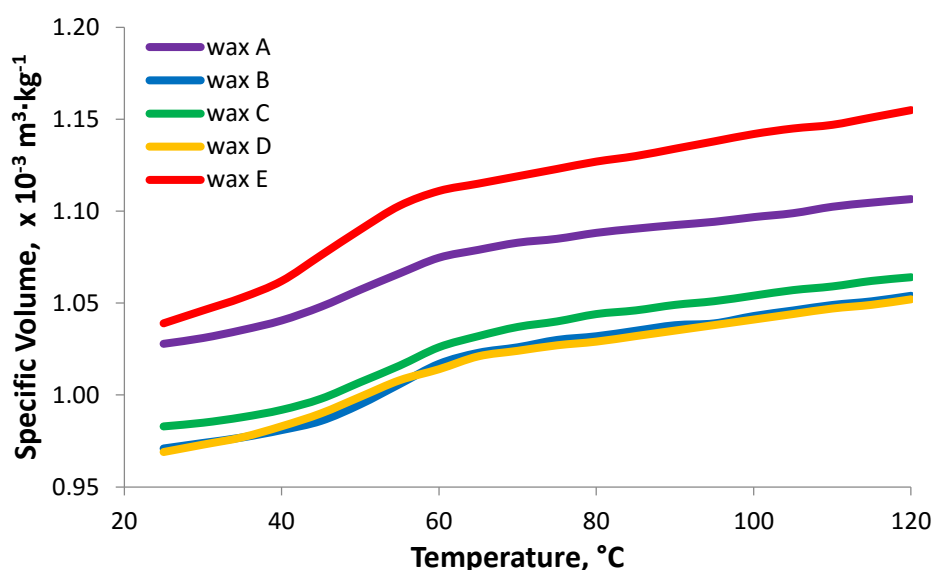


Figure 4-21: Thermal expansion measured by NPL for Wax A-E

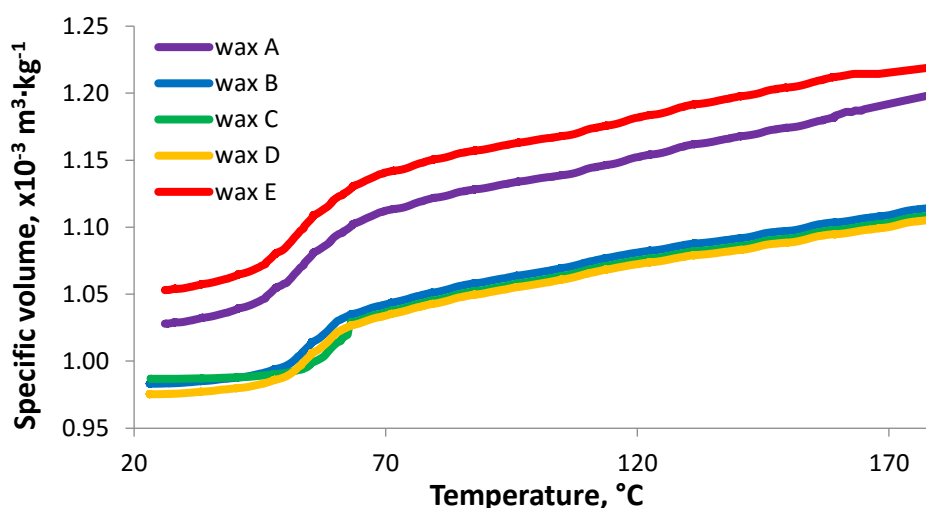


Figure 4-22: Thermal expansion tests using NETZSCH capsule for Wax A-E

The density bottle method was first validated to ensure no volume was lost due to the chemical reaction between the silicone oil and the wax (Figure 4-23). In the procedure, the wax and silicone oil were heated separately in a beaker at 180 °C for three hours and then mixed together. The final volume was found to be 0.34 % less than expected but this was within experimental error. A separate test was carried out by heating the wax to 180 °C which resulted in a 0.22 % loss of mass after three hours. This shows that the

majority of volume lost in the mixture of wax and silicone was attributed to the loss of volatile components in wax, and that no obvious volume lost was caused by chemical interaction between the wax and the silicone fluid. Following validation of the method, the derived thermal expansion curves for the waxes are shown in Figure 4-24 and are discussed in the following section. The standard deviation for the data obtained in this method ranged from $0.1 - 0.9 \times 10^{-5} \text{ m}^3 \cdot \text{kg}^{-1}$. The higher standard deviation of this method is largely due to the air bubbles that are in the wax pellet.

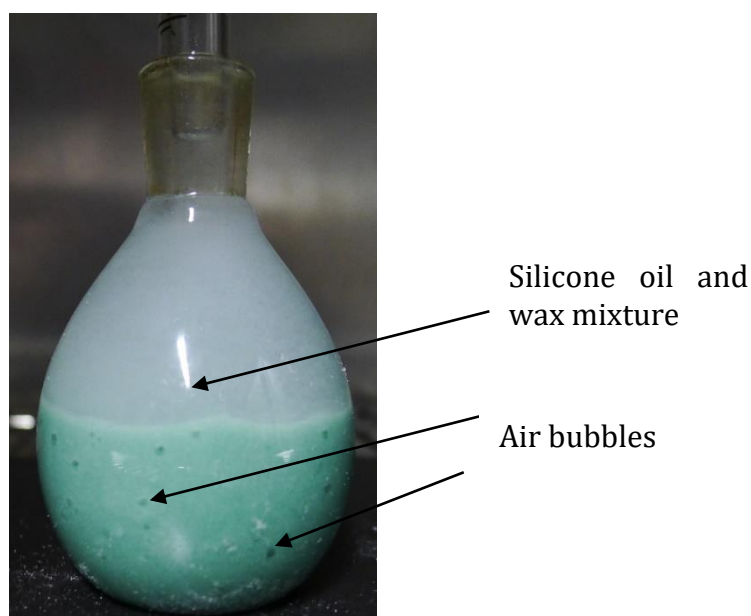


Figure 4-23: Modified density bottle with wax, silicone oil mix during cooling down. Wax crystals start forming causing the silicone oil appear to be cloudy. Air bubbles from wax pellets are observed.

The PVT measurements were determined during cooling while in the other two methods (Netsch capsule and modified density bottle method) measurements were made while heating. With the latter two methods, wax sticking to the instrument on cool down made it impractical to measure in that temperature regime. PVT was measured at 20 MPa, while the density bottle measurements were made at ambient pressure and the pressure developed by the back pressure of the expanding silicone seal on wax in the Netsch

capsule was unknown. During the de-waxing phase in the autoclave for wax, shell to cast steel is expected to crack within the pressure range of 2 to 7 MPa. This range of pressure is obtained from the flexural test as the shell fails at a maximum pressure of 6.26 MPa. This is intermediate between those tests carried out at atmospheric pressures and in the PVT.

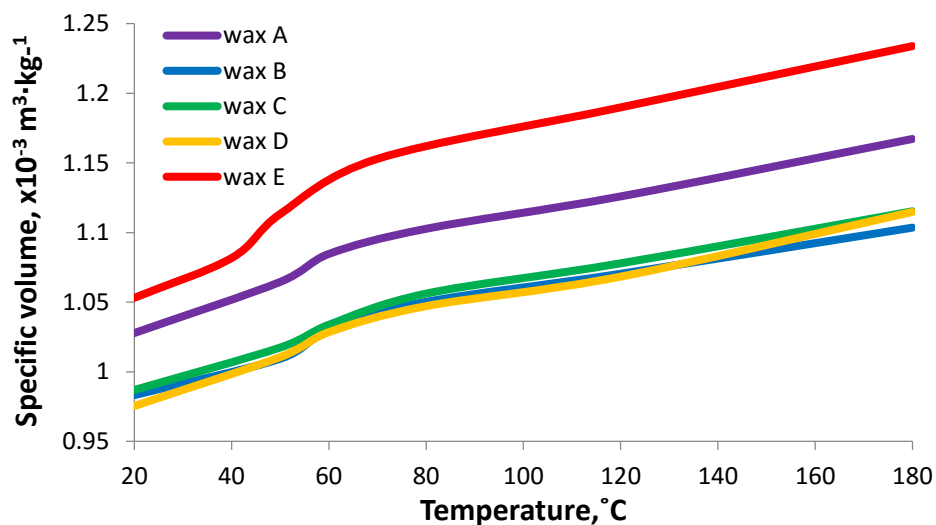


Figure 4-24: Thermal expansion using the density bottle for waxes A-E

The comparison of the three analysis methods on Wax C is shown in Figure 4-25. Specific volume measured using the density bottle was slightly higher than the PVT method but the NETSCZH capsule method measure significantly lower values below 50 °C. This may be because movement in the capsule only occurred when the wax was fully in contact with the seal.

The PVT data (NPL) was obtained at 20 MPa and PVT measurements can be made at higher pressures. Torres (2003) reports PVT data for other commercial waxes over a higher pressure range and by extrapolation the expansion, behaviour at 0.1 MPa (1 atm) can be estimated. Applying a similar correction to the PVT data on the project waxes leads to the extrapolated PVT line shown in Figure 4-25. It can be seen that above 50 °C

the modified density bottle data lies between the two PVT curves. This suggests that the pressure in the operating range has little influence on specific volume as a function of temperature and that the density bottle data can be used for modelling the wax behaviour. However, it is important to note that density bottle method has a larger standard deviation compared to the other two methods. This error was believed to be caused by the air bubbles in the wax pellets and pre-melting the wax prior to filling into the density bottle could reduce the error by allowing better evacuation.

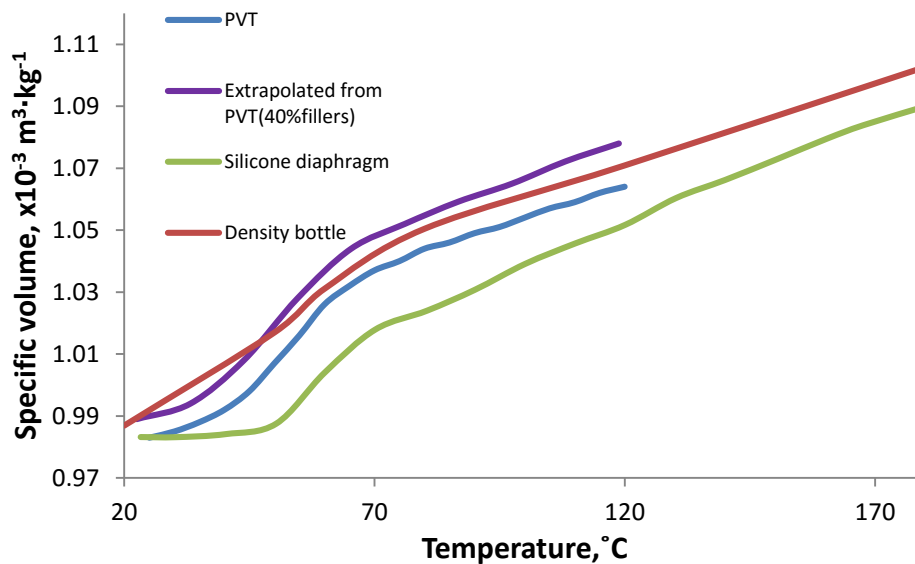


Figure 4-25: Comparing thermal expansion obtained using three different methods on Wax C

4.7 Specific heat capacity

The specific heat capacity of shell and waxes was measured by DSC during a heating ramp of 10 °C·min⁻¹ as it represents the situation in the autoclave during de-waxing. The specific heat capacity of the shell is presented in Figure 4-26. The shell sampling method makes the assumption that the specific heat capacity for each layer of shell is similar and the material is homogenous across the shell. It was observed that the specific heat capacity of shell rose sharply at the early stage of the test and then increase

progressively over the temperature range from 800 – 1300 J·kg⁻¹·K⁻¹. The sharp rise observed was attributed to the nature of the instrument measuring the sample heat capacity at ambient temperature and a linear extrapolation to represent the specific heat capacity is more realistic. However, for simplification in the simulation, 1000 J·kg⁻¹·K⁻¹ was used for the shell.

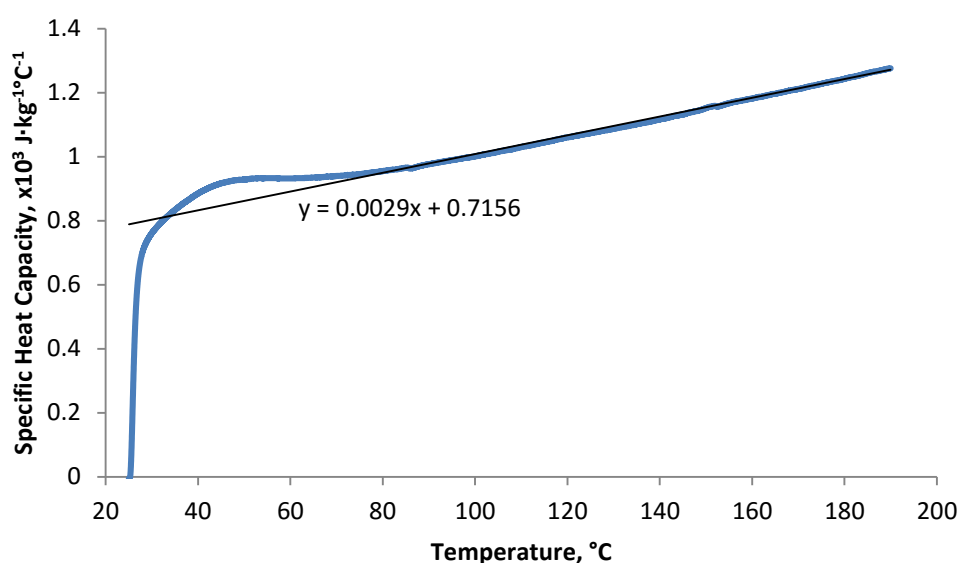


Figure 4-26: Specific heat capacity of shell measured using DSC

The specific heat capacity of the waxes is presented in Figure 4-27. It was found that Wax E had the highest specific heat capacity among the five waxes and all of the filled waxes had very similar specific heat capacity over the entire temperature range. Wax D had the lowest specific heat capacity among the four filled waxes. The broader endothermic peak in unfilled wax indicates the absence of fillers which tend to increase the heat capacity of wax. These results agree with the findings of Torres (2003) where the fillers acted as a thermal conductor reducing the specific heat capacity compared to a full wax system. As a comparison, Torres (2003) found that the maximum specific heat capacity for a filled wax is approximately 6000 J·kg⁻¹·K⁻¹ over the phase transition

temperatures. The specific heat capacity obtained by Cendrowiz (2004) for Blayson A7-11 and Hyfill B417 waxes was between $5000\text{--}6000\text{ J}\cdot\text{kg}^{-1}\cdot\text{K}^{-1}$. The complete set of heat capacity data for waxes was used in the simulation instead of an average value.

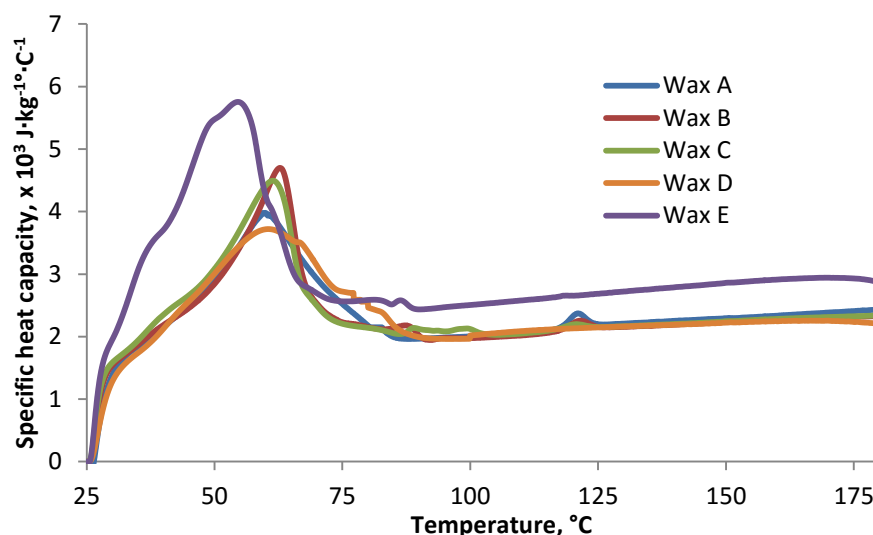


Figure 4-27: DSC heating scan with $10\text{ }^{\circ}\text{C}\cdot\text{min}^{-1}$ heating rate to observe the specific heat capacity of different waxes

4.8 Solid to liquid phase transformation

Specific volume data obtained from the density bottle method was extrapolated with a linear extrapolation to obtain the starting point (onset) of wax melting to the end point where wax is completely melted (Figure 4-28). The phase transition points of waxes were also obtained from the DSC results. The method to obtain the value from DSC data is shown in Figure 4-29. The results of both method are presented in Table 4-9.

It was observed that the onset points obtained from the two different methods are similar. However, the end points vary significantly. The only wax that had a similar end point was Wax E the unfilled wax. With extrapolation from the specific volume data, Wax E was found to have largest phase transition temperature of $26.5\text{ }^{\circ}\text{C}$. This could be related to the absence of fillers which are known to increase the thermal conductivity.

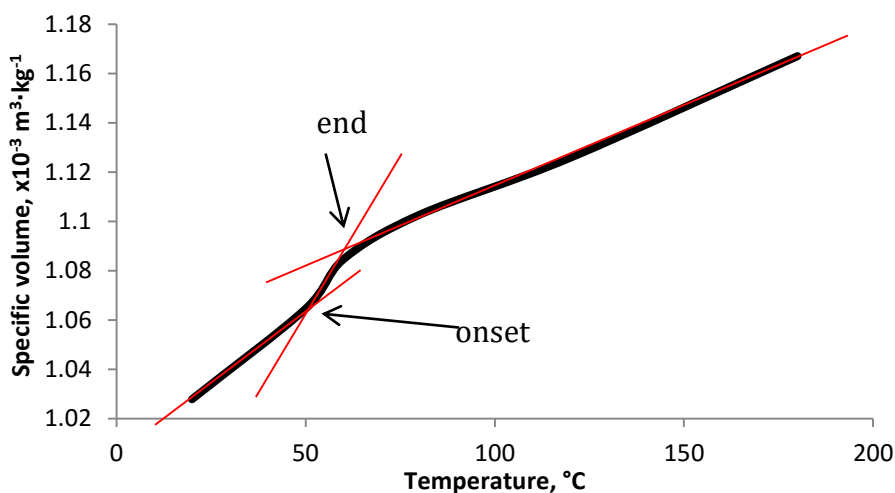


Figure 4-28: Solid and liquid phase transition line is extrapolated from density bottle method data to obtain the start of semi-solid phase (onset) and end of semi-solid phase (end)

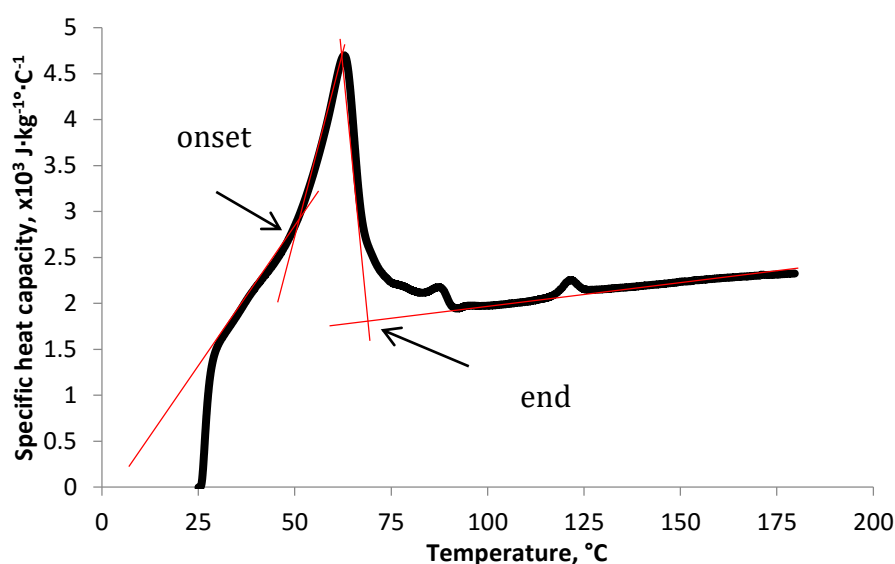


Figure 4-29: Solid and liquid phase line is extrapolated from DSC data to obtain the start of semi-solid phase (onset) and end of semi-solid phase (end)

The unfilled wax had a lower onset point, approximately 10°C lower than filled waxes. Filled Wax A was found to have the highest end point among the five waxes from the specific volume data. Extrapolating from the DSC data, Wax D had the highest end point. This also means Wax D has the largest phase transition range according to the DSC data (33°C). DSC provides a larger range of phase transition temperatures and the reason

behind this was uncertain. It was possible that the heating rate affected how the fillers in waxes interact with the melting process. The density bottle method results were obtained at set temperatures following equilibration and sampling in DSC was carried out at a heating rate of $10\text{ }^{\circ}\text{C}\cdot\text{min}^{-1}$ where reading were taken continuously. Some uncertainties must be eliminated before the DSC data can be used to determine onset and end of wax melting. However, the DSC data is required to provide the latent heat of melting using the Equation 2-3.

Table 4-9: The temperature range of wax in solid and liquid form

Wax	Wax Type	Specific volume		DSC			
		Onset ($^{\circ}\text{C}$)	End ($^{\circ}\text{C}$)	Onset ($^{\circ}\text{C}$)	End ($^{\circ}\text{C}$)	T_m point ($^{\circ}\text{C}$)	Latent heat ($\text{kJ}\cdot\text{kg}^{-1}$)
A	Filled	51.5	72.0	49.0	77.5	60.0	72.8
B	Filled	51.0	64.0	49.0	69.0	62.5	105.3
C	Filled	51.5	65.0	49.0	67.5	62.5	101.6
D	Filled	51.0	64.0	48.0	81.0	60.0	78.9
E	Unfilled	40.5	67.0	41.0	67.5	55.0	113.2

For comparison, the wax properties provided by wax suppliers are shown in Table 4-10. The melting point was measured with the drop melt point (as discussed in Section 2.6) and congealing point by spinning wax at the tip of a thermocouple. However, only Wax D has a complete data set (congealing and melting point) for comparison. The temperature range between the minimum congealing point and maximum melting point for Wax D was $10\text{ }^{\circ}\text{C}$ (Table 4-10). The difference between the onset point and end point extrapolated from the specific volume data for Wax D was $13\text{ }^{\circ}\text{C}$ (Table 4-9). Both measurements gave a similar temperature difference, however, the onset point was approximately $12\text{ }^{\circ}\text{C}$ lower than the minimum congealing point. The phase transition range provided by the supplier suggests melting to occur over a lower temperature

range. This was believed to be related to the heating and cooling rate of the wax. In Shobanjo's work (2010), she showed that at a heating rate of $5\text{ }^{\circ}\text{C}\cdot\text{min}^{-1}$, the melting point of her wax was at $59\text{ }^{\circ}\text{C}$ and at $20\text{ }^{\circ}\text{C}\cdot\text{min}^{-1}$, it appeared to increase to $67\text{ }^{\circ}\text{C}$. The higher the heating rate, the higher the melting temperature indicated. It could be the same case here, where drop melt technique uses heating methods such a laboratory torch (high heating rate) compared to a fan oven use to obtain the wax specific volume data. For simulation purposes, the melting point provided by the wax suppliers was used.

Table 4-10: Melting point and congealing provided by wax supplier

Wax	Melting point ($^{\circ}\text{C}$)	Congeaing point ($^{\circ}\text{C}$)
A	-	64-69
B	72-79	-
C	73-80	-
D	70-73	63-67
E	60-66	-

4.9 Thermal conductivity

The thermal conductivity of shell is one of the parameters that will determine how quickly the wax starts to melt and be fully removed from the ceramic mould. The conventional method to measure the thermal conductivity of shell utilizes laser flash however, the technique would not take into account the effect of steam and condensate in pores that would modify the thermal conductivity. Another way to obtain the thermal conductivity is to model the process of steam penetrating the porous shell during autoclaving to understand the heat transfer rate. This however, would be complicated and many assumptions would have to be made. Assumptions would include the tortuosity of the shell pores, the steam thermal energy penetrating shell, condensation of steam and depth of steam (or condensate) penetration. To further complicate the

situation, Cendrowicz (2004) suggested that steam in vapour phase cannot exist in the pores of a cold shell long enough to penetrate through to any meaningful thickness without condensing first. These unknown parameters have limited the characterization of the shell thermal conductivity numerically.

Therefore, to simplify the process of understanding the heat transfer rate, the thermal diffusivity of heat transfer across the shell was measured in the autoclave. Thermal diffusivity can be related to the thermal conductivity providing that the specific heat capacity and density are known. The advantage of carrying out the test in autoclave is that the high heating rate from the steam offers large temperature differences between thermocouples that were placed through the thickness of the shell. This method also allows the measurement of thermal conductivity with the existence of steam gas and condensed steam. It should be noted that the density and heat capacity were measured in commercial equipment in which no steam was present and thus some error may be introduced.

The effect of steam penetrating into pores is included in the thermal profile and by inverse calculation of the thermal conductivity using Equation 3-9. A cylindrical geometry was chosen for the test as it has the most significant heat transfer in horizontal direction (mid-section) and allowed the vertical direction to be assumed infinite, so that a one dimensional solution was applicable. The thermal profile is shown in Figure 4-30. It is important to mention there is a spike in the autoclave thermal profile when steam enters the chamber (up to 210 °C). This was because of the steam entering the autoclave chamber rapidly, overshooting the temperature reading rate.

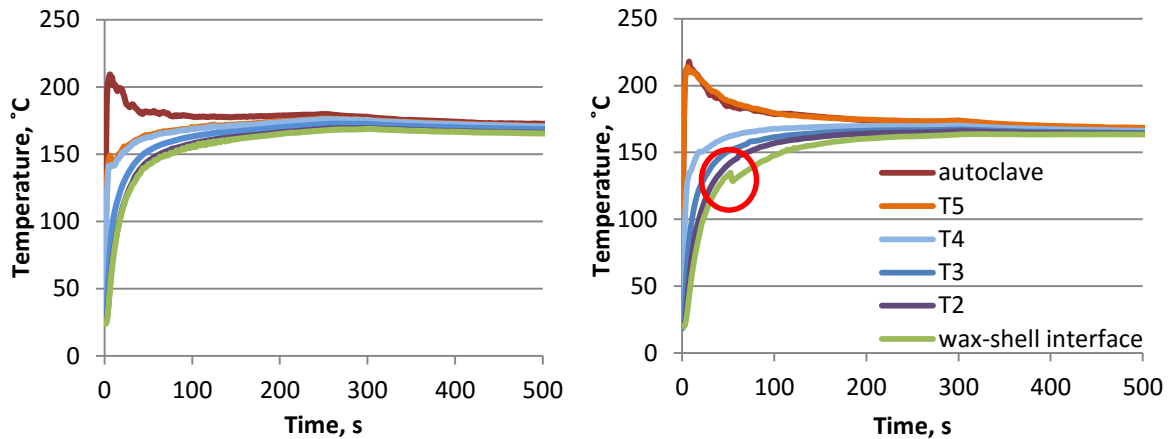


Figure 4-30: Comparison of the two thermal profile across shell obtained using same procedure

Good repeatability of thermal profile across the shell during de-waxing was difficult to obtain due to variation in porosity, thickness of the shell and the uniformity of stucco coated. Other variability includes the heat transfer coefficient reduction when vapour starts to condense on the surface of the shell. The effect of variability is evident in Figure 4-30, the T5 profile in the right hand figure does not follow the trend of the T5 profile on the left hand figure. When comparing the gradients of thermal profile in first 100 seconds, the thermal profile on left appears to be slightly steeper. Another difference was on the wax-shell interface thermal profile where there is a drop of temperature registered (indicated by the red circle in Figure 4-30). Other possible variations of profile are present such as kinks on profile where steam has penetrated the shell and contacted the thermocouple. Therefore, taking the average of thermal profile is not recommended. The thermal profile for analysis was chosen based on shells with the most 'sensible' thermal profile. For the purpose of modelling work in Part 2, thermal profile on the left was chosen to represent the thermal profile of all shell moulds during de-waxing process.

Comparison of the two thermal profiles given in Figure 4-31 where one shell is unsheathed and the other sheathed with copper foil shows that the gradient of the wax-shell interface thermal profile was lower without steam penetration into shell. Note that T5 profile however, are similar in both graphs. This indicates that the copper foil conducts heat from steam efficiently (same thermal profile trend in both graphs) and no heat loss occurred during heat transfer onto the shell surface. This suggests that steam does penetrate into the porous shell and the steam penetration contributes to give a higher heat transfer rate across the shell.

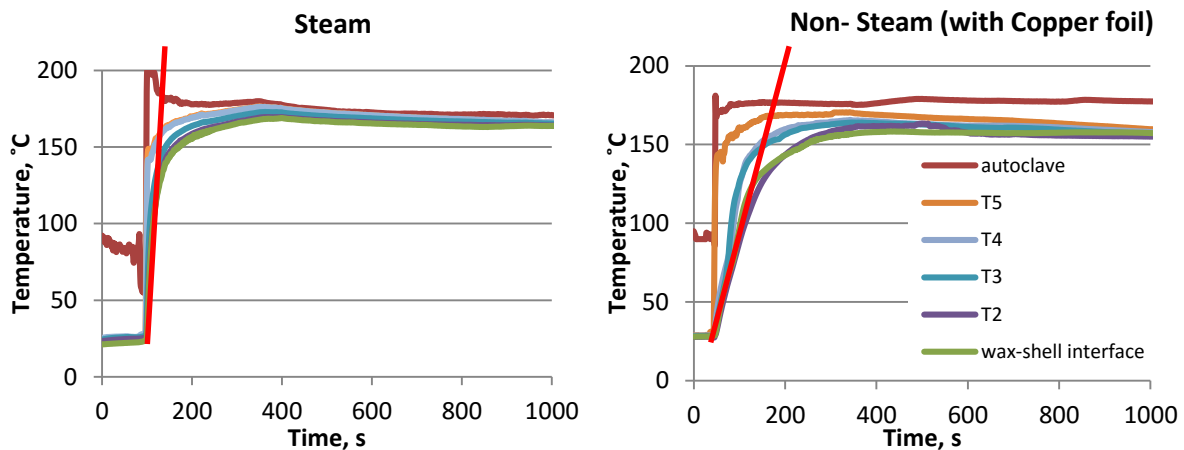


Figure 4-31: Comparison of thermal profile across the shell with and without steam penetration. Red linear line indicates the gradient of the thermal profile when steam is released into the autoclave chamber.

The thermal conductivity of shell in the autoclave is presented in Figure 4-32. The estimated thermal conductivity varies depending on the duration of the test. It was found in the first 20 s, the calculated thermal conductivity is large and reduces with time reaching a constant when the heat transfer across the shell ceases. An unsteady thermal conductivity profile was observed at approximately 90 s (highlight in yellow) during the autoclaving and this was postulated to occur when the steam penetrated the porous shell and approached the thermocouples. This unsteady behaviour could also be because

the heat transfer reached equilibrium and no thermal gradient was present to allow heat transfer to occur.

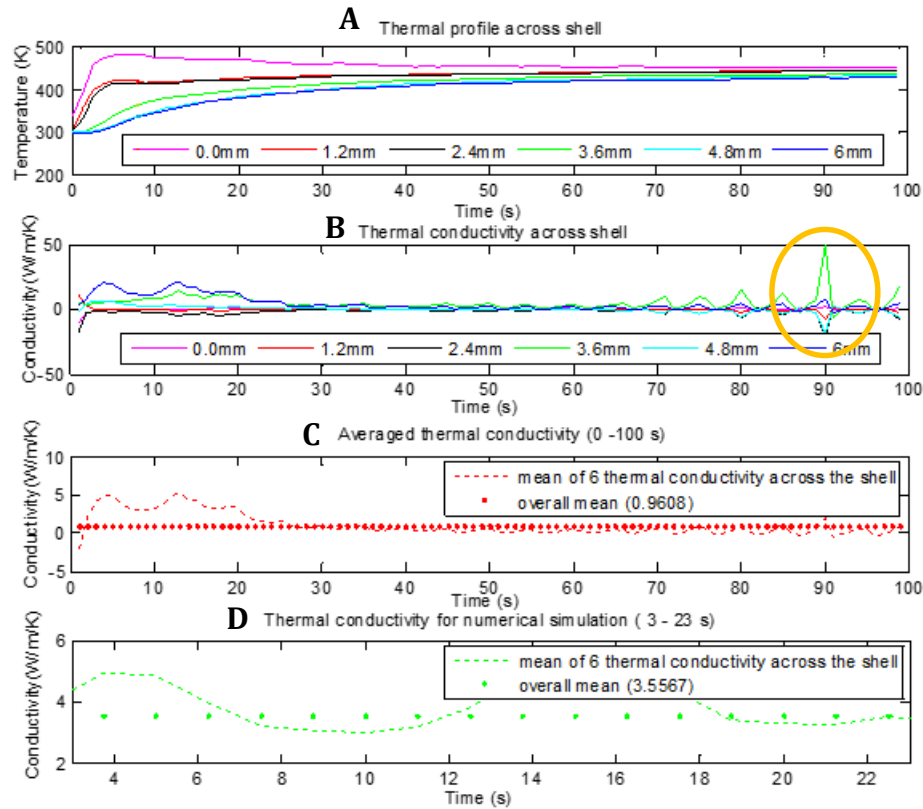


Figure 4-32: Thermal conductivity back calculated from the thermal profile using MATLAB. Graph D shows the average value taken as a constant for simulation.

Due to these uncertainties, the thermal conductivity was taken over a time range from 3 to 23 s and this gave a value of $3.56 \text{ W} \cdot \text{m}^{-1} \cdot \text{K}^{-1}$. This was selected because the thermal conductivity value includes the steam effect. Compared to literature data, this value is relatively high. Cendrowicz (2004) obtained an average thermal conductivity of $0.6 \text{ W} \cdot \text{m}^{-1} \cdot \text{K}^{-1}$ for shell to cast aluminium at atmospheric pressure with molten metal as heat source. Jones *et al.* (2003) found that the thermal conductivity of shell to cast aluminium to be approximately $0.5 \text{ W} \cdot \text{m}^{-1} \cdot \text{K}^{-1}$ when molten metal is used as heat source and $1.0 \text{ W} \cdot \text{m}^{-1} \cdot \text{K}^{-1}$ when hot water was used. This shows that the lower surface tension of hot water compared to molten alloy has allowed the water to penetrate the shell

better and thus presenting a higher thermal conductivity. Snow (1998) mentioned that shells with 25 % porosity where that porosity was filled with water had double the thermal conductivity of the dry shell. It is suggested the thermal conductivity ($3.56 \text{ W}\cdot\text{m}^{-1}\cdot\text{K}^{-1}$) in this test is reasonable since the heat source is steam pressurised at 0.8 MPa. In the computer simulation, a constant thermal conductivity was assumed with steam fully penetrating the pores. This assumption however disregarded the effect of steam penetrating into shell at different times. This allows the heat transfer coefficient in relation with time to be manipulated to take into account of the variation in heat transfer.

The thermal diffusivity of wax was measured using the same method as the shell. However, the thermal conductivity value was not taken in early stages of de-waxing because the wax is still solid and would not be representative since only one value is taken as the thermal conductivity of wax. This assumption is made even though it is known that the transformation of wax from solid to liquid phase changes the thermal conductivity. When the wax is fully melted, the heating rate is not sufficient to give a difference in temperature across the sample, causing fluctuation in the calculated thermal conductivity. Data acquired between 400 - 500 s was used for calculation to represent the thermal conductivity of wax as an average value (Figure 4-33). This range of temperatures was taken when the temperature profile measured at different location were sufficiently different to allow the calculation of thermal conductivity (between the two vertical red line in Figure 4-33).

The thermal conductivity calculated for the filled wax by this method was $0.22 \pm 0.05 \text{ W}\cdot\text{m}^{-1}\cdot\text{K}^{-1}$. This value was reasonable when compared to the literature

measured using the laser flash method. Cendrowicz (2004) found that the thermal conductivity for Hyfill B417 ranged between 0.15 and $0.18 \text{ W}\cdot\text{m}^{-1}\cdot\text{K}^{-1}$ and for A7-11 between 0.15 and $0.25 \text{ W}\cdot\text{m}^{-1}\cdot\text{K}^{-1}$ over the temperature range of 23 to 100°C . Torres (2003) measured the thermal conductivity of wax prepared in the laboratory and the results are shown in Table 4-11. He showed that the variability of thermal conductivity range does overlap and filler percentage does not significantly affect the thermal conductivity of wax. Therefore, only filled wax (Wax D) was measured in this study to represent the thermal conductivity for all five waxes.

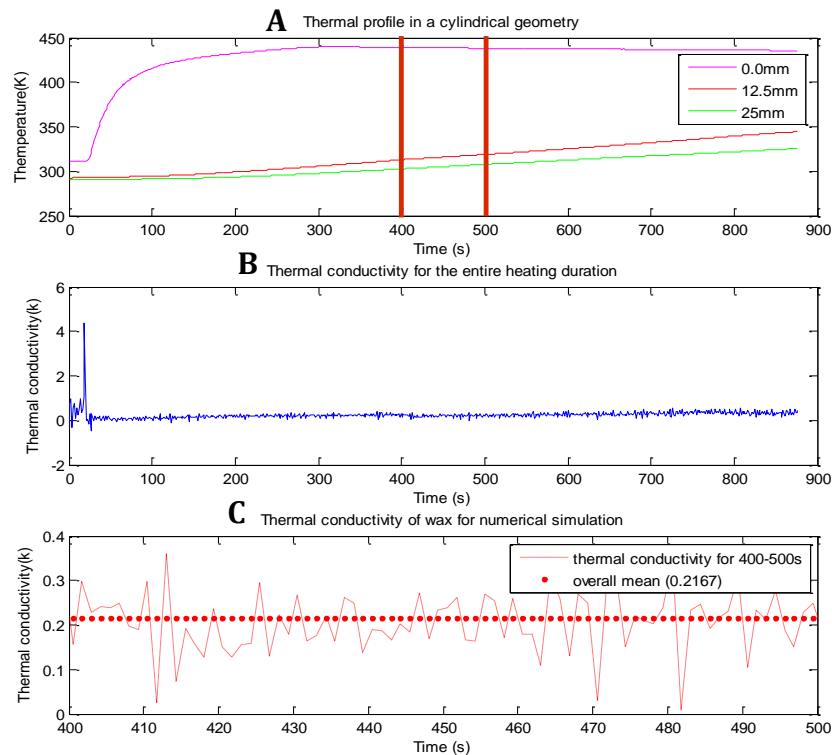


Figure 4-33: Thermal profile of wax measured in autoclave. MATLAB calculation for wax thermal conductivity for filled wax

For simulation purposes, the thermal conductivity of unfilled wax in this work was assumed to be $0.02 \text{ W}\cdot\text{m}^{-1}\cdot\text{K}^{-1}$ lower than the filled wax.

Filler percentage (%)	Thermal conductivity range ($\text{W}\cdot\text{m}^{-1}\cdot\text{K}^{-1}$)
0	0.135 - 0.185
20	0.128 - 0.234
40	0.150 - 0.233

Table 4-11: Thermal conductivity of wax blend varies with filler percentage measured with laser flash analysis (Torres, 2003)

4.10 Parallel plate rheometry

Rotational plate rheometry was used to understand the rheology of wax in the liquid state. This section will discuss in sequence the requirement of pre-shear, the presence of a yield stress, hysteresis of the up and down flow curves (thixotropy) and the repeatability of the instrument.

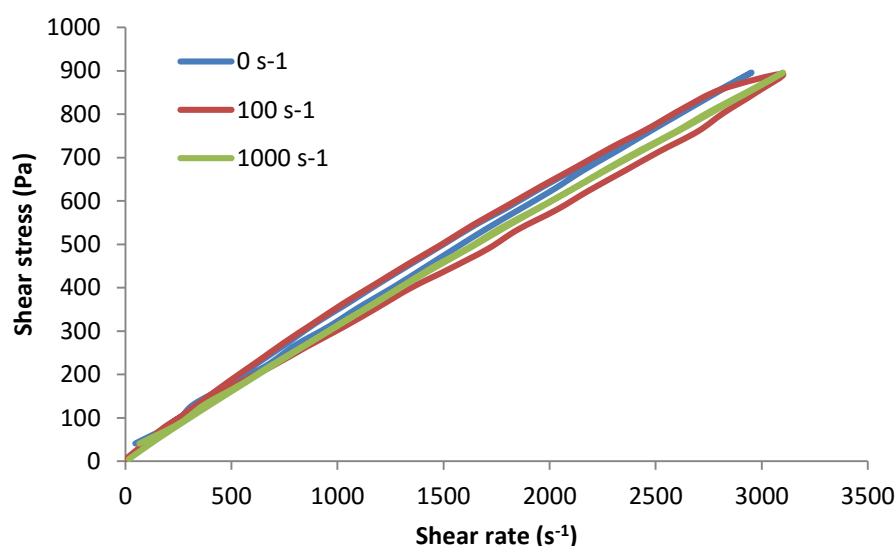


Figure 4-34: Test to determine the importance of pre-shear prior to rheological testing. Shear stress versus shear rate for Wax C is plotted.

Before carrying out the test, there was uncertainty of the need to apply pre-shear. Different pre-shear rates were applied (on Wax D as a trial) to understand the importance of applying a pre-shear before the full rheology evaluation. Researchers including Cendrowicz (2004) and Shobanjo (2010) showed pre-shearing is necessary and claim that pre-shear could eliminate trapped air and ensure a uniform distribution

of wax between the plates. However, Figure 4-34 shows that pre-shearing had no significant effect on the rheological behaviour of the wax. This was because when re-melting the wax prior to testing, the wax particles had sufficient time to rearrange regardless of how much shear was applied during the pre-shear step. Of course, if the shear stress during pre-shearing is sufficiently large to change the structure of polymers in wax, the pre-shear will be significant. Pre-shear before a rheology test was found unnecessary and was not carried out in the reported rheology tests.

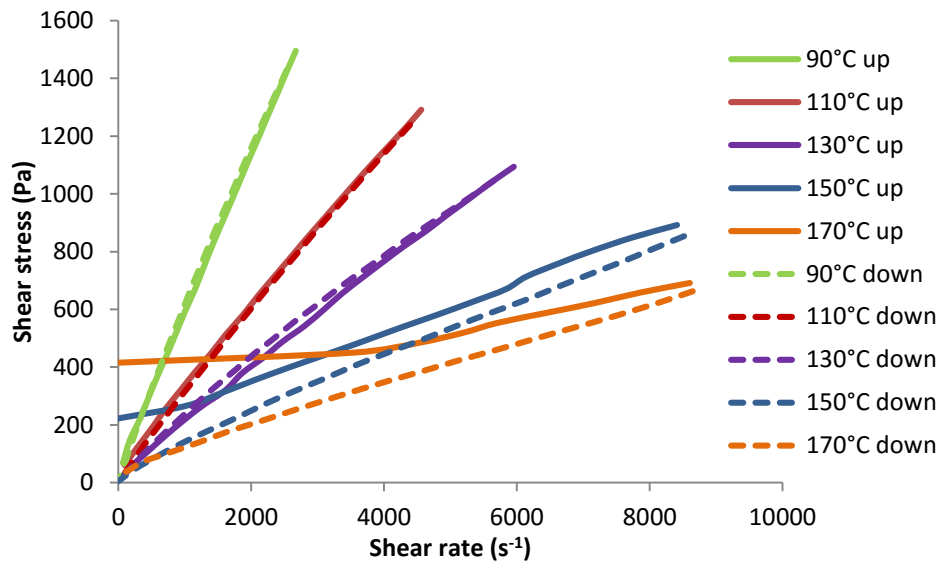


Figure 4-35: Shear stress vs. shear rates for Wax B. Results exhibit a higher yield stress as the temperature increases. The thixotropy hysteresis occurs when the temperature increases.

Figure 4-35 and Figure 4-36 shows that an apparent yield stress develops as the temperature rises in Wax B and C. This behaviour was only occasionally observed in waxes containing terephthalic acid filler (Wax B and C). The possible explanation of this behaviour is discussed later in this section. It was also observed that the hysteresis loop between the increasing shear stress curve and the decreasing shear stress curve of Wax B and C increases as temperature increases. At lower temperature, the waxes behave as a Newtonian fluid.

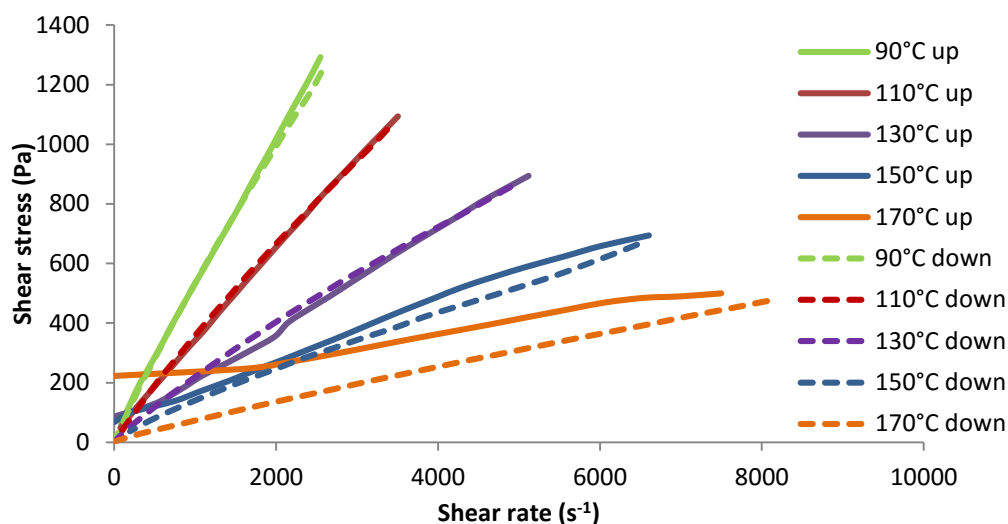


Figure 4-36: Shear stress vs. shear rates for Wax C. Results exhibit a higher yield stress as the temperature increases. The thixotropy loop occurs when the temperature increases.

Wax A and D which were only filled with cross-linkage polystyrene fillers did not show any yield stress (Figure 4-37 & Figure 4-38). It has been commercially reported that Wax D shows a greater tendency to break shells than Wax A. This tendency may be attributed to the filler geometry of Wax D but the two waxes have similar shear rheology. Another observation was that Wax A exhibits shear thickening behaviour (dilatant) as shear stress increases but apparent shear thinning behaviour on the down curve. This behaviour is opposite to what observe in Wax D. In Wax A, the effect is obvious and repeatable at all temperatures while in Wax D occasionally it is shear thinning as shear stress increases but less repeatable.

The hysteresis loop in Wax B and C was found to increase as the measurement temperature was increased (Figure 4-36) and Wax D followed the same trend. Wax A however, shows the opposite behaviour and Wax E exhibited Newtonian fluid behaviour (Figure 4-39).

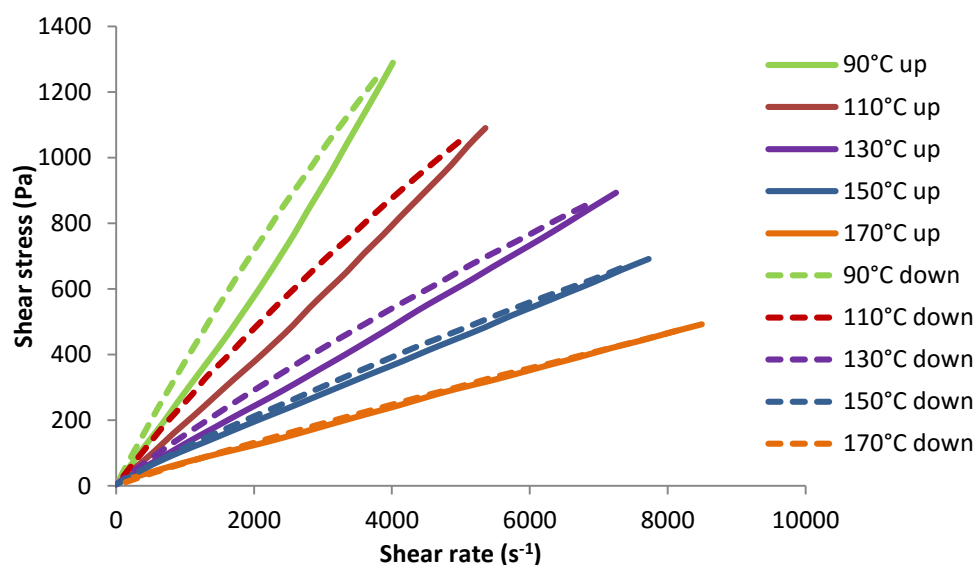


Figure 4-37: Shear stress vs. shear rates for Wax A. Results exhibited no yield stress and the repeatability of the rheological behaviour at any temperature is very high. It has a dilatant behaviour.

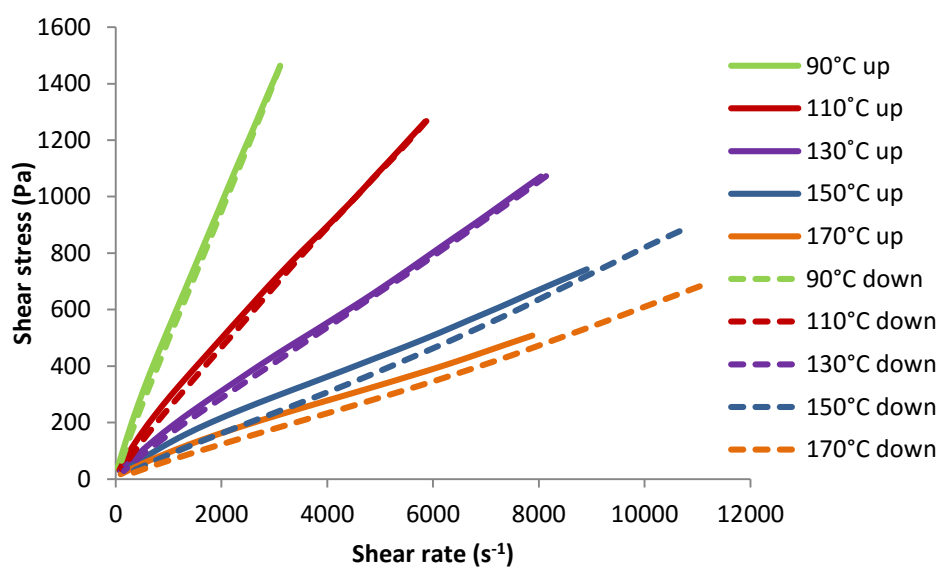


Figure 4-38: Wax D has no obvious yield stress at low shear rate. The shear thinning and shear thickening effect is less obvious in Wax D.

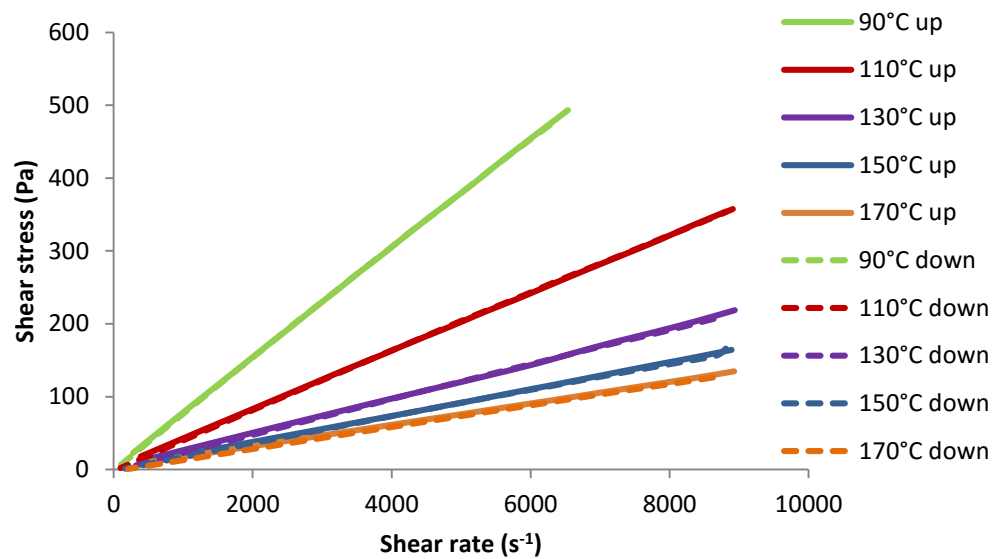


Figure 4-39: The shear stress against shear rate relationship obtained from Wax E pattern wax is very reproducible. Wax E exhibits a Newtonian fluid behaviour.

To further evaluate the yield stress behaviour the experiment was repeated three times leaving the sample in the geometry between each run. It showed that the yield stress was only observed on the first run and was therefore a transient stage. It should be noted that this stage was not due to the inertia effect since consequence repetition does not show any yield stress (Figure 4-40). The yield stress however was not seen in unfilled wax (Figure 4-41). From wax microstructure figures shown in section 4.1, terephthalic filler has a wider size distribution compared to cross linked polystyrene. The finer particles of terephthalic fillers could contribute to the restriction of flow. Finer particle size, which would increase the rate of collisions cause greater internal resistance to flow (Fielder, 1999). At higher shear stresses, particles size makes little difference to the rheology (Torres, 2003). This could affect the variability of yield stress observed. Torres (2003) also found that non spherical particles in shear flow may increase the frequency of the contact and trap layers of liquid on to their surfaces. Irregular-shaped solids may also interlock and scrape harshly causing high energy loss

(Pal, et al., 1992). Other researchers have also observed the yield stress behaviour. Gebelin *et al.* (2004) observed the yield stress in the first measurements made and not in the cyclic test.

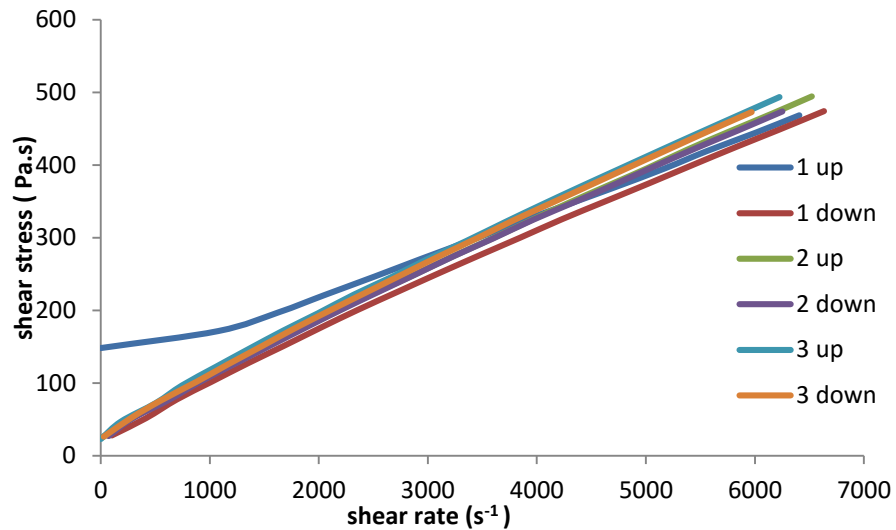


Figure 4-40: Shear stress vs. shear rate relationship for Wax C at 170°C. The first up curve exhibiting yield stress behaviour and all subsequent steps on same sample do not exhibit a strong yield

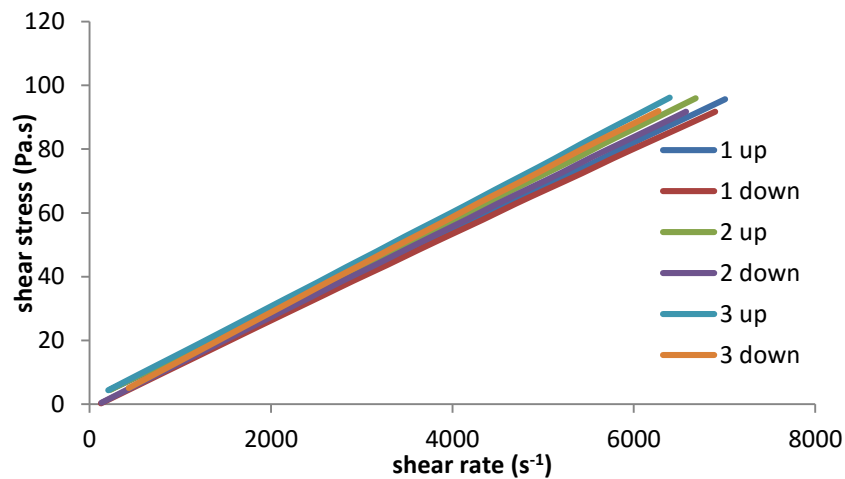


Figure 4-41: Shear stress vs. shear rate relationship for Wax E at 170°C and no yield stress behaviour is observed

The value of the yield stress produced depends very much on the fillers thermal expansion, location on the plate, the uniformity of fillers on the plate, phase separation, deterioration, oxidation or even fillers interlocking (Gebelin, et al., 2004). They suggest that the yield stress effect is only a transient phenomenon occurring when the wax starts to flow between the two plates. With all the supporting findings and at high temperature, the intensity of particles interlocking increases further as the collision of particles increased along with temperature. This could explain why the yield stress was only observed when the temperature was increase up to 150 °C or 170 °C. As soon as the shear stress exceeds a certain limit (yield stress), the interaction of particles is overcome and the flow commences reaching a value of viscosity in line with the materials behaviour in the subsequent repeat runs. The current postulation that the yield stress is caused by the fillers in wax, however there is a possibility that the structure of filler is broken destroying the network structure.

Gebelin *et al.* (2004) suggested that the yield stress might be the results of filler expansion as temperature increased. Figure 4-42 shows that the inconsistent yield stress can be caused by the thermal expansion of fillers which exerts normal stresses in the system restricting the rotation of the top plate. The presents of terephthalic acid fillers in Wax B and C were believed to be the main cause of the inconsistent 'yield stress' results. This could be the result of the angular-shaped filler or the fillers having high thermal expansion. This finding shows that in addition to the possibility of interlocking particle, the yield stress can also be relate to the normal stresses due to expansion of fillers (Figure 4-42).

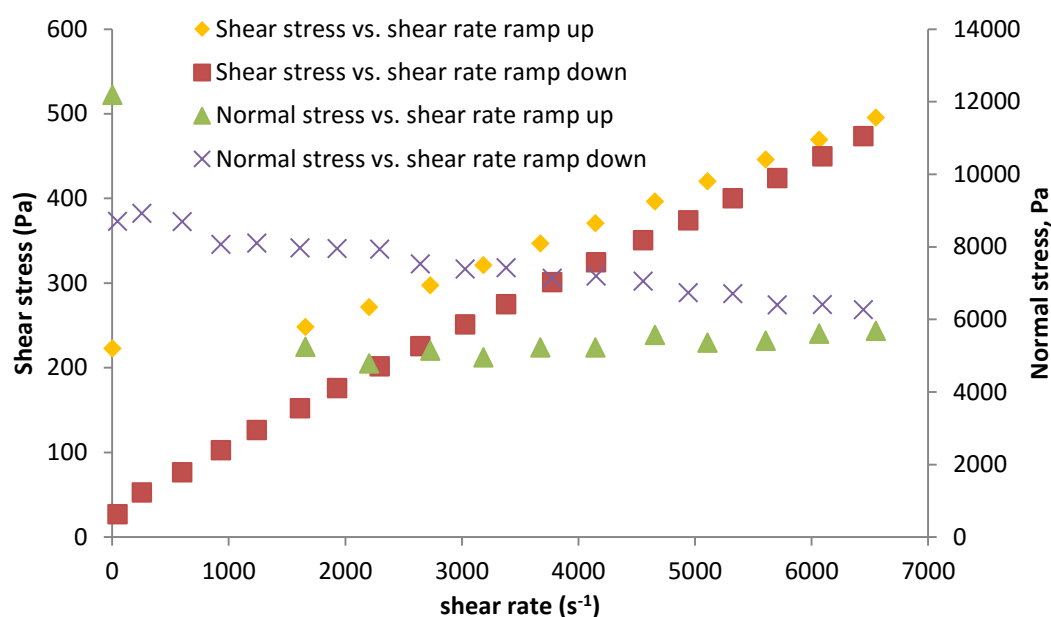


Figure 4-42: Example of relationship between yield stress and normal stress. Results shows that the two parameter have a close relationship measured at 170°C on wax C.

The normal stress on the wax was observed to drop rapidly in the up curve and then remain constant with shear rate; in the down ramp, the normal stress continue to increase again. The increasing of normal stress is possibly due to the increasing expansion of filler with heat from the hot plate. However, the value did not return to the initial normal stress value. The possible explanation was that the filler particles could have been swept to the side of the plate or even sheared to finer fragments in the first run and therefore no yield stress is observed in the subsequent up curve runs or in the down ramp cycles. The cause of the 'yield stress' remains an item for discussion, however, it is certain that it is a transient phenomenon.

The repeatability of results was investigated on Wax A, C and E and results analysis was focussed at a low shear rate (10 s^{-1}). All three waxes showed that as shear stress increased the standard deviation of viscosity decreased (see Appendix B for repeatability results). Wax E has the lowest standard deviation of viscosity among the

three waxes compared. For Wax A, the standard deviation of the viscosity was 0.18 Pa·s and 0.69 Pa·s at 90 °C and 170 °C respectively (shear rate 10 s⁻¹). When the test was undertaken on Wax C at 90 °C, the standard deviation of the viscosity was 2.96 Pa·s and 2.77 Pa·s at 170 °C. It shows that the repeatability of viscosity measurement for Wax C was approximately four times lower than Wax A. This was attributed to the low repeatability of the yield stress behaviour of Wax C. The repeatability analysis was also undertaken for the normal stress analysis. For Wax A, the standard deviation of the normal stress was 1363 Pa and 1673 Pa at 90 °C and 170 °C respectively at 10 s⁻¹. For Wax C at 90 °C, the standard deviation of the normal stress was 2340 Pa and at 170 °C was 4152 Pa. The normal stress of Wax E was found to have similar standard deviation to Wax A. It shows that the repeatability of measurements for Wax C is approximately two times lower than Wax A. In the test, it was found that there is a correlation between standard deviation of normal stress and the standard deviation of viscosity.

In terms of modelling the rheological data, yield stress will not be taken into account as it is only a transient phase and the down curve is suggested to be used to model the behaviour of wax. The experimental data was fitted to a generic “Carreau” model and the curve fitting parameters were to be used in the simulation of the de-waxing process. The fitted parameters are presented in section 5.1.2.

4.11 Capillary rheometry

Capillary rheometry allows the measurement of wax viscosity in the semi-solid state. The results for viscosity of all waxes were presented in Figure 4-43 - Figure 4-47.

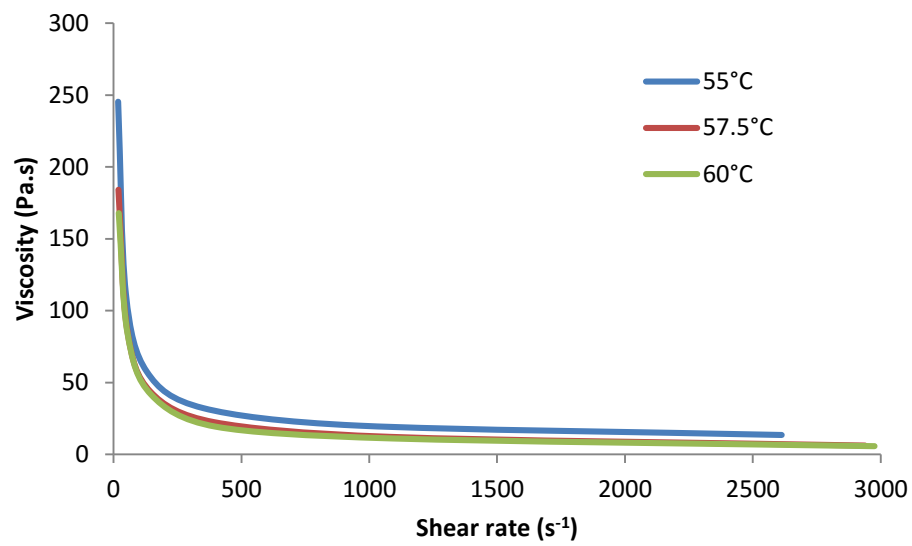


Figure 4-43: Viscosity and shear rate relationship at 55°C, 57.5°C and 60°C for Wax A

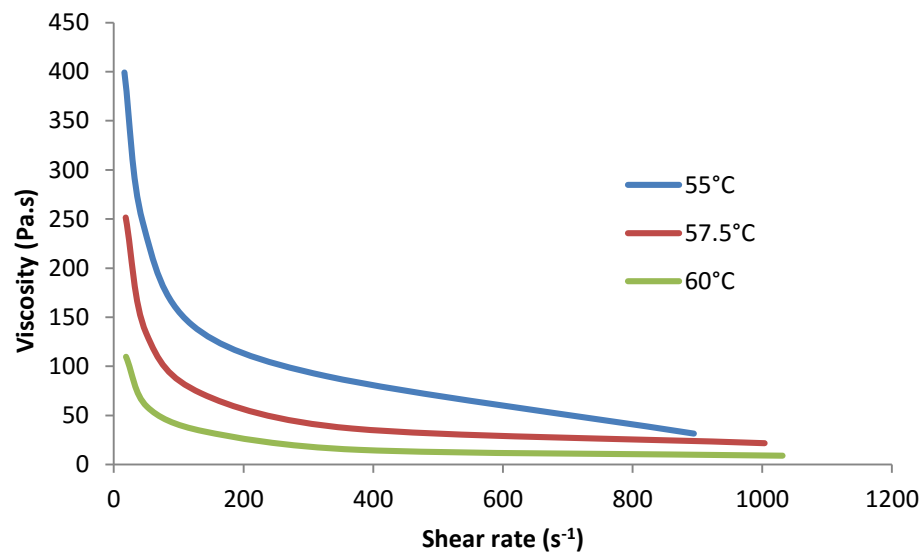


Figure 4-44: Viscosity and shear rate relationship at 55°C, 57.5°C and 60°C for Wax B

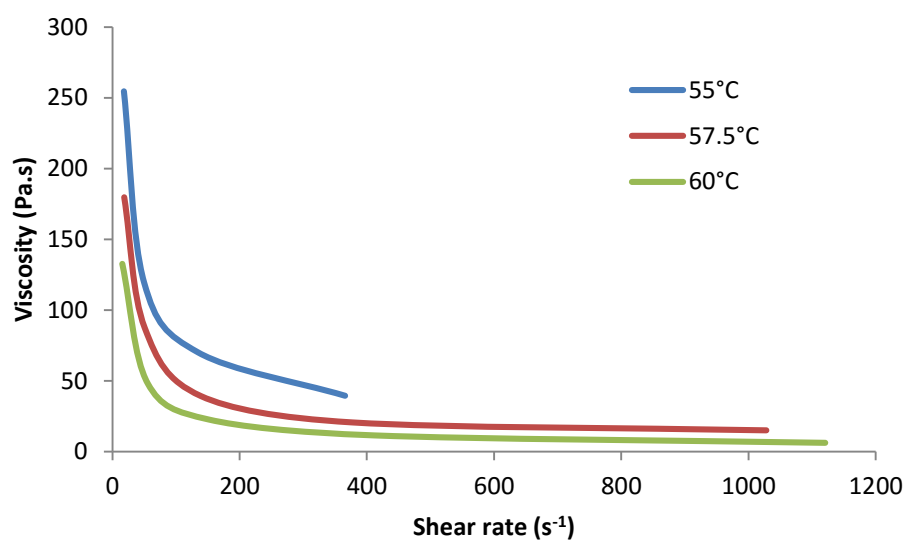


Figure 4-45: Viscosity and shear rate relationship at 55°C, 57.5°C and 60°C for Wax C

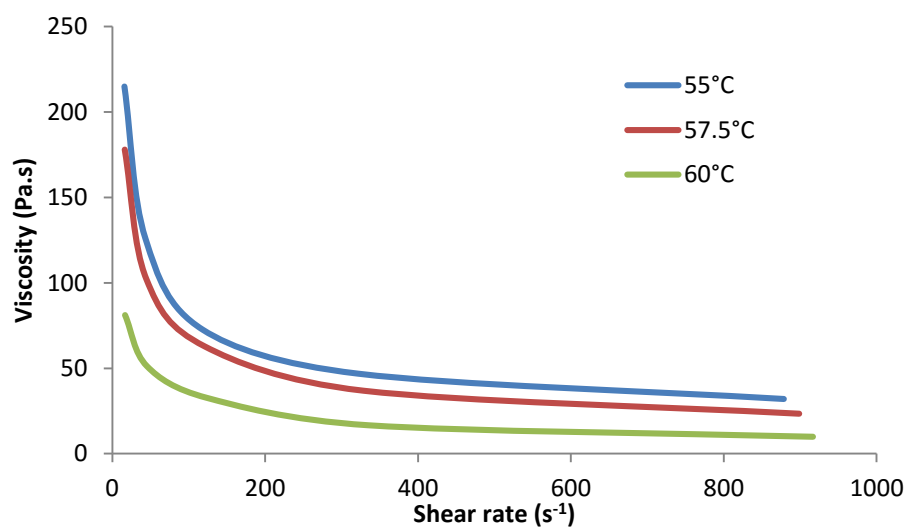


Figure 4-46: Viscosity and shear rate relationship at 55°C, 57.5°C and 60°C for Wax D

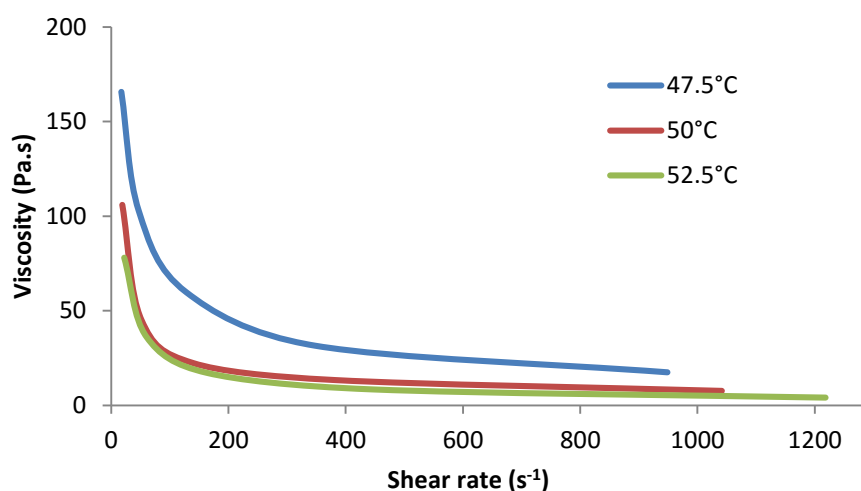


Figure 4-47: Viscosity and shear rate relationship at 47.5°C, 50°C and 52.5°C for Wax E

As expected viscosity of all the waxes decreases with increasing temperature. Given the melting temperatures reported in section 4.8 the range of temperature was limited to just below the stated melting points. Under these conditions viscosity is both higher than above the melting point and increases more rapidly with each degree of cooling. Figure 4-48 shows the viscosity changes at $15\ s^{-1}$. It is clear the unfilled wax has a lower viscosity below its melting point ($60\text{--}66\ ^\circ\text{C}$) than the filled waxes. Of the filled waxes, the slopes of the curve varies between waxes. Wax A has the lowest rate of viscosity increase with temperature fall over the range studied probably because it has the lowest melting point and the widest filler particle size distribution. The greatest viscosity change with temperature is seen with Wax B.

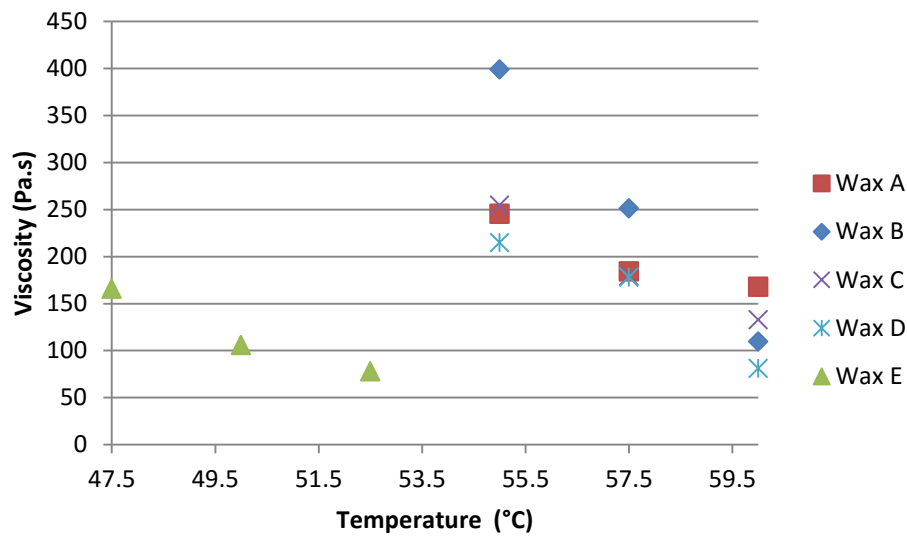


Figure 4-48: Viscosity change with temperature increases has good relation with solid loadings at 15 s^{-1} shear rate.

For comparison, the rheological data of Wax B from capillary rheometer was combined with the data obtained from rotational rheometer (Figure 4-49). It shows that the values obtained from capillary rheometry decrease significantly only with minor change in temperature compared to data from rotational parallel plate. The right hand image shows that below the average melting temperature, there was a rapid rise in viscosity as crystallisation increased. For simulation the de-waxing process, it is suggested to use rheological data obtained with rotational rheometer only. This was because wax data from capillary rheometry will increase the overall viscosity returned in the Carreau fit which will then bias the result of the simulation. The assumption of neglecting the capillary rheology is reasonable since the only external force exerted on wax during de-waxing would be gravitational and therefore the flow of wax is less likely to occur at low shear rates and low temperatures.

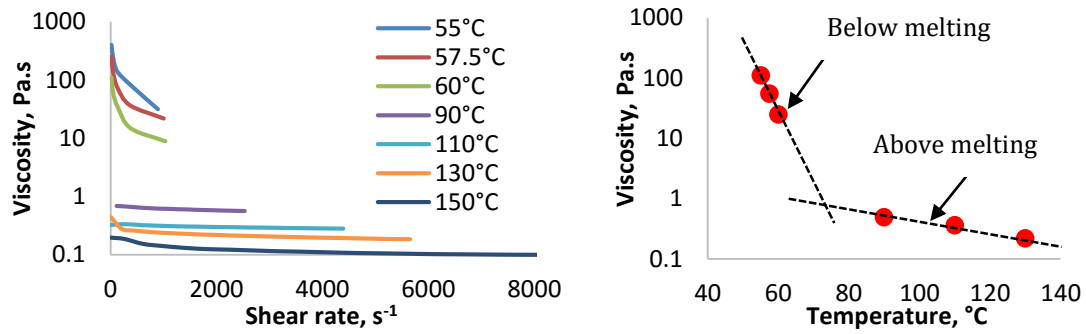


Figure 4-49: Combination of rheology data of Wax B from rotational rheometry and capillary rheometry after converting strain rate to shear rate (left). Viscosity plotted against temperature at constant 200 s⁻¹ shear rate.

The relationship of viscosity as a function of shear rate and temperature for the five waxes can be modelled using the “Carreau” model (Equation 2-8). The viscous heating in Wax C which has the maximum pressure difference, ΔP (1.76 MPa with 16 L/D capillary) are calculated using Equation 3-18 and shown to be low, approximately 0.35 °C. It was assumed to be negligible and not taken into account. The effect of viscous heating on the temperature rise of wax is low and the reason for this is because the capillary test was carried out at a relatively high temperature and therefore the pressure difference is not large enough to have any noticeable viscous heating effect.

4.12 Surface tension/Adhesion tension of wax

Wax permeating into shell and wax flowing out of the mould are two critical properties required in order to understand the shell cracking issue. Wax surface tension or the adhesion tension between wax and mould is required to predict the penetration of wax into the shell and the rate of wax flowing out of the mould. However, it is not understood if the surface interaction between the ceramic mould and wax is significant. Conventionally, surface tension of wax is measured by the Du-Nuoy ring method but this

does not account for any difference between the surface energy of the ceramic and the platinum of the ring.

With Du-Nuoy ring test, it would not represent the interaction between wax and ceramic. Adhesion tension is suggested as a complimentary measure to the Du-Nuoy ring because other solids may have surface energies significantly different to platinum. If the Du-Nuoy ring method is used then the contact angle of the wax and ceramic would have to be measured separately and at elevated temperatures this becomes an issue due to light diffraction and reflection and therefore errors can be significant.

For each wax material evaluated there was a linear fall of adhesion tension with temperature. The force measured represents the adsorption of liquid to the surface of the ceramic. The higher the adsorption energy, the higher the adhesion force and the smaller the contact angle will be. The adhesion tension force of Wax A for example reduced with temperature at a rate of $5.8 \times 10^{-8} \text{ N}\cdot\text{mm}^{-1}\cdot^{\circ}\text{C}^{-1}$. The linear relationship allows the data to be extrapolated to the temperature that is representative of the condition in autoclave, and this is approximately 180 °C. The limitation of the equipment prevented the oven reaching 180 °C. By extrapolation to 180 °C, the adhesion tension force of the filled waxes dropped to approximately $2.3 \times 10^{-5} \text{ N}\cdot\text{mm}^{-1}$.

A linear relationship was found between the adhesion tension force between ceramic and wax with respect to temperature. The adhesion tension force reduced with increase of temperature in a manner similar to most materials (Torres, 2003; Vargaftik, Volkov & Voljak, 1983). The slope for unfilled wax was approximately half that of a filled wax (Figure 4-50). The adhesion tension of filled wax was greater and fell more rapidly with temperature compared to the unfilled wax. It was observed that the adhesion tension for

filled wax at 170 °C was similar to the unfilled wax at 90 °C. In the filled waxes it appears that in the top 1 mm of the wax sample there is a progressive loss of particulate material until 180 °C when the filled and unfilled waxes have similar adhesion tension values. This could be explained if the filled wax exhibit flocculation and/or sedimentation.

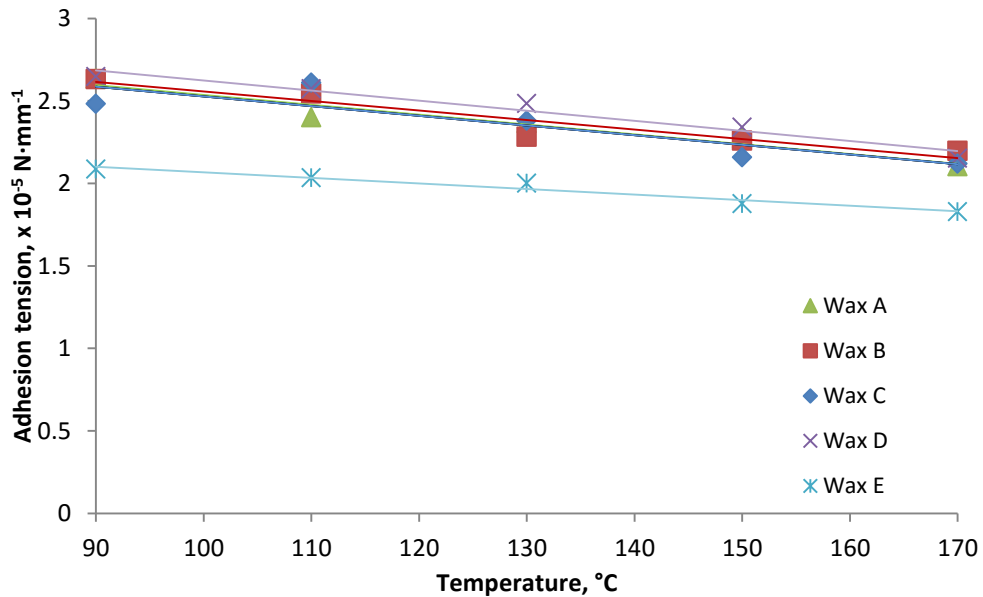


Figure 4-50: The adhesion tension force of molten wax is averaged and plotted

The sedimentation rate would increase with temperature because the viscosity of the based wax would reduce. This is in accordance with Stokes's law which shows that the frictional force between the fluid and particle is proportional to the dynamic viscosity of the fluid. This is also supported by Torres (2003) work, where he observed sedimentation in filled pattern waxes while undertaking rheological studies at elevated temperatures. Furthermore, increased Brownian motion with temperature and greater collision intensity may lead to greater filler flocculation and an increase in sedimentation velocity according to Stokes's law. Barnes *et al.* (2005) stated that flocculation is strongly size-dependent; it is only influential when the particle size is below 1 μm . Even if it is only smaller particles which flocculate by this mechanism,

sedimentation may well account for the more rapid fall in surface tension with temperature which is observed in the filled waxes compared to the unfilled. The reduction in adhesion tension of the unfilled wax with temperature was mainly controlled by the entropy of the system as no sedimentation was occurring. Thus, the tension force reduces to a lesser extent than in the filled wax as temperature increases.

The average pores diameter of the shell system fired under the conditions used in casting was 131.2 nm measured using the mercury porosimetry and porosity on the inner surface of shell (prime coat) is known to be smaller than the average porosity and the structure can therefore act as a filter. Figure 4-51 shows wax fillers that were 'filtered' onto the inner surface of the mould. Thus, it would be more representative to measure the tension force of the waxes when the particles are sedimented from the carrying wax.

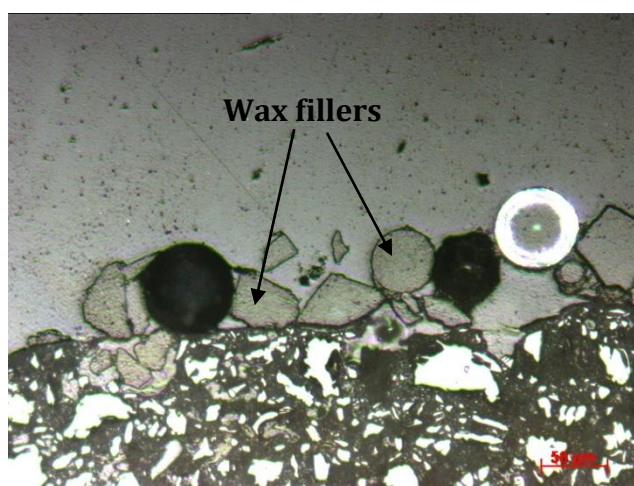


Figure 4-51: Morphology of wax on inner surface of shell after de-waxing process with fillers particles remains on the surface

To compare the adhesion tension to the surface tension, the contact angle has to be measured or assume to be zero. For Wilhelmy method, the system is most likely to have zero contact angles if there is no contact angle hysteresis between the advancing and

receding curves. Sauer & Nicholas (1991) suggest that hysteresis is only observed when the contact angle is greater than zero. This also means that if hysteresis is not observed, contact angle can reasonably be assumed to be zero. Figure 3-30 representing Wax A shows a slight contact angle hysteresis which is sufficiently small to be considered negligible. The slight hysteresis could be due to sample surface preparation error or even surface contamination. This was observed for all the tested waxes. Surface tension obtained by assuming the contact angle to be zero provide very similar results compared to the surface tension measured using Du-Nuoy ring method. This shows that the surface energy of a ceramic was similar to platinum. It was suggested that zero contact angle between wax and primary slurry ceramic is a reasonable assumption to be made. Torres (2003) showed that the surface tension of wax decreases with increased temperature and generally there was an increase in surface tension with filler addition. Torres (2003) obtained surface tension values between $2 - 3 \times 10^{-5} \text{ N}\cdot\text{mm}^{-1}$ using the Du-Nuoy Ring method with varying fillers and wax compositions.

Figure 4-52 shows that there is a small difference in the surface tension value measured using the ring method and those reported by assuming the contact angle to be zero for the results obtained from Wilhelmy method. This difference could be coming from the correction factor value used for ring method. The error could occur because the density of wax is assumed to be $1000 \text{ kg}\cdot\text{m}^{-3}$ and not to change with temperature. Another possible reason could be that the contact angle is not actually zero. The slight hysteresis in Figure 3-30 supports this hypothesis. The difference could also be caused by the material preparation where the surface which was not completely smooth and contained pores despite the sintering and polishing process. However, the two experimental comparisons between Wilhelmy method and Du-Nuoy ring method of Wax

A showed that the interaction between the wax and ceramic is not significant. The contact angle of wax with ceramics is insignificant. For practical experimental work it is suggested Du-Nuoy ring is a simpler method. The corrected and uncorrected adhesion tension forces are similar as shown in Figure 4-52. Both lines have the same gradient but a slightly different intercept. This also shows that correction factors applied when using the Wilhelmy method are not significant in the case of molten waxes. It is suggested that the application of correction factors is unnecessary if Wilhelmy method is used.

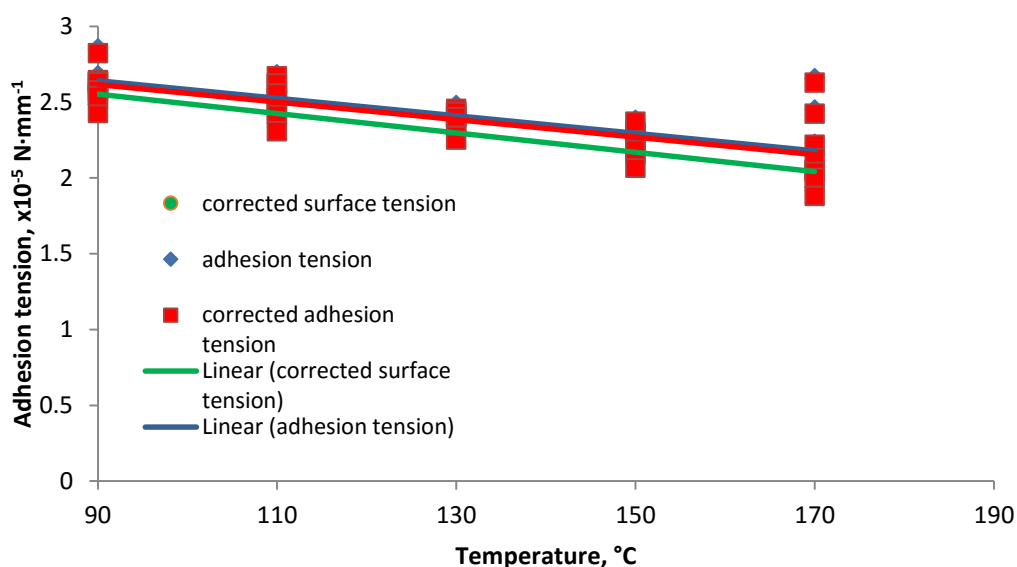


Figure 4-52: The surface tension force of molten wax is averaged and plotted for wax A

The main assumption made in this study is that the hydroxyl group on the surface of the sample has not changed during the sintering process at 1650 °C. The material surface is in fact changed when the organic compounds and hydroxyl group are burnt off. A test to compare the effect of organic compounds and hydroxyl group on sample surface is however not trivial as the un-sintered sample would absorb the wax into the pores and result in a non-repeatable data. It is suggested that a larger number of test would be required to acquire a sufficiently reliable result if porous samples were used.

Part 2 – Modelling

This part consists of two chapters – Chapters 5 and 6. Chapter 5 discussed the modelling work to simulate the de-waxing process and Chapter 6 discusses the experimental work to validate the model. The main criteria to consider for stress prediction on mould is the pressure exerted on the internal surface of the shell due to thermal expansion of the wax and flow of wax during the de-wax cycle. The simulation does not take into account of the wax permeation into shell and this parameter was address in terms of compressibility. This is discussed in the sensitivity analysis section.

5. COMPUTER SIMULATION

There are few commercial packages available that potentially allow the simulation of the de-waxing process to be carried out even though all packages have certain limitations that prevents the entire de-waxing mechanism to be modelled simultaneously. ANSYS® Fluent software for example was found to be suitable to simulate the heat transfer of steam and heat across the shell to melt the wax. ANSYS® Fluent is required to interact with ANSYS® Structural to allow the simulation of a coupled condition between fluid (wax) and the solid structure surrounding it (mould). ANSYS® Structural was not available when this work was undertaken. The fluid flow domain can be simulated and results generated be exported to packages such as ABAQUS® to observe the mechanical analysis in a structural domain. However, this would prevent the continuous interaction between the fluid and solid. PROCAST®, MAGMASOFT® and FLOW-3D® are a few commercial packages commonly available to model the investment casting process especially during metal casting and wax injection stages. These packages have built in codes to closely evaluate the interaction between the fluid and structure containing the fluid. However, PROCAST® is specially developed to only allow fluid flow into a cavity for example during metal pouring into a ceramic mould or wax injection into an aluminium mould. Simulation of drainage is not well catered for and this is believed to be because the market for developing a de-waxing package is relatively small compared to metal casting. MAGMASOFT® is not available in PRISM2 (Partnership for Research in Simulation of Manufacturing and Materials) for simulation trials and the package capability was uncertain. Therefore, in this project, FLOW-3D® was chosen to simulate the de-waxing process. Flow-3D® has the capability to solve the coupled solid dynamics

and fluid flow equations simultaneously which is better known as the fluid structure interactions (FSI) model. FLOW-3D® has its limitation when modelling the de-waxing process as it does not allow FSI model to simulate the porous mould and methods to understand this issue will be discussed.

5.1 Theoretical basis of the model

Simulating the full process of de-waxing taking into account of every active mechanism is not possible in FLOW-3D® but neither could any other packages available at the start of this work have done so. Condensation of steam gas to liquid, while simultaneously interacting with molten wax requires analysis of three fluids, which is more than FLOW-3D's capability. FLOW-3D® was only developed to model two fluids concurrently; however, it was thought to be unnecessary to model the condensation of steam gas to liquid. This is because the effect of steam flow through the shell was taken into account in the thermal profile of shell. The effect of steam directly on wax can also be manipulated from the steam-wax heat transfer coefficient. Furthermore, modelling the steam flow in FLOW-3D using the full Navier-Stokes equations would be much more computationally intensive considering the steam component to be a constant supply of thermal energy to the surface of the wax. Therefore, the physical mechanism of steam condensation was neglected in the model. The de-waxing process was thus simulated with a one fluid model where molten wax was the only fluid.

Generally, a numerical model starts with computational meshing where physical spaces are discretised. Discretisation is a process of dividing the physical space (in this case the wax fluid and mould) into a number of small volumes (or cells) and connected with nodes. In FLOW-3D®, the finite difference method (FDM) is used for the fluid flow

calculations. For solid components, the finite element method (FEM) is used for the solid mechanics analysis. The fluid and solid calculations then interact through the boundary conditions that are applied along the interface of the fluid and the solid. The basics of the meshing are well describe in most CFD and mechanical analysis simulation textbooks for example Anderson (1995) and Zienkiewicz (2005) and will not be discuss further here. The important detail to understand is how FLOW-3D interprets the physical mechanism and convert it into a numerical solution.

When the wax is in its solid form, the solid fraction is denoted as " f_s " and takes the value 1 and as soon as the wax melts from steam interaction, $f_s=0$. When more heat is introduced, the wax starts to flow and break off from the bulk wax creating 'free surfaces'. At this moment, the wax parameters such as density, pressure and velocity experience discontinuity. To address this condition, FLOW-3D® employs the Volume of Fluid (VOF) method where the initial wax volume occupied by steam is replaced with empty space. The finite difference method was used to discretise the VOF equations, which describe the location of wax. The VOF function represents the volume of fluid per unit volume and satisfies Equation 5-1. The fluid fraction ranges between zero ($f=0$) and one ($f=1$), with 1 identifying cells completely filled with a wax fluid. Regions with $f=0$ represents a region of uniform properties (for example - pressure, temperature, compressibility) with a density that is much less than the density associated with $f=1$. This region of uniform properties represented a void or steam in this project. Therefore, FLOW-3D® handled the one fluid model for the de-waxing process with three options:

1. $f=1, f_s=1$: Solid wax
2. $f=1, f_s=0$: Liquid wax
3. $f=0$: Steam gas or void

$$\frac{\partial F}{\partial t} + \frac{1}{V_F} \left[\frac{\partial}{\partial x} (FA_x u) + R \frac{\partial}{\partial y} (FA_y v) + \frac{\partial}{\partial z} (FA_z w) + \xi \frac{FA_x u}{x} \right] = F_{DIF} + F_{SOR} \quad \text{Equation 5-1}$$

where u , v , w are the velocity components in the x , y and z direction respectively. A_x , A_y and A_z are the area fractions for flow in the x , y and z direction respectively. F is volume fraction, F_{DIF} is the time rate of change of the volume fraction of fluid (wax) associated with turbulent diffusion and F_{SOR} is the time rate of change of the volume fraction of fluid associated with the mass source. In this study where Cartesian coordinates is used, ξ is zero.

The solution to a model begins with a set of governing equations. In this project for example, the equations involved are conservation of mass, momentum (Navier-Stokes), and energy in the fluid; the VOF equation (essentially an equation to identify the fluid locations); conservation of energy in the solid, the stress equation for the solid (for the FSI model); and other parameters such as the surface tension model and the bubble model which is introduce in the succeeding subsections. Each governing equation is then discretized according to a certain applied method for example the finite difference method or the finite element method. In the simplest case (finite difference method), all derivatives in the governing equation were replaced with finite difference approximations based on the cell size and time step size. This gives an equation for each computational cell (or element) that depends on each of the neighbouring cells and the solution at the previous time step. The final result of this approach is a system of equations (for example, total = one equation per cell * the number of cells) for each governing equation.

Finally, the system of discretised equations for each governing equations according to the specified initial and boundary conditions are solved. Note that some of these equations may interact with each other through the boundary conditions (for example, the conservation of energy for the fluid depends on the conservation of energy in the solid). On occasions where an explicit method of solution was chosen, the component was updated with a numerical solution found during the previous time step. This method has the advantage of simplicity and rapid computation during each step. However, occasionally, the numerical stability limit can be very small and an implicit method can be selected to eliminate the time-step limit. The disadvantage of such implicit methods is that computation time is much greater and it can dampen out oscillations that may physically occur.

In this project, simulating the wax flowing during de-waxing process had used eight different physical models coded in the package. These models are combined with the Fluid structure interaction (FSI) model to allow the mechanical analysis of the shell. The function of these models is discussed in the following sub-sections.

5.1.1 Heat transfer

A full energy equation was used to solve the heat transfer from steam to mould and then to the wax. Energy was assumed to be a linear function of temperature. Latent heat was removed/added linearly with temperature between solidus and liquidus temperatures. In this section, the heat transfer from steam to mould is discussed first, followed by the mould to wax heat transfer.

Heat transfer coefficient (HTC) and thermal conductivity are the two main parameters involved in transferring the heat across the shell to the wax. In reality, thermal conductivity of shell or wax varies with the presence of steam. However, in this project, the thermal conductivity of shell and the boundary condition temperature (temperature on the shell-autoclave surface) was set to be constant. To take into account of the high heating rate of steam, especially in the initial stage of de-waxing, the HTC of shell-autoclave as a function of time was manipulated. This was reasonable since if the volume of condensed fluid on the surface increased, an uneven water-film on the surface will form, thus changing the thermal profile and would require the adjustment of heat transfer coefficient. The assumption made is that the latent heat energy from the steam condensation has contributed to the rise of shell temperature. The manipulation of HTC is required to take into account the energy transferred across the mould surface. The heat transfer coefficient as a function of time in the model was manipulated to obtain similar thermal profile to that found in the experimental work (Figure 5-1). The heat transfer coefficient for the model in the autoclave and shell was obtained by trial and error with values from the literature as guidance. Coulson & Richardson (1993) suggest that the heat transfer coefficient of film-wise condensation is relatively large, between 10000 and 28000 $\text{W}\cdot\text{m}^{-2}\cdot\text{K}^{-1}$. However, Brown (1988) suggests that if the heat transfer coefficient is larger than 6000 $\text{W}\cdot\text{m}^{-2}\cdot\text{K}^{-1}$, it can be considered as infinite and is comparable to the thermal conductivity of the neighbouring solid. The autoclave-shell HTC was not specifically measured because the temperature gradient across the condensation film was expected to be not repeatable as the shell surface is not constant mould to mould. It was found that 7000 $\text{W}\cdot\text{m}^{-2}\cdot\text{K}^{-1}$ for first 10 seconds and 1000 $\text{W}\cdot\text{m}^{-2}\cdot\text{K}^{-1}$ for the rest of simulation best fitted the thermal profile of the

experimental data. Figure 5-1 shows the experimental and simulated profile. Temperature simulation profile remained constant above 300 s whereas the thermal profile in experimental work started to decrease after 300 s. This is however not a concern in the model since mould cracking or even full de-waxing of the mould is expected to occur in less than 300 s. The autoclave-wax HTC was assumed to be $7000 \text{ W}\cdot\text{m}^{-2}\cdot\text{K}^{-1}$ throughout the de-waxing cycle.

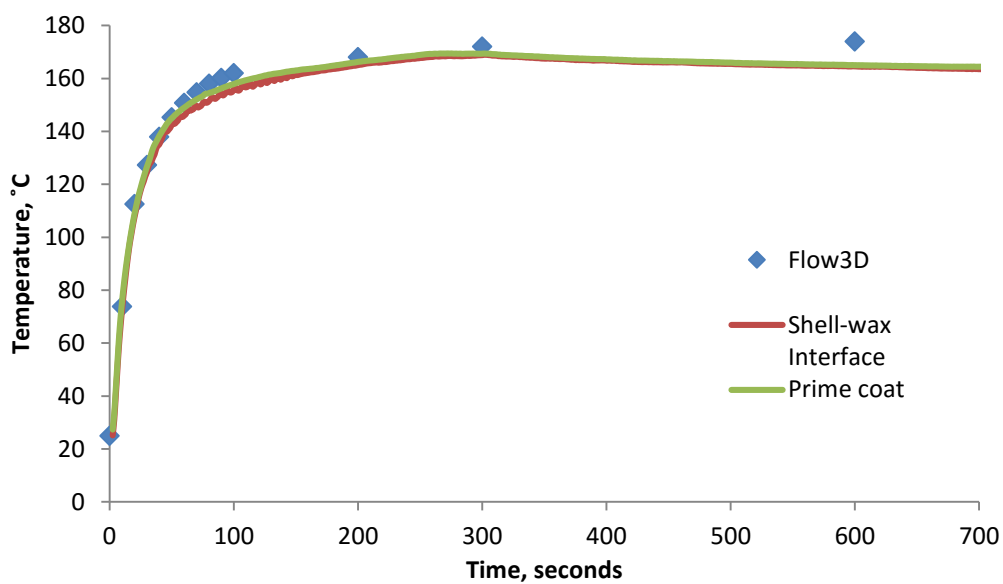


Figure 5-1: Thermal profile in FLOW-3D was found by trial and error to match the experimental thermal profile to represent the temperature at prime coat surface

At the wax-shell interface, the HTC can be seen to be extremely high with intimate contact between the two surfaces due to the shell being coated directly on the surface of wax. An air gap at the wax-shell interface could exist if the shell system is over dried, where wax shrinks and pull away from the shell. However, during de-waxing the wax would expand and push onto the shell to close the gap. Since the interface is smooth and no steam condensate droplets can form, the distance of heat transfer is known and HTC can be estimated using the heat balance equation. The heat transfer coefficient on the

wax-shell interface was calculated using Equation 5-2 to obtain the same temperature profile as measured in the experimental work. Heat transfer across the wax-shell interface was assumed to be completely transferred to heating the wax.

$$hA (T_{prime} - T_{wax}) = -V \rho C_p \frac{dT}{dt} \quad \text{Equation 5-2}$$

where h is the heat transfer coefficient, A is the heat transfer surface area, T_{prime} is temperature on prime coat surface and T_{wax} is temperature on wax surface, V is volume of wax, ρ is the density of wax and C_p is the heat capacity of wax and the last term is the temperature difference of wax over time.

The wax-shell interface HTC was calculated based on wax parameters in the solid phase. This was because when liquid phase starts to form and flow, the value of heat transfer coefficient is expected to fluctuate resulting in non-repeatable results. The formation of liquid wax is postulated to appear when time reaches 800 s as shown in Figure 5-2. HTC calculated after 800 s does not allow the linear interpolation of temperature since the wax melted and temperature difference is low (HTC is starting to drop). Time below 300 s is not taken as the system is at equilibrium and no temperature difference detected between two surfaces.

These values are only valid for the particular model structure. The wax-shell interface HTC was observed to increase linearly with time. For simplification in the modelling work, the HTC was assumed to be constant at $13384 \text{ W}\cdot\text{m}^{-2}\cdot\text{K}^{-1}$ taken at 600 seconds.

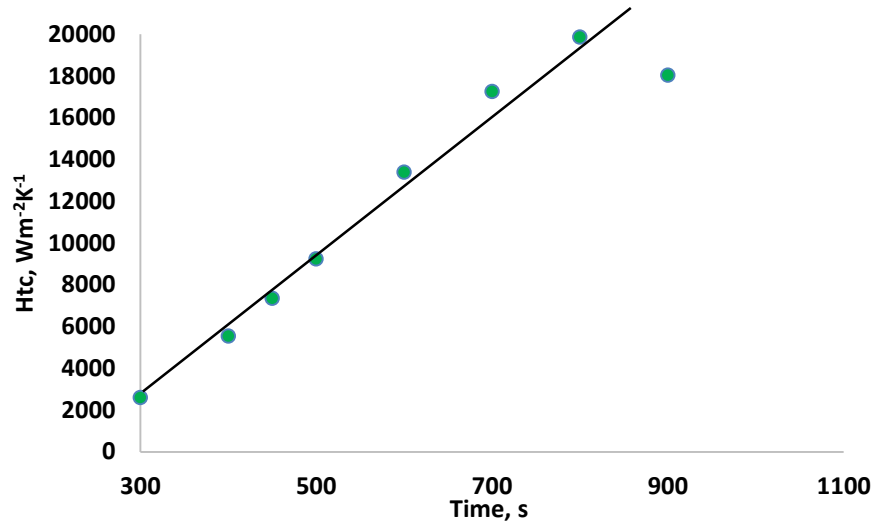


Figure 5-2: Heat transfer coefficient for wax-shell interface increases linearly as wax is heated and expand. HTC is starting to drop after 800 s due to wax starting to melt and temperature difference at interface is low.

5.1.2 Solidification drag model

In FLOW-3D by default, when the fluid is solid, it is not able to move under gravitational force or with any fluid alongside it. However, to allow the solid wax to move with the fluid wax, the solidification drag coefficient was set to zero allowing the software to use a linear function of viscosity versus solid fraction. As soon as there was any liquid wax formed, then the solid wax would be able to move ‘sliding’ on the liquid wax.

5.1.3 Viscosity

The de-waxing process depends strongly on the wax viscosity. The higher the viscosity the more difficult flow will be, however with the solidification drag coefficient activated, solid wax is still able to partially float on any liquid wax. The viscosity coefficients fitted in “Carreau” model (Equation 5-3) were obtained by curve fitting to the raw viscosity data determined experimentally and entered into FLOW-3D.

The rheological experimental data was only taken from the rotational rheometer and the reason for this was discussed in Section 4.11. Furthermore, the actual value of strain rate is unknown and probably relatively small compared to that in the capillary rheometer which uses an external force to drive the piston. At free surfaces, the external fluid (steam) is presumed to exert negligible stress on the fluid surface. The shear rate on the cell neighbouring the wall are computed using a generic expression based on the "Carreau" model:

$$\mu = \mu_{\infty} + \frac{\mu_0 E_T - \mu_{\infty}}{\lambda_{00} + [\lambda_0 + (\lambda_1 E_T)^2 2e_{ij}e_{ij}]^{\frac{1-n}{2}}} + \frac{\lambda_2}{\sqrt{2e_{ij}e_{ij}}} \quad \text{Equation 5-3}$$

where μ_0 , μ_{∞} , λ_{00} , λ_0 , λ_1 , λ_2 , are constants and e_{ij} is fluid strain rate computed from velocity field and E_T is given by:

$$E_T = \exp \left[a \left(\frac{T^*}{T - b} - c \right) \right] \quad \text{Equation 5-4}$$

where T^* , a , b and c are also constants, and T is the fluid temperature.

Note that the expression is not the typical Carreau model and it is modified to account for how viscosity varies with temperature and shear rate. It introduces extra constants (λ_{00} , λ_0 , λ_1 , λ_2) to fit experimental data and E_T term which allows the viscosity to vary with temperature. During the fitting, the highest viscosities from rotational capillary rheometer data were eliminated as they gave poor fitting. The poor fitting is due to limited number of parameters in the 'Carreau' model and restrict the flexibility to fit all

the data points. The fitting of rheological data was carried out graphically. Sum of error, $\sum e^2_{\text{norm}}$ during fitting the data was determined with Equation 5-5:

$$\text{Sum of Error} = \sum \frac{(N - O)^2}{O^2} \quad \text{Equation 5-5}$$

where N is the curve fitted viscosity at a temperature and O is the experimental viscosity at the same shear rate.

The values fitted with the curve was first calibrated with FLOW-3D at zero strain (very high viscosity) and at significant strain (liquid viscosity). Comparing values fitted with “Carreau” model in spreadsheet and value observed from the FLOW-3D simulation output, the error was up to 12 %, but this is because FLOW-3D values are approximated using single-precision logic and in the spreadsheet, the values are estimated graphically.

Table 5-1: Carreau model shear rate and temperature dependent fitted coefficients for Waxes

Wax	A	B	C	D	E
COEFFICIENT	Value Used				
$\mu_0, \text{kgm}^{-1}\text{s}^{-1}$	0.0008302	0.000607	0.000714	0.000648	0.000696
$\mu_\infty, \text{kgm}^{-1}\text{s}^{-1}$	0	0.060528	0.014454	0.032720	0.006934
$\lambda_{00}, \text{dimensionless}$	0	0	0	0	0
$\lambda_0, \text{dimensionless}$	0	0	0	0	0
λ_1, s	0.090732	0.169221	0.134731	0.107202	0.133284
λ_2, Pa	7.38E-07	5.03E-09	5.03E-09	5.03E-09	5.03E-09
n, dimensionless	0.925827	0.841220	0.861143	0.750088	0.918968
a, dimensionless	243.6507	286.2917	270.4640	303.6527	245.6070
b,K	1.29E-07	1.29E-07	1.29E-07	1.29E-07	1.29E-07
c, dimensionless	0.011171	0.024882	0.01797	0.02312	0.02713
T^*, K	14.31700	20.40865	17.7207	20.6924	17.9456
FITTED $\sum e^2 \text{ norm:}$	0.51	0.18	0.44	0.20	0.28

In this modelling work, the wax is assumed to start to flow in the shear rate range where rotational rheometer produces data. The “Carreau” equation parameters were fitted

using solver iteration in Microsoft Excel 2010. The fitted viscosity has a behaviour of an exponential rather than the typical Carreau model. The parameters fitted in the “Carreau” model are summarised in Table 5-1.

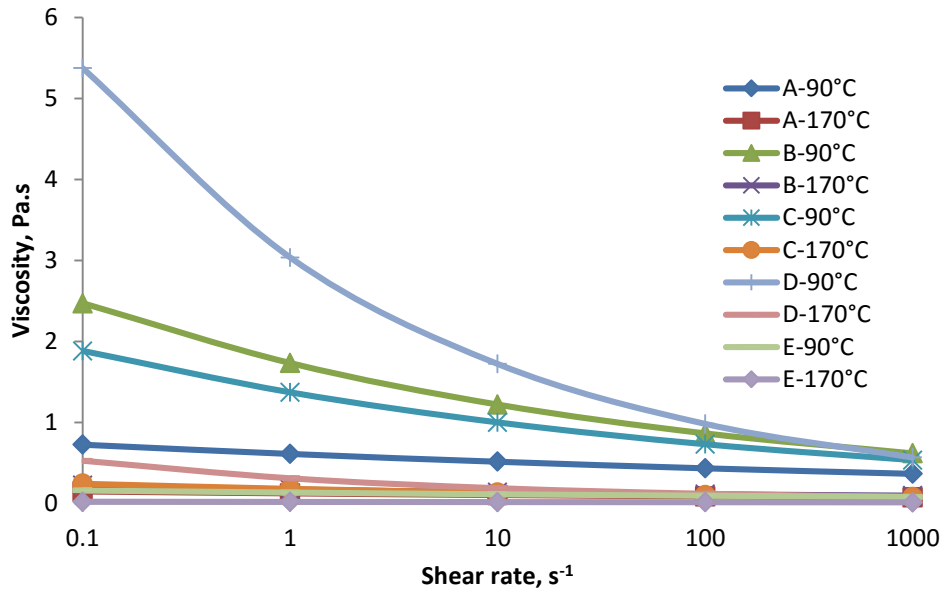


Figure 5-3: Wax A-E viscosity behaviour after fitting into the “Carreau” model.

It was observed that the wax is behaving as expected according to the experimental data Table 5-2.

Table 5-2: values of viscosity obtained from curve fittings to experimental data by FLOW-3D.

	Wax	A	B	C	D	E
Flow rate, 0 s⁻¹						
Temperature, °C	65	1.874	12.371	7.497	37.132	0.500
	90	0.971	4.546	3.230	14.227	0.217
	170	0.196	0.363	0.408	1.345	0.025
Flowrate, 10 s⁻¹						
Temperature, °C	65	0.996	3.244	2.304	4.448	0.254
	90	0.516	1.221	1.000	1.723	0.112
	170	0.104	0.139	0.135	0.189	0.016
Flow rate, 100 s⁻¹						
Temperature, °C	65	0.839	2.269	1.678	2.516	0.212
	90	0.435	0.865	0.730	0.983	0.094
	170	0.087	0.115	0.102	0.121	0.015

Note that the viscosity differences become less significant as the shear rate increases. This is because the curve fitting at low shear rate is less accurate.

5.1.4 Gravity/Force

The main source of force acting on the wax allowing the wax to flow out of the mould is gravity. In the model, this was set as constant at -9.81 ms^{-2} . Gravity was set to align with the mould rotational axis with the hole at the bottom. Another force acting on the system is internal pressure which develops when the wax expands and initiates the flow of wax. Pressure must build up at the source to move the fluid away from the source. The equation of motion in FLOW-3D is governed by Navier-Stokes equations with some additional terms as shown in Equation 5-6:

$$\begin{aligned} \frac{\partial u}{\partial t} + \frac{1}{V_F} \left\{ u A_x \frac{\partial u}{\partial x} + v A_y R \frac{\partial u}{\partial y} + w A_z \frac{\partial u}{\partial z} \right\} - \xi \frac{A_y v^2}{x V_F} \\ = -\frac{1}{\rho} \frac{\partial p}{\partial x} + G_x + f_x - b_x - \frac{R_{SOR}}{\rho V_F} (u - u_w - \delta u_s) \end{aligned} \quad \text{Equation 5-6}$$

where G is body accelerations, f is viscous accelerations, b is flow losses in porous media, final term accounts for injection of mass at a source represented by a geometry component. R_{SOR} is the density source term which is zero in this case.

5.1.5 Surface tension

Surface tension effects are included in the calculations by defining the surface tension coefficient, σ . Surface tension forces is taken into account in terms of external pressure on the surface of the liquid. The surface tension of molten wax was measured as a function of temperature (as discussed in Part 1). Wax-wall adhesion is represented by

the contact angle in degrees. This is the angle in the fluid between the wall tangent and the fluid surface tangent. The contact angle between wax and shell was assumed to be zero as discussed in section 4.12 which means the surface of shell is fully wetted by wax.

To compute the net surface tension force acting on a surface cell, FLOW-3D views each cell as a control volume and calculates the net surface tension stresses acting at the sides of the cell. It was assumed that surface tension forces can be replaced by an equivalent surface pressure. In terms of an equivalent surface pressure, these forces must be equal to this pressure times the projected surface area in each coordinate direction. In the z-direction, in particular, it is assumed that the projected area is the entire cell cross-sectional area ($\delta x \delta y$) because the normal surface is principally in the z-direction. The equivalent surface pressure is, therefore the net z-direction force divided by this area. To compute the net z-direction force, the cell-face located in the positive x-direction is first considered. Surface tension forces act tangentially to the surface and can be resolved into components directed along two principal tangent directions. One tangent is in the cell-face so that forces in this direction do not contribute to the net force across the face. The force in the direction of the second principal tangent is of interest. The z-direction component of this force can be shown to be:

$$S = \sigma \int \cos(\theta) \left[\frac{dy}{\cos \varphi} \right] \quad \text{Equation 5-7}$$

where σ is the surface tension coefficient, θ is the angle of the second principal tangent with respect to the z axis, and φ is the angle of the first principal tangent with respect to the y axis. The factor $dy/\cos(\varphi)$ is the length of the surface intersecting the cell-face and must be included because σ is a force per unit length.

5.1.6 Density evaluation

The density of wax was simplified in this one fluid model with the assumption that there was no condensation or evaporation of steam and only the wax is changing phase. Density of wax was evaluated as a function of temperature applying the results obtained from the modified density bottle method.

The simulation was created as a principally incompressible model with limited compressibility effects being added to the incompressible hydrodynamics computer nodes. For the limited compressibility model to be valid, it has to be assume that the changes of density due to compressibility are small, (for example - $d\rho/\rho \ll 1$). This assumption is reasonable when compared to the compressibility data available in the literature. As part of the FOCAST programme, Torres (2003) in collaboration with Moldflow Corporation measured the compressibility of waxes (Figure 5-4-Figure 5-6). They measured the PVT behaviour of blends of wax/resin (50/50 w/w) with 0, 20 and 40 wt% of filler in suspension (Torres, 2003). The specific volume for each type of wax was measured at four different pressures - 0, 50, 100 and 200 MPa. The availability of the relationship between specific volume and pressure measured by them allows the calculation of wax compressibility, β using Equation 5-8:

$$\beta = -\frac{1}{V} \frac{dV}{dP} \quad \text{Equation 5-8}$$

where V is volume of wax and P is external pressure introduced on wax.

At lower temperatures (below the melting temperature), the compressibility increases as the temperature increases. After melting, the compressibility apparently remains constant. It was also observed as the testing pressure increases, the compressibility

reduces at higher temperatures. The compressibility of wax was found to increase by $1 \times 10^{-10} \text{ Pa}^{-1}$ when the pressure was doubled. This indicates that the wax specific volume does not vary significantly even with large increases of pressure. In the range of phase transformation between solid to liquid of the waxes, a peak in compressibility is observed indicating the maximum compressibility when the wax is in the semi-solid phase. In reality, wax penetration into the inner surface of shell should relieve the pressure in the mould. In this simulation work, the amount of wax permeation into shell was not taken into account. This was because as wax expands, it requires certain pressure to allow wax to permeate the shell. The amount of wax that permeates into the shell for the duration of wax expansion is non-trivial to determine experimentally. Relationship of wax permeation with time is required for the simulation of permeability during de-waxing to be accurate. However, the sensitivity of this parameter was analysed by varying the value of wax compressibility.

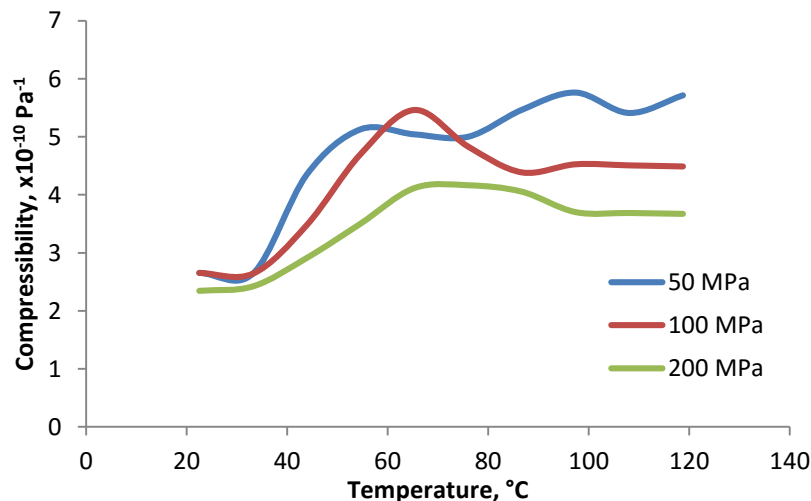


Figure 5-4: Compressibility of 40 % in-house blend filled wax at different temperatures with an average of $4.5 \times 10^{-10} \text{ Pa}^{-1}$ is observed (Torres, 2003)

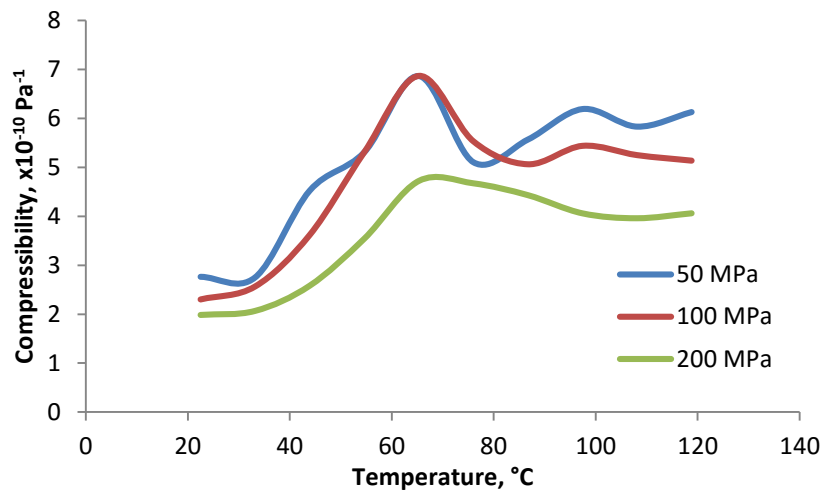


Figure 5-5: Compressibility of 20 % in-house filled wax at different temperatures with an average of $5 \times 10^{-10} \text{ Pa}^{-1}$ is observed (Torres, 2003)

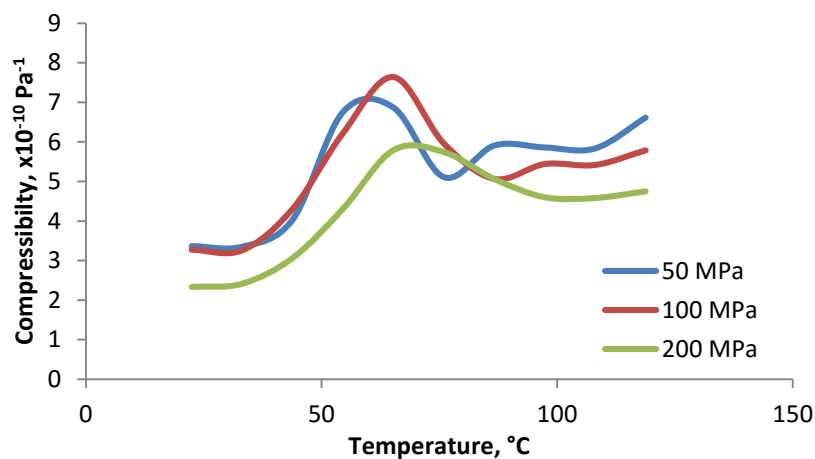


Figure 5-6: Compressibility of 0 % in-house filled wax at different temperature with an average of $5.5 \times 10^{-10} \text{ Pa}^{-1}$ is observed (Torres, 2003)

The compressibility of waxes with different fillers percentage does not vary significantly (Figure 5-7). The compressibility data available is limited to a maximum temperature of 120 °C and compressibility above this temperature was assumed to be constant.

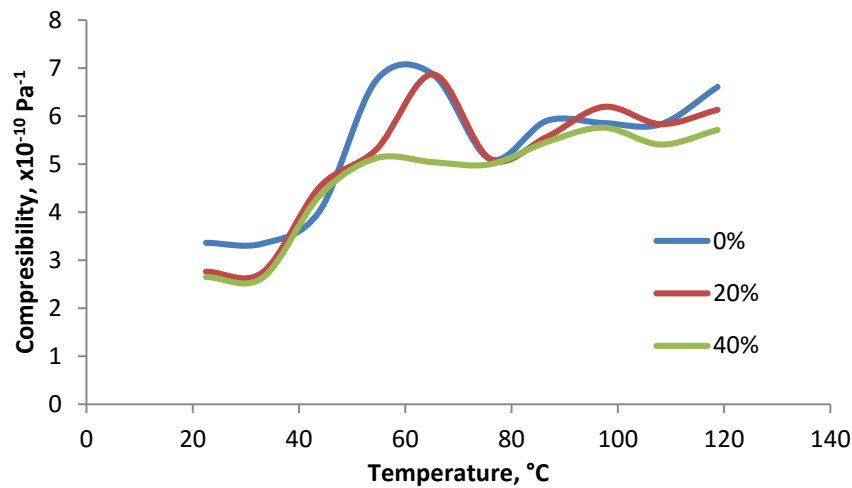


Figure 5-7: Compressibility of three different waxes at 50 MPa pressure

For simulation purposes, the lowest wax compressing pressure that is closest to the shell cracking pressure was used, which in this case was 50 MPa (assuming shell cracking occurs as indicated in the 3-point bend test). The compressibility value was taken at higher temperature (above 80 °C) when the values remain steady and Wax A, B, C, D are assumed to have 40 wt % fillers and wax E to have 0 wt % fillers. The compressibility of wax was assumed to be $5.5 \times 10^{-10} \text{ Pa}^{-1}$ for all waxes.

5.1.7 Bubbles and phase change

The one fluid model sets each separate void (steam) region with a uniform temperature and pressure with zero velocity. In this simulation, a void is represented with the adiabatic bubble model. The adiabatic bubble model approach is used when the density of the gas is much less than the density of the fluid, there is no heat exchange between the fluid and the bubbles, the bubbles are compressible, and the bubbles do not have significant pressure and thermal gradients inside them. This model allows the bubble to expand, contract, exchange mass and exchange heat with its surroundings. This adiabatic model has two assumptions: (i) The inertia of the gas is negligible relative to

the inertia of the liquid phase. (ii) The bubble pressure and temperature are uniform within each bubble. Based on the two assumptions, no velocity or temperature computations are performed in bubble regions. This is reasonable since the expansion of the wax would keep the air bubbles (steam) from entering the shell throughout the times of interest. This leads to a considerable savings in computational effort since accuracy and numerical stability issues associated with a low density gas/high density fluid combinations are eliminated. Ignoring the inertia of the gas is usually a good approximation since gas densities are typically orders of magnitude smaller than the liquid density.

Solid wax will be melted by the high temperature and starts to flow out of the shell mould under the force of gravity. However, one can imagine, as the solid wax develops a melt surface it would slide down the shell wall. If this occurs, it creates a negative pressure cavity (vacuum) and slows the discharge rate of wax Figure 5-8.

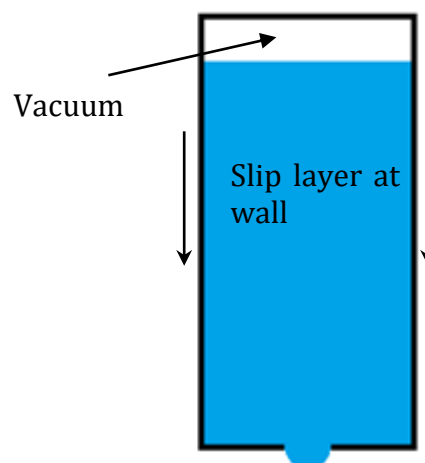


Figure 5-8: Wax slide down the shell wall during de-waxing creating a vacuum region

However the shell in reality would be porous and one can imagine the pressure in the void is in equilibrium with the external environment. This allows free flow of the wax.

However, there is a possibility that neither situation actually exist but it is almost impossible to observe this experimentally. In the model, if vacuum is created, it was taken into account as it is a 'by-product' of the continuity equation. As the mass of wax is lost in a cell, it is replaced with a void with the same properties as steam surrounding the shell. This was done by activating the adiabatic bubble model in FLOW-3D®. Mass continuity equation for limited compressible fluid was described by:

$$\frac{\partial}{\partial x}(uA_x) + R \frac{\partial}{\partial y}(vA_y) + \frac{\partial}{\partial z}(wA_z) + \xi \frac{uA_x}{x} = \frac{R_{SOR}}{\rho} \quad \text{Equation 5-9}$$

Without activating this model the wax would not flow out of the mould as a vacuum was created, which did not represent the de-waxing process. This is because the incompressible continuity equation forces the divergence of the velocity components (u , v , w in Equation 5-9) to be zero. This means that the fluid near a solid object cannot pull away from the solid object unless there is an adjacent void cell.

5.1.8 Elastic stress model

This model was activated to work around the complication of the solidification drag model (section 5.1.2) where the solidification drag option freezes material in the mesh, so it cannot move under the influence of gravity. This scenario limits the flow of wax during the de-waxing simulation. To address this, elastic stress model was activated for the fluid and set the coefficient of solidification drag to zero to allow solid and liquid wax to flow together. The static friction coefficient was set at -1 which allows the wax to slip off the wall either in the solid or liquid phase. This treats the solidified wax as an elastic fluid (which can still move in the mesh) but does not affect the liquid phase

properties. This gives a better prediction since the solidified wax can move in response to gravity and other forces in the fluid.

5.1.9 Fluid structure interaction (FSI) model

The deformation in the solid due to forces exerted on it by the fluid can be calculated and presented as a stress field developing in the solid. For the flow region, the wax is subdivided into a mesh of fixed rectangular cells and the finite difference method (FDM) was used to calculate fluid flow and heat transfer. In the solid region (mould), an unstructured finite element method (FEM) was conformed to the mould which deforms along with the mould. At the interface of wax and mould, the nearest node points are moved to the surface of the mould along the normal to the surface (Figure 5-9).

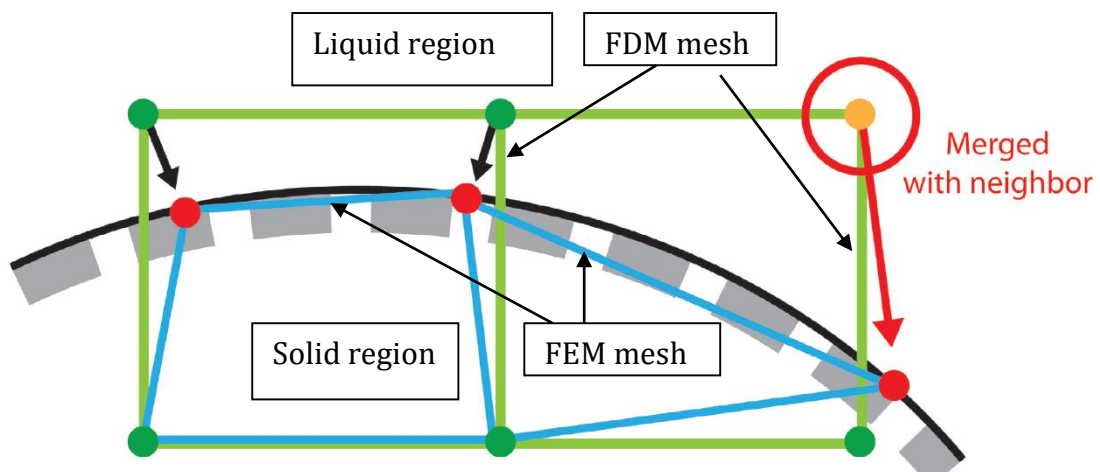


Figure 5-9: Merging the nodes with the nearest interface nodes (Flow-3D, 2014)

In the simulation, the shell mould wall was treated as an elastic wall. FLOW-3D® treats all FSI deformable components as being elastic up to their yield stress. In FLOW-3D®, an elastic wall is an elastic object of arbitrary shape, and its surface deformation is small and proportional to hydraulic pressure. The strain or deflection of shell mould was predicted using:

$$w = -\frac{(p - p_{ref})L}{E} \quad \text{Equation 5-10}$$

where w is local deflection in surface normal direction, p is local pressure, p_{ref} is a reference pressure, E is Young's modulus and L is a length scale comparable to the depth of the elastic wall.

The equation of motion and stress on the shell mould was described using:

$$\rho \frac{d^2x}{dt^2} = \nabla \cdot \sigma + \rho b \quad \text{Equation 5-11}$$

where ρ is the density of shell, t is time, x is the coordinate of a point in the material, σ is the Cauchy stress tensor (a measure of stress in the material related to strain, thermal and other internal stress) and b is the body force vector. Cauchy stress tensor is a function of Young's modulus and Poisson's ratio.

The FSI model allows the simulation of de-wax cracking, however there were a few limitations to the model. The main limitation to the code is that the deformation is assumed to be small (deflection of elastic wall is smaller than its computational cell size). With this assumption, the actual change in the position of the deforming surfaces can be ignored. Thus, the deforming walls are fixed through the calculations as defined in the initial program setup. Another limitation is that the elastic wall cannot be porous. This means that the simulation of a permeable shell mould has to be neglected however it will be taken into account in the compressibility of wax.

5.2 Modelling procedure

The geometry chosen is important to allow representation of the shell cracking. In this study, simple wax cylinder geometry was chosen to be modelled as it is mathematically and conceptually easier to describe. Experimentally, shell cracking occurrence is relatively easy to be manipulate of cylindrical geometry mould is also relatively easy to be made and a small volume wax pattern is required. This geometry was also favoured by Rosmait (2007) who observed the effect of refractory particle size, polymer selection and colloid selection on autoclave shell cracking.

The geometry selected to model the de-waxing process was a cylindrical mould which was coated onto a 150 mm long and 50 mm diameter wax pattern. Average thickness of shell was 5.93 mm and for the purpose of the simulation, the shell thickness was assumed to be 6 mm. The de-waxing outlet of either 5 mm or 2.5 mm diameter was set in the centre of one end. The “orifice” diameter was varied to observe how the restriction of discharge flow affects shell cracking. This diameter was determined by initial trial and error work on Wax D where all shells consistently crack when a diameter of 2.5 mm was used. In the simulation model, the outside edge of the cylinder was assumed to have a 10 mm radius. This is a reasonable estimation base on the cylinder corners observed and measured experimentally (Figure 5-10). Note that this assumption also takes into account of the shell being thinner at the corner of the cylinder mould.

A support component was required in the model to “hold” the mould in space. The nodes between the mould and support are attached and cannot move. The supports will however have zero deflection and zero net force moment.

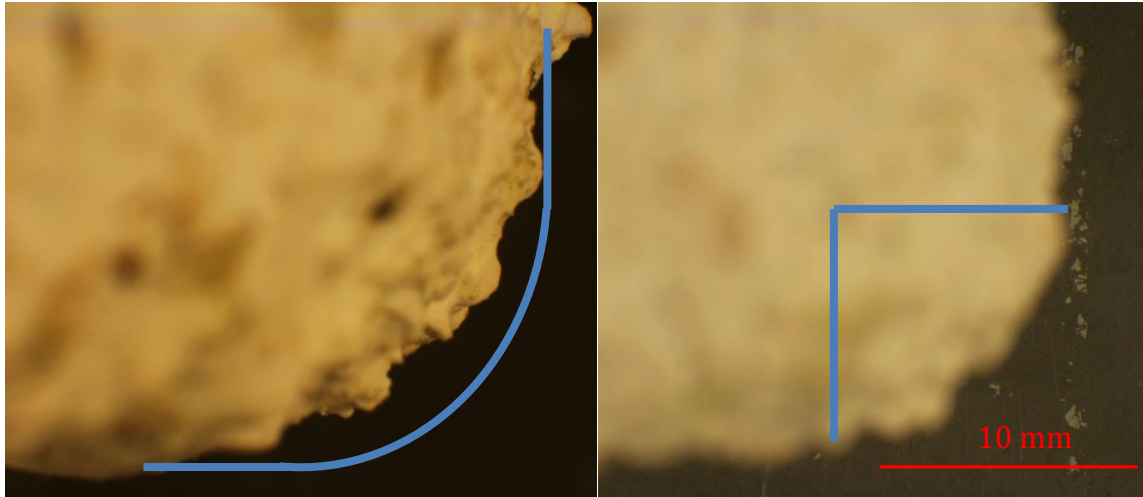


Figure 5-10: In focus of cylindrical mould corner (left) and out of focus (right). Mould radius is approximately 10mm.

The de-waxing process simulation was carried out with FLOW-3D® version 11.0.3.5. The model script was submitted to be solved with 8 processors in parallel code available in the computing cluster.

5.2.1 Mesh Type

The finite difference mesh size for the fluid region was set at 1 mm. For the FSI model simulation, automatic tetrahedron meshes were used to observe the stress analysis in the mould region and cell size was set at 1 mm. Dark (black) region in the meshes is set as the steam region and it has constant properties throughout the simulation. In the simulation, the mesh on the Z-axis (Figure 5-11) was set to be one cell thick. This allows the simulation to be solved in shorter duration (2 weeks) than the full 3-dimensional de-waxing of the cylinder. The disadvantage is that any hoop stress that might develop on the shell is neglected. This is acceptable since the hoop stress is possibly less crack sensitive compared to the sharp edge in a cylindrical geometry due to lower stress concentration (Figure 5-12).

The time step was set to automatic selection which means the code adjusted the time step up or down with 5 % changes per cycle for greater efficiency. It automatically adjusted the time step to be as large as possible without violating the stability condition and reduced it when pressure and/or temperature iterations exceed the corresponding nominal values.

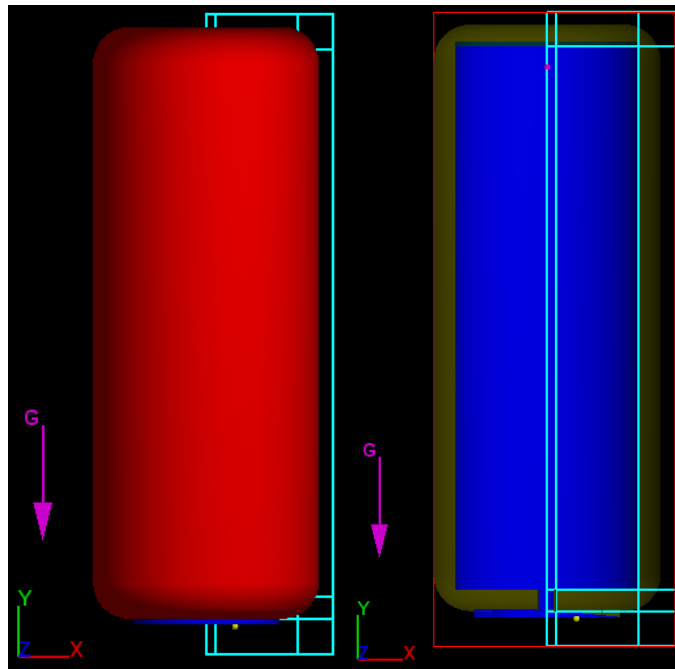


Figure 5-11: 2-dimension mesh boundary setup in FLOW-3D. Red is the mould and blue is support component (left) and cross section of the cylinder (right)

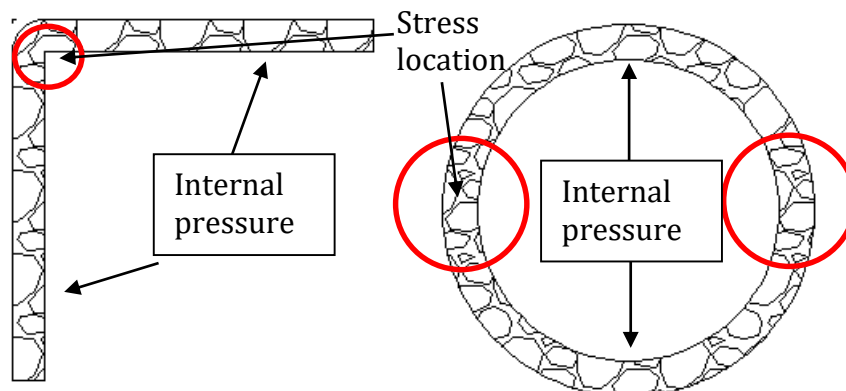


Figure 5-12: Location of stress at top edge (left) and hoop stress (right) of a cylindrical shell.

5.2.2 Model conditions

The initial condition of the solid wax and shell temperature was set at 25 °C. Any region classed as void was set as temperature 180 °C and pressure 0.8 MPa.

There are two boundary conditions specified in the model. The mechanism that allows wax to flow out of the system is a continuative outflow boundary. This allows the fluid to flow smoothly out of the mesh causing no upstream effects. All other boundaries are specified as pressure boundaries which represent things such as confined reservoirs of fluid, ambient laboratory conditions, and applied pressures arising from mechanical devices.

The setup of FSI models automatically determines the boundary conditions on each element face of the solid component. The results simulated from the liquid wax are passed on to the solid component at the boundary nodes.

5.2.3 Model assumptions

There are a few limitations to the model which require assumptions to be made for the simulation to be carried out.

1. Initial condition of shell and wax is 25 °C and not affected by the heat from the autoclave until steam is release into the chamber.
2. Latent heat from steam condensation contributes to the rise of shell temperature and in turn affects the wax.
3. The autoclave-wax HTC was assumed to be $7000 \text{ W}\cdot\text{m}^{-2}\cdot\text{K}^{-1}$ throughout the de-waxing cycle.
4. Autoclave temperature is constantly 180 °C and the pressure 0.8 MPa.

5. Shell is not permeable and no wax permeates into the shell.
6. Thermal profile of shell is the same for all the shells.
7. The rotational axis of the cylindrical wax is parallel with the gravitational direction during de-waxing.
8. The external radius of shell corner is 10 mm.
9. Thermal shock stress is not taken into account in this model.
10. The permeation of wax is not taken into account and will be discussed in terms of compressibility in the sensitivity analysis section, section 5.3.2.
11. Poisson ratio of shell is 0.24.
12. The FSI model is partially coupled - Partial coupling means that the solid “react” to the surrounding fluid, but the deformation of the solid does not affect the fluid flow. The fully coupled model is computational intensive and the benefit to the result is believed to be insignificant with respect to shell cracking. This is because shell cracking occurs in the first few seconds when steam is introduced before wax starts to flow (relieve pressure) and the shell deflects back to the initial (time is zero) location.
13. Solid cylindrical wax - there is no internal shrinkage of wax after wax injection.

5.2.4 Stress analysis method

The model was not able to simulate physical cracks. It was assumed that once the stress in a cell exceeds the ultimate tensile stress measured experimentally (wedge test or 3-point bend test), crack initiations occur at that particular cell. The mould is also assumed to be always elastic and show no plastic deformation. This is a fair assumption since the colloid bonded assembly (shell) are known to be stiff and brittle especially at

low temperature. The basic tensor stress commonly known as Cauchy tensor stress, is represented as in Figure 5-13.

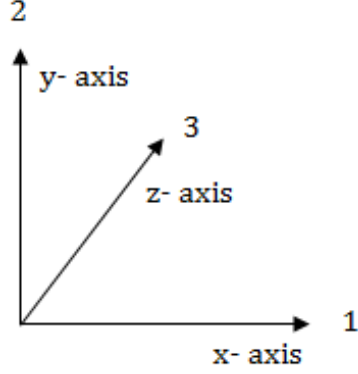
$$\sigma = \begin{pmatrix} \sigma_{11} & \sigma_{12} & \sigma_{13} \\ \sigma_{21} & \sigma_{22} & \sigma_{23} \\ \sigma_{31} & \sigma_{32} & \sigma_{33} \end{pmatrix}$$


Figure 5-13: Indication of basic tensor stress direction

The basic tensor stress can be analysed in terms of Principle stress and Von Misses stress. Principal stress represents an object with the stress normal to a plane on three different axis and the max principle stress was used for comparison. Equation 5-12 can be solved for the principal stress, σ_p which gives 3 principal stresses. The maximum principal stress is used as a good safety margin before shell cracks develop.

$$\sigma_p^3 - I_1 \sigma_p^2 + I_2 \sigma_p - I_3 = 0 \quad \text{Equation 5-12}$$

where,

$$I_1 = \sigma_{11} + \sigma_{22} + \sigma_{33}$$

$$I_2 = \sigma_{11}\sigma_{22} + \sigma_{22}\sigma_{33} + \sigma_{11}\sigma_{33} - \sigma_{12}^2 - \sigma_{23}^2 - \sigma_{31}^2$$

$$I_3 = \sigma_{11}\sigma_{22}\sigma_{33} + 2\sigma_{12}\sigma_{23}\sigma_{31} - \sigma_{12}^2\sigma_{33} - \sigma_{23}^2\sigma_{11} - \sigma_{31}^2\sigma_{22}$$

Von Misses stress, σ_{vm} known as the equivalent tensile stress can be seen to be the average of all three principle stresses,

$$\sigma_{vm} = \sqrt{\frac{(\sigma_{11} - \sigma_{22})^2 + (\sigma_{22} - \sigma_{33})^2 + (\sigma_{33} - \sigma_{11})^2}{2}} \quad \text{Equation 5-13}$$

FLOW-3D calculates the basic tensor stress in terms of Von misses stress and the basic tensor was further used to calculate the Principal stress with Equation 5-12. In FLOW-3D, when the Von Misses stress exceeds the yield stress set for the material, the stress will then remain constant and strain continue to increase slightly. In the model, yield stress was set higher than the ultimate tensile stress measured in tensile test and wedge test. This allowed the calculated results to be analyse manually in terms of principle stress. The maximum principle stress was compared to the Von Misses stress and the larger stress value was evaluated to determine if the mould in the model would have failed. This is to avoid any underestimation of the stress the shell experienced. The time taken to simulate either the Principal stress or Von Misses stress will be considered in the analysis.

5.3 Results and discussion

The simulations to observe shell stress were only run to approximately 20 seconds because the simulation slowed down drastically at around 16 seconds. At around 16 seconds, the wax starts to melt and the merging of several solvers including the shell analysis had increased the computational intensity. The restriction of wax flowing out of the mould (relatively small outlet diameter) further complicates the simulation. The computational effort and the dropping of time step to help the different solvers converge, both of which slow the overall computation. However, 20 s is sufficient for shell cracking analysis since the stress predicted in the shell has already exceeded ultimate tensile stress within this time frame. Therefore, only 2 simulations were run to completion and compared to the full shell cracking experiments carried out for validation. These were done assuming the shell has infinite ultimate tensile strength. Each full simulation took approximately 2 weeks to run on an 8 processors setup in the computing cluster.

5.3.1 *Shell stress analysis*

The simulation result is presented in terms of temperature, mould internal pressure and Von Mises stress contour plot for Wax A with a 2.5 mm orifice diameter. The Von Mises contours demonstrate the location of stress concentration in the shell mould which is the point of interest for this project. The results for other permutations of wax and orifice dimension are summarised in Figure 5-20 and Figure 5-21.

The left hand image in Figure 5-14 shows that at 4 s after heat introduction, the shell external surface had reached 400 K (127 °C) and the wax-shell interface remains at 299 K (26 °C). In the right hand image, the shell external surface reached 437 K (164 °C) and the internal surface 355 K (82 °C) after 10 seconds exposure to steam. The interface temperature had risen approximately 56 °C in 6 seconds. This temperature difference could cause sufficient expansion of wax to crack the shell. According to the thermal expansion data in section 4.6.4, this temperature difference especially at the stage of solid to liquid transition had contributed to the largest volume expansion of wax.

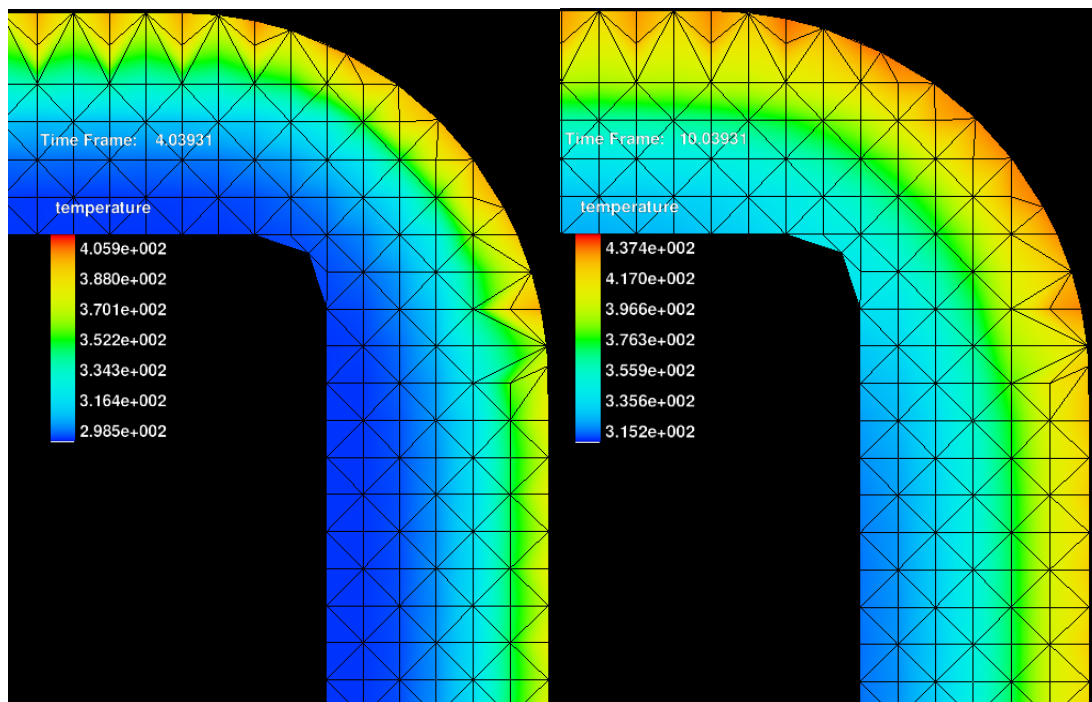


Figure 5-14: Temperature contour of Wax A with 2.5 mm orifice diameter when steam is introduced for 4 s (left) and 10 s (right).

Figure 5-15 (left hand image) shows the temperature of wax at the orifice is approximately 430 K (157 °C) 10 seconds after the heat is introduced. This is reasonable since as wax melts and leaves the mould, more wax moves to the orifice and therefore temperature will not reach 180 °C. The pressure contour (right hand image) illustrates the internal pressure developed due to thermal expansion of wax. High internal pressure is observed at both upper and lower sharp corners and the upper sharp corner reached 5 MPa in 10 seconds. The vectors on right hand image indicate the direction of the wax leaving the orifice.

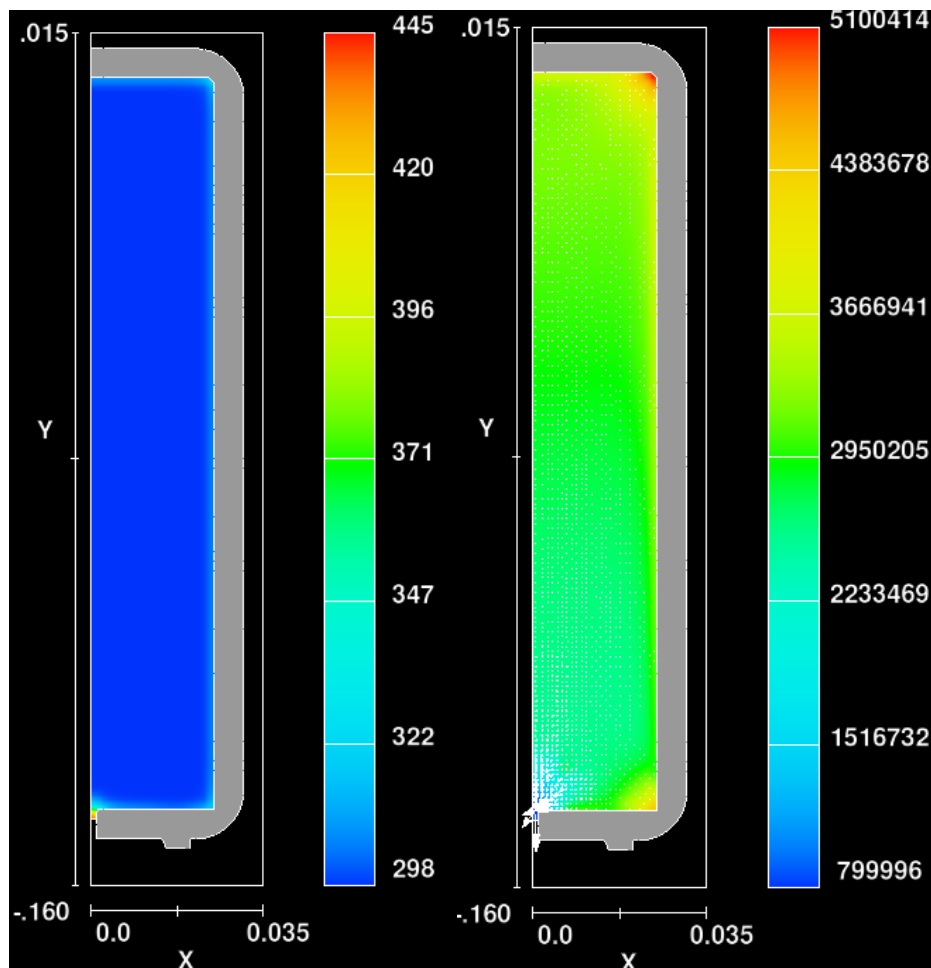


Figure 5-15: Wax A with 2.5 mm orifice diameter. Temperature profile in Kelvin (left) and pressure with vector in Pa (right) at 10 s.

Figure 5-16 shows the pressure from wax had caused stress on the shell and this value had exceeded the ultimate tensile stress of shell (3.6 MPa) measured in the 3-point bend test. This occurs approximately 10 seconds after the heat is provided to the system. The critical stress node with the coordinates of 0.0245, 0.00515 and 0.0005 (X, Y and Z respectively) was the focus of investigation in this study. The 1 mm mesh size would possibly cause discontinuity of the elements and affect the stress state (as seen right hand figure 5-16) but it was chosen without compromising on the simulation time and the importance of mesh size analysis on accuracy is addressed for future work.

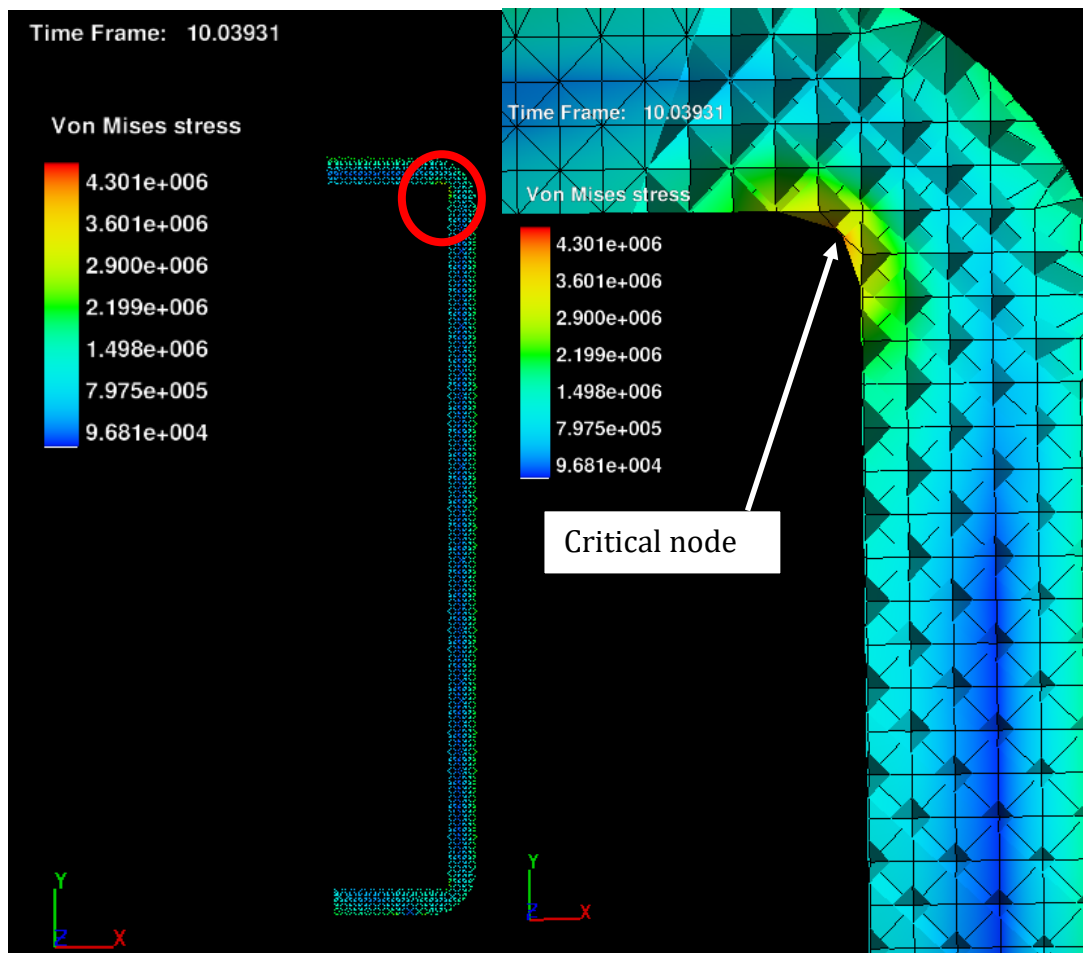


Figure 5-16: Wax A with 2.5 mm orifice diameter. Sharp top corner indicating Von misses stress is at 4.3 MPa. The shell of this setup is expected to crack at 10 s.

Figure 5-17 compares the Von misses stress at 9 and 11 s showing how the stress develops with time and how shell cracking time was determined for this study. The shell cracking time was determined to be when the stress at the critical node exceeded the experimentally determined shell strength. Just using this method, the time frame exceeding the failure stress at the critical node was approximately 10 s.

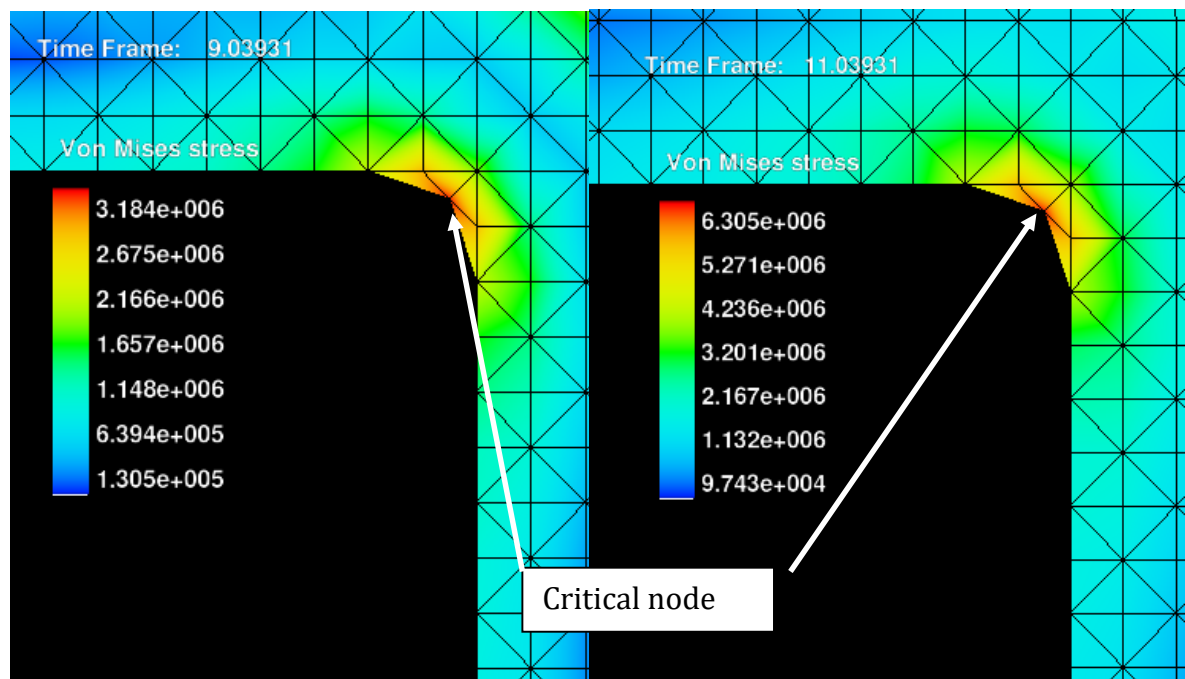


Figure 5-17: Wax A with 2.5 mm orifice diameter. Von Misses stress (Pa) taken for analyse is the time (seconds) that just exceeded the shell stress limit.

Figure 5-18 compares the wax condition (pressure) at the same time frame but with different orifice diameters revealing that greater pressure is developed in the upper corner in the system with a 2.5 mm diameter compared to a 5 mm diameter. This difference will be transmitted to change the stress in the shell especially at the critical node.

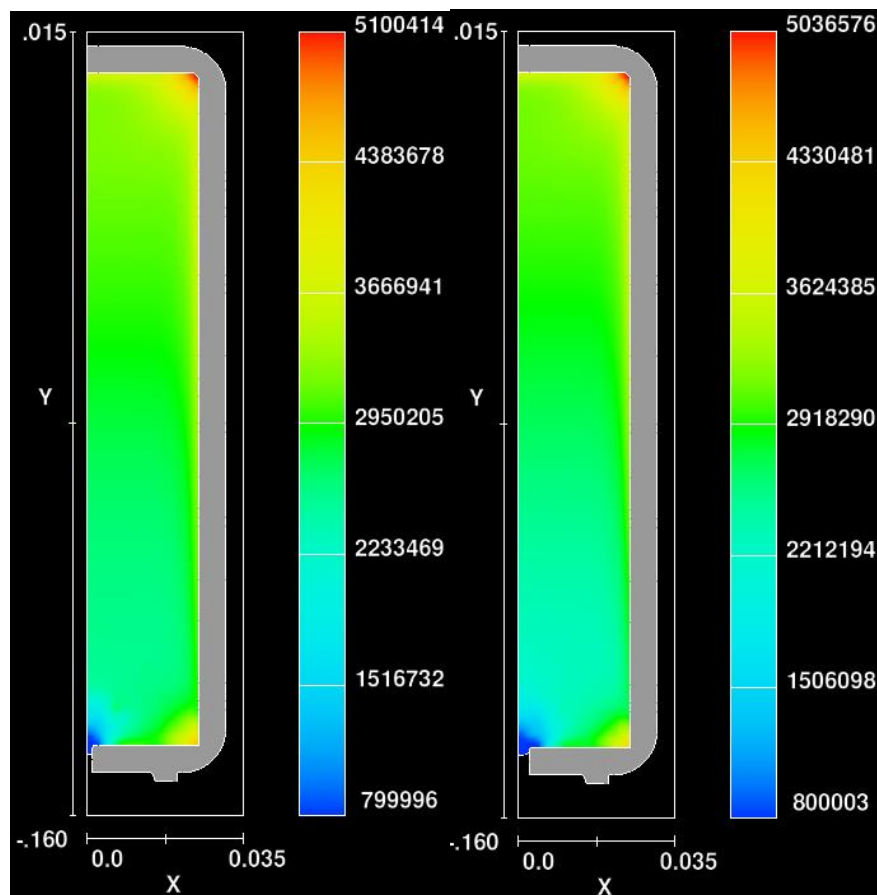


Figure 5-18: Internal pressure (Pa) comparison between 2.5 mm (left) and 5 mm (right) orifice diameter at 10 s.

Figure 5-19 presents the displacement experienced by the shell at 10 s which is when the shell cracks. The shell deflects coincidentally by 0.0024 mm in both x and y direction when the shell cracks. The locations indicated with red circle are the common areas where shell cracking would be predicted to occur.

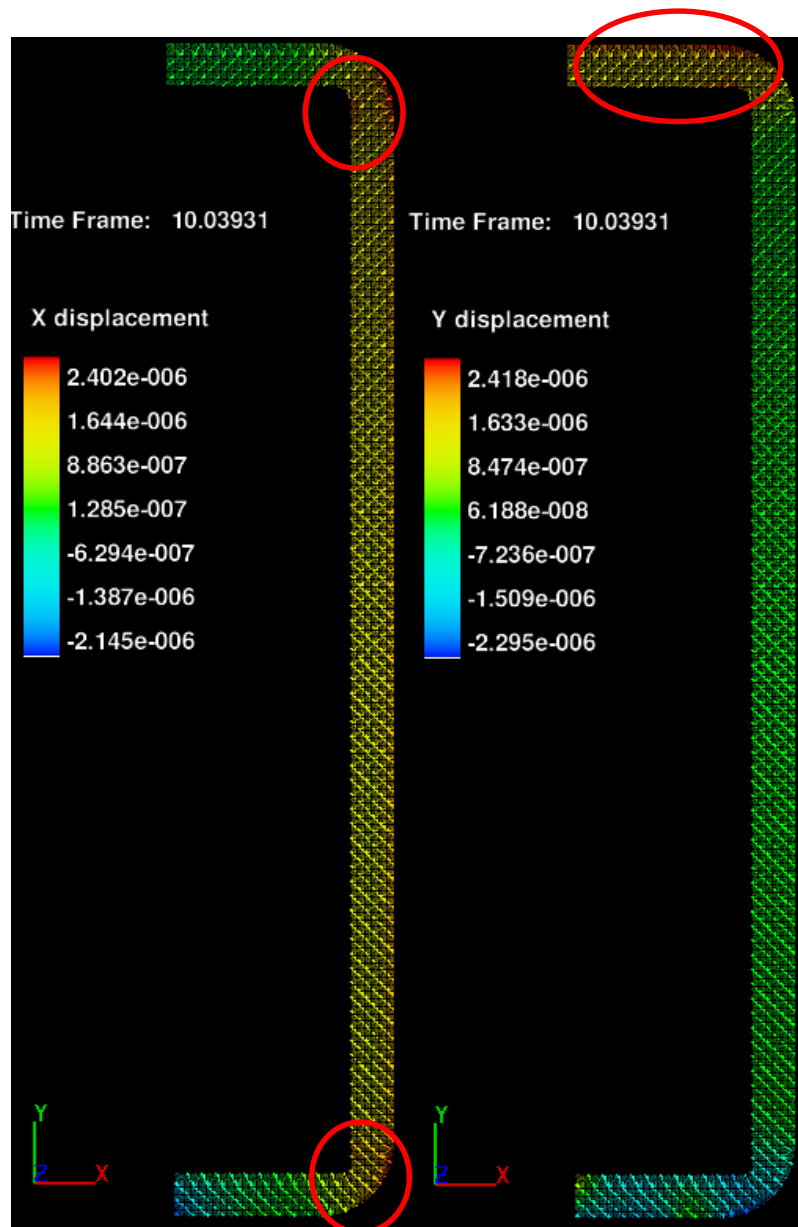


Figure 5-19: Illustration of shell displacement in metres

The simulation results are sufficient to indicate the probability of shell cracking caused by different waxes. From the results shown in Figure 5-20 and Figure 5-21, it can be seen that the simulation actually predicted that all shells would fail after a short time, with some waxes being quicker than others to reach the predicted failure stress. In reality, the delay allows more time for the wax to penetrate into the shell and avoid shell cracking. The probability of shell survival should increase if permeability is taken into account as the loss of wax volume into shell allows the mould cavity to accommodate more bulk wax expansion.

Comparing the Von misses and maximum principal stress (Figure 5-20 and Figure 5-21), it was found Von misses stress is generally higher. This implies that the propensity for shell cracking will be underestimated if maximum principal stress is used to analyse the simulated data. The range of maximum principal stress was also found to be narrower compared to Von misses stress for the same time duration. This is reasonable since principal stress is calculated based on stresses of all six directions (Equation 5-12). Analysing the stress at critical node with principal stress has reduced effect of different waxes clustering the time to reach the critical failure stress. This has made it difficult to differentiate the effect between waxes. It was also found that principal stresses are not sufficiently sensitive to differentiate the effect of the two different orifice diameters. Therefore, in this study, it is suggested to use Von misses stress as the parameter to analyse shell cracking.

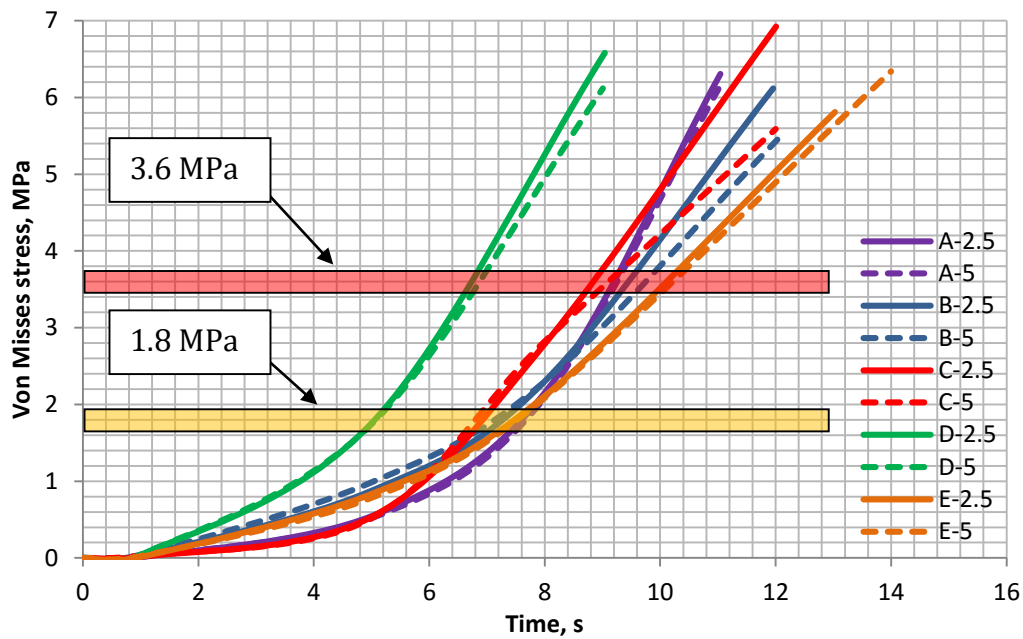


Figure 5-20: Von Mises stress in the shell at the identified critical node in relation to time after heat is introduced. The red region indicates the failure pressure for the shell from experimental data (3-point bend test) and the yellow region is the failure pressure for wedge test data. The values indicate the mean strengths of the experimental data. Solid lines represent results for 2.5 mm orifice diameter and dashed lines for 5.0 mm orifice diameter

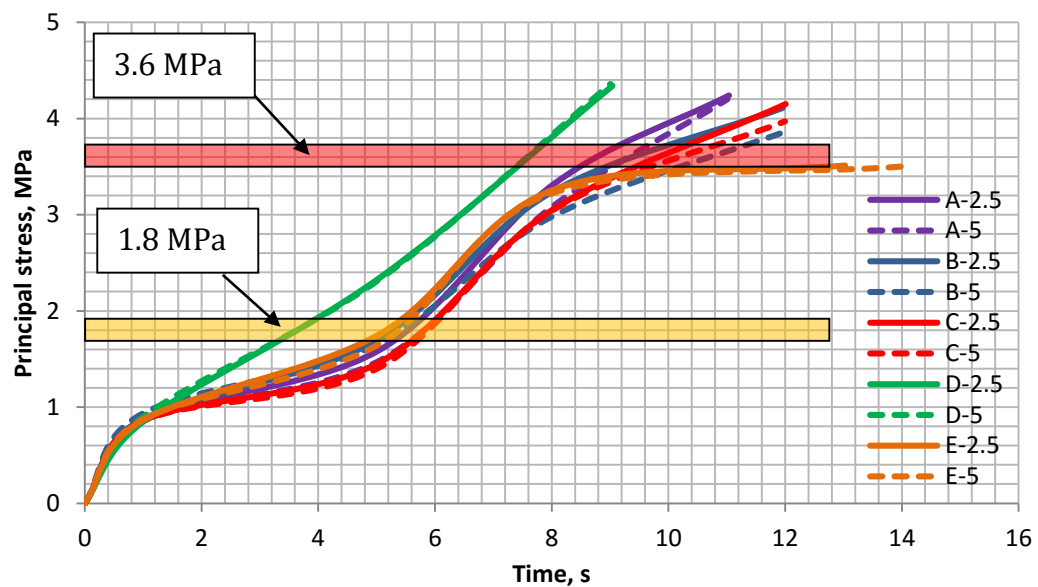


Figure 5-21: Maximum principal stress at critical node in relation to time after heat is introduced. The red region indicates the failure pressure for the shell from experimental data (3-point bend test) and the yellow region is the failure pressure for wedge test data. The values indicate the mean strengths of the experimental data.

Wax A and E show that the Von misses stress is similar between the two orifice diameters of 2.5 mm and 5 mm. One possible reason is due to the low viscosity of the two waxes where the effect of wax flow is relatively low compared to other waxes and the difference between the two orifice diameters does not impact on relieving the internal pressure where the effect of wax thermal expansion is dominant. Another possible reason is that if the simulation is left longer to run and the Von Misses stress assumed to exceed 7 MPa, there is a possibility that the curve starts to diverge. Wax B, C and D show that 5.0 mm orifice diameter will crack later than a 2.5 mm diameter. Among the three waxes, Wax D shows the smallest stress difference when comparing the two different orifice diameter.

The model unfortunately does not appear very sensitive to changes in the waxes. It is not surprising since the parameters fed into the model not significantly different. Overall, the analysis shows that Wax D has the highest probability of causing shell cracking and shows a distinct difference compared to the other waxes. This is mainly attributed to higher viscosity of Wax D when fitted to the “Carreau” model. Whitehouse & Dahlin (2008) showed that wax viscosity had a significant effect on shell cracking, the higher the viscosity the more shell cracking was observed. Wax E has delayed prediction of the cracking the longest and this is expected since it is an unfilled wax. The simulation shows that Wax A which is commercially considered to be a non-shell cracking wax took longer than Wax B and C to reach the critical stress if the 1.8 MPa is taken to be the shell ultimate stress. If the 3.6 MPa is considered as the shells ultimate stress then Wax A will crack slightly later than Wax C but still earlier than Wax B. The simulation results do not indicate Wax A to outperform the other waxes in terms of stress development. If the shell is heat treated in autoclave (3-point bend strength is 6.26 MPa), then the shell will

have better chance to differentiate the effect of orifice diameter in the simulation. Or if the failure tensile stress can be delayed further by introducing permeability to the shell, it could allow the model to differentiate better between the two orifices especially for Waxes B, C and D based on the trend lines in Figure 5-20. The larger time frame should increase the sensitivity of different waxes properties.

In comparison to the literature, Cendrowicz (2004) used 4 mm thick shell for aluminium casting and obtain 2.66 MPa ultimate tensile stress from a 3-point bend test. He predicted in a 1-dimensional model that 12 seconds after pressurisation, the stress in the shell reached 2.32 MPa. Note that, wax permeation into shell was introduced after the stress exceeded 2.32 MPa. This is similar as the lower bound limit observed in this thesis where the wedge test gave an ultimate tensile stress of 1.80 MPa. On average, the model developed here suggests that the shell would crack after 8 seconds following heat introduction. The probability of shell cracking would be expected to be 4 seconds earlier than Cendrowicz work. This could be because in a 1-dimensional model, no stress concentrators exist. It is therefore no surprise that his simulation took longer to reach the critical stress level. If it were to look at the stress on shell walls (parallel to y-axis) in this study, it would take longer and that is due in part having thicker shell.

5.3.2 Sensitivity analysis

This section discuss on the effect of changing the parameters in the simulation including wax permeation in terms of wax compressibility, Poisson ratio, radii of external shell corner profile and orifice diameter.

In FLOW-3D®, fluid structure interaction (FSI) model does not work in conjunction with a porous model of the shell. The shell structure has to be considered non porous and rigid which deflects only as the wax expands. The porous model in FLOW-3D could not be used to represent the shell because of an internal limitation when using the FSI model. To take into account of the permeability of wax in the primary layer of shell, a “mass sink” method was applied. The compensation of wax volume loss as it permeates into the shell is accounted for as compressibility of the wax. The volume loss represented as compressibility is estimated from mercury porosimetry data.

$$\beta_{app} = \beta + K_v \quad \text{Equation 5-14}$$

where β is the wax compressibility from experimental data, K_v is the wax volume lost from the cylindrical wax pattern per unit pressure due to shell permeability and β_{app} is the apparent compressibility of wax.

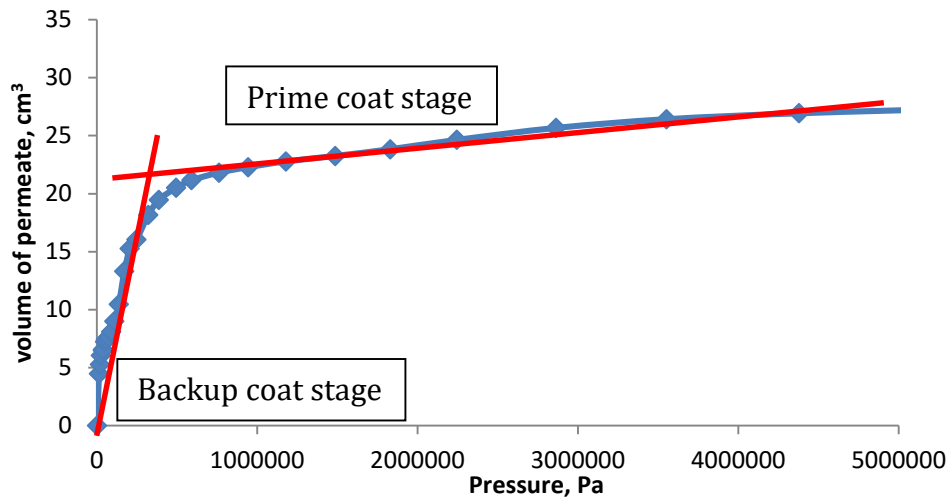


Figure 5-22: Data obtained from mercury porosimetry test. Two different gradient of the profile indicates the permeability of two different structure of shell and prime coat gradient was used to represent the volume loss as a function of pressure.

Permeability of shell is obtained as a function of volume permeated versus pressure (Figure 5-22). The prime coat stage was taken for the analysis with the assumption that

prime coat is the only layer absorbing wax, permeability of shell is linear with pressure and volume of wax penetration is at equilibrium. If the prime coat stage is considered then the apparent wax compressibility is $5.92 \times 10^{-9} \text{ Pa}^{-1}$. It was almost ten times the compressibility of wax measured by Torres (2003). This value was used as an estimation to demonstrate the effect of wax permeation taken into account using the wax compressibility. Note that even with this value, the limited compressibility theory in FLOW-3D (changes of density per unit density of wax $\ll 1$) is still valid.

Figure 5-23 shows that if the compressibility assumption is valid and compressibility is valid between 5×10^{-10} and $1 \times 10^{-9} \text{ Pa}$, the shell failure stress is exceeded over a time range of 6 - 25 s respectively if 1.8 MPa is assumed to be the shell failure limit. If the shell ultimate strength is assumed to be 3.6 MPa or higher, shell cracking could be prevented. The simulation model is highly sensitive to the changes in compressibility of waxes. It is therefore important to accurately acquire a compressibility model value for each wax to compensate for both the moulds true permeability and waxes true compressibility.

It is unclear if this feature of the simulation adequately reflects reality. One of the uncertainties in assuming the wax permeation in terms of wax compressibility is that compression of wax starts whenever there is pressure and wax permeation into the shell only occurs when the internal pressure exceeds the permeation limit providing that wax is sufficiently molten to flow. Furthermore, in mercury porosimetry, volume of mercury permeate was taken after 10 seconds equilibrium time. The volume of permeate is less if the equilibrium time is reduced. In reality, the permeation of wax occurs spontaneously and only a short time is given for the wax to penetrate the shell,

thus the permeability will be overestimated in this case and mould cracking probability will be apparently lower. It is also important to first verify the compressibility of Waxes A-E if the apparent compressibility were to be used to take into account of the wax permeation into shell.

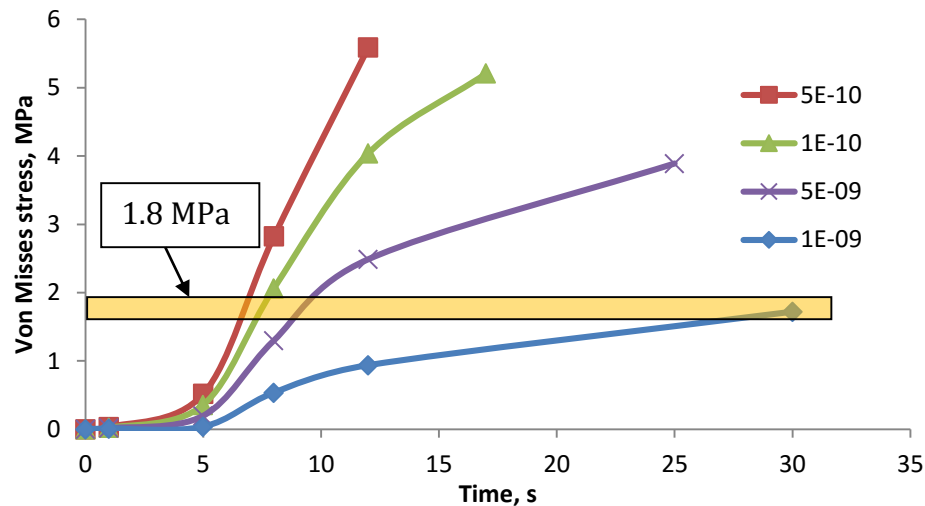


Figure 5-23: Stress observed as the compressibility is increased to take into account of the wax permeation into shell.

Poisson ratio was assumed to be 0.24 in the simulations discussed in shell stress analysis section. In this section, the Poisson ratio of shell was changed to 0.22 and 0.26. Figure 5-24 shows that as the Poisson ratio increases, the stress experienced by the shell reduced. However, the effect is not significant. It is therefore suggested that the 0.24 for Poisson ratio is acceptable for shell system with similar composition.

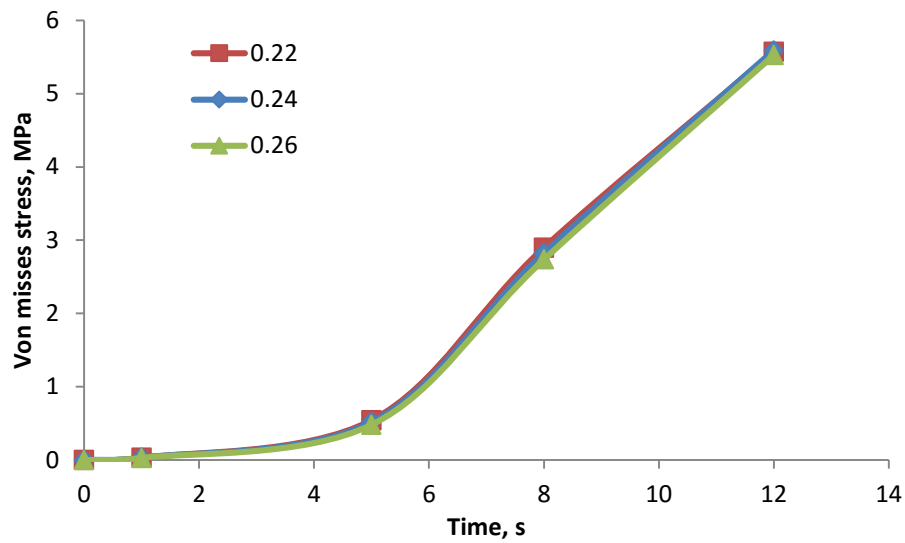


Figure 5-24: Effect of shell Poisson ratio on shell stress

Li *et al.* (2014) found that moulds were less susceptible to crack development with corner radii. Figure 5-25 agrees with this observation, literature showing that shell without radii has double the stress on the shell with 10 mm radii at the same critical location. It shows that this is because the heating rate of shell has been increased with a radii and that relieves the pressure by allowing wax to flow (Figure 5-26). The temperature difference between the two geometries at the critical node was approximately 15 °C. However, the time difference for the shell failure stress to be exceeded (1.8 MPa) is less than a second.

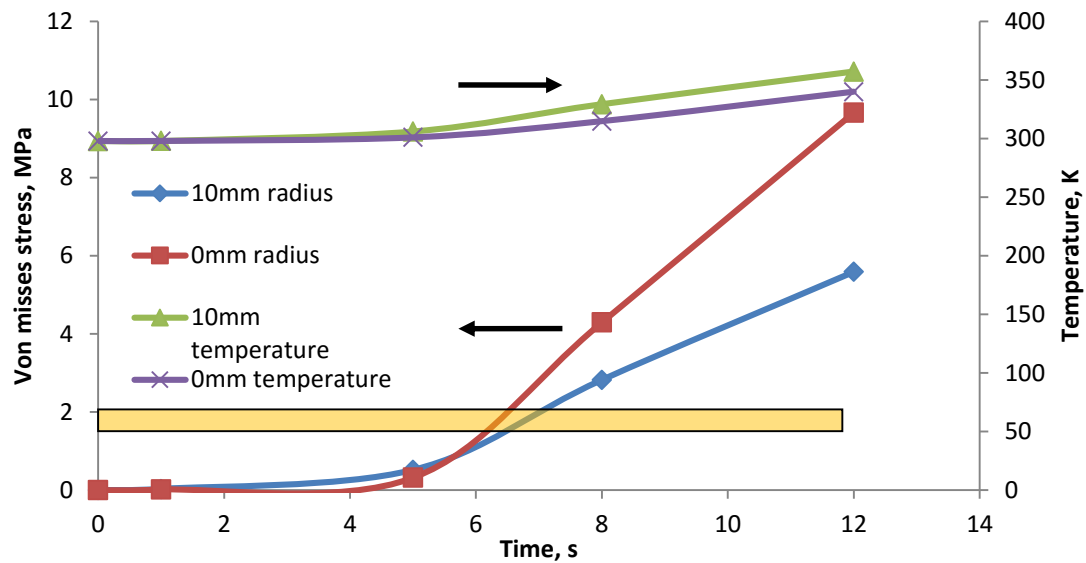


Figure 5-25: Temperature of shell at the wax top edge and effect of shell corner radii on shell stress

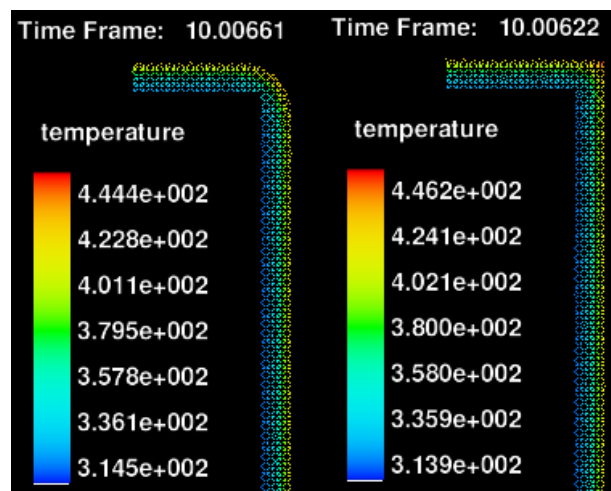


Figure 5-26: 10 mm external external radii (left) and 0 mm radii at 10 s. Temperature contour showing the wax-shell interface temperature for 10 mm radii geometry is higher than 0 mm radii.

When orifice diameter was varied up to 10 mm, it was found that the Von Mises stress on the critical node had further reduced (Figure 5-28). It can be observe in Figure 5-28 that a portion of wax has been lost by 10 seconds and the internal pressure is relatively low. Experimental trials had led to selection of only 2.5 mm and 5 mm orifice diameter in this study. The de-waxing rate for a 10 mm orifice diameter would be too high and not allow the wax properties to be differentiated. If 1.8 MPa ultimate tensile strength is

considered, the shell will crack 1 second later as shown in Figure 5-27 and this cracking will delay longer if higher ultimate tensile strength in flat bars is considered.

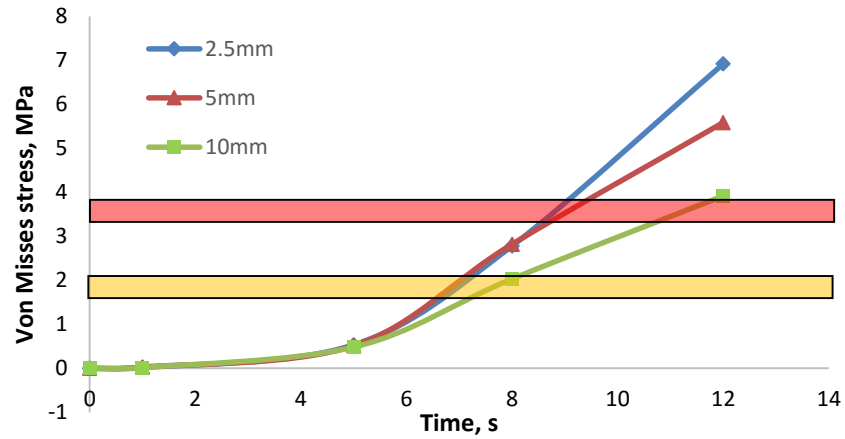


Figure 5-27: Effect of the orifice diameter

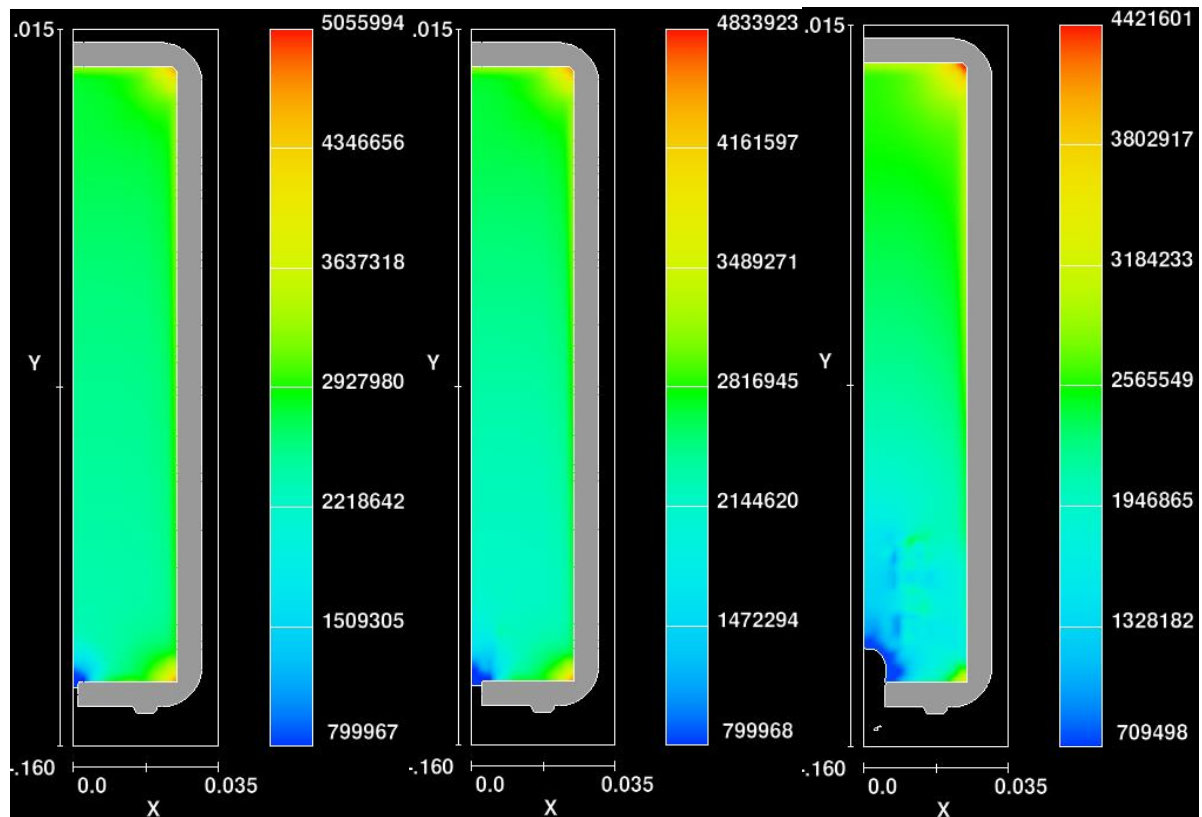


Figure 5-28: 2.5, 5 and 10 mm (left to right respectively) orifice diameter. Internal pressure in Pa.

6. MODEL VALIDATION

This chapter describes the work implemented to validate the computer model simulated in FLOW-3D with input parameters obtained in Part 1. Two validation tests were carried out (i) Physical cracks visualisation and (ii) Flow rate of wax leaving cylindrical shell mould.

6.1 Procedures

The shell moulds were made according to the standard procedures outlined in the introduction to Chapter 3. Cylindrical geometry waxes were prepared from five waxes (Wax A, B, C, D, E) for comparison. Wax patterns were injected using a MPI injection machine (MODEL 55 wax injector) into an aluminium die to obtain cylindrical wax geometry measuring 150 mm long and 50 mm diameter with no corner chamfering.

Wax injector reservoir (5 litres) and pipeline was cleaned by purging wax in the reservoir and 'washed' with the replacement wax required for the subsequent injection. The washing process was repeated until no residual wax from previous batch (by visual inspection was observed). The pressure on the injection piston and the temperatures in the injection machine were varied to accommodate different waxes to obtain same geometry after cooling to room temperature (each different wax had different shrinkage rate) to a ± 0.5 mm tolerance. Any flashes (wax flow into gap between two sides of aluminium die) were removed from the wax pattern prior to degreasing to avoid any unnecessary shell cracking. A 2 mm thick hook made of steel rod was heated and implanted into one end of the cylindrical wax. The pattern wax was then cleaned with degreasing solution and coated with the standard shell system.

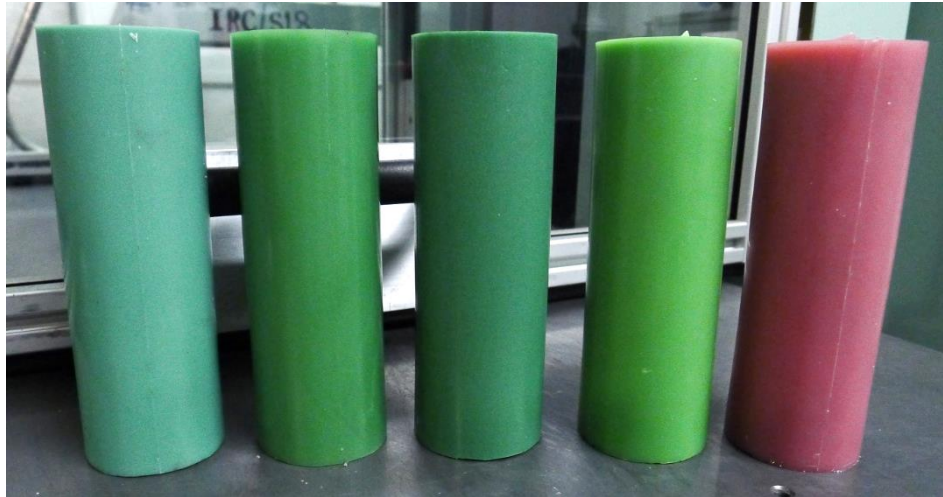


Figure 6-1: Cylindrical pattern wax-150 mm and 50 mm diameter. Wax A, B, C, D, E in sequence from left to right.

After drying, the hook was removed and the hook hole diameter was enlarged to either 2.5 mm or 5 mm diameter by drilling. The diameter of the hole is believed to vary slightly due to the stucco erosion during the drilling operation however the difference is not measurable. Any shell residuals in the holes were blown off with an air gun. The moulds were then de-waxed in the autoclave with same de-waxing settings described in the introduction to Chapter 3.

6.1.1 Visual shell cracking inspection

Inspection was undertaken to observe any visible cracks on the shell post de-waxing. Serious cracking was indicated by wax seepage out of the shell. Less obvious cracks were identified by coloured dye (Methylene blue from Sigma-Aldrich®). After de-waxing, Methylene blue dye was poured into the mould to the top and soaked for ten minutes. Methylene blue solution was prepared by mixing 1 wt % Methylene blue powder with de-ionized water. The shell cracks in moulds made on the five waxes and with two different orifice diameters were compared. If any crack was detected visually with the

naked eye after dying it was considered to have failed or the shell cracked. Mould cracks were however not evaluated for degree of severity - quantitative analyse were not undertaken on the length, thickness and frequency of cracks. Such evaluation would be complicated as the measuring method would be very subjective and personal. Therefore, shell moulds that were observed to crack were simply noted as 1 and a non-cracked mould as 0.

Ten cylindrical waxes for each type of wax were prepared and five cylindrical moulds of the same orifice diameter were de-waxed each time with the standard autoclave de-waxing cycle. These moulds were place in the middle of the de-waxing tray. The importance of number of moulds and de-waxing location has been discussed in the literature. Jones *et al.* (2001) suggested that de-waxing should be carried out without significantly varying the amount or size of the shells as this affects thermal/pressure profiles and could be responsible for unexpected cracking. Furthermore, placing the moulds in different locations within the vessel for de-wax could be responsible for the random shell cracking (Jones, et al., 2004).

6.1.2 Mould discharge flow rate

This test allowed the flow rate of wax to be estimated in the autoclave chamber. The autoclave condition is complex where the chamber is relatively large, dark, foggy and highly pressurised. These conditions restricted the application of any conventional flowrate measurement method (such as Optical videography, X-Ray videography, Particle image velocimetry or thermal imaging).

In the flow rate tests, the waxes coated with shell were individually clamped with a retort stand in middle of the autoclave (de-waxing orifice facing downwards). The autoclave was preheated prior to carrying out the flow rate test. The flow rate of wax was measured using high sensitivity Type J thermocouples. Eight thermocouples were used and they were placed 20 mm apart vertically in a steel container of 45 mm diameter and 300 mm long (Figure 6-2). The first thermocouple was at the bottom of the container.

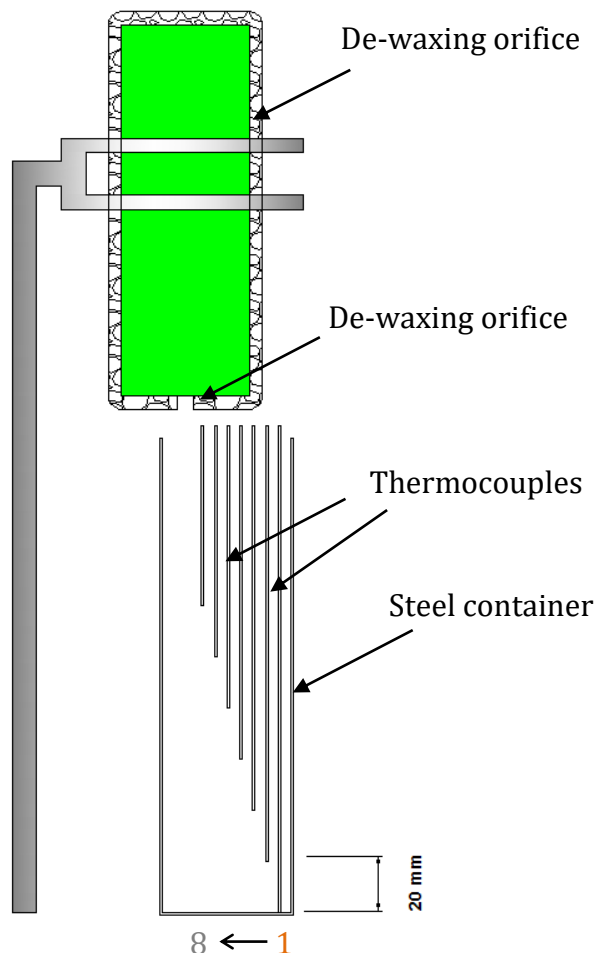


Figure 6-2: Schematic diagram of the setup carried out in the autoclave to measure the flowrate of wax. Each increment of 20 mm is one stage.

When steam entered the de-waxing chamber, the temperature in the autoclave and in the container rose rapidly up to around 170 °C. The wax in the mould started to melt

and flowed into the steel container with thermocouples. Wax that came in contact with the thermocouples reduced the temperature measured due to the low thermal conductivity of wax which remained at the melting temperature (approximately 65 °C) for some time. The temperature was recorded in real time using LabVIEW® 2012 (32 bit). When a 'kink' in the thermal profile curve was observed, it was assumed that the flow of molten wax has filled the vessel to the height of the responding thermocouple (Figure 6-3). With the known duration to fill each stage (20 mm), the flow rate for each stage could be calculated. There are 7 stages (8 thermocouples) in total and the flow rate of the melting cylindrical wax was taken as the average of the 7 stages. In this test, only one cylindrical mould was de-wax each time due to the limited number of ports available for the thermocouples. Three tests for each type of wax were carried out and the average flow rate was used.

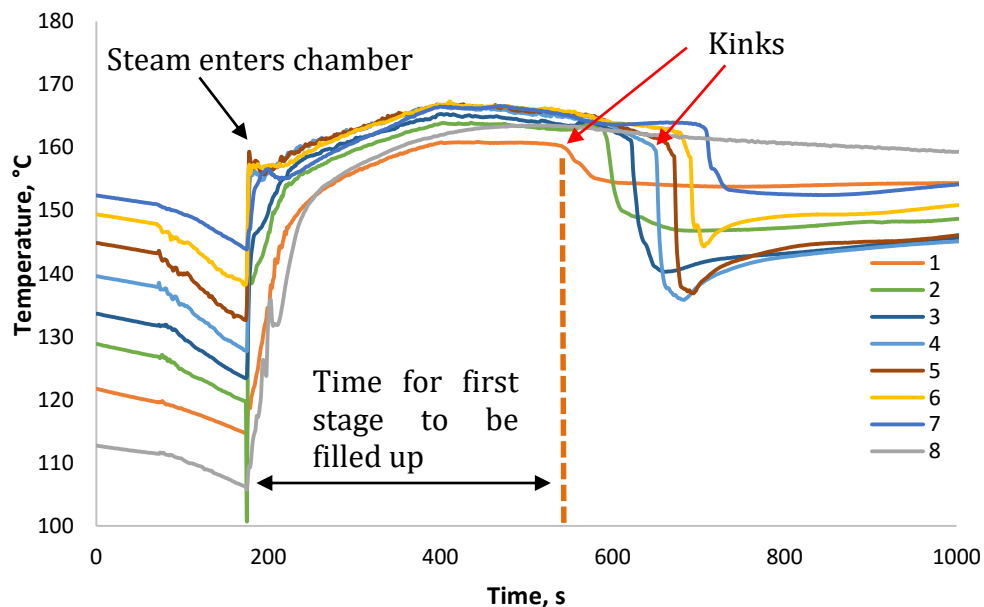


Figure 6-3: Thermal profile of thermocouples in container measuring flowrate of wax. 'kinks' of thermal profile (red arrow) assumed molten wax had reached the level.

After the de-waxing cycle, the moulds were broken in half to check on the residue wax to assure wax was completely removed (Figure 6-4).

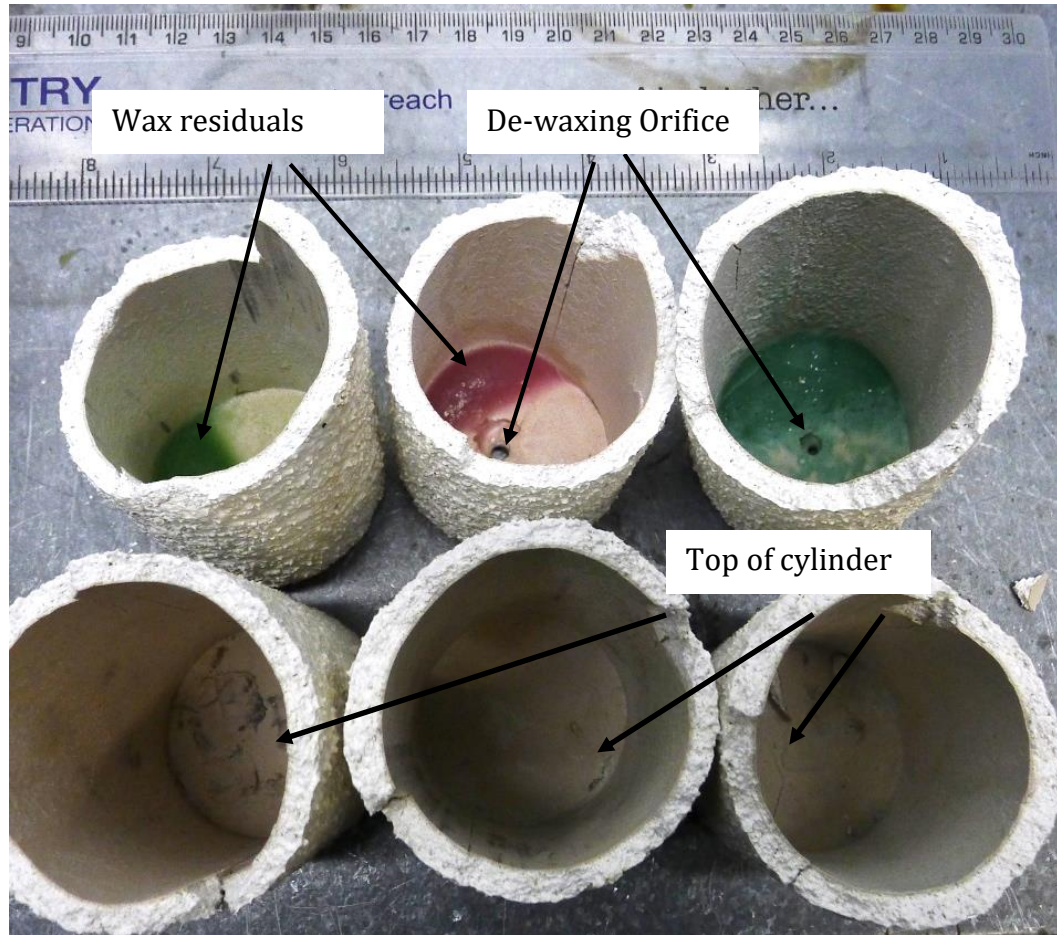


Figure 6-4: Cylindrical shell mould wax broken after the de-waxing cycle. Residuals of wax below was observed after de-waxing.

In a separate test, repeatability of the flow rate test was evaluated on Wax D. Eight shells moulds were produced in one batch for comparison. For this test, the stucco of 4-7th layer of shell layer was coated with rainfall sander to give the shell extra strength. The reason for this is explained in the discussion section. The repeatability test had four shell moulds drilled with 2.5 mm diameter and another four with 5 mm diameter.

6.2 Results and discussion

The accuracy of the computer model was validated by visually inspecting the cracks on the shell and measuring the flow rate of wax out of the mould during de-waxing. This section will discuss both tests concurrently as they are inter-dependent. Note, however, that the shell moulds for the two different tests were produced in different batches and thus the shell strength possibly varied.

After de-waxing, the shell moulds were visually inspected. Some cracks were obvious and easily identified (Figure 6-5) but for cracks that were less obvious, die penetration was used to assist (Figure 6-6). It was observed that the location of cracks on mould varied but they were commonly found at the close end of the mould (as shown in both figures). This location for shell cracking was predicted in the FLOW-3D simulation (Chapter 5). Occasionally, cracks were found at the edge at the orifice end of the shell and also cracks on the midsection caused by the hoop stress (Figure 6-7). However, the locations of crack were not recorded. More samples would be required if quantitative analyse of the locations of cracks was to be undertaken.

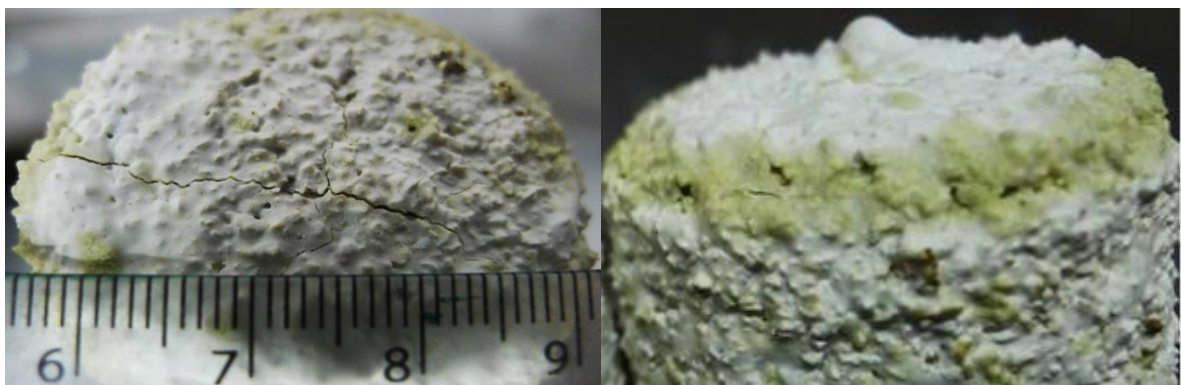


Figure 6-5: Serious shell cracking on a cylindrical geometry on the closed end and at the corner (close end)



Figure 6-6: Methyl blue stain to detect cracks on the top (left) and at the edge (right) after de-waxing

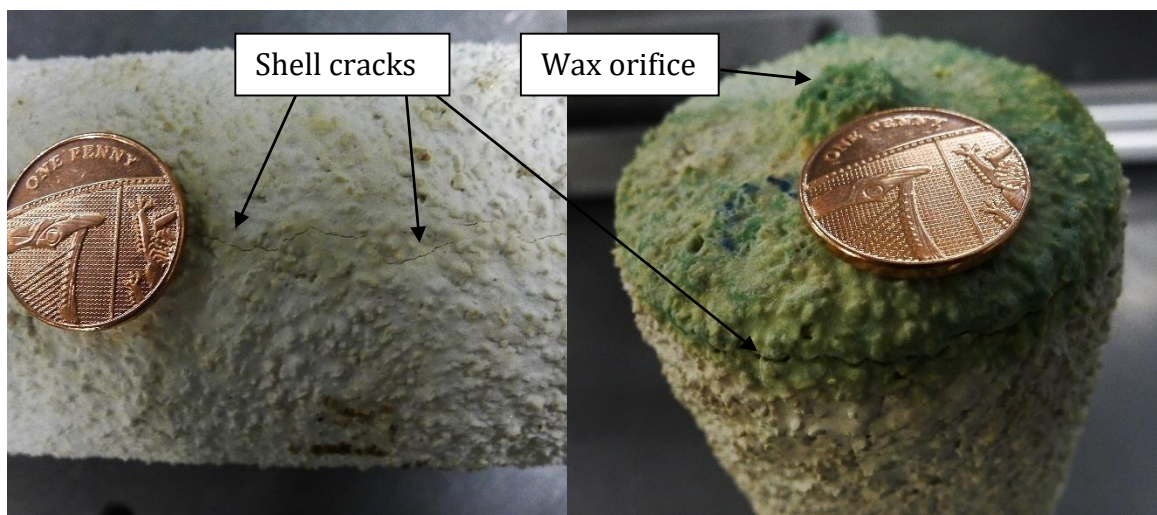


Figure 6-7: Shell cracking on cylinder mid-section due to hoop stress (left) and at the sharp edge of the orifice end (right). One penny coin for scale.

The results of both validation tests were analysed and are summarised in Table 6-1. Wax A which is known in the industry environment as the non-cracking shell wax showed no difference in percentage of cracking between the two different orifice diameters. Both orifice diameters gave 60 % cracking which was surprisingly high given the industrial results. This was predicted in the simulation results where the critical stress on shell is similar for the 2.5 and 5 mm orifice diameters even if the ultimate tensile strength is assumed to be 6 MPa or higher. From this finding, the wax should perhaps to not be

referred to as 'non-shell cracking wax'. In the flow rate test, the flow rate of Wax A with 5 mm orifice was found to be higher (almost double) the flowrate measured with a 2.5 mm orifice.

Wax B and C which contains two types of fillers exhibit a similar flow rate pattern to Wax A where it was higher for the 5 mm orifice diameter compared to 2.5 mm. The flow rate increased by approximately 2.5 fold when the orifice diameter was increased. In both waxes, there was a 40 % decrease in shell cracking percentage observed when the orifice diameter was doubled (surface area is quadrupled). In the model, there was only 0.5 s difference in the simulation failure prediction between the two different orifice diameter if 3.6 MPa is considered as the ultimate tensile strength and almost no difference at 1.8 MPa.

Wax D which has one type of wax filler but with both angular and spherical filler morphologies showed a different flow rate behaviour. The 5 mm orifice diameter had lower average flow rate than the 2.5 mm hole. It was also observed that the percentage of cracking did not change by varying the orifice diameter. This was predicted in the simulation where the shell cracking was implied to occur at the same time for both the 2.5 and 5 mm orifice diameter if the ultimate strength of shell was set at 3.6 MPa. The simulation also predicted Wax D to reach the failure stress at the earliest time in the process compared to the other four waxes. However experimentally, some moulds survived and this could due to some other active mechanism. It could due to the nature of the shelling process where shell strength varies. The probability is that the model is not capturing a pressure release mechanism either by permeation of wax into the shell or drainage through the hole correctly.

Wax E which has no filler behaved in a similar manner to Wax D in term of flow rate. The flow rate was found to decrease from 1.32×10^{-6} to $0.50 \times 10^{-6} \text{ m}^3\cdot\text{s}^{-1}$ when the diameter of the orifice was doubled which clearly throws the experimental data into question. In the simulation, Wax E exceeds the failures stress at the same time for both orifice diameters and so this would suggest similar failures number should be expected. In the experimental investigation, the failures were 100 % with a 2.5 mm orifice and 20 % with a 5 mm hole, which is clearly counter the simulation prediction. However, in the de-waxing flow rate test, the 2.5 mm diameter orifice shell survived the complete de-waxing process while the 5.0 mm diameter orifice shell failed (Table 6-1). Generally, there is an evidential correlation behind the simulation and the experimental work for all waxes where the orifice diameter did not differ significantly except wax E. Wax E exhibit a large difference in percentage cracking in the validation test which would not be expected from the simulation results.

In Table 6-1 it can be seen that there is a correlation between shell cracking and the flow rate measured in all waxes (Shell that cracked are noted as red and green indicates non-cracked). It was observed that shells that cracked had lower flow rates (disregarding the orifice diameter) and this was observed in all waxes. It is uncertain if shell cracking is caused by the low flow rate or vice versa. One possible explanation to describe how shell cracking reduces flow rate measured is that the cracked shell relieve the internal pressure and so there is no pressure forcing the wax into the container through the orifice. There are other possibilities that may affect the flow rate measured such as the wax flowing through the cracks and delay the flow into the container underneath the mould. If the wax did flow into the container, it may or may not have splashed and/or stuck to the thermocouple in the next stage, giving a false reading. In addition to these

possibilities, the higher shell mass could also contribute to a stronger shell, thus affecting the probability of shell cracks developing.

Table 6-1: Percentage crack and de-waxing flow rate test results. Green flowrate indicates non-crack shell and red is cracked during the flow rate test

Wax (mm)	Average shell mass, g	Percent age crack, %	De-waxing flowrate, $\times 10^{-6} \text{ m}^3\text{s}^{-1}$	Flowrate standard deviation, $\times 10^{-6} \text{ m}^3\text{s}^{-1}$	Wax starts flowing, s	Wax end flowing, s	Time to Flow, s
A							
2.5	288.56	60	1.09	0.18	351.6	573.4	221.8
5.0	287.66	60	1.85	1.04	374.3	534.6	160.2
B							
2.5	290.76	100	0.92	0.14	430.9	691.6	260.8
5.0	288.42	60	2.31	1.00	418.7	532.2	113.5
C							
2.5	283.06	80	1.10	0.19	377.0	596.8	219.8
5.0	283.44	40	2.53	0.65	353.0	446.4	93.4
D							
2.5	279.26	80	0.31	0.05	139.0	915.0	776.0
5.0	279.70	80	0.26	0.13	138.9	1071.5	932.6
E							
2.5	281.70	100	1.32	0.39	107.1	314.8	207.8
5.0	276.04	20	0.50	0.09	139.0	620.5	481.5

The average shell mass coated on Wax D for example weighed approximately 9 grams less than Wax A shell batch and this could contribute to the higher percentage of shell cracking in Wax D compared to Wax A. The flow rate test has errors for the reasons discussed but there was also the shell failure error. If the shells failed at a fixed load (no variance) then the test would probably more reliable but of course the shells do have a large variance in strength and so this will reflect in the data. No shells completely survived (0 %) and as only 5 samples were used in each test, confidence was limited. In the strength tests, the standard deviation is about 10 %. Thus the strongest shell could have a strength of 2.34 MPa ($1.8 + (1.8 \times 0.34)$). The strongest shell might be 2.34 MPa and the weakest 1.26 MPa (almost a factor of 2). This is because standard deviation does not account for the entire spread of possible strengths. Only 68 % of the samples will fail

in the range of one standard deviation and to get 99.7 % of all possible results, it needs three times standard deviation.

In the repeatability test with Wax D, the outer layers of the backup coat (4-7th layer) were stuccoed with a rainfall sander to increase the mechanical strength of shell. The purpose of doing this was to eliminate any issue caused by the shell cracking that affects the flow rate measured. It was observed that in the repeatability test, the wax flow rate from a 5 mm orifice is higher than from 2.5 mm diameter orifice (Figure 6-8). This is intuitively more reasonable compared to the results for Wax D in the de-waxing flow rate test. However, the error indicates that it would be possible to produce opposite flow rate results. But these results are more consistent compared to the flow rates found in Table 6-1 where the stuccoing was performed by hand (stucco in a sieve). It was also observed that flow rate from hand stuccoed mould had slightly higher flowrate than those found in rainfall stuccoed materials for both orifice diameter (Table 6-2).

These tests show that shell cracking does affect the measurement of flow rate by this method of determination. The variability of measurements with this method is inevitable and the result obtained is not sufficiently sensitive to differentiate the wax flow rate between different waxes. This is mainly because the shelling process is variable and consequently the shell failures are variable. The flow rate measurements do however give a good indication of when to expect the wax start to flow and when it might end for comparison with the computer simulation.

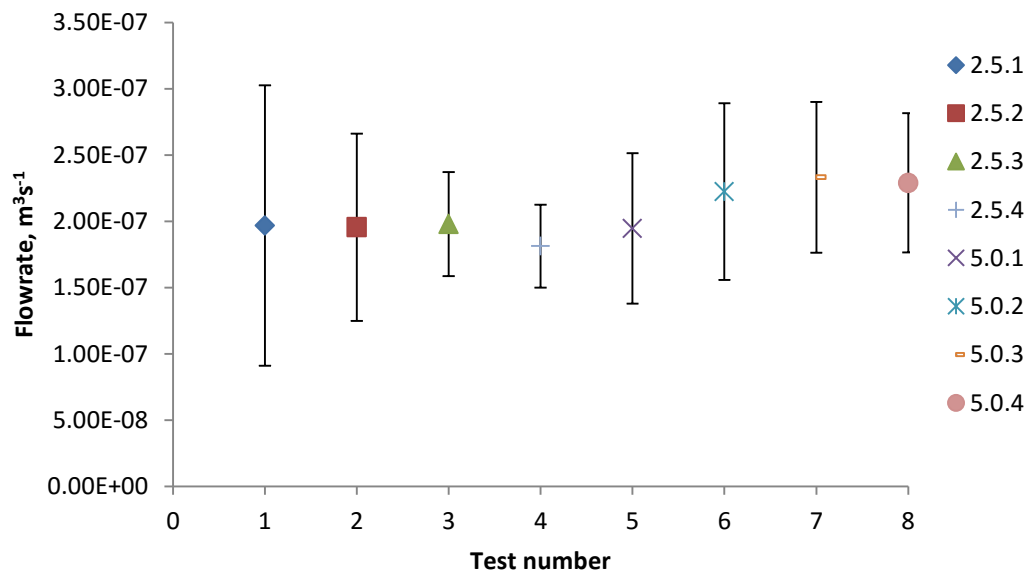


Figure 6-8: Repeatability test on Wax D to observe the flowrate and the graph legend indicates the orifice diameter and sample number. It was found that some flow rates does overlaps.

Table 6-2: Summary of the flow rate results from preliminary flow rate test and the repeatability flow rate test on Wax D.

Flowrate, m ³ ·s ⁻¹	Orifice diameter, 2.5 mm	Orifice diameter, 5.0 mm
Preliminary test	3.11 x10 ⁻⁷	2.56x10 ⁻⁷
Repeatability test	1.93x10 ⁻⁷	2.20x10 ⁻⁷

The flow rate test was also used to validate the computer simulation model. The results are compared in Figure 6-9 and Table 6-3. This was only undertaken for Wax C as a complete simulation required long computational time (approximately 2 weeks). It was found that the ‘actual’ wax flow starts 323 s later in simulation than in validation work for the 2.5 mm orifice. For 5 mm orifice, flow commenced 247 s later in the simulation. Generally, it took the simulation 377 s longer to completely de-wax relatively to the experiment for a 2.5 mm orifice and for 5 mm orifice is 387 s longer. The flow rate in experimental work for 2.5 mm orifice diameter is 2.4 times slower than in 5 mm orifice.

In the simulation however, the 2.5 mm model flows only 1.2 times slower than the 5 mm model. The large difference in flow rate between experiment and simulation may be due to the assumption that the autoclave-wax HTC is similar to the autoclave-shell HTC. The autoclave-wax HTC could be larger in reality (steam condensation on shell surface and pores and higher surface shell roughness gives smaller autoclave-shell HTC) and with time, the effect was magnified in the complete de-waxing simulation. However, this assumption should not affect the shell stress simulation in short simulation runs (less than 15 s) as the exposed orifice surface is relatively small compared to the shell surface.

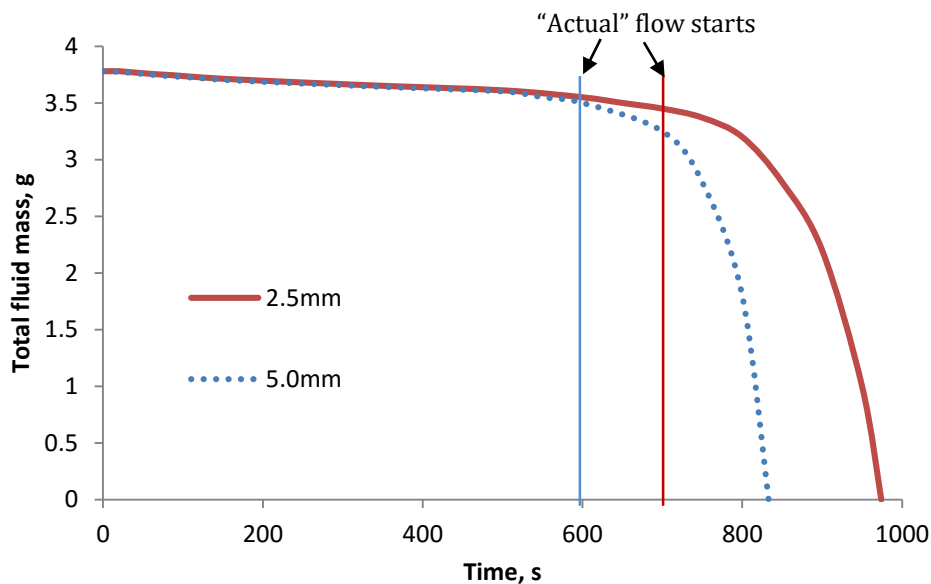


Figure 6-9: Comparing the time required for two different orifice diameter to be fully empty. Wax starts to flow from 0 s but the “actual” flow start around 600 and 700 s for respective orifice diameter.

Table 6-3: Summary of flow rate comparison on Wax C from the time steam enters the chamber

Wax outflow diameter (mm)	Experimental			Simulation		
	Recorded duration to flow, s	Wax Start to flow, s	Time wax actually flow, s	Recorded duration to flow, s	Wax Start to flow, s	Time wax actually flow, s
2.5	597	377	220	974	700	274
5.0	446	353	93	833	600	233

The flow rate measurement method is sufficiently good method to understand the flow rate of wax in the autoclave. This measurement could tell if the simulation is valid by comparing the total wax flow time. However, improvements could be made to reduce the error. Simulation was found to be apparently 300-400 s slower than the experiment. Further work is required to clarify the issue of slower wax flow in simulation in regards to the autoclave-wax HTC.

7. CONCLUSION AND FUTURE WORK

The objective of the project was to predict the shell cracking during the de-waxing process. The research programme was divided into an experimental and a modelling phase. The experimental work aimed at determining key thermo-physical parameters required by the modelling framework as well as characterising the shell microstructure.

In this project, the experimental data obtained was sufficient for the modelling work. The project had developed a property database for the wax and shell, which could be used for future model analysis and development of the shell structure or wax understanding. The few parameters found to be significantly important during data acquisition for simulation work were the viscosity of wax, thermal expansion of wax and the permeability of shell. Geometry and composition of fillers was found to affect the viscosity of wax and consequently the de-waxing flowrate. These fillers also affects the thermal expansion rate of the wax that results in shell cracking. A restriction of wax permeating shell was found to be due to the combination of wax properties and microstructure of shell such as wax viscosity, heat capacity, thermal conductivity, and shell porosity. One important limitations in the experimental work is the reliability of the 3-point bend test to represent the stress on the particular shell geometry remains uncertain.

In the modelling framework, it has been proposed with a model that accounts for the viscous flow of the wax and the stress state development in the shell would be adequate to predict failure in the shell. With the fluid-structure interaction module, the model is able to predict the evolution of stress state during the de-waxing process. It was found

that the present framework is not able to derive a criteria for shell cracking. It is not enough to determine location with high stress levels. This is because it require information of damage evolution as function of the shell microstructure (ie., void distributions, and grain size, among others), which is variable. Therefore, predicting shell cracking is a statistical phenomenon. One limitation in the simulation model was the permeability of the shell being neglected and this could affect the probability of shell cracking. It is still unclear if permeability of shell can be compensated for by wax compressibility in the simulation and adequately reflects reality. Another limitation in the model was that the mesh sensitivity was not completely validated. Smaller mesh simulation without compromising the computation effort needs to be further understood.

The model validation method base on the de-waxing flow rate in the autoclave has shown to be a good indication of differentiating flowrate of different waxes. However, the test method require improvement to eliminate the uncertainties of wax splashing on thermocouples or mould leaks affecting the recorded reading. At current time, this method is most suitable for validating the model.

In conclusion, the proposed modelling approach provides a basic framework for the implementation of damage mechanism models that can predict failure conditions. Further future work is suggested in section 7.2 to allow progress towards the objective.

7.1 Conclusions for subsections

- Microstructural investigation of the wax has shown that waxes A and D contain one type of filler (cross-linked polystyrene), in Wax A the filler was rounded where as a proportion of the filler in wax D was also angular in shape. Waxes B and C contained two types of filler, cross-linked polystyrene and terephthalic acid, where the terephthalic acid was angular and the polystyrene rounded and almost spherical.
- FTIR results did not show any significant differences in chemical compounds between the filled waxes. The unfilled wax (Wax E) was found to have higher proportion of carbonyl groups. Wax A contained small amount of those carbonyl groups.
- The flexural strength evaluation of the shell system showed that different methods of sample preparation affected the strength measured and therefore it is important to identify the strength which best represents the process of interest. It was established that the shell strength varied with preparation of the sample. Materials treated in the autoclave had higher strength than those de-waxed by refrigeration and this was shown to be due to colloid aging (curing). Wax which permeated into the shell pores appeared to also increase the mechanical strength of shell tested at ambient condition. It was found that within the repeatability of the test the specimen orientation was not a significant factor. Testing the specimens while they were wet had a significant influence on strength, reducing it by as much as 50 %. For the simulation work it was concluded that two strength are required, the strength of the shell prepared by fridge de-waxing tested with 3-point bend test and wedge test as these give value without cure and

with no remnant wax. Wax permeating into the shell as shown to increase the measured strength.

- Flat bars had a Young's modulus of 2.26 GPa and the wedge geometry shell had an average of 6.27 GPa. For the simulation, Young's modulus of shell mould was determined from the stress-strain curve (3-point bend test) based on samples prepared by the fridge de-waxing method. This was done in preference to vibrational analysis because of the greater reliability and the simplicity of the method. The data obtained was considered with respect to known literature data and deemed usable. Young's modulus from the wedge test was not used in the simulation due to the relatively large error developed in the test.
- Two methods were evaluated to determine thermal expansion and correlated with PVT data generated by a third party. The dilatometry method using a capsule was found to be unusable while a density bottle method was shown to give a viable alternative to PVT. It was found that the thermal expansion of the filled waxes was similar in all cases. The unfilled wax expansion was larger in comparison. Thermal expansion of wax measured by modified density bottle is suggested to be used for measuring thermal expansion up 180 °C, this method is not ideal but it is reliable and more accessible than either capsule dilatometry or PVT measurements. The results are acceptable as the influence of pressure is small however the standard deviation is relatively high compare to PVT measurements.
- The average pore diameter of the shell measured by mercury porosimetry was 131.2 nm and the percentage porosity was 21.63 %. The bulk density of the shell was 1925 kg·m⁻³ and the apparent (skeletal) density was 2456 kg·m⁻³. The

thermal expansion of shell was $2.55 \times 10^{-6} \text{ m} \cdot ^\circ\text{C}^{-1}$. The thermal expansion of wax to be used in this project was obtained from a density bottle method.

- Specific heat capacity of shell is constantly increasing over the temperature range of interest, ranging between $0.9 - 1.3 \text{ J} \cdot \text{g}^{-1} \cdot ^\circ\text{C}^{-1}$. Filled waxes were found to have lower specific heat capacity than non-filled and it was suggested that this is due to the fillers acting as thermal conductors.
- The solidification and melting point of waxes determined from the specific volume data and DSC by extrapolation of the thermal expansion data requires further justification. For simulation purposes, the melting point provided by the wax suppliers was used. The latent heat of waxes was determined from the DSC data.
- The thermal conductivity of shell was found to be $3.5567 \text{ W} \cdot \text{m}^{-1} \cdot \text{K}^{-1}$ and the thermal conductivity for filled wax $0.2167 \text{ W} \cdot \text{m}^{-1} \cdot \text{K}^{-1}$. The thermal conductivity for the unfilled wax was assumed to be $0.1967 \text{ W} \cdot \text{m}^{-1} \cdot \text{K}^{-1}$.
- The permeability of shell was found to be 90 nm^2 with water as permeate and 22740 nm^2 when wax was use as the permeate. The results of these tests remain debatable.
- Viscosity was measure by capillary flow and rotational plate methods. The plate method gave the more reliable and useful results. The rheological data obtained as a function of shear rate at different temperature were fitted into the Carreau model. More work is recommended to understand the yield stress measured during the examination of wax B and C. It was postulated that these observations of a yield stress were because of the waxes having angular filler particles that affected the flow wax depending on how the fillers were oriented. The rheological

behaviour of wax measured using the capillary rheometer is not comparable to viscosity measured using the rotational rheometer. The viscosity measured by the capillary rheometer is too large and was not use in the computer simulation of the de-waxing process.

- The adhesion tension test was compared to the surface tension results to estimate the contact angle between wax and mould. For the interaction between the shell primary surface and wax, the contact angle can be assume to be zero. This assumption will equate to the surface tension measured using the Du-Nuoy ring.
- FLOW-3D® was used to simulate the dewax process. The FSI model was used to predict the interaction between shell mould and wax. The model gives a prediction of stress development during de-wax and the location where those stresses first exceed the experimentally measured critical fracture stress. This indicated the probable location of failure. The prediction and experimental results agree. However, the model did not appear to be very sensitive to changes in the wax properties. Only waxes with significantly different rheological parameters appear to indicate differences in the time taken to reach critical stress. The limitation of the model was that the permeation of wax into shell by wax was not addressed directly. The penetration of wax into shell was taken into account in terms of compressibility and it was showed that the effect on shell stress was significant by varying the values. It was therefore important to determine the compressibility of each wax. The simulated geometry was evaluated experimentally by dewaxing cylindrical waxes in the autoclave. The drainage time and the propensity of the shell to crack were determined. Due to

the nature of ceramic failure the spread in the data was significant and so only limited conclusions could be drawn.

- Given the limitation imposed by the assumptions made, the model still allows comparison with the experimental observations. The time to reach critical failure stress reflects the degree of cracking determined experimentally. The faster the critical stress was reached the higher the probability the shell would crack. The model predicts that there can be little difference in the time taken to reach the critical stress if the orifice diameter different is small and this stops the drainage, not allowing pressure relief before the critical stress is reached regardless of the orifice diameter. Larger orifice diameter allow pressure relief sooner only if the orifice becomes sufficiently large. The only significant difference between model and experiment was observed in the unfilled wax. The reason for this remain unclear. Shell cracking was found to have a correlation with the low flow rate but it is uncertain which issue initiates the problem. The flowrate of the simulation was found to be slower than the experiment, this is mainly due to the lack of autoclave-wax HTC data from experiment.

7.2 Future work

There is more work required before the model can be used to predict the shell cracking of waxes accurately. More trials of various shell systems and construction techniques should give additional confidence in the measurement methods.

Despite the methodologies explored in this thesis, it remains a largely unexplored research area (the measurement of the physical properties related to de-waxing). All of

the physical properties have been measured as a function of temperature, however the effect of rate of change of temperature was not taken into account.

- The occasional presence of a yield stress in wax B and C still remain unexplained. It was suggested though not proven that terephthalic acid thermal expansion causes the yield stress, however, more work needs to be carried out to verify this. The influence of a yield or presence of yield during the de-wax process is not known but may become so by further developing the simulation software.
- Oscillatory rheology test was not carried out in this project because the macroscopic mechanical behaviour is out of the modelling capabilities of the software. This behaviour would allow the model to predict more closely the interaction between the wax and mould.
- It was suspected the hydroxyl group compounds that are found in the prime coat slurry do burn off at 1650 °C and this will have affected the adhesion tension results (see section 4.12 for discussion). More work is required to identify the effect of hydroxyl group on the adhesion tension measured.
- The shelling process is operator sensitive and more experiments could be carried out with different operators to clarify any errors that interfere with the result. This includes the variability of pores that affect the thermal conductivity measured. The shell could also be stuccoed using a rainfall sander or fluidised bed to bring about greater consistency. This includes the wax flow rate measured for the validation work.

- Thermal conductivity/thermal diffusivity can be plotted as a function of shell porosity. This function would help future researchers to just measure the thermal diffusivity of shell using in-line flash and incorporate those results in the function to obtain the thermal diffusivity caused by the penetration of steam. For the current modelling work, the measured temperature at the interface between shell and wax is used as a boundary condition. The interface temperature is expected to be different between a flat surface and sharp edge as the heat of penetration should be doubled.
- Shelling crack location could be quantitatively analysed for the severity of cracks. This would require a larger number of samples and at least 25 samples are suggested (since there are 5 different possible cracking location). When the recurrence with respect to location of a crack is identified, a strain gauge could be used to quantitatively analyse the magnitude of the stress causing the cracking at that particular location.
- The difference of orifice diameter of the model test geometry should be increased to give better comparison and to observe obvious differences in flowrate. However, diameter should be small enough to differentiate between different waxes. Alternatively, it may be more useful to vary the volume of wax to orifice diameter ratio by varying the volume of the cylindrical pattern wax. It is suggested to use 2.5, 5 and 10 mm holes with the same geometry. For other geometries, it is suggested to use orifice diameter to wax volume ratios of 0.0085, 0.0170, and 0.0340.

- Permeability of shell was not explicitly included in the computer model due to the software package constraints. Evidence suggest that this parameter may have significant impact on shell failure and directly including this parameter would allow a more accurate computer simulation. The geometry of the wax pattern will change the interaction of the expanding wax with the mould. A model that evaluates this issue would be advantageous. This was not be captured in the current model. It is suggested that a relationship of wax penetration depth with temperature, pressure and time needs to be established. It is suggested to have fluorescent die mixed with the wax to allow clearer observation of wax penetration into the porous shell. Generic permeability tests only offers the permeability of shell when the flow rate is at equilibrium. The initial non-equilibrium penetration of wax into the shell is a critical aspect of de-wax cracking. With the penetration data and in combination with developing the FSI model to work with a porous component should give better simulation result.
- The simulation heating rate is currently obtained from the thermal profile in the autoclave. In future, the simulation can be modelled with a porous model, allowing the steam to be modelled as mass and heat diffusion into the shell.
- This project only focused on shell cracking caused by the expansion of the wax. It is well known that depressurisation rate in the autoclave can also cause cracking and so this should be studied.
- This project had used 1 mm mesh size on shell for finite element analysis. Further studies on the mesh size is required to observe the accuracy on the mechanical stress simulated without compromising too much on the computational time.

- Simulating $\frac{1}{4}$ of the cylindrical shell would allow the observation of hoop stress with shorter simulation time. This would develop a better understanding of the shell cracking.
- The flowing pattern of wax out of the cylindrical container should be better understood. Particle Image Velocimetry (PIV) can be used to demonstrate the flow of fluid with similar viscosity as wax in the same geometrical setup. The fluid properties and container material however requires justification to represent the investment casting process correctly. Or, X-ray videography could be used to observe the melting of wax in an oven furnace.
- It is still unclear if an impermeable mould in the simulation would reduce the flow rate of wax compared to the experiment. It is suggest to carry out the same flowrate test as undertaken in this study but with an impermeable cylinder mould (steel can for example).

8. REFERENCES

- Anderson, J. J. (1995). *Computational Fluid Dynamics, The basics with Applications* (International Editions ed.). New York: McGraw-Hill.
- Asmania, M., Kermela, C., Lerichea, A., & Ourakb, M. (2001). Influence of porosity on Young's modulus and Poisson's ratio in alumina ceramics. *Journal of the European Ceramic Society*, 21(8), 1081-1086.
- ASTM C1161-13. (2013). Standard Test Method for Flexural Strength of Advanced Ceramics at Ambient Temperature.
- ASTM C1259-14. (2014). Standard Test Method for Dynamic Young's Modulus, Shear Modulus, and Poisson's Ratio for advanced Ceramics by Impulse Excitation of Vibration. ASTM International.
- ASTM D790-10. (2010). Standard test method for Flexural Properties of Unreinforced and Reinforced Plastics and Electrical Insulating Materials. ASTM International.
- Barnes, H., Hutton, J., & Walters, K. (2005). *An Introduction to Rheology* (Third Edition ed.). London: Elsevier.
- Beeley, P., & Smart, R. (1995). *Investment Casting*. London: The Institute of Materials.
- Bergna, H. E., & Roberts, W. O. (2005). *Colloidal Silica Fundamentals and Application*. CRC Press.
- Blayson, R. (2013). *Wax Matters*. Issue 19.
- Branscomb, T. (2002). The importance of green MOR for Autoclave cracking. Chicago: Investment casting institute - 50th technical conference & expo .
- Branscomb, T. (2010). Innovative Dewax Method Unlocks Potential for Investment Casters. Dearborn: Investment Casting Institute.
- Brinker, C. J., & Scherer, G. W. (1990). Sol-gel science: The physics and chemistry of sol-gel processing. *Academic Press inc*.
- British standard. (1994). *Section 10.2: Determination of permeability and standard air flow capacity at elevated temperatures*.
- Brown, R. P. (1988). *Handbook of Plastic Test method*. Essex: Longman Scientific & Technical.
- Bryne, L. E. (2008). *Aspects on wettability and surface composition of modified wood* (Thesis ed.). Stockholm: KTH, Royal Institute of Technology.
- Campbell, J. (2011). *Complete Casting Handbook*. University of Birmingham: ELSEVIER.
- Cendrowicz, A. (2004). *The characterisation of wax injection moulding and de-wax processes in investment casting, Phd thesis*. University of Birmingham: Chemical Engineering.

- Chakravorty, S. (1999). Assesment of Properties of Investment Casting Waxes. *Proc. of 24th BICTA conference on Invesment Casting*. Oxford, UK.
- Chen, X., Li, D., Wu, H., & Tang, Y. (2011). Analysis of ceramic shell cracking in stereolithography-based rapid casting of turbine blade. *International Journal of Advance Manufacturing Technology*, 55, 447-455.
- Darcy, H. (1856). *Les Fontaines Publiques de la Ville de Dijon*. Paris: Victor Dalmont.
- Fabio, J., Sandro, C., Ivo, V., & Jaime, A. (2009). Microwave dewaxing applied to the investment. *Journal of Materials Processing technology*, Issue 209 pp 3166-3171.
- Ferg, B. (2001). Mold Cracking case study using six sigma Approach. *49th Annual Technical Meeting* (p. 16). Orlando, Florida: Invesment Casting Institute.
- Ferreira, J., & Mateus, A. (2003). A numerical and experimental study of fracture in RP stereolithography patterns and ceramic shells for investment casting. *Journal of Materials Processing Technology*, 134, 135-144.
- Fielder, H. (1999). The effect of fillers on the Physical Properties of Investment Casting Waxes. *24th BICTA Conference on Invesment Casting*, (p. 17). Oxford, UK.
- Flow-3D. (2014). *User Manual v10*, FLOW Science.
- Gebelin, J. -C., Jolly, M. R., Cendrowicz, A. M., Cirre, J., & Blackburn, S. (2004). Simulation of Die Filling for the Wax Injection Process:Part I. Models for Material Behavior. *METALLURGICAL AND MATERIALS TRANSACTIONS B*, 35B, PP 755-759.
- Gebelin, J.-C., Jones, S., & Jolly, M. (2001). Modelling of the de-waxing of Invesment Cast Shells. San Diego: Proceedings of computational modelling of Materials, Minerals and Metals Processing.
- Hahn, T., & Rosmait, R. (2002). High Temperature Shell Permeability. *50th Techninical Conference& Expo* (p. 12). Chicago: Invesment Casting Institute.
- Harkins, H. N., & Harkins, W. D. (1929). The surface tension of blood serum, and the determination of the surface tension of biological fluids. 7(2).
- Hendricks, M. J., Wang, M. P., Filbrun, R. A., & Well, d. K. (2002). The Effect of Seal Dips on Ceramics Shell Properties and Performance. *50th Technical Conference& Expo 2002* (p. Paper number 18). Chicago: Invesment Casting Institute.
- Hyde, R., Leyland, S., Withey, P., & Jones, S. (1995). Evaluation of the Mechanical Properties of Invesment Casting Shells. *22nd BICTA Conference* (p. Paper 7). BICTA.
- Iler, R. K. (1978). *The Chemistry of Silica*. Wiley-Interscience.
- Imerys. (2009, November). *Molochite, product specification*. Retrieved March 2011
- Jones, S. (2005). rapid shell build for investment casting: Wax to De-wax in Minutes. Dearborn, Detroit, USA: 53rd ICI technical Conference and Expo.

- Jones, S., Cendrowicz, A., Jolly, M., Gebelin, J.-C., Lewis, K., & Al-Dawery, I. (2002). Boilerclave Thermal Profiles and the Effect of Moisture Upon Ceramic Shells During the Steam De-wax Process. *50th Technical Conference & Expo 2002* (p. Paper number 14). Chicago: Investment Casting Institute.
- Jones, S., Jolly, M., Blackburn, S., Gebelin, J.-C., Cendrowicz, A., & Lewis, K. (2003). Effect of moisture upon mechanical properties of ceramic moulds during high pressure steam dewaxing. *material science and technology*, Vol 19.
- Jones, S., Jolly, M., Blackburn, S., Gebelin, J.-C., Cendrowicz, A., & Lewis, K. (2004). Autoclave thermal profiles during steam de-waxing of investment shells: Part 1. *Materials Science and Technology*, 24.
- Jones, S., Jolly, M., Gebelin, J.-C., & Cendrowicz, A. (2001). Dewaxing of Investment Shells- Preliminary Results . *FOCAST*. Cheltenham, England,: 25th BICTA Conference,.
- Jones, S., Yuan, C., & Jolly, M. (2003). Fluid bed and rain fall sanded shells - An investigation into fundamental structural and mechanical property differences. *51 st Technical Conference & Expo* (p. 14). Cleveland, Ohio: Investment Casting Institute.
- Kawanishi, T., Seimiya, T., & Sasaki, T. (1970). Corrections for surface tension measured by Wilhelmy method. *Journal of Colloid and Interface Science*, 32(4), 622-627.
- Konrad, C., Brunner, M., Kyrgyzbaev, K., Volkl, R., & Glatzel, U. (2011). Determination of heat transfer coefficient and ceramic mold material parameters for alloy IN73*LC investment castings. *Journal of materials Processing Technology*, 211, pg 181-186.
- Krupaa, I., & Luyt, A. (2001). Physical properties of blends of LLDPE and an oxidized paraffin wax. *Polymer*, 42(17), 7285–7289.
- Kumar, G., & Prabhu, K. N. (2007). review of non-reactive and reactive wetting of liquids on surfaces. *Advances in Colloid and Interface Science*, 133, pg 61-89.
- Kvitek, L., Pikal, P., Kovarikova, L., & Hrbac, J. (2002). The study of the wettability of powder inorganic pigments based on dynamic contact angle measurements using wilhelmy method. *Facultas Rerum Naturalium 2002, CHEMICA 41*, 27-35.
- Lander, L., Siewierski, L., Brittain, W., & Vogler, E. (1993). *Langmuir* 9, 2237.
- Latief, F. D., & Fauzi, U. (2011). Kozeny–Carman and empirical formula for the permeability of computer rock models. *50 (2012)* 117–123.
- Li, H., Chandrashekhara, K., Komaragiri, S., Lekakh, S., & Richards, V. (2014). Crack prediction using nonlinear finite element analysis during pattern removal in investment casting process. *Journal of Materials Processing Technology*, 214, 1418-1426.
- Liu, D.-M. (1996). *Porous ceramic materials*. Switzerland: Trans Tech Publications Ltd.

- Masoodi, R., & Pillai, K. M. (2010). Darcy's law-based model for wicking in paper-like swelling porous media. *Alche Journal*, 56(9), Pp 2257-2267.
- Mueller, T. (2007). A Method to Autoclave QuickCast Pattern. 55th Technical Conference& Expo: Investment Casting Institute.
- Niles, J. C., Anibarro, M., & Fielder, H. (2002). Wax Characterization. *50th Technical Conference& Expo 2002* (p. Paper number 4). Chicago: Investment Casting Institute.
- Oberg, E. (2012). *Machinery's Handbook 29th Edition*. New York: Industrial press.
- Olympus. (n.d.). *Basics of Polarising Microscopy*. Retrieved 2015
- Pal, R., Yan, Y., & Masliyah, J. (1992). *Rheology of Emulsions. In Emulsions: fundamentals and application in the petroleum industry*. Washington D.C: American Chemical Society.
- Paton, N. (2001). *Encyclopedia of Materials - Science and Technology* (Vols. Volumes 1-11). ELSEVIER.
- Pattnaik, S., Karunakar, D., & Jha, P. (2012). Developements in investment casting process- A review. *Journal of Materials Processing Technology* (212), 2332-2348.
- Pavlik Jr., R. S., & Holland, H. J. (2001). Thermal Decomposition of Zircon Refractories. *84[12](2930-36)*.
- PerkinElmer. (2014, September). *DSC 7 specific heat capacity user manual*. Retrieved from <http://www.mse.iastate.edu/files/2011/07/ThermalAnalysisManuals.pdf>
- Peter Wang, M. (2012). How Shell materials and shell properties influence shell cracking. 13th world conference on Investment Casting: Japan Foundry Society.
- Petric, M., Kutnar, A., Kricej, B., Pavlic, M., Kamke, F. A., & Sernek, M. (2009). Surface free energy of viscoelastic thermal compressed wood in: contact angle, wettability and adhesion. *VSP/Brill*, 301-309.
- Piwonka, T., Woodbury, K., & Wiest, J. (2000). Modelling casting dimensions: effect of wax rheology and interfacial heat transfer. *Materials and design*, 21, 365-372.
- Rani, D., & Karunakar, D. B. (2013). Recycling of Pattern Wax in The Investment Casting Process Using Microwave Dewaxing. *IOSR Journal of Engineering*, Vol 3, issue 5, PP 5-10.
- Reilly, C. (2010). Development of Quantitive Quality Assessment Criteria Using Process Modelling. (PhD Thesis).
- Richards, V. L., & Connin, G. (2001). Four-Point Bend Testing to Characterize the strength of Ceramic Mold Shells. *49th Annual Technical Meeting 2001* (p. Paper No.13). Orlando, Florida: Investment Casting Institute.
- Richards, V. L., Jackson, P., Mascree, S. A., & Hahn, T. (2003). Statistical Analysis of three-point and four-point bend testing for the characterization of ceramic mold

- shells. *51th Technical Conference and Expo* (p. paper number 8). Cleveland, Ohio: Invesment Casting Institute.
- Rogers, G. F., & Mayhew, Y. R. (1994). *Thermodynamic and Transport Properties of fluids: S. I. Units*. Fourth Edition: Wiley-Blackwell.
- Rosmait, R. (2007). How refractory particle size, polymer selection and colloidal silica effect autoclave performance. Pittsburg State University: Investment casting institute.
- Sabau, A. S., & Viswanathan, S. (2003). Material properties for predicting wax pattern dimensions in invesment casting. *Materials Science and Engineering*, A362, 125-134.
- Sabau, A., & Viswanathan, S. (2001). Determining Wax Pattern Dimensions in Invesment Casting Using Viscoelastic Models. *49th Annual Technical Meeting* (p. Paper No. 3). Orlando, Florida: Invesment Casting Institute.
- Sabau, A., & Viswanathan, S. (2002). Prediction of Wax Pattern dimensions in Invesment Casting. *American Foundry Society, AFS Transactions 02-103*, 1-14.
- Sauer, B. B., & Dipaolo, N. V. (1991). Surface Tension and Dynamic Wetting of Polymers Using the Wihelmy Method: Applications to High Molecular Weights and Elevated Temperatures. *Journal of Colloid and Interface Science*, 144(2), 527-537.
- Shobanjo, O. (2010). *Fundamental Study of the Waxes Used in Investment Casting*, EngD thesis. University of Birmingham: Chemical Engineering.
- Snow, J. D. (1998). What Happens During Autoclave Dewaxing. *46th Annual Technical Meeting* (p. 5). Invesment Casting Institute.
- Snow, J. D., Scott, D. H., & Synder, B. S. (2002). Permeable Prime Coats: Effect on Dewax Shell Cracking. *50th Technical Conference& Expo* (p. 17). Chicago: Invesment Casting Institute, 50th Technical Conference & Expo.
- Steffe, J. (1996). *Rheological methods in food Process engineering (second edition)*. Freeman Press.
- Sunderland, B., & Richards, V. (2001). Thermal expansion of investment casting pattern wax. 49th Annual technical meeting: Investment casting institute.
- Synder, B. S., Scott, D. H., & Snow, J. D. (2003). A New Combination Shell Strength and Permeability Test. *51th Technical Conference& Expo 2003* (p. 11). Cleveland, Ohio: Invesment Casting Institute.
- Torres, J. (2003). *Thermophysical Properties of Invesment Casting Waxes*, Phd thesis. University of Birmingham: Chemical Engineering.
- Vargaftik, N. B., Volkov, B. N., & Voljak, L. (1983). International Tables of the Surface Tension of Water. *The Journal of Physical Chemistry Reference data*, 12(3), 817-820.

- Verta, C. (2013). RENEW wax technology. Pittsburgh: Investment Casting Institute, 60th Technical Conference& Proceedings.
- Washburn, E. W. (1921). The Dynamics of Capillary Flow. *Phys. Rev* 17, XVII(No.3), 273-283.
- Whitehouse, C., & Dahlin, B. (2008). Effect of wax viscosity and permeability on shell cracking. Dallas: 12th World Conference on Investment Casting .
- Wolfe, C. M., Dickerson, K. L., & Hendricks, M. J. (2009). A New Look at Shell Permeability and the Factors That Impact It. Maumee, Ohio: Ransom & Randolph.
- wolff, T. (1999). Incast 12. (2) 22-24.
- Yang, X. (2009). *United States Patent No. US 20090294086A1*.
- Yao, W., & Leu, M. (1999). Analysis of shell cracking in investment casting with laser stereolithography patterns. *Rapid Prototyping Journal*, 5, 12-20.
- Yuan, C., Jones, S., & Blackburn, S. (2004). The influence of autoclave steam on polymer and organic fibre modified ceramic shells. *Journal of the European ceramic society*, volume 25, issue 7(pg 1081-1087).
- Zienkiewicz, O., Taylor, R., & Nithiarasu, P. (2013). *The finite element method for fluid dynamics* (Seventh edition ed.). Butterworth Heinemann.
- Zienkiewicz, O., Taylor, R., & Zhu, J. (2005). *The Finite Element Method: Its Basis and Fundamentals* (Sixth ed.). Elsevier.

9. PUBLICATIONS

1. Kevin Lee - Wax Thermal Expansion Characterisation, European Investment Casters' Federation 28th International Congress, Lugano – Switzerland 15th-18th June 2014

2. Kevin Lee, Stuart Blackburn, Stewart T. Welch - Adhesion tension force between mould and pattern wax in investment castings
Journal of Materials Processing Technology (2015) Volume 225, pp. 369-374.

10. APPENDICES**Appendix A: Derivation of Strain in wedge test**

Equation of a beam

Radius of a circular segment, R

$$R = \frac{\delta}{2} + \frac{L^2}{8\delta}$$

From bending theory,

$$\varepsilon_x = \frac{y}{R}$$

For edge test

Assumption

d>>displacement of crosshead

Thus,

$$\delta = c. \tan \theta$$

Δ is the deflection of the midpoint with respect to the loading point.

L=2xd

$$\varepsilon_x = \frac{y}{\frac{c. \tan \theta}{2} + \frac{d^2}{2.c. \tan \theta}}$$

Appendix B: Viscosity repeatability test results

Viscosity is measured at 90°C as this the temperature for all wax is fully melted and not too high that starts to affect the viscosity of any wax.

Wax A	90°C				170°C			
Shear rate	Viscosity	Standard deviation	Normal	Standard deviation	Viscosity	Standard deviation	Normal	Standard deviation
10	0.76	0.18	8149.1	1363.5	2.821	0.69	72928	1672.9
100	0.64	0.08	8349.9	1262.0	0.532	0.13	72522	1461.5
1000	0.58	0.06	8420.5	1171.2	0.099	0.02	71972	1352.04
1000	0.60	0.07	8612.5	1103.1	0.096	0.016	72068	1509.4
100	0.71	0.08	8848.2	1121.0	0.494	0.17	72351	1833.5
10	0.88	0.19	9009.9	1135.1	2.931	1.023	72763	1607.3

Wax C	90°C				170°C			
Shear rate	Viscosity	Standard deviation	Normal	Standard deviation	Viscosity	Standard deviation	Normal	Standard deviation
10	2.125	2.965	7736	2340.6	5.95	2.77	62352	7248.6
100	0.879	0.046	7533.7	1947.3	0.469	0.129	62551	5966.6
1000	0.725	0.025	7645.7	2030.4	0.101	0.008	62893	5497.3
1000	0.726	0.022	7595.1	2001.0	0.098	0.013	62911	4849.2
100	0.957	0.174	7977.6	1909.5	0.396	0.149	63009	4524.4
10	1.351	0.195	8190.2	1963.9	3.99	2.178	63520	4553.1

Wax E	90°C				170°C			
Shear rate	Viscosity	Standard deviation	Normal	Standard deviation	Viscosity	Standard deviation	Normal	Standard deviation
10	0.0824	0.0072	8773.6	736.142	0.0211	0.0269	66670	1579.3
100	0.0758	0.0059	8915.8	633.425	0.016	0.0041	67267	1475.6
1000	0.0752	0.0058	8992.6	479.154	0.015	0.0029	67706	1409.8
1000	0.0755	0.0057	9081.1	455.232	0.015	0.0028	68086	1369.2
100	0.0767	0.00579	9265.3	371.012	0.016	0.0028	68389	1214.2
10	0.0787	0.0065	9338.1	361.744	0.026	0.0342	68580	1076.9